Sorption of Eu(III) and Cm(III) on C-S-H phases and bentonite in presence of oxalate and EDTA at low to intermediate ionic strength conditions

Zur Erlangung des akademischen Grades einer

DOKTORIN DER NATURWISSENSCHAFTEN

(Dr. rer. nat.)

von der KIT-Fakultät für Chemie und Biowissenschaften

des Karlsruher Instituts für Technologie (KIT)

genehmigte

DISSERTATION

von

M.Sc. Aline Kathrin Thumm

aus

Ludwigsburg, Deutschland

1. Referent: Prof. Dr. Horst Geckeis
2. Referentin: Prof. Dr. Petra Panak

Tag der mündlichen Prüfung: 22.04.2024

Hiermit versichere ich, dass ich die vorliegende Arbeit selbstständig verfasst und keine anderen als die angegebenen Quellen und Hilfsmittel benutzt habe. Weiterhin versichere ich, dass alle Stellen der Arbeit, die wörtlich oder inhaltlich a*us* anderen Werken übernommen wurden, als solche kenntlich gemacht sind. Die elektronische Fassung dieser Arbeit stimmt mit der schriftlichen Fassung überein. Ferner wurde die vorliegende Arbeit in gleicher oder ähnlicher Form bislang nicht an einer Hochschule des In- oder Auslands als Bestandteil eines Promotionsverfahrens vorgelegt. Ich versichere weiterhin, dass ich keinen vorausgegangenen Promotionsversuch unternommen habe, und dass an keiner anderen Fakultät ein Promotionsverfahren läuft oder erfolglos abgeschlossen wurde. Die Satzung des Karlsruher Instituts für Technologie (KIT) zur Sicherung guter wissenschaftlicher Praxis wurde in der jeweils gültigen Fassung beachtet. Ferner versichere ich, dass die Abgabe und Archivierung der Primärdaten gemäß Absatz A (6) der Regeln zur Sicherung guter wissenschaftlicher Praxis des KIT am Institut gewährleistet ist.

_____ _____

Ort, Datum Unterschrift

Table of Contents

Abstract

In this work, the retention of Eu(III) and Cm(III) by C-S-H phases and bentonite MX 80 in presence of EDTA and oxalate is studied. Cementitious materials and bentonites are frequently used in repositories for high-, intermediate- and low-level radioactive waste (HLW, ILW, LLW) as near-field barrier components. Organic ligands such as EDTA and oxalate are abundant in ILW and LLW as waste components due to their application as decontamination reagents in nuclear facilities. All experiments were performed in NaCl and $CaCl_2$ electrolyte solutions from low to intermediate ionic strength. While some experimental data for low ionic strength systems exist in the literature, this is not the case for solutions of high salinity. Such conditions are, however, relevant for potential host rocks in the vicinity of rock salt formations as is the case in northern German clay rock formations. Batch sorption experiments and Time Resolved Laser Fluorescence Spectroscopy (TRLFS) were used as the primary analytical methods. Different experimental parameters were varied, *e.g.* [EDTA], sorption time, ionic strength (I_m), pH, Calcium to Silicon ratio (C/S).

High retention of Eu(III) (log R_d = 5 – 6, with R_d in L/kg) on C-S-H phases is observed in presence of [Oxalate] ≤ 10^{-3} M in NaCl and $CaCl_2$ solutions. This is explained by the quantitative precipitation of $Ca(Ox)\cdot H_2O(s)$, which significantly decreases the concentration of oxalate in the aqueous phase. For [EDTA] ≤ 10^{-3} M, an equally high retention is observed. It is concluded, that low [EDTA] have no significant impact on the sorption of Eu(III) on C-S-H phases. This observation is confirmed by TRLFS measurements, which shows exclusively the presence of a Cm(III) species incorporated into the C-S-H structure.

At [EDTA] = 10^{-2} M, different results are obtained: In NaCl solution at C/S ~ 1.0, a low retention of Eu(III) (log R_d = 2 – 3) is detected after 7 d, while an increasing retention (log R_d = 5 – 6) is shown after 50 d. TRLFS shows the presence of two ternary Cm(III)-OH-EDTA species in the aqueous phase after short contact times. After longer equilibration times, the incorporation of Cm(III) into the C-S-H phase is observed. In NaCl solution (C/S ~ 1.3) and $CaCl_2$ solution (C/S ~ 1.0 and C/S ~ 1.3), low retention of Eu(III) (log R_d = 2 – 3) is observed over the whole experimental time range of 50 d.

This is explained by the stabilization of Eu(III) in solution by the formation of stable ternary Ca-Cm(III)-EDTA complexes.

The examination of the Eu(III) and Cm(III) speciation of the Ca containing ternary and quaternary complexes is and their structural characterization is further carried out in the context of this work. The analytical methods used hereby are TRLFS and Extended X-ray Absorption Fine Structure (EXAFS). TRLFS spectra and fluorescence lifetimes are recorded for two different series, which differ primarily in the ionic strength. Respective solutions contain various concentrations of Ca, and the pH_m is varied between 8.5 - 12.5. All of this serves the preliminary determination of the stability constants. The structural characterization of Ca-Cm(III)-EDTA and Ca-Cm(III)-OH-EDTA is performed by EXAFS. Two independent series were measured for these systems, which are distinguished by different pH values (pH_m = 8.7 and 11.2) and different Ca concentrations. The results support the predominance of the ternary Ca(II)-Am(III)/Cm(III)-EDTA species at pH_m = 8.7. At pH_m = 11.2, a mixture of the ternary and the quaternary Ca containing species is found. Furthermore, the first structural information on these species has been obtained. This can be derived as follows: The Am(III) center is 8-fold coordinated, with six sites occupied by EDTA with Am(III)-N- and Am(III)-O-bonds. The other two coordination sites are occupied by OH and H_2O ligands. The Ca atoms are supposed to be located in the outer coordination sphere of Am(III) and are associated with the non-chelating O atoms of the carboxyl groups.

In case of the bentonite samples, oxalate decreases the uptake of Eu(III) only when calcium ions are excluded from the system. It is concluded that the precipitation of solid $Ca(Ox)\cdot H_2O(s)$ effectively removes oxalate from the solution. In presence of [EDTA] = 10^{-2} M, the retention of Eu(III) on bentonite is significantly reduced up to pH_m = 10 with log R_d ~ 2, while at higher pH the retention increases to values of log R_d ~ 4 – 6. In contrast to oxalate, this effect is observed for NaCl as well as for $CaCl_2$ solutions. This might be explained with the successive formation of negatively charged ternary Ca-Eu(III)-EDTA complexes between pH_m = 3 – 10. For pH_m > 10, Eu(III) binding to deprotonated surface OH functional groups of montmorillonite prevails and outcompetes EDTA complexation. This results in increasing retention. The results

obtained in this study provide quantitative insights into sorption mechanisms occurring in cement/bentonite-*Ln*/*An*(III)-ligand systems. The present work clearly emphasizes the strong impact of oxalate and EDTA on the sorption of Eu/Cm(III) by cement phases and bentonite under specific hydro chemical conditions. This study also provides strong evidence for the key role of Ca in the formation of ternary/quaternary complexes with trivalent *An* and EDTA, and thus in the retention processes. Moreover, the results of the present study provide a solid basis for the quantitative description and the mechanistic understanding of the uptake of *An*(III)/*Ln*(III) by cement phases and bentonite in the presence of key organic ligands that are expected in repositories for the disposal of L/ILW.

Zusammenfassung

In dieser Arbeit wird die Rückhaltung von Eu(III) und Cm(III) durch C-S-H-Phasen und Bentonit MX80 in Gegenwart der organischen Liganden EDTA und Oxalat untersucht. Zementartige Materialien und Bentonite werden häufig als Nahfeldbarrieren in Endlagern für hoch-, mittel- und schwach radioaktive Abfälle (HLW, ILW, LLW) eingesetzt. EDTA und Oxalat sind aufgrund ihrer Verwendung als Dekontaminationsreagenzien in kerntechnischen Anlagen als Abfallkomponenten in den radioaktiven Abfällen reichlich vorhanden. Alle Experimente wurden in NaCl- und $CaCl_2$-Elektrolytlösungen mit niedriger bis hoher Ionenstärke durchgeführt. Während es in der Literatur einige experimentelle Daten für Systeme mit niedriger Ionenstärke gibt, ist dies nicht der Fall für Lösungen mit hohem Salzgehalt. Solche Bedingungen sind jedoch für potenzielle Wirtsgesteine, die in der Nähe von Steinsalzformationen, wie sie in norddeutschen Tongesteinsformationen vorkommen, relevant. Als primäre Analysemethoden wurden Batch-Sorptionsexperimente und zeitaufgelöste Laserfluoreszenzspektroskopie (TRLFS) eingesetzt. In diesem Zusammenhang wurden verschiedene experimentelle Parameter variiert, z.B. [EDTA], Sorptionszeit, Ionenstärke (I_m), pH-Wert, Calcium-Silizium-Verhältnis (C/S).

Eine hohe Retention von Eu(III) (log R_d = 5 - 6, mit R_d in L/kg) an den C-S-H-Phasen wird in Anwesenheit von [Oxalat] ≤ 10^{-3} M in NaCl- und $CaCl_2$-Lösungen beobachtet. Dies ist auf die quantitative Ausfällung von Ca(Ox)-H_2O(s) zurückzuführen, die die Oxalat Konzentration in der wässrigen Phase erheblich verringert. Für [EDTA] ≤ 10^{-3} M wird eine ähnlich hohe Retention beobachtet. Daraus kann geschlussfolgert werden, dass niedrige [EDTA] keinen signifikanten Einfluss auf die Sorption von Eu(III) an C-S-H-Phasen haben. Dies wird durch TRLFS-Messungen bestätigt, die ausschließlich die Anwesenheit einer inkorporierten Cm(III)-Spezies in der C-S-H-Struktur zeigen.

Bei [EDTA] = 10^{-2} M, werden davon abweichende Ergebnisse erzielt. In NaCl-Lösung bei C/S ~ 1.0 wird nach 7 d eine geringe Retention von Eu(III) (log R_d = 2 - 3), nach 50 d eine zunehmende Retention (log R_d = 5 - 6) beobachtet. TRLFS zeigt die Anwesenheit von zwei ternären Cm(III)-OH-EDTA-Spezies in der wässrigen Phase nach kurzen Kontaktzeiten. Nach längeren Äquilibrierungszeiten wird der Einbau von Cm(III) in die C-S-H-Phase beobachtet. In NaCl-Lösung (C/S ~ 1.3) und $CaCl_2$-Lösung

(C/S ~ 1.0 und C/S ~ 1.3) wird über den gesamten Versuchszeitraum von 50 d eine geringe Retention von Eu(III) (log R_d = 2 - 3) beobachtet. Dies wird durch die Stabilisierung von Eu(III) in Lösung, die zur Bildung stabilen ternäre Ca-Cm(III)-EDTA-Komplexe führt erklärt.

Im Rahmen dieser Arbeit wird die Untersuchung der Eu(III)- und Cm(III)-Speziation von Ca-haltigen ternären und quaternären Komplexen und deren strukturelle Charakterisierung durchgeführt. Als analytische Methoden werden TRLFS und Extended X-ray Absorption Fine Structure (EXAFS) eingesetzt.

Dabei werden TRLFS-Spektren und Fluoreszenzlebensdauern für zwei verschiedene Serien aufgenommen, die sich hauptsächlich in der Ionenstärke unterscheiden. Die jeweiligen Lösungen enthalten unterschiedliche Ca-Konzentrationen und der pH-Wert wird zwischen 8.5 und 12.5 variiert. All dies dient der vorläufigen Bestimmung der Stabilitätskonstanten.

Die strukturelle Charakterisierung von Ca-Cm(III)-EDTA und Ca-Cm(III)-OH-EDTA erfolgt mittels EXAFS. Für diese Systeme wurden zwei unabhängige Serien gemessen, die sich durch verschiedene pH-Werte (pH_m = 8.7 und 11.2) und Ca-Konzentrationen unterscheiden. Die Ergebnisse zeigen die dominierende Stellung der ternären Ca(II)-Am(III)/Cm(III)-EDTA-Spezies bei pH_m = 8.7. Bei pH_m = 11.2 erhält man ein Gemisch bestehend aus der ternären und quaternären Ca haltigen Spezies. Darüber hinaus wurden erstmals strukturelle Informationen gewonnen. Diese können wie folgt abgeleitet werden: Das Am(III)-Zentrum ist 8-fach koordiniert, wobei sechs Stellen durch EDTA mit Am(III)-N- und Am(III)-O-Bindungen besetzt sind. Die beiden anderen Koordinationsstellen sind durch OH- und H_2O-Liganden besetzt. Die Ca-Atome befinden sich wahrscheinlich in der äußeren Koordinationssphäre von Am(III) und sind an die nicht-chelatisierenden O-Atome der Carboxylgruppen gebunden. Im Falle der Bentonit Proben reduziert Oxalat die Aufnahme von Eu(III) nur dann, wenn Calciumionen aus dem System ausgeschlossen sind. Daraus wird geschlussfolgert, dass die Ausfällung von festem Ca(Ox)-H_2O(s) Oxalat wirksam aus der Lösung entfernt. In Gegenwart von [EDTA] = 10^{-2} M ist die Retention von Eu(III) an Bentonit bis pH_m = 10 mit log R_d ~ 2 deutlich reduziert, während bei höheren pH-Werten die log R_d-Werte auf Werte von log R_d = 4 - 6 ansteigen. Im Gegensatz zu Oxalat wird dieser

Effekt sowohl für NaCl- als auch für $CaCl_2$-Lösungen beobachtet. Dies kann möglicherweise auf die sukzessive Bildung von negativ geladenen ternären Ca-Eu(III)-EDTA-Komplexen zwischen pH_m = 3 - 10 zurückgeführt werden. Bei pH_m > 10 überwiegt die Bindung von Eu(III) an die deprotonierten funktionellen OH-Gruppen der Montmorillonitoberfläche und verdrängt die EDTA-Komplexbildung. Dies führt zu einer Erhöhung der Retention.

Die in dieser Studie erzielten Ergebnisse geben einen quantitativen Einblick in die Sorptionsmechanismen, die in Zement/Bentonit-*Ln*/*An*(III)-Ligand Systemen auftreten. Die vorliegende Arbeit unterstreicht deutlich den starken Einfluss von Oxalat und EDTA auf die Sorption von Eu(III)/Cm(III) durch Zementphasen und Bentonit unter bestimmten hydrochemischen Bedingungen. Diese Studie liefert auch starke Beweise für die Schlüsselrolle von Ca bei der Bildung von ternären/quaternären Komplexen mit dreiwertigem *An* und EDTA und damit bei den Retentionsprozessen. Die Ergebnisse dieser Studie liefern eine solide Grundlage für die quantitative Beschreibung und das mechanistische Verständnis der Aufnahme von *An*(III)/*Ln*(III) durch Zementphasen und Bentonit in Gegenwart wichtiger organischer Liganden, die in Endlagern für L/ILW erwartet werden.

1 Introduction

1.1 Nuclear waste disposal

Disposal of radioactive waste in underground repositories is the preferred approach for high-level radioactive waste (HLW) internationally.[1, 2] For low and intermediate level waste (L/ILW) a storage above ground (*e.g.* France) or at shallow deeps near the earth surface (*e.g.* Sweden) is favorized by some of countries. The primary objective of all repository concepts is to minimize the release of radionuclides (RN) into the geo- and the biosphere.[3, 4] In Germany, all types of radioactive waste will be disposed in deep geological repositories.[5-7]

The potential intrusion of water into the repository, which could lead to the migration of RN, is a major concern. For this reason, the repository concept includes a multi-barrier approach, consisting of various technical-, geotechnical- and geological barriers. The first so called technical barriers are waste matrix and container walls. Backfill materials such as crushed salt (in rock salt host rocks), bentonite (in crystalline or clay rock host rocks), dams and seals shall prevent water from entering the repository as part of the geotechnical or geoengineered barrier. Finally, the host rock represents the geological barrier.

In this context, a precise and quantitative description of the interaction processes between the RN and the constituents present in the near- and far field of repository systems is required. The chemical environment in the near field is determined by the corrosion of the waste, the waste containers and the liner and backfill materials and their interaction with the respective intruding ground- or porewater. In the far field, the chemical behavior of the RN is affected by the natural groundwater composition and the natural rocks associated with the porewater.[8, 9]

Cementitious materials are considered in some repository concepts as waste matrix to condition the radioactive waste and/or for construction purposes.[10, 11] They offer favorable properties such as strong RN immobilization capacity, easy availability and comparatively low costs. Water intrusion into a potential repository, in which the water comes into contact with the cement, leads to pH values in the alkaline to hyperalkaline

range (pH = 9 - 13.3). Cementitious materials have the ability to maintain this high pH value over a long period of time. Moreover, reducing conditions are also expected to develop due to the anoxic corrosion of Fe and steel components. Cement shows high sorption capacities, due to the high surface area of the C-S-H phases. C-S-H phases are the major binding component of cementitious materials. High sorption capacities increase the retention of many RNs and thus limit their migration.[10, 11] Clay materials (*e.g.,* bentonite) are often used in certain disposal concepts as they are used as backfill materials. Bentonite is a clay composed of clay minerals and other components, where montmorillonite is the main component. Montmorillonite belongs to the smectite clay group, which are primarily characterized by high swelling capacities in the presence of water. This, in turn, enables bentonite to seal potential fractures and suppress water ingress. It also offers high sorption capacities towards many RNs including tri- and tetravalent *An* and *Ln*, resulting in their strong retention and thus their immobilization.[2, 12]

In Germany, three types of host rocks are considered: Salt, clay and crystalline rock (*e.g.,* granite). All three materials have been investigated in the past decades for their properties with regard to their suitability for a potential repository.[2] With respect to clay rocks in Germany, Opalinus clay (OPA) in the southern part, or Jurassic and Cretaceous clay formations in the northern part are currently considered as potential host rocks for a repository for HLW (see Figure 1).[7] Also the German licensed repository for I/LLW is shaft Konrad is located in the northern part of Germany close to Braunschweig. It shall start operation in the beginning of the 2030s. Shaft Konrad is a former iron ore mine, where the foreseen emplacement caverns are overlain by 160-400 m thick layers of cretaceous clay rock.[13] The clay formations in northern Germany contain highly saline pore waters dominated by NaCl and $CaCl_2$ solutions. Ionic strength up to I_m = 4.9 m are reached due to the vicinity to evaporite formations, with an increase of the salt content with the depth.[14] The high salt content in the pore water can significantly affect the migration and retention behavior of RN: In particular, Ca, being present in concentrations from 0.13 to 0.35 M, is known to form stable complexes with EDTA and oxalate.[15] The formation of these complexes may result in a reduced effect of the organic compounds on the RN mobilization, due to a significantly lower concentration of free ligand in solution.

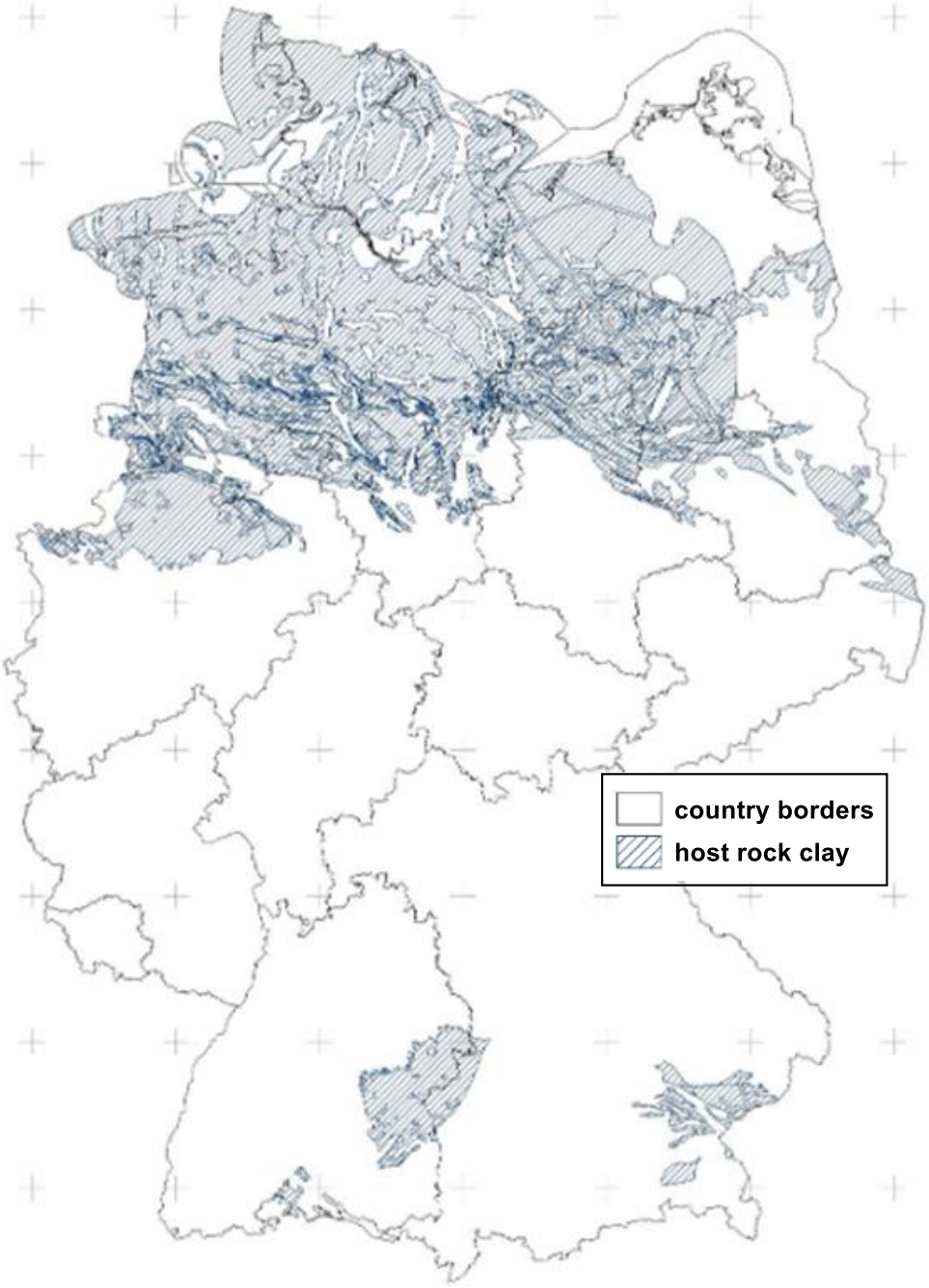

Figure 1: The map of Germany: On top: The northern clay formations (Jurassic and Cretaceous) marked in grey. Their porewater mainly contain NaCl and $CaCl_2$ up to high ionic strength of I_m = 4.9 m. The southern German clay formations are marked in grey at the bottom of the map.[14, 15]

There are different classifications of radioactive waste: High Level Radioactive Waste (HLW) or Highly Active Radioactive Waste (HAW), Intermediate Level Radioactive Waste (ILW) and Low Level Radioactive Waste (LLW).[16] HLW/HAW is mostly

produced from spent fuel elements or originates from reprocessing of spent fuel. They are categorized as radioactive waste with high heat generation. In this context, the use of cementitious materials is part of the Supercontainer concept currently discussed for the disposal of HLW/HAW in deep geological layers in Belgium. The Supercontainer consists of various barriers: A carbon steel container contains the radioactive waste surrounded by a thick concrete buffer. The highly alkaline conditions of cementitious porewaters lead to the formation of a passive oxide film at the carbon steel container material and by this a low and uniform rate of corrosion is achieved.[17] I/LLW is designated as radioactive waste with intermediate to low heat generation. It is a heterogeneous mixture resulting from the decommissioning or operation of nuclear facilities, industry or scientific research and to a minor degree from the medical sector. I/LLW makes up the largest volume percentage of radioactive waste in Germany, with however < 5% of the total radioactivity to be disposed.[18] Due to its diversity of origin, it contains a large variety of additional compounds, like strong organic complexing agents. Cement additives, for instance gluconic acid (GLU), are used to improve the mechanical properties of cement as *e.g.,* retarding admixture. Further organic materials originate from cellulose-based materials, ion exchange resins or decontamination agents such as ethylenediaminetetraacetic acid (EDTA) or nitrilotriacetic acid (NTA).[19] Oxalate, the anion of oxalic acid, is present in some waste streams from the reprocessing processes, where it is used for the precipitation of uranium and plutonium as oxalates and subsequent formation of the respective oxides for the production of MOX fuel elements.[20] The presence of organic materials in these waste forms can increase the solubility of the waste matrix by forming soluble complexes with the RN. Therefore, it is possible that organic substances reduce the retention of RN by forming soluble complexes.

1.2 Actinides (An) and Lanthanides (Ln)

Ln and *An* form the “f-block” of the periodic table of the elements. *Ln* include the elements from cerium to lutetium with the atomic numbers Z = 58 – 71, where thorium to lawrencium with the atomic numbers Z = 90 – 103 belong to the *An* (see Figure 2). The focus of this work is on trivalent *Ln* and *An*. This low oxidation state is of high relevance for a deep geological repository, as strongly reducing conditions are expected in the near-field due to the corrosion of the steel containers.[21] A major contributor of the trivalent *An* in I/LLW is Am(III), but also Pu(III).[22, 23] The long-term radiotoxicity of this waste forms is mainly determined by Pu, and the minor actinides Am, Cm and Np. These elements are formed from ^{238}U by neutron capture such as (n, γ) and (n, 2n) reactions in a ^{235}U fission reactor. The neutron capture reactions, followed by β^--decay in the reactor are shown below.[24]

$$^{238}_{92}U\ (n,y)\ ^{239}_{92}U \xrightarrow{\beta^-} {}^{239}_{93}Np \xrightarrow{\beta^-} {}^{239}_{94}Pu \quad and \quad {}^{238}_{92}U\ (n,2n)\ {}^{237}_{92}U \xrightarrow{\beta^-} {}^{237}_{93}Np$$

$$^{239}_{94}Pu\ (n,y)\ ^{240}_{94}Pu\ (n,y)\ ^{241}_{94}Pu \xrightarrow{\beta^-} {}^{241}_{95}Am \quad and \quad {}^{241}_{94}Pu(n,y){}^{242}_{94}Pu(n,y){}^{243}_{94}Pu \xrightarrow{\beta^-} {}^{243}_{95}Am$$

Under strongly reducing conditions, Pu will be present in the trivalent oxidation state, while Am and Cm are almost exclusively present as trivalent cations in aqueous solution. In addition, due to their very similar chemical properties, Eu(III) can be used as chemical analogue for *An*(III). *Ln* can occur in HAW/HLW as fission products of *An*.[22] Trivalent *An*/*Ln* are able to form very stable complexes with strong organic ligands such as oxalate and EDTA, which might affect their mobility in the near- and far-field of a nuclear waste repository.[15]

The electron configurations of the *Ln* include 4*f*-electrons, while *An* additionally have 5*f*-electrons.[24] The most stable oxidation state of *Ln* is +III, but they can also be stabilized in other oxidation states such as +II or +IV. These include Sm(II), Eu(II), Tm(II) and Yb(II), which can be present in divalent form and Ce(IV), Pr(IV), Nd(IV), Tb(IV) and Dy(IV), which can under certain conditions exist as tetravalent ions.[24, 25]

In case of *An* with Z > 95, the most stable oxidation state is +III. Only No(II) forms the exception, as it shows the most stable oxidation state of +II. In contrast, the “lighter”

An (Z < 95) show a greater variety of the oxidation states from +III to +VII. All possible oxidation states of *Ln* and *An* are illustrated in Figure 2.[26]

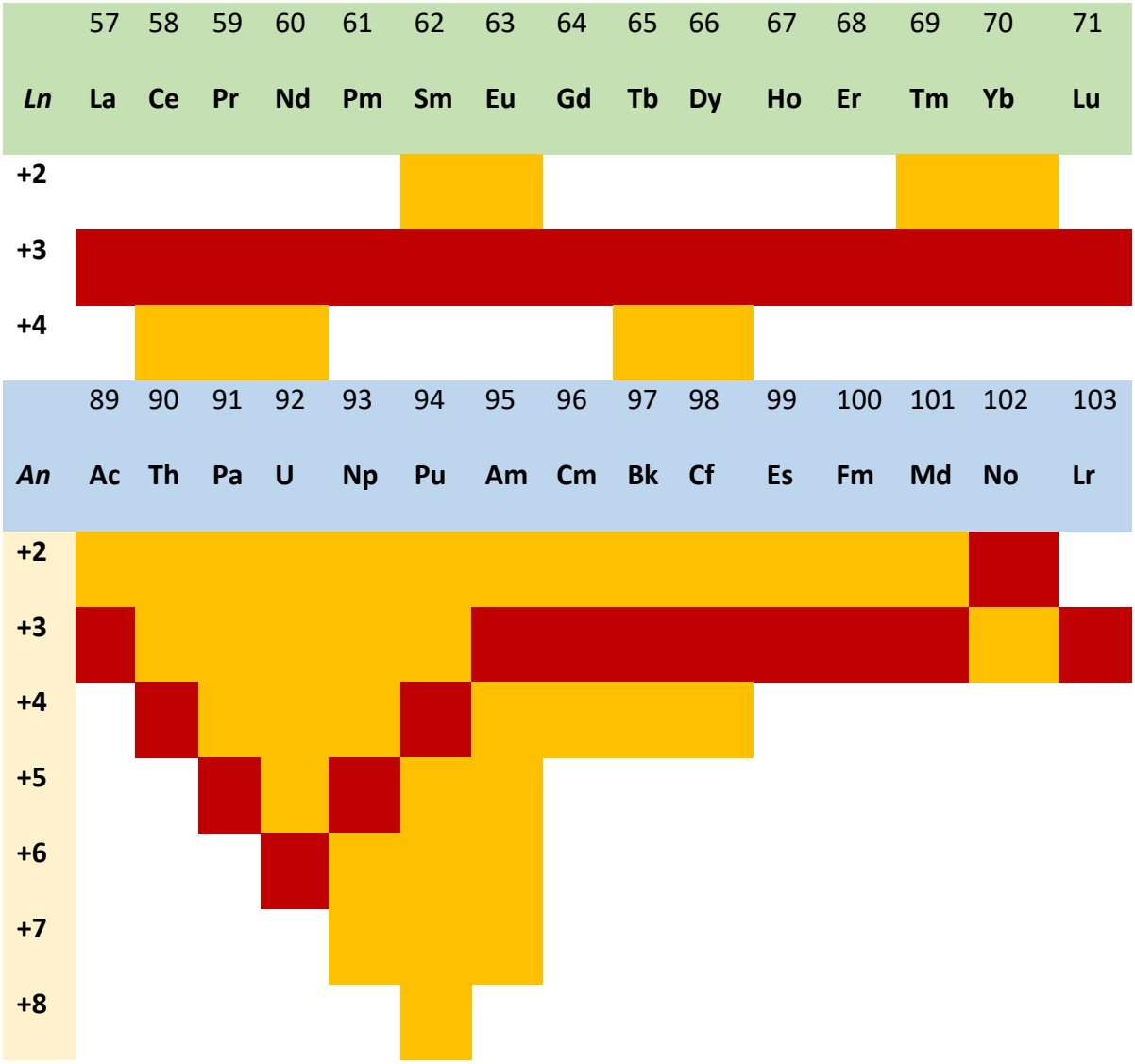

Figure 2: The elements of the f-block in the periodic table of the elements: Top: *Ln* (marked in green, Z = 57 – 71) and center: *An* (marked in blue, Z = 89 – 103). *Ln* commonly have their most stable oxidation state with +III. *An* can have several oxidation states ranging from +III to +VII. For every element the most stable oxidation state is marked in red, while the other possible oxidation states are marked in yellow.[26]

The trends of the oxidation states of the *Ln* and *An* are explained as follows: In general, the f-orbitals are large and diffuse and the respective f-electrons are less localized, compared to the s-, p- and d- electrons. Hence, the screening of the positive charge of the nucleus by the f-electrons is weak, leading to a stronger attraction of the outer s-

and p-electrons. For the *Ln*, this results in a large energetic gap between the 4f and 5d orbitals, favoring a trivalent oxidation state of the *Ln*. In contrast, the inner s- and p-electrons of the *An* exhibit a significant increase of their radial velocity, resulting in an increase of their relativistic mass. This leads to a stronger attraction of these electrons to the nucleus and a stronger shielding of its positive charge. Due to this shielding effect, the 5f electrons of the lighter *An* are less strongly bound to the nucleus and are spatially more expanded, as is illustrated by the radial electron density distribution of U^{3+} and Nd^{3+} in Figure 3, adapted from Crosswhite *et al.*.[27] This allows the lighter actinides to participate in covalent chemical bonds, and also enables them to access higher oxidation states, due to the smaller energetic difference of the 5f and 6d orbitals. However, as the charge of the nucleus increases in the *An*-series, the 5f orbitals are successively contracted and the energetic difference of the 5f and 6d orbitals increases. For $Z \geq 95$ (Am to Lr), the variety of oxidations states is reduced and the ions favor almost exclusively the trivalent oxidation state. An exception hereby is No(II), with its fully filled 5f shell. The chemical properties of the "heavier" *An* are therefore similar to those of *Ln*.[24, 26, 28-30]

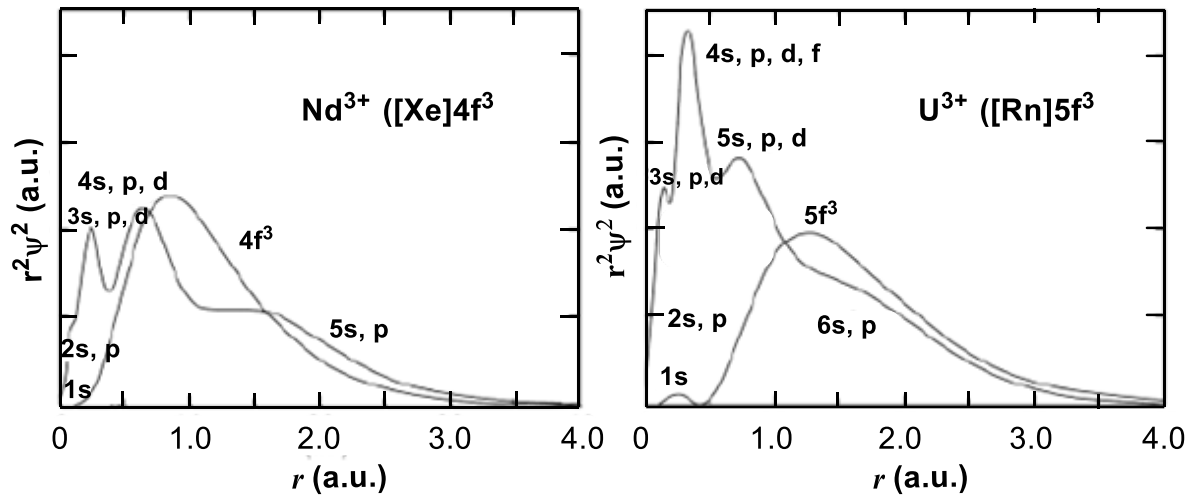

Figure 3: Radial electron density distribution of the orbitals of Nd^{3+} with electron configuration $[Xe]4f^3$ and of U^{3+} with the electron configuration $[Rn]5f^3$ adapted from Crosswhite *et al.*.[27]

In aqueous systems and absence of complexing ligands, tri- and tetravalent *An* are usually present as solvated cations, *e.g.* An^{3+}, An^{4+} in the acidic pH region. Hydrolyzed

species occur with increasing pH values. At higher oxidation states +V and +VI, actinyl species such as AnO_2^+ or AnO_2^{2+} are formed (see Figure 4).[31]

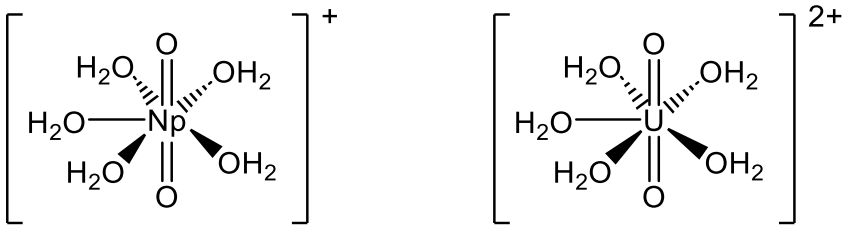

Figure 4: Structural formula of the Np(V) and U(VI) actinyl ions, which are common for higher oxidation states in aqueous solutions.

The oxygen atoms of the actinyl ions are linearly coordinated to the metal center. The strongly electronegative oxygen atoms, transfer charge density from the metal ion to the oxygen. As a result, the effective charge at the metal center of *An* in oxidation states V and VI no longer corresponds to the formal charge of the actinyl ion (+I or +II). The effective charge Z_{eff} of actinide ions for the different redox states follows the order: An^{4+} (Z_{eff} = 4) > AnO_2^{2+} (Z_{eff} = 3.3±0.1), An^{3+} (Z_{eff} = 3), AnO_2^+ (Z_{eff} = 2.3±0.2).[26 32]

The redox potential (E_h) in solution controls the redox reactions of the *An*(IV)/*An*(III) and *An*(VI)/*An*(V), which is reflected *e.g.* by the following reactions:

$$\mathbf{An^{4+} + e^- \rightarrow An^{3+}}$$

$$\mathbf{AnO_2^{2+} + e^- \rightarrow AnO_2^{+}}$$

Besides the E_h, the transition from *An*(V) to *An*(IV) is also related to the pH value. This is reflected in the following reaction.

$$\mathbf{AnO_2^{+} + 4\ H^{+} + e^- \rightarrow An^{4+} + 2\ H_2O}$$

Plutonium is a particularly interesting example of the interplay between the E_h and the pH on the speciation. As shown in Figure 2, Pu can be present in different oxidation states in aqueous solution. The dominant oxidation state of Pu is a function of the E_h and pH of the solution, as can be seen in the Pourbaix diagram in Figure 5.[33] In this context it is noteworthy, that without controlled redox conditions, the oxidation state and with it the speciation of Pu (or other redox sensitive RN) can significantly change.

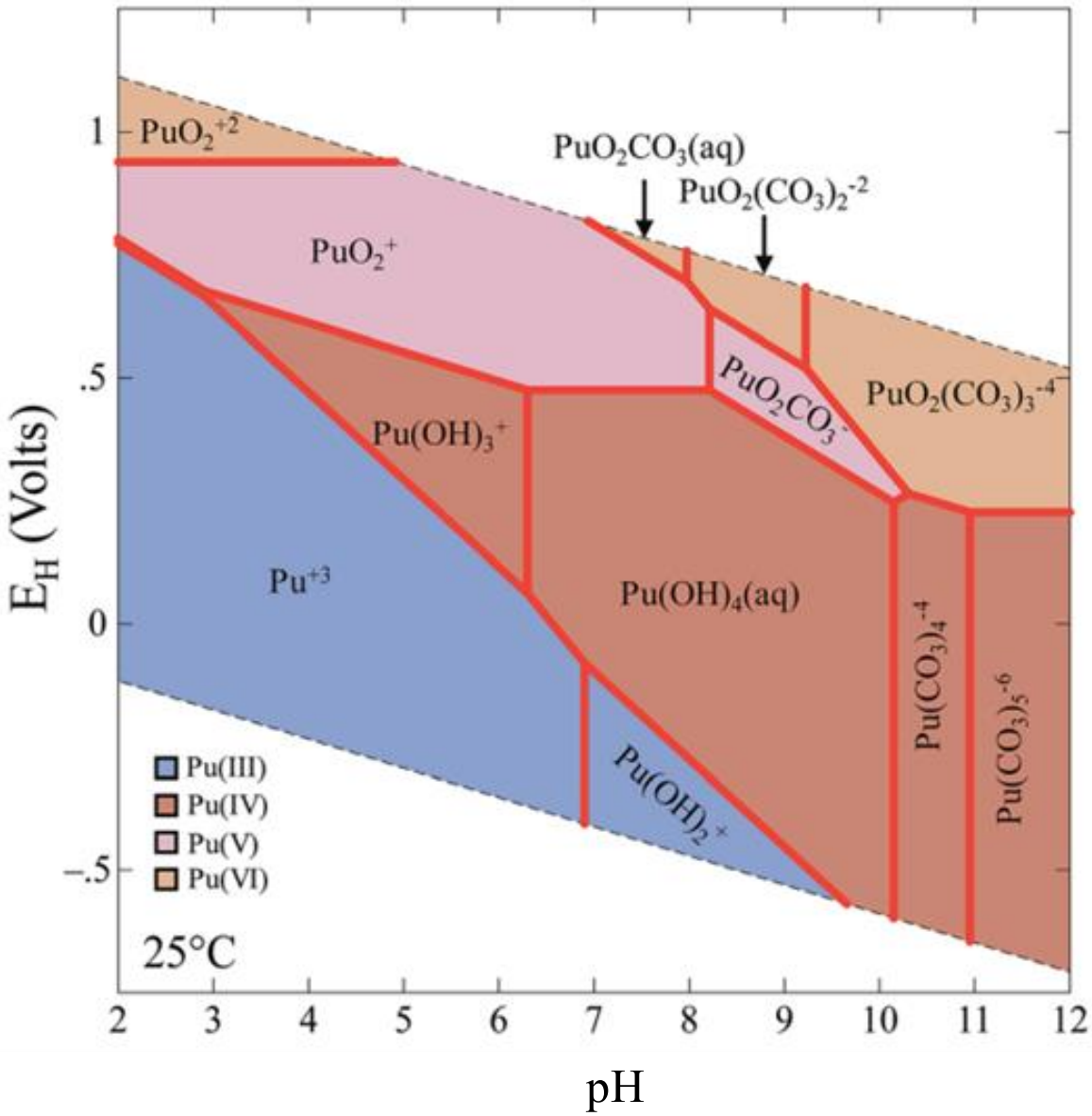

Figure 5: Pourbaix diagram of Plutonium under ambient conditions. The diagram reflects the effects on the Pu speciation and the interaction between the E_h and pH value.[33]

An and *Ln* cations are known as strong electron acceptors with low polarizability. They are classified as hard Lewis's acids in the context of the "hard and soft acids and bases" (HSAB) concept. This makes them particularly accessible to hard Lewis bases such as oxygen-containing functional groups.[34] For trivalent *An* and *Ln*, the following inorganic ligands are sorted by their complex stability in the following series below:[29]

CO_3^{2-} > OH^- > F^-, HPO_4^-, SO_4^{2-}> NO_3^- > Cl^- > ClO_4^-

1.3 Complexation with the organic ligands oxalate and EDTA

In the frame of this work, oxalate and EDTA are investigated with respect to their effects on the retention of Eu(III) and Cm(III) on C-S-H phases and bentonite MX80. Their structural formulas are illustrated in Figure 6, while the stability constants for the different *An*(III)/*Ln*(III)-oxalate/EDTA complexes are given in Table 1.[15] Both ligands are known for their strong complexing properties towards trivalent *An* and *Ln*.

Oxalate, as the anion of oxalic acid, naturally occurs in soils and water due to animal and plant residues.[35] It is also present in certain waste streams from reprocessing processes, *e.g.* through precipitation of uranium and plutonium as oxalates for the production of MOX fuels.[20] Oxalate is a strong ligand, which can bind to metal ions with the two carboxylic acid functional groups in mono or bidentate mode (see Figure 6). The polyamino carboxylic acid EDTA is present in I/LLW repositories due to its use as a decontamination or cleaning reagent in nuclear facilities.[36] As hexadentate chelating ligand, EDTA contains four carboxylic acid functional groups and two nitrogen atoms with two lone electron pairs.[37,24]

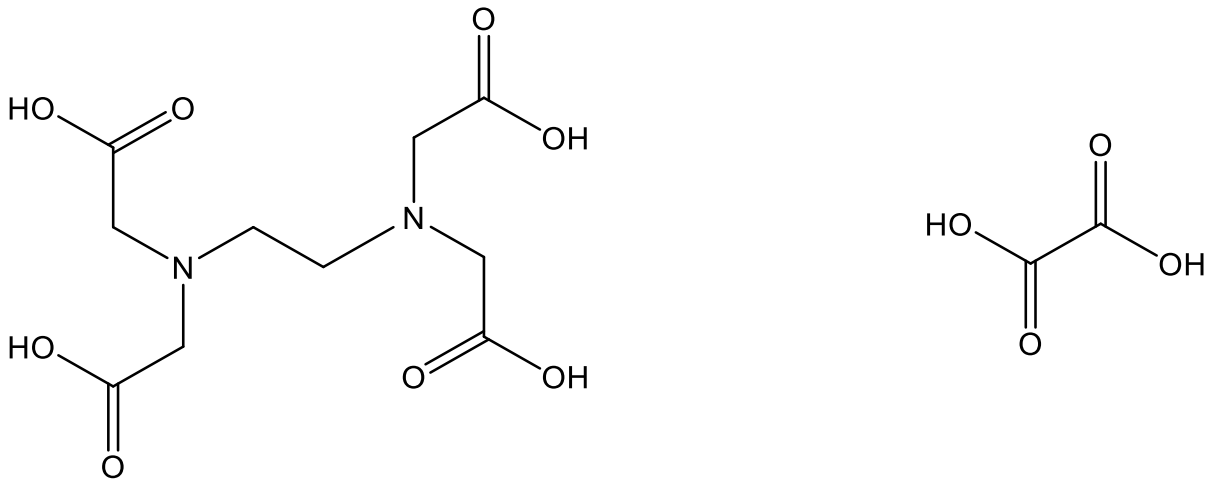

Ethylendiamintetraaceticacid (EDTA) **Oxalic acid**

Figure 6: Structural formula of EDTA (left), including four carboxylic functional groups and the nitrogen atoms, and oxalate (right) with two directly linked carboxylic acid functional groups.

The high salt content of the pore waters in the northern German clay formations can strongly affect the aqueous speciation of RN and organic ligands. Thus, the aqueous

speciation of Am(III) as well as EDTA and oxalate is described in NaCl and $CaCl_2$ solutions. First, the effects of pure NaCl solutions, then a mixture of NaCl and $CaCl_2$, and finally a pure $CaCl_2$ solution are discussed. For the mixture of NaCl and $CaCl_2$, [Ca] = 0.02 M is chosen. This represents the maximum [Ca] in aqueous solutions in contact with C-S-H phases, with a Calcium-to-silicon ratio of 1.65.[23] It is used as an example, to demonstrate the effect of Ca in NaCl solutions for C-S-H phases. Generally C/S ratios for C-S-H phases can vary between 0.66 – 1.7.[38]

Figure 7 shows the Am(III) speciation as well as the oxalate speciation in solution in presence and absence of Ca. Figure 8 shows the aqueous speciation of Am(III) and EDTA in presence and absence of Ca. The corresponding complexation constants of the individual complexes are listed in Table 1. Due to the lack of SIT ion interaction coefficients for some of the *An*(III) species, ionic strength corrections have been performed using the Debye- Hückel method, which may result in some inaccuracies when used at I = 1.0 M.

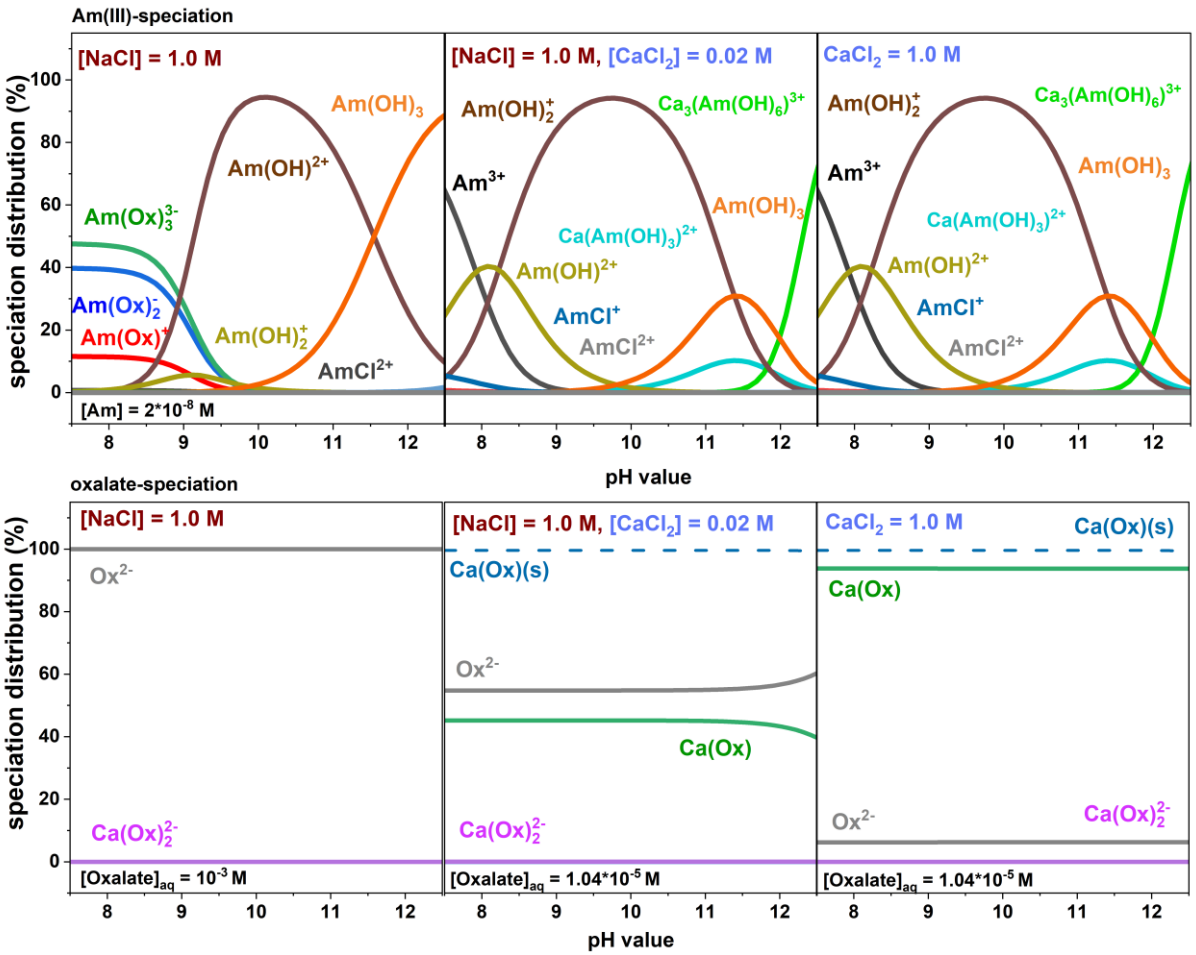

Figure 7: Speciation diagrams for the aqueous Am(III) (top) and Oxalate (bottom) speciation between pH = 7.5 – 12.5. Left: NaCl system, I = 1.0 M; Center: NaCl system, I = 1.0 M and [Ca] = 0.02 M, Right: $CaCl_2$ system, I = 1.0 M. For the Am(III) speciation, [Am] = $2 \cdot 10^{-8}$ M was chosen. In absence of Ca, [Oxalate] = 10^{-3} M is used for the aqueous speciation (left). In the presence of Calcium, $9.90 \cdot 10^{-4}$ M of the used oxalate precipitates as Ca(Ox)(s) (center and right). Thus, the aqueous speciation was modeled with an oxalate concentration of $1.04 \cdot 10^{-5}$ M.

In NaCl solution and in the absence of Ca^{2+}, the aqueous speciation of Am(III) is mainly determined by the Am(III) oxalate species $Am(Ox)^{+}$, $Am(Ox)_2^{-}$ and $Am(Ox)_3^{3+}$ between pH = 7.5 – 9.0, with the latter one being the main species. For pH > 9.5, Am-hydroxo species control the aqueous speciation. Regarding the oxalate itself, the free oxalate species Ox^{2-} predominates over the whole studied pH range.

In NaCl solution and in presence of [Ca] = 0.02 M, the aqueous Am(III) speciation is mainly determined by hydroxo-complexes such as $Am(OH)_3$ and $Am(OH)^{2+}$ among others. At pH > 10, additionally $Ca(Am(OH)_3)^{2+}$ and $Ca_3(Am(OH)_6)^{3+}$ contribute to the aqueous speciation. Due to the very low solubility product (K_L = $2.7 \cdot 10^{-9}$ M) of

Ca(Ox)(s), about $9.90 \cdot 10^{-4}$ M of the initial oxalate is precipitated as Ca(Ox)(s), while $1.04 \cdot 10^{-5}$ M oxalate remains in solution.[24] Furthermore, about 50% of the dissolved oxalate is complexed by Ca, which further reduced the free oxalate species. In the pure $CaCl_2$ solution, the aqueous Am(III) species is again determined by hydroxo and calcium hydroxo complexes between pH = 8 - 12. Again, most of the Ca(Ox) precipitates ([Oxalate] = $9.90 \cdot 10^{-4}$ M), and the aqueous speciation is determined almost exclusively by $Ca(Ox)_{aq}$. The corresponding speciation distribution for [EDTA] = 10^{-2} M is shown in Figure 8.

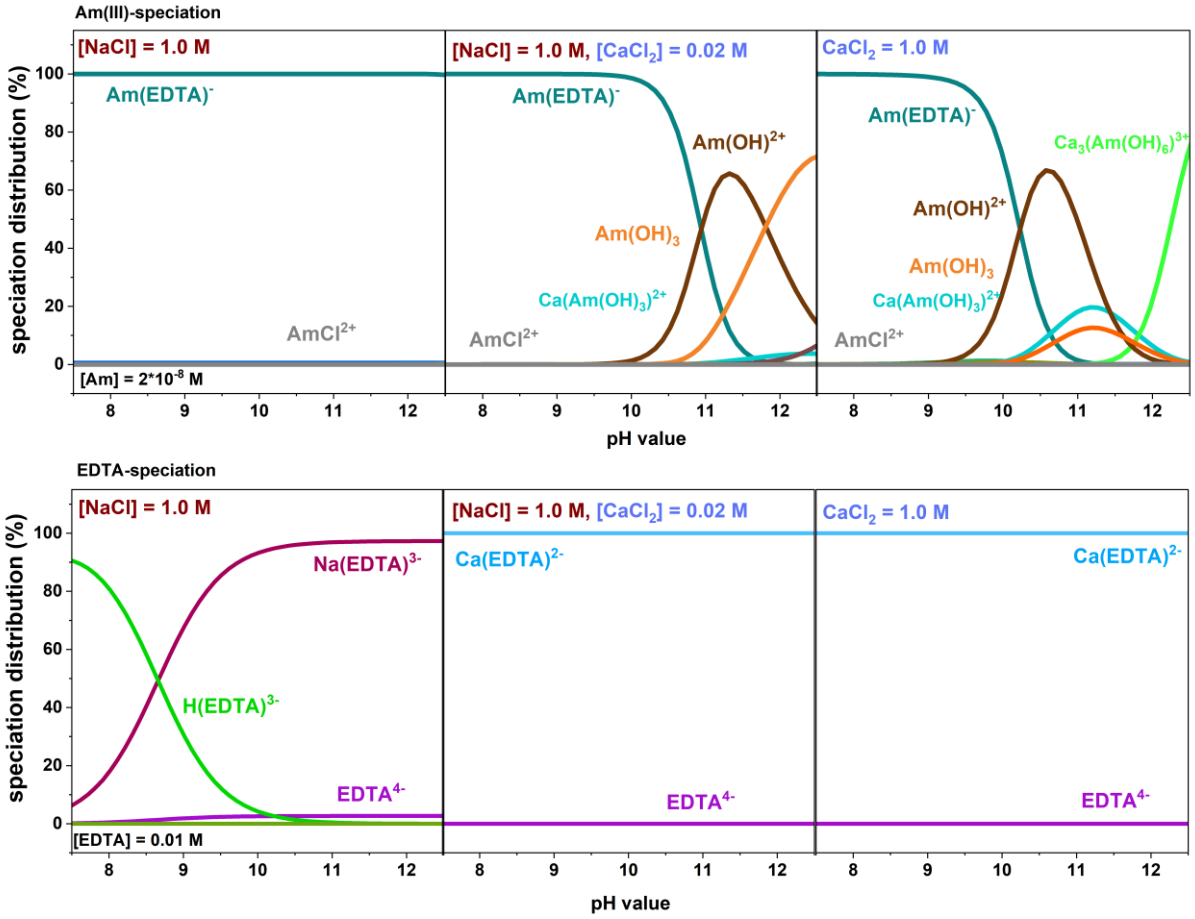

Figure 8: Speciation diagrams for the aqueous Am(III) (top) and EDTA (bottom) speciation between pH = 7.5 – 12.5. For the Am(III) speciation, [Am] = $2 \cdot 10^{-8}$ M was chosen, while [EDTA] = 0.01 M was used for the EDTA speciation. Left: NaCl system, I = 1.0 M; center: NaCl system, I = 1.0 M and [Ca] = 0.02 M, right: $CaCl_2$ system, I = 1.0 M.

At [NaCl] = 1.0 M and in the absence of Ca^{2+}, the species $Am(EDTA)^-$ dominates the aqueous Am(III) speciation up to pH ~ 11, since it has a high stability constant of log $K^0 = 19.67 \pm 0.11$. The aqueous EDTA speciation is mainly composed of the $H(EDTA)^{3-}$

species between pH = 7.5 - 10 and the $Na(EDTA)^{3-}$ species between pH = 7.5 - 12.5. Especially the latter species dominates the region with pH > 10. In the speciation diagram calculated for the mixed NaCl/$CaCl_2$ solution, the Am(III) speciation between pH = 8 - 10.5 is mainly dominated by $Am(EDTA)^-$. The formation of hydroxo complexes occurs between pH = 10 - 12, *e.g.* $Ca(Am(OH)_3)^{2+}$ exists only as a minimal fraction. $[EDTA]_{free}$ is significantly reduced by the formation of $Ca(EDTA)^{2-}$ which has a high stability constant of log K^0 = 12.69 ± 0.06. Rather similar observations are made for the pure $CaCl_2$ solution: $Am(EDTA)^-$ contributes mainly to the aqueous speciation of Am(III) between pH = 8 - 10. Hydroxo complexes as well as Ca containing species such as $Ca(Am(OH)_3)^{2+}$ and $Ca_3(Am(OH)_6)^{3+}$ form in the more alkaline pH range. $Ca(EDTA)^{2-}$ controls the aqueous speciation of EDTA. In the presence of Ca^{2+}, free EDTA almost disappears in the aqueous speciation. These calculations emphasize that in the alkaline conditions defined by cementitious systems and considering the currently available thermodynamic data, Ca is expected to outcompete *An*(III) for the complexation of oxalate and EDTA.

Table 1: Complexation reactions and corresponding stability constants selected for the Am-oxalate and EDTA systems in the presence and absence of Ca from the NEA-TDB.[15]

Complexation reactions	Log K^0
$Am^{3+} + H_2O(l) \rightarrow Am(OH)^{2+} + H^+$	7.20 ± 0.50
$Am^{3+} + 2\ H_2O(l) \rightarrow Am(OH)_2^{+} + 2\ H^+$	15.10 ± 0.70
$Am^{3+} + 3\ H_2O(l) \rightarrow Am(OH)_3 + 3\ H^+$	26.20 ± 0.50
$Am^{3+} + Cl^- \rightarrow AmCl_2^+$	0.74 ± 0.50
$Am^{3+} + 2Cl^- \rightarrow AmCl^{2+}$	0.24 ± 0.35
$Ca^{2+} + Am^{3+} + 3\ H_2O(l) \rightarrow Ca(Am(OH)_3)^{2+} + 3\ H^+$	26.30 ± 0.50
$2\ Ca^{2+} + Am^{3+} + 4\ H_2O(l) \rightarrow Ca_2(Am(OH)_4)^{3+} + 4\ H^+$	37.20 ± 0.60
$3\ Ca^{2+} + Am^{3+} + 6\ H_2O(l) \rightarrow Ca_3(Am(OH)_6)^{3+} + 6\ H^+$	60.70 ± 0.50
Oxalate	
$Ca^{2+} + Ox^{2-} \rightarrow CaOx$	3.19 ± 0.06
$Ca^{2+} + 2\ Ox^{2-} \rightarrow Ca(Ox)_2^{2-}$	0.83 ± 0.19
$Am^{3+} + Ox^{2-} \rightarrow Am(Ox)^+$	6.51 ± 0.07
$Am^{3+} + 2Ox^{2-} \rightarrow Am(Ox)_2^-$	10.71 ± 0.12
EDTA	
$Ca^{2+} + EDTA^{4-} \rightarrow Ca(EDTA)^{2-}$	12.69 ± 0.06
$Ca^{2+} + H^+ + EDTA^{4-} \rightarrow Ca(HEDTA)^-$	3.54 ± 0.09
$Na^+ + EDTA^{4-} \rightarrow Na(EDTA)^{3-}$	2.80 ± 0.20
$Am^{3+} + EDTA^{4-} \rightarrow Am(EDTA)^-$	19.67 ± 0.11
$Am(EDTA)^- + H^+ \rightarrow Am(HEDTA)$	2.17 ± 0.25

By calculating the aqueous speciation of Am(III) in the presence of EDTA, it has been shown that EDTA stabilizes Ca and Am(III) in solution by forming stable, negatively charged binary complexes (Table 1). In the last few years it has also been shown that ternary Ca-*An*(III)-EDTA species can form, with a high stability in aqueous solution.[37, 39-42]

Significant work in this regard was done by Di Blasi *et al.*, who studied the aqueous Pu(III)-EDTA and Cm(III)-EDTA system in the presence and absence of Ca^{2+} using solubility experiments and TRLFS, respectively.[39] In their work, the hydrolysis species

$Cm(OH)(EDTA)^{2-}$ was reported to form in the absence of Ca^{2+}. In the presence of Ca^{2+}, the ternary Ca-Cm(III)-EDTA species is formed. They also suggested the presence of a possible quaternary Ca-Cm(III)-(OH)-EDTA complex. Analogous studies on Eu(III)/Am(III) and Cm(III)-OH-EDTA complexes have been reported by Griffiths *et al.*[43]; Choppin *et al*.[44]; Thakur *et al.*[45]; Felmy *et al.*[46]; Roughley *et al.*[47] and Shalinets *et al.*[48] over the past decades.

The formation of soluble ternary and possibly quaternary species in aqueous solutions can significantly inhibit the retention of *An*(III)/*Ln*(III) and thus significantly increase the mobility of the RN. To understand the behavior of these RN under repository conditions, it is necessary to understand the formation of these complexes and to examine their impact on sorption reactions. In addition, respective thermodynamic data, *e.g.,* stability constants, to model the migration of the RN over long time scales are required. In order to support thermodynamic calculations, knowledge on those complexes on a molecular level and, therefore, insight into related structures is of interest.

1.4 General Spectroscopy

When molecules or atoms are excited into higher electronic states, an emission process called photoluminescence can occure. There are two types of emission processes: Fluorescence and phosphorescence. Both processes are shown in the Jablonski diagram in Figure 9.

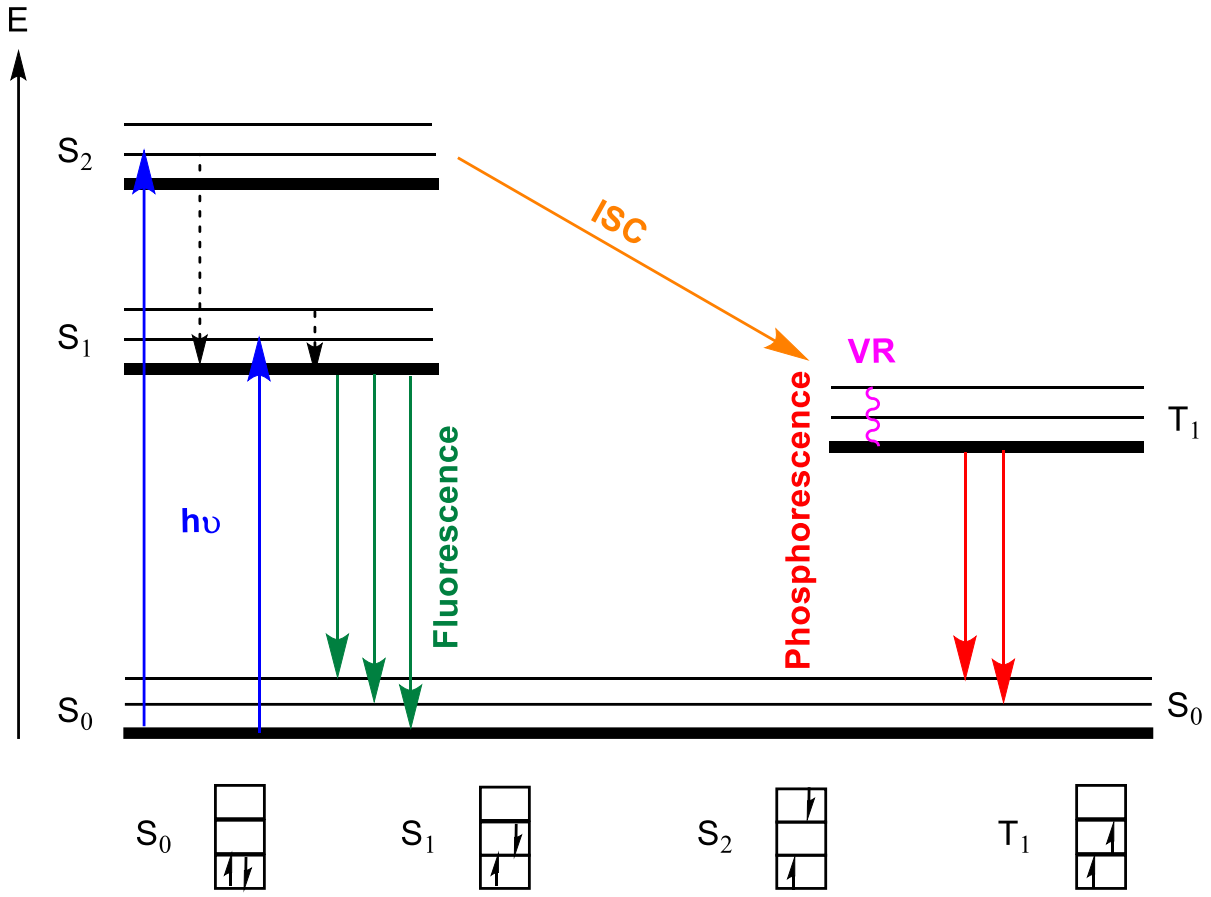

Figure 9: Jablonski diagram, to describe the processes of photoluminescence: Fluorescence and Phosphorescence. S_0 = Singlet ground state, S_1 = excited singlet state, T_1 = excited triplet state, ISC = Intersystem Crossing, VR = Vibronic Relaxation, Fluorescence (green arrows), Phosphorescence (red arrows), hν = Absorption of light, E = Energy.

In a first step, a molecule is excited from the singlet ground state (S_0) to the singlet excited states (S_1, S_2). This process is followed by non-radiative relaxation of the molecule in the lowest vibrational level of the first excited state with the same spin state. This is called Internal Conversion (IC). Now the emission of a photon can occur

by two processes: Fluorescence or phosphorescence.[49] In case of the fluorescence process, the emission of a photon takes place from the first excited state (S_1) to the ground state (S_0) without changing the spin multiplicity ($\Delta S = 0$). In general, fluorescence is a very fast process. In the phosphorescence process, ISC takes place and subsequently photon emission occurs from the excited triplet state (T_1) to the singlet ground state (S_0), resulting in a change in spin multiplicity ($\Delta S \neq 0$). Phosphorescence is a rather slow process and takes considerably longer than fluorescence.[50]

1.4.1 Fluorescence properties of Cm(III)

There are a number of trivalent *An*, such as Am(III), Cm(III), Bk(III) and Cf(III), that exhibit fluorescence properties. *Ln* such as Eu(III), Gd(III), Tb(III), Sm(III), Ce(III), Yb(III) and Dy(III) should also be mentioned here.[51] The optical spectra of *An* are generated by the transition between partially occupied electronic states in the f-shell. Generally, the splitting of the f-shell determines the energy of the characteristic f → f transitions. This can be affected by various factors such as the oxidation state or the presence of complexing agents. Generally, the spectra are characterized by a series of weak and sharp emission bands.

The actinide Cm(III), with the ordinal number Z = 96, has a half-filled f-shell, with the electron configuration of [Rn] $5f^7$ in the ground state. Due to the 7 unpaired electrons in the ground state, a multiplet term $^8S'_{7/2}$ results.[29, 52] According to Hund's rule, the term symbol $^8S_{7/2}$ is expected. However, the term symbols of *An* cannot be described by the Russell-Saunders (RS) term alone due to the increased spin-orbit coupling. Since the Coulomb interaction is of a similar order of magnitude compared to the spin-orbit interaction, mixed terms are used as a linear combination of RS states. Consequently, the term is written as $^8S'_{7/2}$ instead of $^8S_{7/2}$.

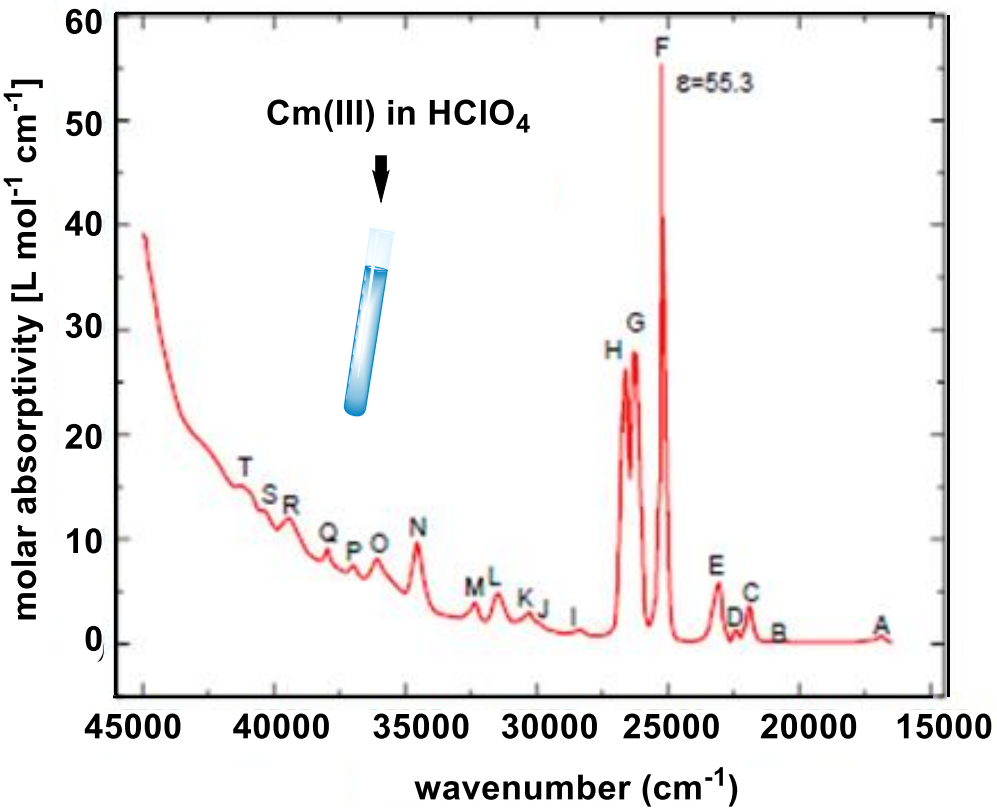

Figure 10: The absorption spectrum of Cm(III) ($[Cm]_{tot}$ = 0.06 M). given in 1.0 M $HClO_4$ solution adapted from Carnall and Rajnak. The three sharpest absorption bands are labelled with H, G and F.[53]

The typical absorption spectra of Cm_{aq} in 1 M $HClO_4$, which was published by Carnall and Rajnak in 1975, shows among others signals, three sharp adsorption bands (H, G and F) at λ = 396.6; 381.1 and 375.4 nm (see Figure 10).[53] These represent the second excited singlet states (S_2 = F, G and H).[52] As shown in the absorption spectrum of Cm(III), a large number of f → f transitions are visible. Notably, electronic transitions within the f-shell are typically prohibited by the Laporte rule.[49, 50] However, the effect of the ligand field or interactions with vibrational states induces a mixing of configurations with opposite parity, leading to a distortion to lower symmetries. Consequently, the Laporte rule is relaxed during such parity-changing transitions, commonly known as induced electrical dipole transitions. These f → f transitions, as a result, exhibit peaks with low intensities in the spectra. This characteristic gives rise to small extinction coefficients in the absorption spectra (ε < 1000 l/mol·cm).[53] The intensity of an optical

transition from the ground state to an excited state can be determined from the absorption spectrum and is expressed by the oscillator power P_{exp}.[53]

$$P_{exp} = 4.32 \cdot 10^{-9} \int \epsilon_i(\sigma) d\sigma = P_{ED} + P_{MD}$$

The equation of P_{exp} is a combination of the induced electric dipole transitions (P_{ED}) and the magnetic dipole transitions (P_{MD}). Hereby is $\epsilon_i(\sigma)$ the molar absorptivity coefficient of a species I at a given energy and is expressed in cm^{-1}. The precise fluorescence process of Cm(III) is shown in Figure 11.

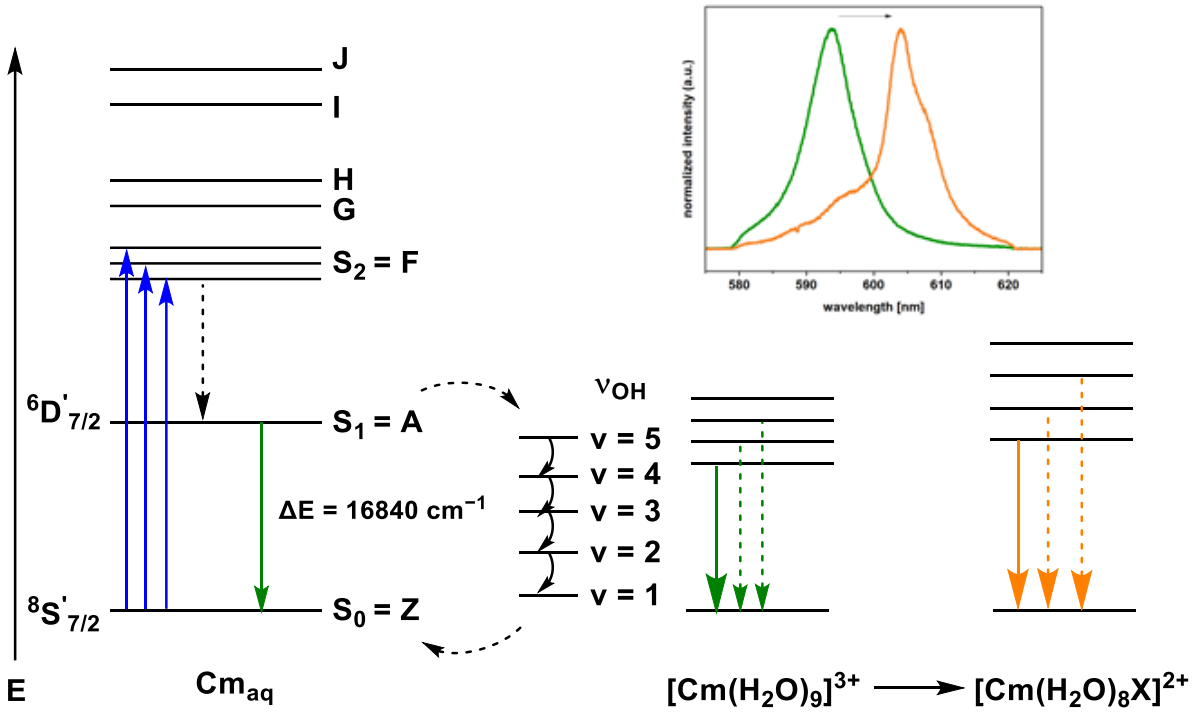

Figure 11: Schematic illustration of the fluorescence processes of the free Cm_{aq} with the ground state Z and the excited states A-J. Fluorescence occurs between the A state with the term symbol $^6D'_{7/2}$ to the ground state (S_0) with the term symbol $^8S'_{7/2}$, resulting in one emission band at λ_{max} = 593.8 nm. In addition, the red shift of the Cm(III) complex in the fluorescence spectrum by a generic monodentate ligand "X" is shown on the right.

Cm(III) can be excited from the electronic ground state (Z = $^8S'_{7/2}$) to the excited F state by laser irradiation at λ = 396.6 nm. The energy levels of the ground state Z are closely spaced, and can be considered quasi-degenerated. After excitation to the F state, IC is followed to the first excited state A with the term symbol $^6D'_{7/2}$. This state is split into four ligand field levels from A_1 to A_4 (split matrix 304 cm^{-1}), allowing four transitions

from the first excited state A to the degenerate ground state Z. Hence, there are four potential emission bands assumed in the fluorescence spectrum. However, the intensity of each band is determined by the thermal population of the ligand field states. The splitting of the excited state A is about 100 cm^{-1} larger compared to the thermal energy at 298 K with kT = 210 cm^{-1}. Thus, at RT the lowest level of the excited state A is primarily occupied and only one asymmetric emission band is detected at 593.8 nm with a half-width of 7.7. The asymmetry is due to the minor thermal population of the higher ligand field levels, resulting in hot bands. The transition between A and Z results in an energy difference of ΔE = 16840 cm for Cm_{aq}.[52, 54]

In aqueous solution in the absence of organic ligands, the Cm_{aq} ion is usually present as the $Cm(H_2O)_9^{3+}$ complex. Introducing a complexing ligand, such as EDTA, in place of a water ligand, enhances the ligand field splitting of the excited state A. This results in the lowering of the A_1 state and thus in a smaller energy difference to the ground state. Thus, the fluorescence emission is shifted towards longer wavelengths, known as a bathochromic shift. Consequently, each species produces a characteristic shift in the spectrum. The experimental spectra, therefore, represent a linear combination of the respective bands of individual species, offering insights into the chemical environment of Cm(III) and the species distribution.

The fluorescence lifetime, also known as fluorescence decay, provides valuable information about the chemical environment, particularly for each specific excited state. As already described above, the Cm_{aq} ion in solution is usually present as the $Cm(H_2O)_9^{3+}$ complex. The measured fluorescence emission lifetime of the excited Cm_{aq} ion in H_2O is determined to be very low with τ = 68 ± 2 µs. This short fluorescence lifetime is primarily attributed to quenching effects. The quenching occurs mainly due to the transfer of energy from the excited state of the metal ion to the OH vibrations of the H_2O molecules in the first coordination sphere. This is shown in Figure 11.[55] However, when the H_2O molecules are displaced from the first coordination sphere of the metal ion, the fluorescence lifetime is prolonged. This observation has been studied extensively by Kimura *et al*. in the following linear correlation.[56]

$$\mathbf{nH_2O = 0.64 \cdot K_{obs} - 0.88}$$

The equation gives the relationship between the fluorescence lifetime and the water molecules coordinated in the first coordination sphere of Cm_{aq}. The number of water molecules is described by nH_2O. K_{obs} Is the inverse of the fluorescence lifetime and thus describes the fluorescence decay. The Kimura equation only considers H_2O as a quencher. Other quenchers (*e.g.*, OH or COO^- groups) are not considered in this equation.

1.5 Cementitious materials

Cement is a mixture of finely ground, non-metallic and inorganic components. The manufacturing process begins with the formation of clinker by heating up limestone and clay to a temperature of ~1450 °C. The clinker is then ground with gypsum to produce ordinary Portland cement. Portland cement consists of dicalcium silicate (Ca_2SiO_4), tricalcium silicate (Ca_3SiO_5), aluminates ($Ca_3Al_2O_6$) and ferrite ($Ca_4(Al_xFe_{1-x})_4O_{10}$). The composition can also include $CaCO_3$, MgO and gypsum among other components.[57] Through the hydration process of Portland cement, hardened cement paste (HCP) is formed. HCP includes C-S-H phases, portlandite ($Ca(OH)_2$), AFm-phases (Calcium-mono-carbo-aluminate) and Aft phases (Ettringite) as the four products of the hydration process.[58] C-S-H phases represent the main binding component of cementitious materials. For the nomenclature of cementitious materials, it is common to only use the first letter of the respective compound, *e.g.*: C = CaO, S = SiO_2, H = H_2O. According to Taylor *et al.*, the full molecular formula of C-S-H phases is then described as $CaO\text{-}SiO_2\text{-}H_2O$.[59] Groundwater infiltration must be considered in the context of the safety case of a potential nuclear waste repository. This initiates cement degradation and leaching processes.[60] Degradation is known as a three-stage process, which is illustrated in Figure 12: In the first stage, HCP and the porewater are in equilibrium at the hyperalkaline pH = 13.3. In the next step, $Ca(OH)_2$ as the solid phase is buffering the porewater solution at pH = 12.5, with [Ca] ~ 20 mM. In the final step, the C-S-H phase dissolution occurs incongruently with a systematic decrease of the C/S ratio, resulting also in a drop of pH from 12.5 to ~ 10.[10, 61]

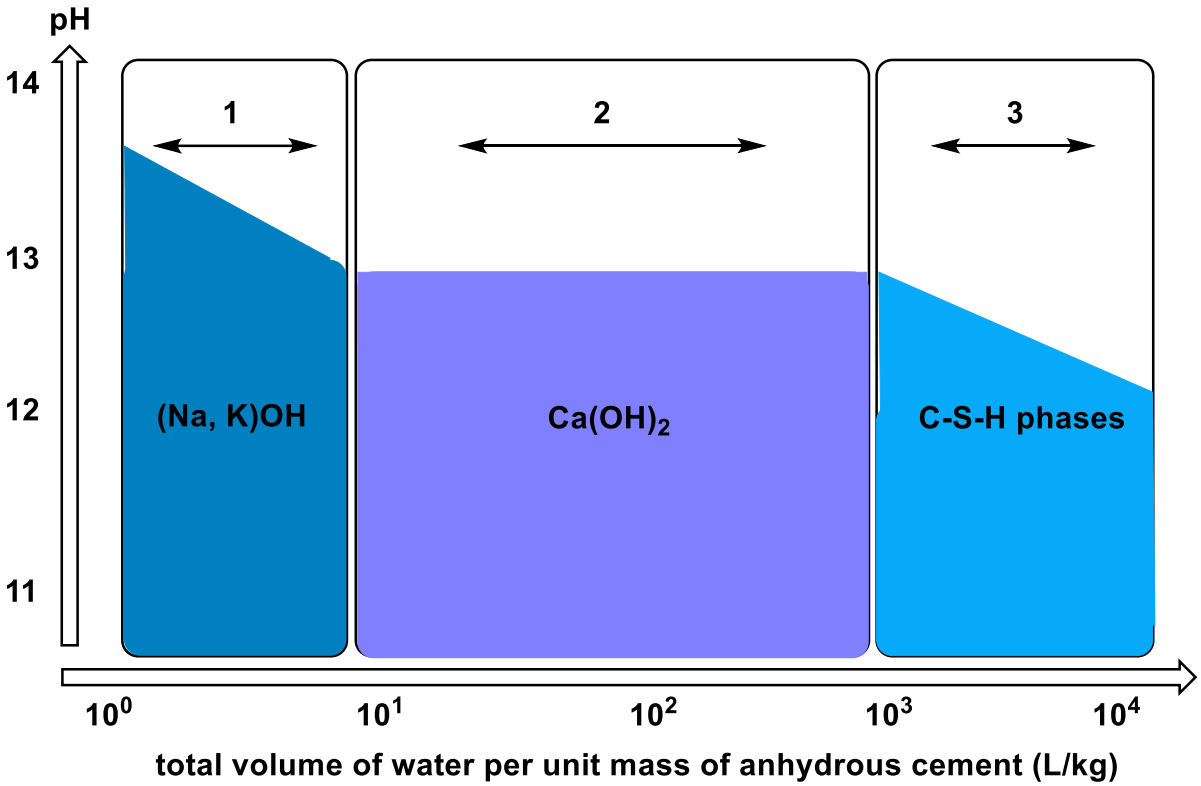

Figure 12: The degradation process of cementitious materials, which occurs in case of water intrusion in a potential repository. The figure is adapted from Jacques *et al.*.[61] It is a three-step process, where HCP and the porewater are in equilibrium at the hyperalkaline pH = 13.3 in a first step. Then, $Ca(OH)_2$ dominates at pH = 12.5, while C-S-H phases occur at pH ~ 10.

1.5.1 C-S-H phases

C-S-H phases are responsible for the high sorption capacities of cementitious materials, especially for metal ions, due to their amorphous structure and high reactive surface areas up to ~ 150 m^2/g.[62] As the main binding component of cementitious materials, C-S-H phases prepared under laboratory conditions commonly show a gel-like structure. The full structure is not fully understood yet. Based on the current knowledge, C-S-H phases show many similarities to 14 Å Tobermorite. Tobermorite is a naturally occurring mineral with a layered structure. The C-S-H structure based on the 14 Å Tobermorite structure is shown in Figure 13: The CaO interlayer in the center of the structure is surrounded by silica chains. Ca from the CaO interlayer is sevenfold coordinated and shares the oxygen atoms with the silica chains. The silica chains show the C-S-H–characteristic “Dreierkette” unit. This arrangement repeats and is composed as described below: Two pairing Si-tetrahedra are connected to the oxygen

of the CaO interlayer. The third Si-tetrahedra represents the bridging tetrahedra and connects the two pairing Si-tetrahedra.[38, 63, 64]

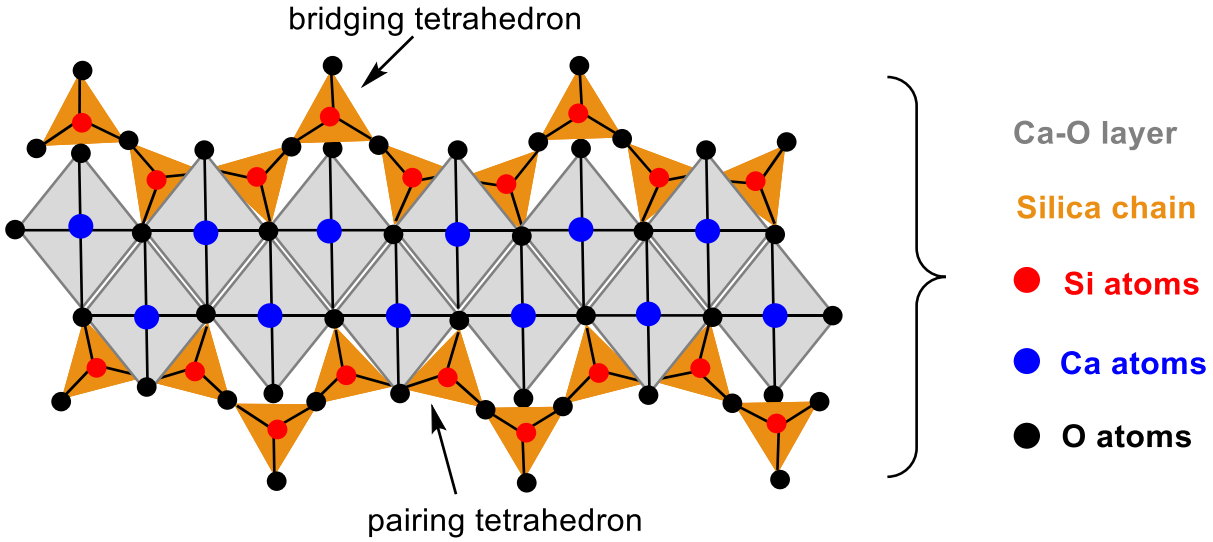

Figure 13: The C-S-H phase structure based on 14 Å Tobermorite. The CaO interlayer is coordinated between the infinite silica chains. The silica chains are arranged in the "Dreierkette" unit, containing two pairing and one bridging Si-tetrahedra.

Another important parameter that determines the properties of C-S-H phases is the Ca to Si ratio (C/S ratio). Common C/S ratios can vary from 0.66 to 1.5, between pH = 10 – 12.5, respectively. The formation of C/S = 1.7 is commonly seen for hydrated cement.[38] Below the C/S = 0.66, amorphous SiO_2 dominates the structure, while above C/S = 1.5 portlandite ($Ca(OH)_2$) prevails.[65] Another important aspect of the C-S-H phase is the surface charge. For low C/S < 1.3, a negative surface is observed, while C/S > 1.3 show positive surface charges.[66] The type of surface charge is determined by the Ca content: At low C/S ratios, the Si content dominates and thus negatively charged $\equiv SiO^-$ and ≡SiOH groups are associated at the surface of the C-S-H phases. In case of high C/S ratios, the Ca content dominates the C-S-H phase and thus positively charged $\equiv SiOCa^+$ and $\equiv SiOCaOH_2^+$ groups are present at the surface.[38, 65-67]

1.5.2 C-S-H phases in saline solutions

As described in section 1.1, the highly saline porewaters of the northern German clay formations are of particular interest in the context of this work. These saline conditions may affect the composition and/or the stability of the C-S-H phases. In the past, C-S-H phases have usually been studied in NaOH or KOH solutions up to concentrations of 1 M.[38, 65, 68-70] According to the studies of Lothenbach *et al.* and Plusquellec *et al.*, Na^+ ions can be adsorbed on the surface of the C-S-H phases, or may be incorporated into the CaO interlayer.[38, 70] In this case, Na^+ is exchanged for Ca^{2+}. The extent of Na^+ adsorption on the C-S-H surface depends on the surface charge, which in turn depends on the C/S ratio (see section 1.5.1). The alkali uptake is preferred for low C/S, to balance the negative surface charge.[65] Häusler *et al.* studied C-S-H phases in presence of NaCl solutions and also demonstrated, that Na^+ ions are incorporated into the C-S-H phase interlayer.[71] In addition, [Ca] in solution rises with increasing [NaCl] up to c(NaCl) = I_m(NaCl) = 1.5 M. No data are available for higher ionic strength. In the presence of NaCl they assumed the formation of $Ca(OH)_2$-SiO_2-NaCl-H_2O and thus (C-(NaCl)S-H)–phases. Apart from this, the structure of C-S-H phases is not significantly affected by the electrolyte solution and comparable to C-S-H phases prepared in ultrapure-water.[71] Plusquellec *et al.* studied C-S-H phases in the presence of $CaCl_2$. Adding $CaCl_2$ to the C-S-H phase, slightly increases the C/S ratio. Further they monitored slightly decreasing pH values. Bernard *et al.* examined C-S-H phases in the presence of $MgCl_2$, resulting in $MgCl_2$-SiO_2-hydrate phases (M-S-H) phases.[72] M-S-H phases are known as components of low pH cementitious materials with pH < 9.6. Contacting C-S-H phases with $MgCl_2$ leads to structural changes reflected by XRD measurements. Here, the characteristic signals at 2Θ = 16.3, 29.2, 32.0 and 43.0° decrease in presence of the electrolyte compared to “normal” C-S-H phases. Additionally, two new signals at 2Θ = 19.7 and 35.0° arise, indicating the presence of M-S-H phases. No precise explanation was given for the decrease in intensity of the C-S-H phase signals in the presence of $MgCl_2$.

1.6 Bentonite

Bentonite shows favorable properties like high sorption capacities towards RN (including *An*(III) and *Ln*(III)) and a low permeability. It is considered as backfill material in certain disposal concepts.[73] In this work Bentonite MX80 was used. It originates from Wyoming, USA and represents a naturally occurring Na-bentonite, formed by hydrothermal alteration of pyroclastic rocks.[74] Bentonite consists of clay minerals and various types of rock materials.[12] The main component is montmorillonite (60 – 80%) with the formula $(Si_{3.96}Al_{0.04})(Al_{1.52}Mg_{0.26}Fe_{0.17}^{III})Na_{0.18}Ca_{0.11}O_{10}(OH)_2$.[75, 76] Montmorillonite belongs to the swellable smectite group of clay minerals and the structure is illustrated below in Figure 14 adapted from Ghadiri *et al*.[77] and Grim *et al*..[78] Further quartz, feldspar, calcite and pyrite are also included within the composition of bentonite.[12, 79] Montmorillonite can be characterized as three-layered clay material in the smectite subgroup. In the structure of these clays, the octahedral Al-O layer is surrounded by two Si-O tetrahedral layers. Due to isomorphic substitution, the basal faces are permanently negatively charged. Isomorphic substitution is characterized by the replacement of cations of higher charge by cations of lower charge in the layers of the clay. The negative charge is compensated by hydrated cations such as Na^+ or Ca^{2+}.[12, 74, 78]

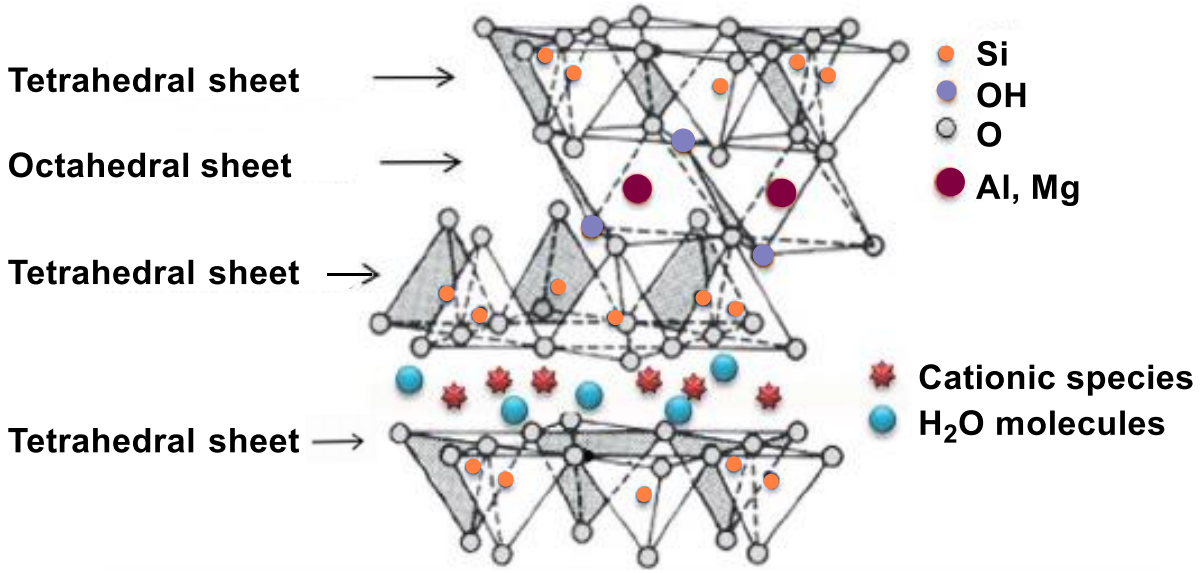

Figure 14: The schematic structure of montmorillonite. It represents a three-layered clay material of the smectite subgroup. The structure is adapted from Ghadiri *et al.*[77] and Grim *et al*..[78]

1.7 Sorption processes of Ln(III) and An(III)

RN sorption onto mineral phases can have a major impact on the retardation of RN within repository barriers. Different possible RN reactions at mineral surfaces are shown in Figure 15, adapted from Geckeis *et al*..[80]

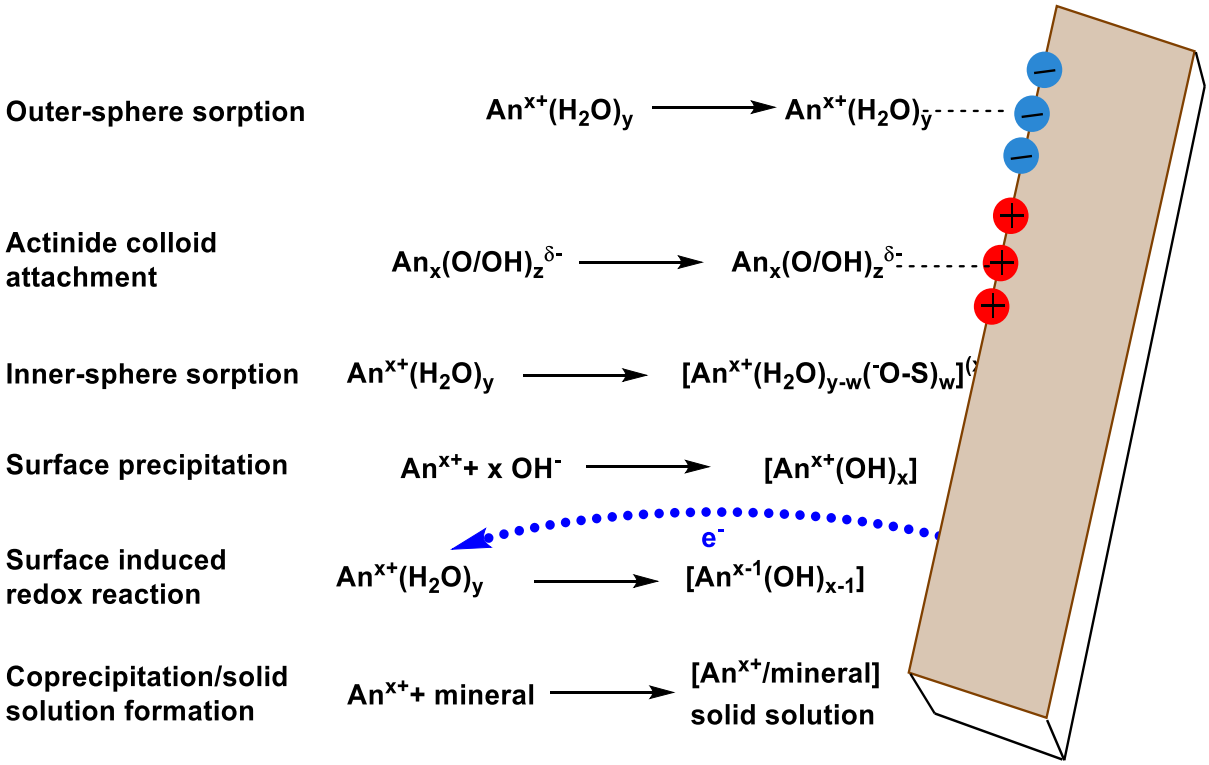

Figure 15: Schematic representation of the different sorption processes adapted from Geckeis *et al*..[80] This includes outer-sphere sorption, inner-sphere sorption, surface precipitation and coprecipitation among others.

Some sorption processes are described in the following: (i) Outer-sphere sorption is characterized by electrostatic attraction between cations on negatively charged mineral surfaces. This can be done analogously with anions on positively charged surfaces. The ion retains its fully intact hydration shell. An example is provided by cation interactions with permanently charged clay surfaces (*e.g.,* montmorillonite). The number of cations that can be exchanged is described by the cation exchange capacity (CEC). Similarly, the number of exchangeable anions can be determined by the anion exchange capacity (AAK); (ii) Inner-sphere sorption, where the hydration shell around the central ion does not remain completely intact. This is the case, when the sorbent forms a chemical bond to functional groups of the mineral surfaces (*e.g.,* amphoteric hydroxyl groups on the mineral-surfaces of clay). (iii) Incorporation, where foreign ions

are incorporated into a crystal structure of the respective mineral; (iv) Surface precipitation, where a dissolved substance from a solution transform into an insoluble solid.

In this context, a mechanistic understanding of the sorption processes on a molecular level and their quantification are required for the accurate assessment of the retention of a sorbent.

1.7.1 Sorption of Ln(III) and An(III) on C-S-H phases

The uptake of Eu(III) and Cm(III) on C-S-H phases has been studied mostly in the absence of organic ligands and at low ionic strength ($I_m \leq 0.1$ m). Pointeau *et al.* conducted a study on the sorption of Eu(III) onto C-S-H phases, revealing rapid sorption kinetics and a high metal ion retention of approximately 99.8%, which corresponds to log $K_d \sim 6$.[81] Tits *et al.* also studied the sorption of Eu(III) on C-S-H phases in absence of organics.[82] They observed a very strong sorption with high log K_d values up to ~ 6, independent from the C/S ratio. The sorption of Cm(III) on C-S-H phases was further studied by Tits and co-workers with TRLFS.[83] It was concluded, that Cm(III) exchanges with Ca from the C-S-H phase interlayer, leading to an incorporation of the actinide ion into these layers.[83] It is suggested that the Eu(III)/Cm(III) uptake on C-S-H phases is a two-step-process: First, the trivalent metal ion forms rapidly complexes on the surface of C-S-H phases, followed by slow incorporation of Eu(III)/Cm(III) in the C-S-H interlayer.[81, 83-87]

Limited data in the literature address the sorption of *Ln*(III)/*An*(III) on C-S-H phases in the presence of organic ligands. Wieland *et al*. studied the sorption of Eu(III) on C-S-H phases in the presence of GLU and observed a significantly reduced retention of Eu(III) with increasing [GLU] = 10^{-2} M.[11] This is in good agreement with the results recently published by Guidone *et al.*.[88] In both studies, the low retention of Eu(III) is explained by the stabilization of Eu(III) and Ca by GLU, leading to the formation of ternary complexes such as Eu(III)-Ca-GLU. Tasi *et al.* investigated the Cement-Pu(IV)-ISA system and observed decreasing log R_d values with increasing [ISA] ≥ 10^{-4} M (R_d in $L \cdot kg^{-1}$). This was attributed to the formation of ternary Ca-Pu(IV)-ISA and quaternary Ca-Pu(IV)-OH-ISA complexes.[89, 90] At high ligand concentrations, however, Tasi *et al.* reported an increased uptake, which was explained by the formation of surface complexes containing Pu(IV) and ISA. Furthermore, complexation constants for the corresponding complexes were observed by Tasi *et al*.: For the formation of $Pu(IV)(OH)_3ISA^{2-}{}_H$, a stability constant of log $K^\circ = 5.03 \pm 0.12$ was determined. [89]

$$\mathbf{Pu^{4+} + ISA^{-} + 3\ H_2O \leftrightarrow Pu(IV)(OH)_3ISA^{2-}{}_H}$$

For the formation of the quaternary Ca containing complexes $Ca(II)Pu(IV)(OH)_3ISA^{+}_{-H}$ and $Ca(II)Pu(IV)(OH)_3ISA_{-2H}$, log K = 3.37 ± 0.16 and log K = 4.22 ± 0.15 are reported.[90] The corresponding complexation reactions are as follows:

$$\mathbf{Pu^{4+} + ISA^{-} + 4\ H_2O + Ca^{2+} \leftrightarrow Ca(II)Pu(IV)(OH)_3ISA^{+}_{-H}}$$

$$\mathbf{Pu^{4+} + ISA^{-} + 5\ H_2O + Ca^{2+} \leftrightarrow Ca(II)Pu(IV)(OH)_3ISA_{-2H}}$$

Since EDTA exhibits strong complexation with calcium, it has been assumed that EDTA has only a negligible effect on the retention of RN in cementitious environments. However, as EDTA has a concentration several orders of magnitude higher than the RN, ligand complexation with Ca may exceed. The group of Maragkou *et al.* investigated the sorption of EDTA on C-S-H phases and reported a destabilization of the C-S-H phases at [EDTA] > 0.01 M.[91] This is explained by the dissolution of $Ca(OH)_2$ resulting in the degradation of the solid phase. They further studied C-S-H phases in presence of [EDTA] < 0.01 and assumed the adsorption of EDTA onto the C-S-H phase. Maragkou *et al.* furthermore studied the sorption of U(VI) on C-S-H phases in presence of EDTA.[91] The sorption of U(VI) on C-S-H phases decreases with increasing[EDTA] > 10^{-3} M. The formation of U(VI)-EDTA complexes is assumed. Moreover Pointeau *et al*. studied the adsorption of EDTA by fresh- and degraded cement (pH = 13.3; 11.9). They observed low log R_d ~ 1 for both systems (R_d in $L \cdot kg^{-1}$). The evolution of the pore water calcium concentration and the surface potential/charge of the hydrated cement were used to explain this behavior.[92] Szabo *et al.* conducted a more extensive work of the sorption of organic ligands on cementitious materials.[93] They found that EDTA, which contains four -COOH and two amine groups, has similar R_d values compared to glutaric acid, which has only two -COOH groups. This suggests that only a limited number of carboxylate units in organic ligands interact with cementitious materials, emphasizing the importance of steric constraints in such interactions.

The retention of Eu(III) in presence of EDTA ([EDTA] = $5 \cdot 10^{-5}$ - $5 \cdot 10^{-3}$ M) on C-S-H phases with C/S = 1.0 was recently investigated by Burešová *et al*.: For [EDTA] ≤ $5 \cdot 10^{-3}$ M, they concluded, that there is no significant impact of EDTA visible on the sorption

of Eu(III) on C-S-H phases.[94] Further Ochs *et al.* reported, that at [EDTA] < 0.1 m, EDTA shows a negligible effect on the retention of Eu(III).[95]

1.7.2 Sorption of Ln(III)/An(III) on bentonite

It is well known that bentonite is mainly composed of montmorillonite (60 - 80%).[96] In this respect, Eu(III) sorbs preferentially to the montmorillonite fraction, as it has many preferred sorption sites. Therefore, the sorption of Eu and montmorillonite is discussed in this chapter. Bradbury and Baeyens did a major approach on this topic, as they investigated the retention of Eu(III), among other elements, on Na- and Ca-montmorillonite in the frame of their 2-site protolysis without electrostatic surface complexation and cation exchange (2SPNE/CE) model. This model is only briefly mentioned at this point. A detailed explanation can be observed in the literature.[97]

The retention of Eu(III) on Ca-montmorillonite is described as follows: At pH = 3 - 4.5, a low retention is detected (log R_d ~ 1.5, R_d in $L \cdot kg^{-1}$). Afterwards, a strong increase of the retention from pH = 5 (log R_d ~ 2) to pH = 8 (log R_d ~ 5) is observed. Between pH = 8 – 10, high log R_d values are observed (log R_d ~ 5 – 6). The retention behavior of Eu(III) at pH < 4.5 is explained with cation exchange reactions (outer sphere sorption) at the permanently charged planar sites. This is shown in the following reaction:[97]

$$\mathbf{3\ Ca\text{-}clay + 2\ Eu^{3+} \leftrightarrow 3\ Eu\text{-}clay + 3\ Ca^{2+}}$$

Up to pH ~ 8 (and higher pH values), inner sphere sorption processes are reported. Hereby Eu(III) binds on the amphoteric surface -OH sites (**≡SOH)** of the clay mineral. In their model, they considered weak (**≡S^wOH)** and strong (**≡S^SOH)** site types of the clay therefore.[97, 98] This is described with the following reactions:[97]

$$\mathbf{\equiv S^SOH + Eu^{3+} \leftrightarrow \equiv S^SEu^{2+} + H^+}$$

$$\mathbf{\equiv S^SOH + Eu^{3+} + H_2O \leftrightarrow \equiv S^SEuOH^+ + 2\ H^+}$$

$$\mathbf{\equiv S^SOH + Eu^{3+} + 2\ H_2O \leftrightarrow \equiv S^SEu(OH)_2^0 + 3\ H^+}$$

$$\mathbf{\equiv S^SOH + Eu^{3+} + 3\ H_2O \leftrightarrow \equiv S^SEu(OH)_3^- + 4\ H^+}$$

Choppin *et al*. investigated the sorption behavior of Ho(III) among other *Ln* on Na-montmorillonite in $NaClO_4$ and $NaNO_3$ solutions (I = 0.025 M, 0.5 M). Significant differences were observed between the two ionic strengths. At low I = 0.025 M, log K_d ~ 4 – 5 is observed for pH = 3 – 7. For pH > 7 slightly lower log K_d values are shown. The log K_d is mainly affected by the cation exchange capacity of the minerals and only shows a weak pH dependence. At high ionic strength of I = 0.5 M, low retention (log K_d ~ 2) is observed at pH < 5. For pH > 5 a strongly increasing retention of Ho(III) is observed up to log K_d ~ 5. It is thus concluded, that only inner-sphere sorption is observed on the amphoteric sites at the edge of the clay particles, which is pH dependent. They concluded that the uptake of Ho among other *Ln* on montmorillonite is thus controlled by the nature of the clay minerals as well as the pH and ionic strength of the electrolyte solutions.[99] The ionic strength dependence of the Eu(III)/Cm(III) sorption on montmorillonite was further investigated by Hartmann *et al*.: They identified outer sphere adsorbed trivalent *Ln*/*An* on different montmorillonites.[100]

Schnurr *et al.* investigated the sorption of Eu(III) and Cm(III) on montmorillonite in NaCl and $CaCl_2$ solutions from low to intermediate ionic strength in absence of organic ligands.[101] In NaCl solutions, at low I_m = 0.09 m, Eu(III) shows an average retention (log K_D ~ 3 - 4, R_d in $L \cdot kg^{-1}$) in the acidic pH region (pH_m < 6). With increasing pH values (pH_m = 6 – 8), the retention of Eu(III) increases up to log K_d ~ 6. At pH = 8 – 12, almost quantitative retention is achieved. In NaCl at intermediate and high ionic strength (I_m = 0.90 – 3.90 m), almost no retention of Eu(III) is visible between pH_m = 3 – 4. From pH_m = 5 - 8, strongly increasing log K_d ~ 5 are observed. Between pH_m = 8 -12, a continuous plateau of log K_d ~ 5.5 (R_d in $L \cdot kg^{-1}$) is reached. This behavior at pH_m < 5 can be explained by cation exchange processes, which dominate the uptake of Eu(III) on montmorillonite and are strongly affected by the ionic strength. In contrast, surface complexation of Eu(III) with the amphoteric -OH groups on the edges of montmorillonite result in increasing retention of Eu(III) at pH_m > 5. The analog system in $CaCl_2$ solutions from low to intermediate ionic strength (I = 0.06 – 4.0 M) was investigated by A. Schnurr in his dissertation: Hereby, low retention of Eu(III) with log K_d ~ 1 – 2 is reached for pH_m < 5.[102] The log K_d are increasing until quantitative retention is reached at pH_m ~ 7. Schnurr *et al*. concluded that increasing the ionic strength only slightly decreases the

sorption edge. The experimental data at pH_m > 8 are not affected by the ionic strength.[102]

The sorption of Eu(III) on bentonite MX80 has been studied in the past mostly in the absence of organic ligands at low ionic strength (I_m ≤ 0.1 m). Wang *et al.* studied the uptake of Eu(III) on bentonite MX80 in $NaClO_4$ solution of different ionic strength (I = 0.01 – 1 M).[76] They observed an ionic strength independent sorption profile for Eu(III). The log K_d values increase from pH = 2 to 4 and remain high for pH > 4. The group of Sheng *et al.* also studied the Eu(III) sorption on bentonite MX80 in absence of organics.[103] They also determined strongly increasing log K_d values from pH 2 to pH 4 with a high retention of Eu(III) on bentonite for pH > 4. It should be noted at this point, that the reason for the ionic strength independence in some cases may be, that soluble components of the bentonite, such as NaCl or $CaSO_4$, were not taken into account.[104] Thus, the Ca or Na concentration in the solution in contact with the bentonite is often much higher than in the electrolyte solution added.

The Eu(III) sorption on purified Na-bentonite (*Jinchan*) in absence and presence of oxalate and EDTA ([Oxalate, EDTA] = $2 \cdot 10^{-4}$ M) was investigated by Guo and co-workers.[105] For the uptake of Eu(III) on bentonite in presence of oxalate, at $[Eu]_{tot}$ = $[Ox]_{tot}$ = $2 \cdot 10^{-4}$ M, the authors observed an increasing Eu(III) sorption at pH > 6. The rising log R_d might be explained by the precipitation of Eu-hydroxide complexes due to the high Eu(III) concentration. At $[Eu]_{tot}$ = $2 \cdot 10^{-7}$ M and $[Ox]_{tot}$ = $2 \cdot 10^{-4}$ M, the sorption coefficients also increase at pH > 7, yet to a much smaller extend (log R_d = 3 - 4). They also studied EDTA under the similar conditions as for oxalate and concluded, that for $[Eu]_{tot}$ = $[EDTA]_{tot}$ = $2 \cdot 10^{-4}$ M, the Eu(III) sorption is significantly lowered by the presence of the organic ligand from pH > 6 on. At $[Eu]_{tot}$ = $2 \cdot 10^{-7}$ M and $[EDTA]_{tot}$ = $2 \cdot 10^{-4}$ M, the sorption of Eu(III) is almost completely suppressed by EDTA complexation. The implications of these effects on the migration of trivalent actinides need to be further investigated.

2 Aim of the thesis

In this work, the effect of the organic ligands oxalate and EDTA is studied on the retention of *An*(III)/*Ln*(III) on C-S-H phases and bentonite under low to intermediate ionic strength conditions. The elevated salinities are representative of porewaters in the northern German clay formations. The primary emphasis is on examining the retention behavior of Eu(III) and Cm(III) on C-S-H phases. The experiments involving bentonite received comparatively less attention and are not detailed in the main text, but rather presented in the appendix.

This work is divided into two parts and combines classical wet-chemical studies and advanced spectroscopic methods. The aim is to provide a comprehensive quantitative description and mechanistic insight into complex systems with direct relevance to potential nuclear waste disposal scenarios.

Part 1: *The investigation of the effect of oxalate and EDTA on the retention of Ln(III)/An(III) on C-S-H phases and bentonite MX80 under the variation of different experimental parameters.*

The studies are performed as batch sorption experiments with systematic variation of the key experimental parameters, *e.g.,* ionic strength of the electrolyte solutions (NaCl or $CaCl_2$), sorption time, pH (bentonite), C/S ratio (C-S-H phases) and [oxalate, EDTA]. The main objective is to determine the log R_d values. For a more detailed study of the sorption processes, TRLFS measurements with Cm(III) are used to identify different aqueous and possible adsorbed species. Previous work has shown that experimentally determined K_d values in some cases depend on the order of how metal ion, ligand and solid phase are added.[106] In those cases kinetic effects play a role, which up to now have not been quantified or understood in detail. In this regard, experiments with different order of addition are performed.

Part 2: *The examination of the Eu(III)/Cm(III) speciation and structural characterization of ternary and quaternary Ca-stabilized Cm(III)-EDTA complexes in aqueous media.*

Recently, the formation of ternary Ca-*An*(III)/*Ln*(III)-EDTA complexes has been discussed in the literature.[37, 39-42] Thus, it is assumed that they can significantly reduce the retention of RN and increase its mobilization. Therefore, the structural elucidation and the Eu(III)/Cm(III) speciation species is necessary. In the context of this work, EXAFS experiments with Am(III) in solution are performed. In addition, dedicated TRLFS studies with Cm(III) as a luminescent sample are carried out to identify individual complexes and to derive tentatively determined stability constants.

3 Experimental

All experimental- and analytical methods used in this work are displayed briefly in this section. The experiments, unless otherwise described, were performed under inert atmosphere in a glovebox (O_2 ~ 2 ppm, 99% Argon). All analytical methods were used in the laboratories of KIT-INE.

3.1 Materials

3.1.1 Chemicals

Solid NaCl (*Honeywell Specialty Chemicals Seelze GmbH,* ***CAS:*** *7647-14-5*) and $CaCl_2$ (*Honeywell Specialty Chemicals Seelze GmbH,* ***CAS:*** *10035-04-8*) were used to set the ionic strength of aqueous solutions. All stock solutions were prepared in deionized water produced by a Milli-Q® system of Millipore (resistance 18.2 MΩ/cm). The deionized water was purged with Argon for minimum three hours before using it. NaCl and $CaCl_2$ electrolyte solutions from middle to high ionic strength were set to I_m(NaCl) = 0.1, 1.02 and 5.05 m; I_m($CaCl_2$) = 0.1, 1.02 and 5.36 m. Attributed to this are the following concentrations of c(NaCl) = 0.1 m, 1.0 m, 5.05 m and c($CaCl_2$) = 0.03 m, 0.34 m and 1.75 m. The ionic strength [I_c] is calculated as follows:

$$\boldsymbol{I_C = \frac{1}{2} * \sum_i c_i * z_i^2}$$

Hereby c_i is the concentration, while z_i is the charge of the ion i. The ligand stock solutions were prepared by adding solid Na_2-Oxalate (*Merck pro analysis,* ***CAS:*** *62-76-6*) and Na_2-EDTA (*Sigma Aldrich,* ***CAS:*** *6381-92-6*), respectively. In case of bentonite samples, the pH-values are varied from 3 to 12. To adjust the pH value of bentonite samples, solutions of HCl (1 M, 0.1 M, 0.01 M, 0.001 M) and NaOH (1 M, 0.1 M, 0.01 M, 0.001 M) were used.

For the Europium stock solution, inactive Eu(III) was mixed together with ^{152}Eu (*Eckert & Ziegler*), which was added as a radioactive tracer. The concentration of the active

^{152}Eu solution was [^{152}Eu] = 3.78·10^{-6} M in 0.5 M HCl. Therefore, inactive Eu(III) (c = 0.01 M) was added to this solution until the total initial concentration of 2.05·10^{-5} M was reached. This solution was diluted accordingly, so that the concentration of Eu(III)$_{tot}$ was fixed to 2·10^{-8} M for all the batch sorption experiments, whereas the initial activity of ^{152}Eu in each experiment was set to A(^{152}Eu(III)) = 2000 Bq. The total sample volume was v_{tot} = 10 ml.

A Curium stock solution ([Cm]$_{tot}$ = 2.13·10^{-5} M, 0.1 M $HClO_4$) was used for TRLFS measurements. The concentration for each sample was set to [Cm]$_{tot}$ = 1·10^{-7} M. The isotopic composition of the stock solution was: ^{248}Cm (89.7 %), ^{246}Cm (9.6 %), ^{243}Cm (0.4 %), ^{244}Cm (0.3 %), ^{245}Cm (0.1 %), ^{247}Cm (0.1 %).

EXAFS measurements were performed with an Americium stock solution ([Am]$_{tot}$ = 1.06·10^{-2} M). The total Americium concentration was set to [Am]$_{tot}$ = 1·10^{-3} M for every sample. The isotopic composition of the stock solution was: ^{243}Am (8 g/L, 98%) and ^{241}Am (0.02 g/L, 0.2%). The stock solution also contains small proportions of Pu with ^{240}Pu (0.1 g/L, 1.2%), ^{239}Pu (0.04 g/L, 0.4%) and Cm with ^{244}Cm (0.01 g/L, 0.2%).

3.1.2 Solid-phases

Two solid phases were used in this work: Bentonite MX80 and C-S-H phases. Bentonite is a mixture of different clay materials, with montmorillonite being the main component.[105] C-S-H phases are the main component of cementitious materials.[23, 107]

Bentonite MX 80

The bentonite (MX80) was purchased from Süd Chemie AG, Duisburg, Germany. It originates from Wyoming, USA. Bentonite MX80 is also found in Montana and South Dakota, where it is widely distributed and found in the layers of marine shale.[108] As already mentioned above, Montmorillonite is the main fraction of Bentonite. The composition is given in chapter 3.4.1. The characterization as well as the results from the batch sorption experiments are presented in Appendix 7.5 – 7.7.

Preparation of C-S-H phases

All C-S-H phases used in this work are prepared according to L'Hôpital *et al*.[109] The preparation is illustrated in Figure 16.

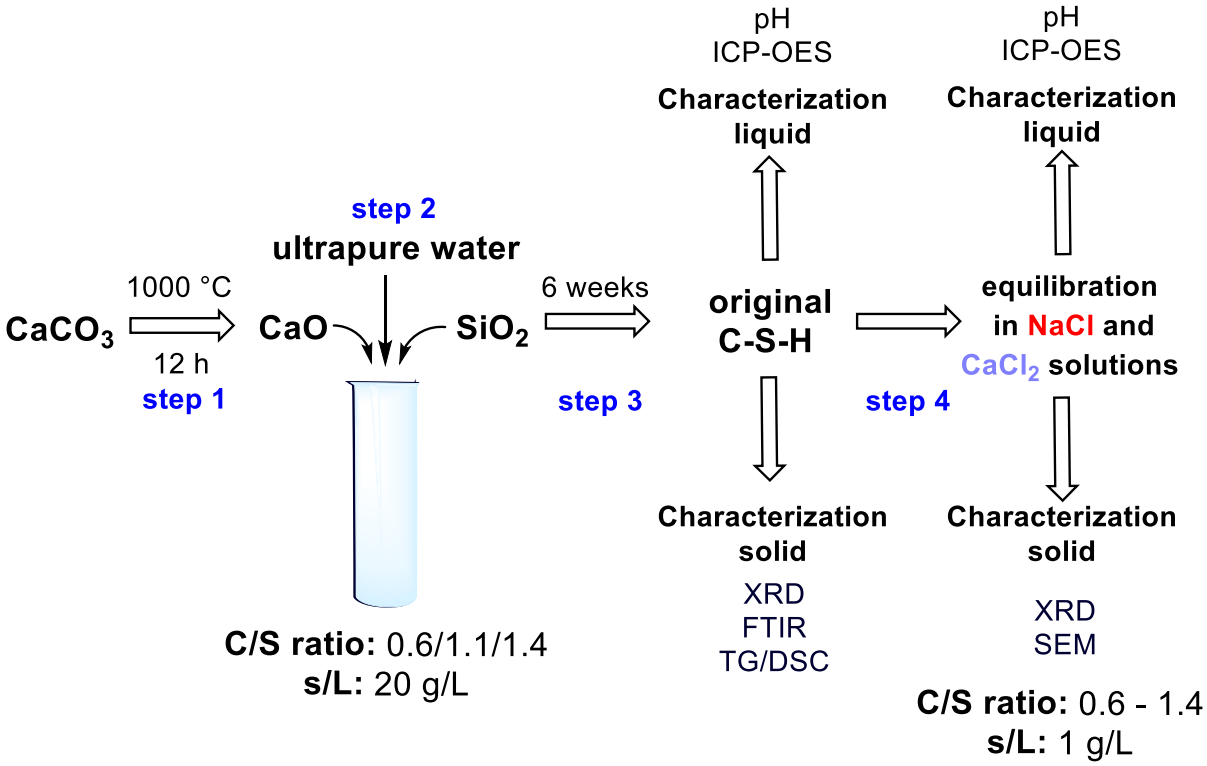

Figure 16: Preparation of C-S-H phases with different target ratios (C/S = 0.6; 1.1; 1.4). The preparation is a two-step-process: 1) Burning of $CaCO_3$ to CaO at 1000 °C for 12 h, 2) Mixing CaO, SiO_2 and ultrapure water in their corresponding ratios at S/V = 20 g/L. They were equilibrated for 6 weeks, before they were used for further experiments.

For the preparation of the C-S-H phases, $CaCO_3$ (*Alfa Aesar, **CAS:** 471-34-1*) was first calcined to CaO in a furnace (*Nabertherm Programm cort*. *with standard controller*) at 1000 °C for 12 hours. After cooling down the furnace to 200°C, the burned powder was transferred into a desiccator (silica gel), which was filled argon gas. The powder was then cooled to RT for 2 h. The yielded CaO was stored in a Glovebox under inert atmosphere. The direct synthesis of CaO and SiO_2 (*Aerosil 200, Evonik*) was then carried out in ultrapure water in 50 mL HDPE-vials (*Thermo Fisher Scientific, Sarstedt™*) with the desired C/S ratios of 0.6, 1.1 and 1.4 at a constant solid/liquid ratio (S/V = 20 g/l). C-S-H phases were contacted for 6 weeks with ultrapure water,

before using them characterization and further experiments. All C-S-H phases in NaCl and $CaCl_2$ solutions were prepared at S/V = 1 g/L. Therefore, a volume of 0.5 mL of the original C-S-H suspension at 20 g/L was diluted with 9.5 mL of the electrolyte solutions, respectively. The C-S-H phase was then contacted with NaCl or $CaCl_2$ before the addition of the RN or the organic ligands.

The final C/S ratios of the investigated C-S-H phases were determined by considering the initial weights of CaO and SiO_2 and the [Ca]- and [Si]-concentrations in solution, which were quantified (NaCl systems) or estimated ($CaCl_2$ systems) by ICP-OES. This is described in more detail in chapter 3.3.4.

3.2 Experimental methods

3.2.1 Batch sorption experiments

Every sample was prepared and stored in HDPE-Bottles (Zinsser Analytics). To separate the solid phase from the solution, the sample was transferred into centrifugation tubes (*Quick-Seal, Beckman Coulter*), which were welded afterwards inside the glovebox. The centrifugation in the ultracentrifuge was performed for 1 h at 90000 rpm at 20 °C (*rotor: 90TI at 90000 rpm, Centrifuge: Beckman Coulter OPTIMATM XPN-90*). After centrifugation, 3 mL of the sample was removed and acidified with 50 µL of nitric acid (*suprapure grade*, *65 %, Supelco*) to avoid the sorption of Eu(III) on the walls on the HDPE-Bottles. The batch sorption experiments were always performed between Eu(III), C-S-H phases or bentonite and oxalate or EDTA. In addition to the Eu(III)-C-S-H-EDTA experiments, the sorption of EDTA on C-S-H phases in the absence of Eu(III) was investigated. Quantification was performed by LSC using ^{14}C-labeled EDTA in combination with inactive EDTA. The sample preparation is described in section 3.3.3.

In the experiments, the main focus was on the variation of the following parameters: (i) ionic strength, (ii) ligand concentration and (iii) order of addition. In each experiment, however, additional parameters such as pH (bentonite), C/S ratio (CSH phase) and sorption times were varied. The solid-to-liquid ratio (S/V) in almost all of the batch sorption experiments was set constant to 1 g/L. Only the experiments described in section 4.4.3, were prepared at S/V = 20 g/L. The detailed experimental conditions are summarized in Table 2. For the experimental series investigating the order of addition of the individual components, three different cases considered. Prior to those experiments, the solid phase (C-S-H or bentonite) was always pre-equilibrated with the respective electrolyte solution. The first sampling took place after 7 days of total contact time. In the first case 1) Eu(III) is introduced for two days, followed by EDTA, which is contacted for another 5 days. In the second case 2) Eu(III) and EDTA are mixed together in parallel and contacted for 7 days. In the third case 3) EDTA is added and contacted for 5 days, followed by Eu(III), which is aged for two more days.

Table 2: Experimental conditions for the different batch sorption experiments with Eu(III) on C-S-H phases and bentonite MX80 in presence of oxalate and EDTA. The main parameter to vary in each experiment is shown in bold.

	C-S-H phases	Bentonite MX 80
(i) Variation of ionic strength		
[EDTA]	10^{-4} m, 10^{-2} m	10^{-4} m
[Oxalate]	10^{-3} m	10^{-3} m
C/S ratio or pH	0.6 – 1.4	pH = 3 - 12
I_m[NaCl]	**0.1 m, 1.02 m, 5.05 m**	**0.1 m, 1.02 m, 5.05 m**
I_m[$CaCl_2$]	**0.1 m, 1.02 m, 5.36 m**	**0.1 m, 1.02 m, 5.36 m**
Sorption time	7 and 50 d	7 and 50 d
(ii) Variation of ligand concentration		
[EDTA]	**10^{-5} m - 0.1 m**	**10^{-5} m - 0.1**
C/S ratio or pH	0.6 – 1.4	5 and 11
I[NaCl, $CaCl_2$]	1.02 m	1.02 m
Sorption time	7 and 50 d	7 and 50 d
(iii) order of addition		
[EDTA]	10^{-2} M	10^{-2} M
C/S ratio or pH	1.0 – 1.4	5, 11
I[NaCl, $CaCl_2$]	1.02 m	1.02
Sorption time	7, 50 d	7, 28 d
Order of addition	**case 1, 2 and 3 (described above)**	
(iv) Higher S/V ratio		
[EDTA]	10^{-4} m - 0.1 m	Not performed
C/S ratio or pH	0.6 – 1.4	
I_m[NaCl, $CaCl_2$]	1.02 m	
Sorption time	7 d	
S/V	**20 g/L**	

Distribution coefficient

Sorption processes of RN on solid phases are commonly expressed in terms of the sorption coefficient (K_d). The K_d describes the distribution between the concentration of the adsorbed species and the species in solution. This is described by the linear correlation of the Henry adsorption isotherm:[50]

$$\boldsymbol{C_{init} = K_d * C_{aq}}$$

For batch sorption experiments, the sorption coefficient can be represented as follows:

$$\boldsymbol{K_d = \frac{(C_{init} - C_{aq})}{C_{aq}} * \frac{V}{m} \left[\frac{L}{kg}\right]}$$

In this equation, [C_{init}] represents the initial concentration of the adsorbed species in mol/L. [C_{aq}] describes the concentration aqueous species and is also expressed in mol/L. [V] is the volume of the liquid phase in L, while [m] describe the mass of the solid phase in kg.

It applies, the higher the K_d value, the stronger the uptake of a RN by a given solid phase. The K_d value, however, requires a chemical equilibrium between the adsorbed and aqueous species, as well as a linear relation between them. However, this linear relationship is only valid for low concentrations of the adsorbed species, since there are then enough equivalent sorption sites available for the ions involved. The Freundlich or Langmuir isotherms are used to describe sorption reactions at higher concentrations (relative to the solid concentration). If a chemical equilibrium has not been proven in laboratory experiments, the R_d value is commonly used. The equation for the R_d value can be formulated analogously to the K_d value, but it represents only a distribution of a compound between the aqueous and solid phase. The R_d value depends on a large number of experimental parameters and can only be applied if the laboratory experiments were performed under consistent conditions.

3.2.2 TRLFS experiments

Time resolved Laser fluorescence spectroscopy (TRLFS) represents one of the most reliable and widely used methods to study the fluorescence properties of *Ln* and *An*. Possible associated shifts, splitting and intensity patterns in fluorescence emission spectra provide information about the chemical environment. The splitting of the f shell determines the energy of the characteristic f-f transitions. This energy depends mainly on the electron configuration, the oxidation state and changes in the first coordination sphere of an element. TRLFS can also give an indication whether a molecule has been associated to a mineral surface (inner-sphere sorption) or incorporated into a mineral phase (outer-sphere sorption).

To characterize further luminescence properties of a molecule, the fluorescence lifetime needs to be required. The measurement of the fluorescence lifetime is an approach of the time resolution included in TRLFS.

The Nd:YAG laser (*Continuum Surelite II*) was applied as pump laser for the coupled dye laser system (see Figure 17). The dye laser is operating at an energy between E = 1 – 4 mJ. The Nd:YAG laser is first excited at a frequency of 10 Hz and then the emission takes place at 1064 nm. The subsequent frequency tripling produces a laser beam at 355 nm, which activates a second laser process in the dye belonging to the dye laser unit (*Radiant dyes Narrow Scan*). Hereby the dye is dissolved in dioxane. The emission of Exalite 398 can be tuned between 391 - 404 nm. For measurements of Cm(III), the laser is operating at the fixed wavelength of λ = 396.6 nm (see section 1.4.1). Fluorescence emission is collected via an optical fiber, which is located perpendicular to the sample surface. Through this, the detection yield of the fluorescence emission is maximized. Then, fluorescence emission is detected with an optical multichannel analyzer including a polychromator unit (*Shamrock 303i, Andor*) and an ICCD-camera (*iStar, Andor; Modell DH720- 18F-63*). For the experimental set up, the grating of 1200 lines/mm with a wavelength range between λ = 580 - 640 nm was utilized.

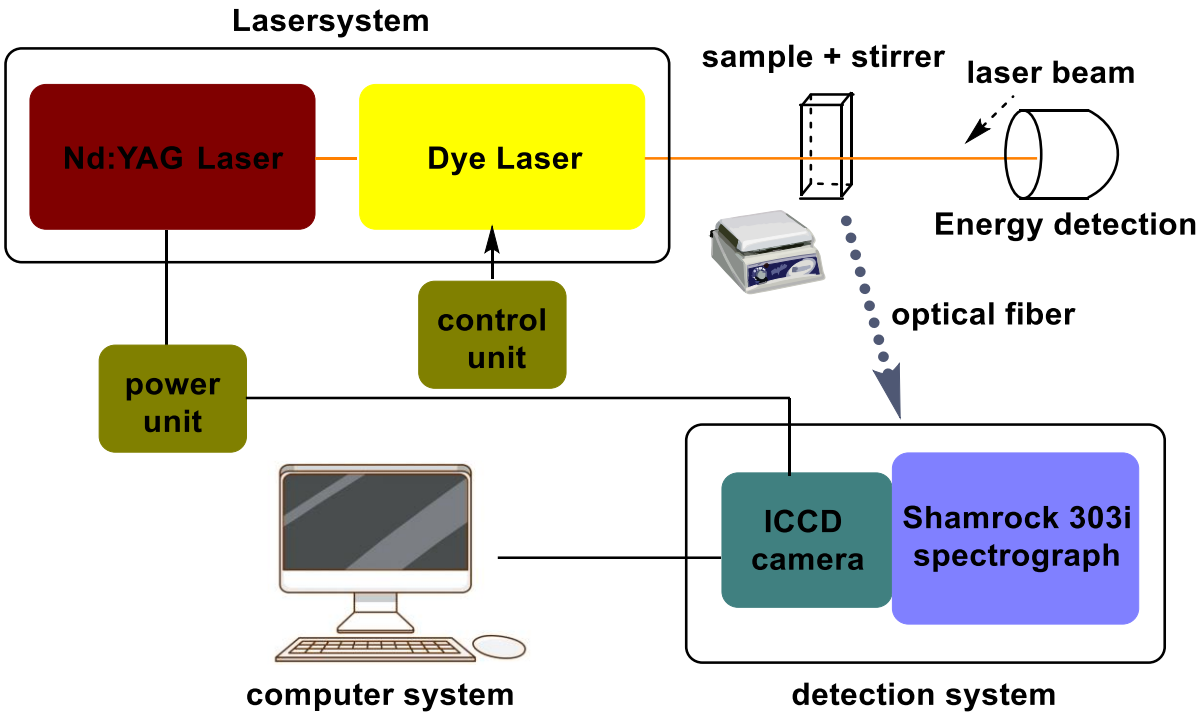

Figure 17: TRLFS setup: The Nd:YAG laser is coupled to a dye laser. Fluorescence emission signals are finally monitored with an optical multichannel analyzer including a polychromator unit and an ICCD-camera.

All TRLFS measurements were performed in two independent series: (i) Cm(III) sorption on C-S-H phases in presence of EDTA in addition to the batch sorption experiments, (ii) Examination of the Eu(III) and Cm(III) speciation.

Sample preparation: Cm(III) sorption on C-S-H phases in presence of EDTA

The sample preparation was performed in 15 mL vials (*Sarstedt)* in NaCl and $CaCl_2$ solutions at a fixed ionic strength (I_m = 1.02 m). All measurements were conducted between 7 and 365 d at two different C/S ~ 1.0 and C/S ~ 1.3 (NaCl), C/S ~ 1.4 ($CaCl_2$). Since the results from the batch sorption experiments between C/S ~ 0.6 and C/S ~ 1.0 are similar in both electrolytes, the focus was only put on C/S ~ 1.0. The experimental conditions for the TRLFS measurements are summarized in Table 3. For every sample, measurements in the solution and suspension were performed without a quantitative phase separation. Examination occurred after sedimentation of the supernatant or suspension. This procedure allowed the measurement of the same sample over the timeframe of one year. For measurements of the solution, 1 mL of the supernatant was filled into a quartz cuvette. This was closed with a cap to prevent the

sample from the interaction with air. Suspension measurements utilized the entire sample, with a stirring bar added. After measurement, the material was returned to the original sample and stored under an inert atmosphere.

Every spectrum was obtained after 1 µs of delay time, with a time window of 1 ms. To normalize the spectrum to the laser energy, the measured intensity was divided by the laser energy. The laser energy is expressed in mJ. For fluorescence lifetime measurements, series of single emission spectra were recorded with increasing delay time. The fluorescence lifetime (τ) was then calculated using the following formula.

$$\mathbf{I\,(\lambda) = I_0(\lambda) \cdot e^{(-t/\tau)}}$$

I_0 represents the intensity at t = 0. Hereby the integrated intensity (I) and the absolute intensity at the peak maximum were expressed as a function of the delay time (t). The fluorescence lifetime is given in µs.[39] The number of water molecules in the first coordination sphere was determined using the Kimura equation. This is described in detail in chapter 1.4. In the context of this work, however, it can only be used as a rough estimation, since the equation is only valid if there are no further water molecules in the first coordination sphere of the Cm(III) ion. Functional groups such as -OH and -COOH groups can also affect the lifetime. In addition, the distance between the ligand and the central ion also plays a role.

Table 3: Experimental conditions of the TRLFS measurements with Cm(III) on C-S-H phases in presence of varying [EDTA] in NaCl and $CaCl_2$ solutions. The main parameters to vary are shown in bold.

Parameters	
[EDTA]	**10^{-4} M – 10^{-2} M**
C/S ratios	1.0 – 1.4
I_m(NaCl/$CaCl_2$)	1.02 m
$[Cm]_{tot}$	10^{-7} M
Sorption time	**7 – 365 d**

Sample preparation: Examination of the Eu(III) and Cm(III) speciation

Two different series with different fixed ionic strength were prepared. The ionic strength was mainly determined by NaCl, whereas the Ca content was varied. Every sample was prepared in 2 mL vials. The measurements were only performed in solution and no solid phase was involved. The pH titration of each sample ranged from pH_m = 8.5 - 12.5 and was monitored for each 0.5 pH step. HCl and NaOH solutions were used to adjust the pH values. After every pH-step, a fluorescence emission spectrum and a fluorescence lifetime were recorded. All spectra were normalized to equal total emission intensity. The FI factors of the different Cm(III) species were assumed to be ~ 1 for all the species. A detailed discussion on the determination of the FI factors is shown in section 4.6. The measurements of the fluorescence emission spectra and the lifetime are similar to the samples described above. A summary of the experimental conditions is illustrated in Table 4.

Table 4: Experimental conditions of the TRLFS measurements for the examination of the Eu(III) and Cm(III) speciation. The main parameters to vary are shown in bold.

Parameters	
[EDTA]	10^{-2} M
I_m(total)	0.51 m, 2.09 m
%[Ca] to total I_m	**0.25; 1.25; 2.5; 6.25; 15 %**
$[Cm]_{tot}$	10^{-7} M
pH_m	**8.5 – 12.5**

3.2.3 In-situ EXAFS Am L_{III}-edge measurements

EXAFS spectra were recorded at the INE-Beamline source for Actinide Research at KARA[110], KIT Campus North for selected samples. The experimental conditions are summarized in Table 5.

Synchrotron radiation covers a broad spectrum, reaching from IR to hard X-ray radiation with energies from 1 – 106 eV. X-ray absorption spectroscopy (XAS) can be used to determine properties such as the oxidation state (XANES) and the coordination chemistry (EXAFS).[111] The principle is based on the absorption of X-rays in atoms by the ionization of electrons.

The absorption coefficient increases drastically, if the photon energy is equal to the ionization energy, *i.e.*, $E_{hv} = E_0$. The expression E_0 is referred to an edge and can be divided into, *e.g.,* K- or L-edge depending on the energy of the ionized electron. The exact location and structure of the edge depends strongly on the oxidation state of the element under study. E_0 values are known for various elements and are reported in the literature.[112] In case of $E_0 < E_{hv}$, no ionization takes place. Excess kinetic energy of the emitting electron ($E_{kin'}$) is available if $E_0 > E_{hv}$. Hereby the relation of De Broglie is essential and illustrated below.[113]

$$\lambda_{el} = h \cdot c \cdot E_{kin}^{-1}$$

The photoelectron can be described as a matter wave within this equation. The resulting photoelectrons are then scattered back to neighboring atoms. This leads to destructive or constructive interference patterns (see Figure 18) between the emitted photoelectrons and backscattered electrons. This depends on the number, type and distance of the neighboring scattering centers. Associated with this are changes in the absorption coefficient, leading to oscillations in the absorption spectrum. Their fine structure is the focus of EXAFS spectroscopy.[114]

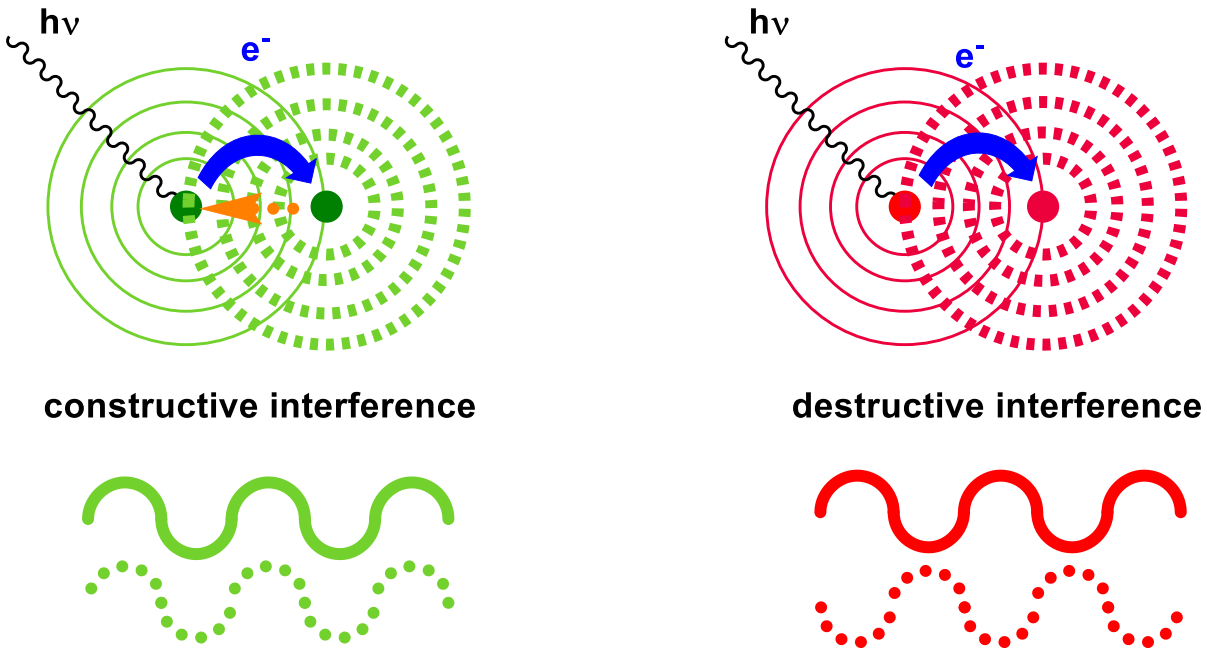

Figure 18: Interference processes in EXAFS spectroscopy: Left: Constructive (waves in phase) in green, right: Destructive interference in red.

Exemplarily a XAFS spectrum is shown in Figure 19. This is divided into the XANES and the EXAFS spectrum. The former ranges from E = ± 50 eV before and after the absorption edge. For E > 50 eV the EXAFS spectrum starts shortly after the edge.[114]

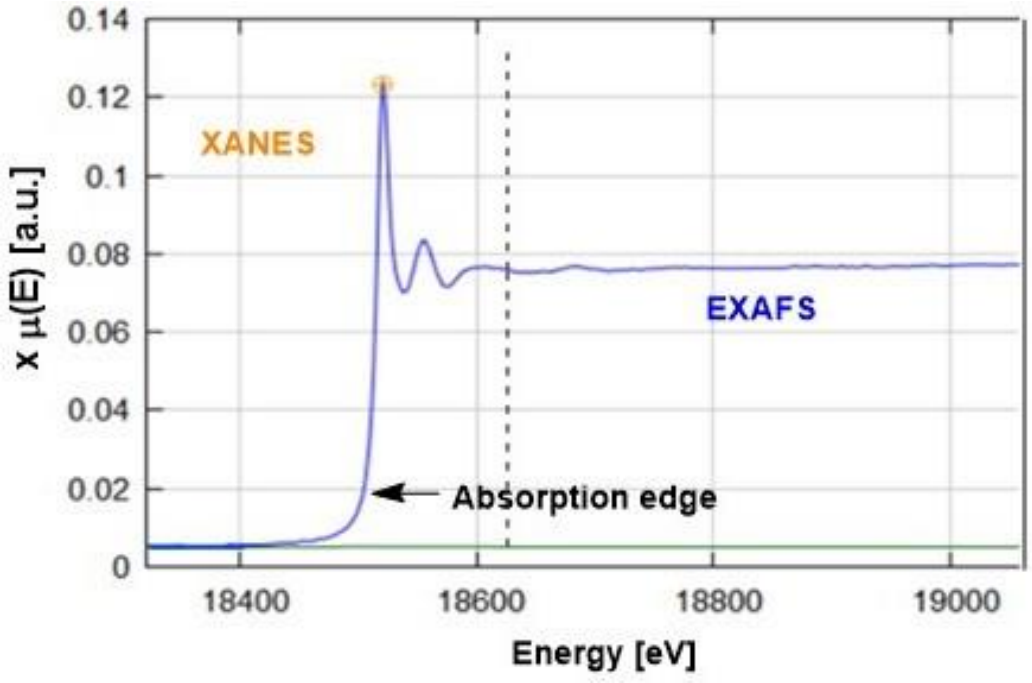

Figure 19: The XAFS spectrum is divided into the XANES spectrum, which is located at E = ± 50 eV before and after the absorption edge. The EXAFS spectrum is exclusively located after the absorption edge at E > 50 eV.

In this work only EXAFS spectra were considered. Destructive interference in the EXAFS range results in damping, while constructive interference leads to a stronger oscillation. The relationship between the absorption coefficient and the interference pattern is as follows:

$$\chi(E) = \frac{\mu(E) - \mu_0(E)}{\mu_0(E)}$$

Subsequently, χ(E) is converted into χ(k), to extract structural information from the experimental data.[115]

$$\chi_{theo}(k) = \frac{1}{k} \cdot \sum_{j=1}^{n} \frac{N_j}{r_j^2} \cdot F_j(k) \cdot S_{0,j}(k) \cdot e^{-2\sigma_j^2 k^2} \cdot e^{\frac{-2(r_j - \Delta)}{\lambda(k)}} \cdot \sin(2krj + \Phi_{i,j}^{l}(k))$$

This function depends on the wave vector k. The wave vector k is defined as $k = \frac{2\pi}{\lambda}$. With the relation according to de Broglie one obtains the complete formula for k:[49]

$$k = \frac{2\pi}{h}\sqrt{2m_e(h\nu - E_i)}$$

$$\text{with } \lambda_e = \frac{h}{\sqrt{2m_e(h\nu - E_i)}}$$

Where h is the Planck constant, m_e is the electron rest mass, ν is the frequency of the absorbed light and E_i represents the ionization energy of the photoelectron. The wave vector k^n with n = 1, 2, 3 is additionally weighted to compensate for the decrease in EXAFS oscillation as K increases. $F_j(k)$ represents the backscatter amplitude. $S_{0,j}$ (k) describes the reduction factor. $e^{-2\sigma_j^2 k^2}$ takes into account the thermal and static damping, where $e^{\frac{-2(r_j - \Delta)}{\lambda(k)}}$ describes the inelastic scattering. Sin ($2kr_j + \Phi_{i,j}^{l}(k)$) represents for the total phase. N_j is the number of backscattering atoms of a type in the shell j. r_j describes the distance between the backscattering atoms in the shell j and the absorber atom. σ_j^2 is the Debye Waller factor. λ_j(k) is the mean free path of the photoelectron in the sample. $\Phi_{ij}^{l}(k)$ determines the phase shift of the electron. The Fourier transformation of χ(k) into the local space yields to a pseudo-radial distribution function F(r). The maxima of this function corelate with the radial coordination shells of the absorber. However, F(r) cannot provide quantitative structure information.

Therefore, the back-transformation of a single maximum is used to obtain structural and chemical information.[115]

Sample preparation

EXAFS spectra were collected for the Am L_{III}-edge at the energy of ~ 18515 eV. Before the measurements, a calibration with the Zr K-edge at an energy of ~ 17998 eV was performed. The data evaluation was conducted with the program package of ATHENA, ARTEMIS and Hephaestus with the support of J. Rothe and K. Dardenne.[116]

Every sample was prepared and stored in 15 mL vials (*Sarstedt*). Am(III) was used with a fixed concentration of $[Am]_{tot} = 1 \cdot 10^{-3}$ M. For the measurements, 350 µL of the sample were transferred into polyethylene vials (first containment). The vials were attached to a sample holder. and sealed with parafilm and tape afterwards. The sample holder was packed into a plastic bag (second containment), which was closed with tape again. The experimental conditions are described in Table 5.

Table 5: Experimental conditions of the EXAFS measurements used for the structural characterization of Ca-Cm(III)-EDTA and Ca-Cm(III)-OH-EDTA species. The main parameters to vary are shown in bold.

Parameters	
c[$CaCl_2$]	**0; 0.03; 0.33; 1.50 mol/L**
I_m[$CaCl_2$]	**0, 0.1, 1.0, 4.5 mol/L**
c[EDTA]	10^{-2} M
c[Am]-243	$1 \cdot 10^{-3}$ M
pH_m of sample	**8.7; 11.2**

3.3 Analytical methods

3.3.1 pH measurements in saline solutions

At I_m > 0.1 m the liquid junction potential affects the salt bridge of the electrode, resulting in a systematic deviation in the pH measurements. Therefore, pH measurement of high ionic strength solutions (I_m > 0.1 m) requires a correction factor to obtain an accurate measurement. This correction factor is the A-value, which entails both the liquid junction potential and the activity coefficient of H^+ at a given background electrolyte concentration. The pH value obtained from the experimentally available pH value (pH_{exp}) and the correction of the ionic strength by the A value is calculated as follows:

$$\mathbf{pH_m = pH_{exp} + A = -log\,[H^+]}$$

The A-values are determined empirically for each background electrolyte, concentration and temperature. The respective A-values in NaCl and $CaCl_2$ solutions of different ionic strength at T = 22 °C are illustrated in Table 6.[117, 118]

Table 6: The A-values reported by Altmaier *et al*. for NaCl and $CaCl_2$ solutions of different ionic strength in Molar and molal units.[117, 118]

I(NaCl/$CaCl_2$)/M	I_m(NaCl)/m	A value	I_m($CaCl_2$)/m	A value
0.1	0.10	-0.08	0.1	-0.11
0.5	0.51	-0.01	0.51	-0.04
1.0	1.02	0.08	1.02	-0.07
2.0	2.09	0.27	2.09	0.19
4.5	5.05	0.80	5.36	0.78

pH_{exp}, was measured with a semi-micro electrode (*Orion Ross Ultra Combination pH electrode, Thermo Fisher Scientific, Waltham, Massachussets*) combined with an Orion Star pH meter (*Orion720 A+)* is used. The calibration of the pH electrode is performed with buffer solutions of pH 3, 6, 9 and 12 (*Merck, Darmstadt, Germany*) before every measurement. NaOH and HCl (*Titrisol, Merck*) solutions (c = 0.001, 0.1, 1 M) were used to adjust the pH values.

3.3.2 Gamma-counter

For the measurement of the ɣ-activity of ^{152}Eu in the batch sorption experiments, a ɣ-counter was used (*2480 Automatic Gamma Counter Wizard 2*, PerkinElmer). The ɣ-counter is shown in Figure 20. The detector consists of a sodium iodide single crystal activated with thallium NaI(Tl). Ionizing γ-rays from the sample enter the crystal. The interaction between the crystal and the γ-rays, lead to their absorption and then the emission of photons. These are then multiplied by a Photomultiplier tube (PMT) and converted into an electronic signal. For each sample, a volume of 1 mL is used. All measurements are limited to a maximum duration of three hours.

Figure 20: The ɣ-counter device, including a thallium doped single NaI crystal to measure Eu-152 samples among others.

3.3.3 Liquid Scintillation Counting (LSC)

The Liquid Scintillation Counting (LSC) device was used for batch sorption experiments with the ^{14}C-labelled EDTA, where the sorption of EDTA on C-S-H phases was investigated. For all measurements, the Tri Carb 3110 TR (*PerkinElmer*) was used (see Figure 21). The principle is described as follows: First, the sample to investigate is added to the LSC-cocktail. This cocktail consists of an organic mixture, the scintillator and the solvent*, e.g.,* toluene. The radioactive decay of the α- and β emitters excites the solvent molecules. The energy of the excited solvent molecules is then transferred to the primary scintillator, which emits the energy by emission of light quants. Those are converted into an electrical impulse by means of a photocathode. This in turn is amplified with a secondary electron multiplier.

Figure 21: The LSC device *Tri-Carb 3110 TR* from the company PerkinElmer for measurements of α or ß emitters.

During sample preparation, inactive EDTA (c = 10^{-2} M) was mixed with C^{14}-labelled EDTA (c = $8.7 \cdot 10^{-8}$ M). The batch sorption experiments were then performed as described in section 3.2.1. After phase separation, a certain amount of the sample was added to the organic cocktail Ultima Gold XR (*Merck*) prior to the measurement. The experimental parameters are shown in Table 7.

Table 7: Experimental conditions for LSC measurements with ^{14}C-labelled EDTA. The main parameters to vary are shown in bold.

Parameters	
[EDTA]	10^{-2} M
C/S ratio	0.6 – 1.4
I_m[NaCl]	**0.1 m, 1.02 m, 5.05 m**
I_m[$CaCl_2$]	**0.1 m, 1.02 m, 5.36 m**
Sorption time	7 and 50 d

3.3.4 Inductively coupled plasma optical emission spectroscopy (ICP-OES)

Inductively coupled plasma optical emission spectroscopy (ICP-OES) is a powerful tool to quantify dissolved elements at low concentrations in particular. ICP-OES shows the advantage to be able to handle moderately high salt concentrations in solution. It is a robust method, and is mostly used for ground- or wastewater analysis.[119, 120] Thus, it is the preferred method in the context of this work under the given solutions up to high ionic strength.

Figure 22 illustrates the working principile as follows: A liquid sample is pumped into the nebulizer, where the sample is dispersed into a fine aerosol with the help of the supplied Ar-gas. The aerosol enters the spray chamber where it is vaporized at a plasma temperature of ~ 6000 - 8000 °C. This process is followed by atomization, ionization and excitation of the sample. The resulting energy is released in the form of light (photons), which are then directed and focused through various lenses into the monochromator. The monochromator split the light into element-specific wavelengths. The light intensity is then measured with a photomultiplier (PMT). This can then be converted into a concentration using calibration.[119 121] More detailed information can be found in the literature.[122, 123]

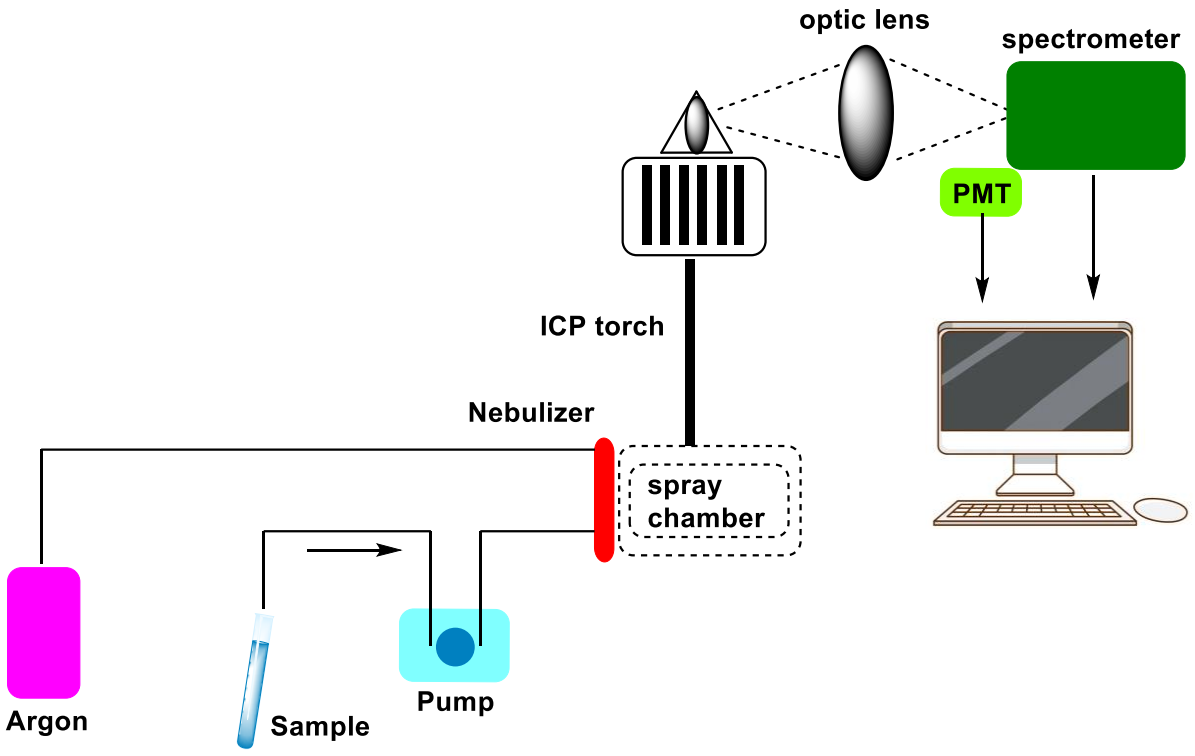

Figure 22: Schematic setup of an ICP-OES instrument. The liquid sample is pumped into the nebulizer, where it is dispersed with the help of the supplied Ar-gas into a fine aerosol. The aerosol is vaporized in the plasma, followed by atomization, ionization and excitation of the sample. This energy is released in the form of photon emission. The photons are directed and focused through various lenses into the monochromator. Here they are split into element specific wavelength. Each element has a characteristic emission spectrum. This is measured with a spectrometer. The resulting light intensity at a specific wavelength is then measured and converted to a concentration by calibration.[119, 121]

[Si] and [Ca] from the C-S-H phases, are measured in the aqueous phase by inductively coupled plasma optical emission spectroscopy (ICP-OES, Avio550 Max, PerkinElmer). For the measurements, all samples were diluted in ultrapure 2%-HNO_3 (*Sigma-Aldrich* ***CAS****: 7697-37-2*). The preparation of the C-S-H phase is described in chapter 3.1.2. The C-S-H phase was then contacted in NaCl or $CaCl_2$ solution for 7 days before the addition of the RN or the organic ligand. In addition, the solid phase was separated from the liquid phase with ultracentrifugation (see chapter 3.2.1).

The final C/S ratios of the investigated C-S-H phases were determined by taking into account the initial weights of CaO and SiO_2 and the [Ca] and [Si] concentrations in solution, quantified by ICP-OES (NaCl systems). Due to the low S/V ratio in the NaCl and $CaCl_2$ experiments, some C/S ratios were lower than the original target value. This

was especially visible for the highest C/S in NaCl systems (C/S ~ 1.3), due to the higher dissolved Ca concentration in the aqueous phase (see section 3.1.2).

For $CaCl_2$ systems, a calculation of the C/S ratio on the basis of the experimental values was not possible, due to the high relative Ca concentration in the aqueous phase of the sorption experiments. Consequently [Ca] was estimated with [OH^-] dissolved in $CaCl_2$ after dilution of the original C-S-H suspension. Hereby it was assumed, that one mole of Ca is dissolved for every two moles of OH^-. With the experimental [Si] it was possible to estimate the semi-quantitative C/S ratio in these C-S-H systems.

3.3.5 Fourier-transformed-infrared spectroscopy (FTIR)

The principle of Fourier-transformed-infrared spectrometry (FTIR) is based on molecular vibrations and rotations by the absorption of infrared photons. The IR spectrum is considered the fingerprint of a substance. In the context of this work, it was mainly used to exclude carbonation of the C-S-H phases. All samples were measured with the INVENIO R-FTIR-spectrometer (*Bruker*).

The principle of the spectrometer is illustrated in Figure 23, using the Michelson interferometer. In a first step, the beam from the light source (L) is split into two individual beams by the beam splitter. One beam is directed onto a stationary mirror (sM) and is reflected, while the other beam is directed to a movable mirror (mM). Then the two beams are recombined and are passing through the sample to the detector (D). The recombination of the two beams leads to constructive and destructive interferences. It results in an interferogram, which is converted onto a spectrum due to Fourier transformation.[24]

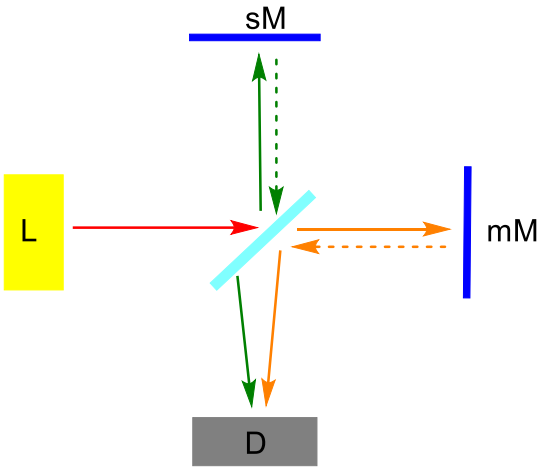

Figure 23: Michelson Interferometer. The emitting light from the light source (L) goes through a beam splitter. One half goes through and is directed on a movable mirror (mM), while the other half of the beam is reflected from stationary mirror (sM). Then the two beams are recombined and are passing through the sample to the detector (D).[24]

Bentonite MX80 and C-S-H phase samples were prepared in ultrapure-water and stored under inert atmosphere, where the samples were dried there for three days. For

every sample, 64 scans with a resolution of 4 cm^{-1} were performed, while the spectra were recorded between 400 cm^{-1} and 4000 cm^{-1}.

3.3.6 X-Ray powder diffraction (XRD)

X-Ray powder diffraction (XRD) is commonly used to determine the composition of dried powder samples. The sample is first illuminated with light of a monochromatic wavelength. At certain angles of incidence Θ, a constructive interference of the radiation which is scattered by the atoms of the sample can occur. The radiation is then diffracted at the same angle Θ of incidence.[24, 50] The principle of XRD can be described with the Bragg equation below:

$$\boldsymbol{n} * \boldsymbol{\lambda} = \mathbf{2} * \boldsymbol{d} * \mathbf{sin}(\Theta)$$

In this equation, [n] represents the diffraction order, [λ] is the wavelength in nm, d is referred to the distance of grid levels with the unit m. The “Bragg angle” Θ describes the angle between the x-ray beam and the grid levels. The Bragg equation can be used to calculate the angle at which incident X-rays must strike the crystal surface in order for constructive interference to be observed. The schematic principle is explained in Figure 24.

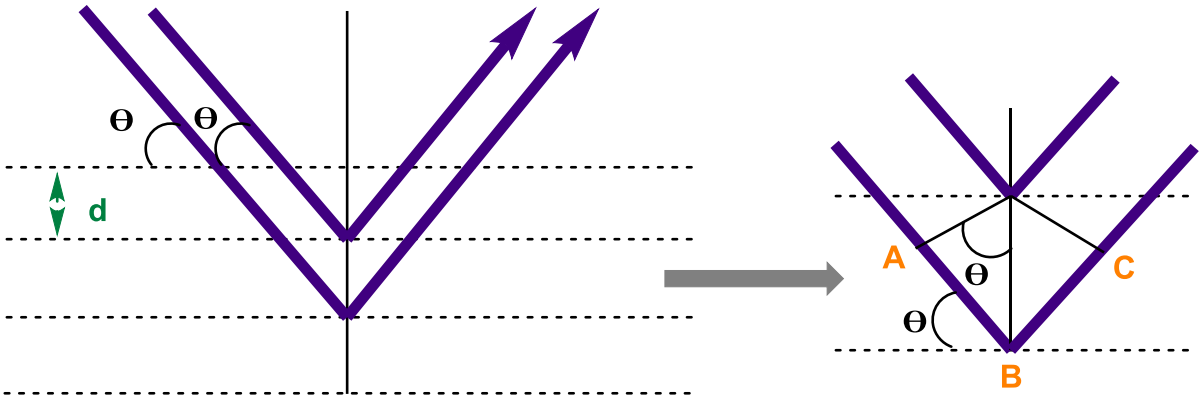

Figure 24: Schematic description of the Bragg equation, which can be used to describe constructive interference.

Every grid plane is treated as a mirror plane at which the incident radiation is reflected. When two X-ray beams arrive at the grid planes, they differ in their path length AB and

BC (Figure 24, right). The angle of incidence θ determines the path length. Constructive interference occurs, if AB and BC are equal to an integer multiple of the of the wavelength.[50]

The XRD measurements were performed with a D8 Advance (*Bruker*) diffractometer with a Cu K - α radiation source (λ = 0.15418 nm, I = 25 mA, U = 40 kV) and an energy dispersive detector (Sol-X). The program DIFFRAC.EVA 3.0 (*Bruke*r) and Origin were used for data treatment. The measurements for bentonite and C-S-H phase samples were carried out at a step width of 0.013°, a step counting of 0.5 s and was set from 2θ = 10 – 80 °.

The XRD analysis of the bentonite samples was performed under ambient conditions. The measurements of C-S-H phase samples were performed with a specific sample holder: The respective sample was placed onto a single crystal silicon wafer. On top of the silicon wafer, a cap prevents the sample from the interaction with air. To remove NaCl and $CaCl_2$ from the C-S-H phase, samples were washed and dried before the experiment according to Bernard *et al.*.[72]

The Scherrer equation was also used to gain insight on the crystallite size, L.

$$\boldsymbol{L = \frac{K \cdot \lambda}{\beta \cdot cos\theta}}$$

where the X-ray wavelength is described by λ in nm, K is the Scherer constant (usually given as 0.9) and β is the full width at half maximum (FWHM).[124]

3.3.7 Scanning electron microscopy Energy dispersive X-ray spectroscopy (SEM-EDX)

The combined method of scanning electron microscopy Energy dispersive X-ray spectroscopy (SEM-EDX) is used to characterize the surface of solid samples with SEM, while EDX provides information on the elemental composition of the sample. For all measurements, the Quanta 650 FEG device with a UltraDry silicon drift X-ray detector (*Thermo Scientific*) was applied. The working principle of SEM-EDX, which is illustrated in Figure 25 is adapted from Taniguchi *et al.*[125] and described as follows: The primary electron beam from the source is directed onto the sample in several steps. This beam scans the sample to be examined. The interaction between the sample's electrons and those of the beam leads to further effects: Most of the electron beam interacts with the sample and is scattered in elastic and inelastic mode. In addition, there are secondary effects such as backscattered electrons, emitted secondary electrons and X-rays. Each primary or incident electron can generate several secondary electrons. These provide topographic information. When an incident electron collides with an atom of the sample, it loses energy. This energy is scattered back, which creates backscattered electrons. These provide information *e.g.,* about ordinal number differences. The signals are then converted into an image, which is characteristic for each sample.[126]

As described above, the primary electron beam hitting the sample also emits X-rays, which are detected by the EDX detector. The resulting spectrum is characteristic for each element and allows the qualitative analysis (*e.g.* identification of the element) and quantitative analysis (*e.g.* atomic %).[127]

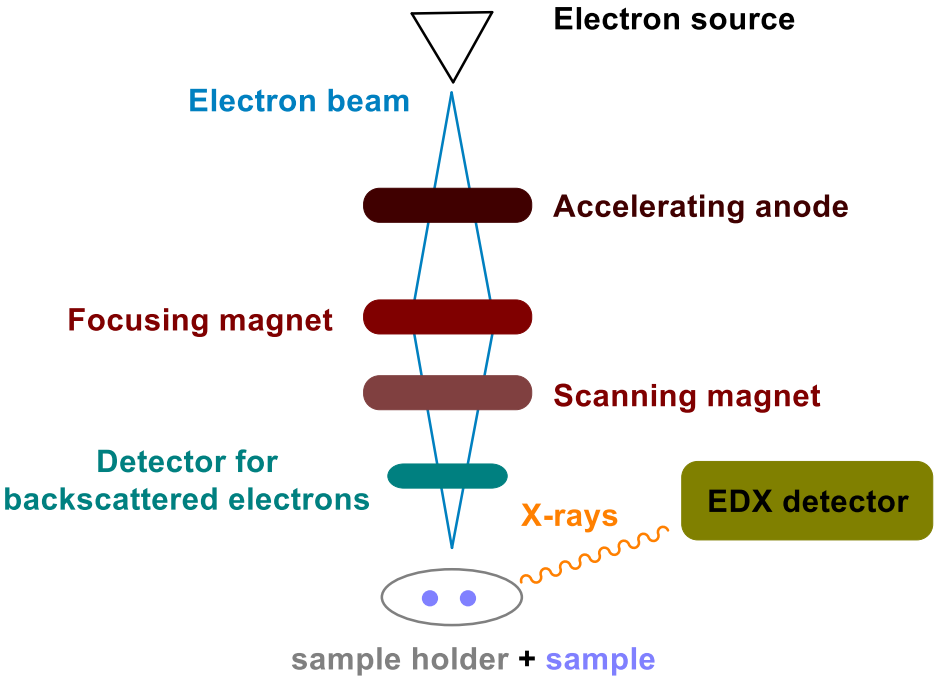

Figure 25: The working principle of SEM-EDX, in which an electron beam is directed at a sample. On the one hand, a characteristic image is produced as part of the SEM measurement. On the other hand, the resulting X-rays are detected by the EDX detector. The EDX analysis provides information about the composition of the sample.

The samples were prepared analogues to section 3.3.7. Then they were placed onto a polished carbon sample holder under ambient conditions.

3.3.8 Thermogravimetry/Differential Scanning Calorimetry (TG - DSC)

Both methods, thermogravimetry (TGA) and differential scanning calorimetry (DSC), provide information about the physical and chemical properties at different temperatures. In TGA, the change in mass of a sample subjected to a controlled temperature profile is measured by recording profile is measured by recording the weight evolution with temperature. Both of these methods are commonly used for the analysis of cementitious materials. TGA is applied in combination with DSC for the identification of hydrated phases, such as C-S-H phases. In addition, TGA-DSC can be used in a complementary manner to XRD to confirm the presence of crystalline or amorphous phases. Further it can be applied quantify the amount of solid matter present, which is complementary to SEM.[128] For the measurements, every sample was heated from RT to 1200 °C under a continuous flow of N_2 a heating rate of 10 °C/min. The measurements were performed with the device STA409 (*Netzsch Gerätebau GmbH*). The samples were only prepared for C-S-H phases. Each sample contained ~ 50 mg dry C-S-H phase.

3.3.9 Specific surface area (N_2-BET)

Specific surface area determination was first discovered by Stephen Brunauer, Paul Hugh, Emmet and Edward Teller in 1938.[129] The working principle is based on low temperature nitrogen adsorption. Hereby the nitrogen gas is passed over a sample, which is cooled down by liquid nitrogen in parallel. A part of the gas adsorbs on the surface. The amount of adsorbing substance depends on the kind of gas, pressure and temperature for instance. In the end adsorption isotherms can be calculated by monitoring changes of the gas pressure. The specific surface can be determined. The SI-unit of the specific surface is m^2/g.[130] All measurements were performed with the Autosorb 1 device (*3P Instruments*).

All measurements were only performed for bentonite MX80 samples. Therefore 600 mg solid phase of the sample were needed.

3.4 Thermodynamic calculations

A chemical equilibrium can be illustrated by a complexation reaction as follows:

$$\boldsymbol{bB} \cdot \boldsymbol{cC} \leftrightarrow \boldsymbol{B_bC_c}$$

The equilibrium is described using the conditional stability constant $\boldsymbol{\beta}'(\boldsymbol{T})$ according to the law of mass action:

$$\boldsymbol{\beta}'(\boldsymbol{T}) = \frac{[\boldsymbol{B_bC_c}]}{[\boldsymbol{B}]^{\boldsymbol{b}} \cdot [\boldsymbol{C}]^{\boldsymbol{c}}}$$

However, $\boldsymbol{\beta}'(\boldsymbol{T})$ refer to the actual physical and chemical state (*e.g.,* ionic strength) of the system under study. In order to ensure better comparability of different data sets, the constants must be related to uniform standard conditions. These standard conditions have been defined by IUPAC such as T = 298.15 K, p_0 = 0.1 MPa, m_B = 1.0 mol/kg H_2O, γ_B = 1 and I_m = 0.[131] Therefore, the stability constant $\boldsymbol{\beta}_{\boldsymbol{n}}^{\circ}(\boldsymbol{T})$ must be based on the activities $\boldsymbol{a_i}$ of the individual components i in the system and not on their concentrations $\boldsymbol{c_i}$. With $\boldsymbol{a_i}(\boldsymbol{T}) = \boldsymbol{c_i} \cdot \boldsymbol{\gamma_i}(\boldsymbol{T})$, the relationship between $\boldsymbol{\beta}'$ and $\boldsymbol{\beta}_{\boldsymbol{n}}^{\circ}$ is as follows:

$$\boldsymbol{\beta}_{\boldsymbol{n}}^{\circ}(\boldsymbol{T}) = \frac{\boldsymbol{a}_{\boldsymbol{B_bC_c}}}{\boldsymbol{a}_{\boldsymbol{B}}^{\boldsymbol{b}} \cdot \boldsymbol{a}_{\boldsymbol{C}}^{\boldsymbol{c}}} = \frac{[\boldsymbol{B_bC_c}]}{[\boldsymbol{B}]^{\boldsymbol{b}} \cdot [\boldsymbol{C}]^{\boldsymbol{c}}} \cdot \frac{\boldsymbol{\gamma}_{\boldsymbol{B_bC_c}}}{\boldsymbol{\gamma}_{\boldsymbol{B}}^{\boldsymbol{b}} \cdot \boldsymbol{\gamma}_{\boldsymbol{C}}^{\boldsymbol{c}}} = \boldsymbol{\beta}'(\boldsymbol{T}) \cdot \frac{\boldsymbol{\gamma}_{\boldsymbol{B_bL_n}}}{\boldsymbol{\gamma}_{\boldsymbol{B}}^{\boldsymbol{b}} \cdot \boldsymbol{\gamma}_{\boldsymbol{C}}^{\boldsymbol{c}}}$$

Hereby γ_i represents the activity coefficient, which is a function of the ionic strength I_m and the temperature. The following models can be used to determine the activity coefficients from low to high ionic strength: Debye-Hückel limiting law, extended Debye-Hückel limiting law, Specific Ion Interaction Theory (SIT) and Pitzer, among others. These are explained in the following. The first model is derived by Debye and Hückel and only valid for diluted solutions of $I_m \leq 0.001$. The activity coefficient is given by the simplified Debye-Hückel equation:[50, 132]

$$\log \boldsymbol{\gamma_i}(\boldsymbol{T}) = -\boldsymbol{z_i^2} \cdot \boldsymbol{A}(\boldsymbol{T})\sqrt{\boldsymbol{I_m}}$$

A(T) represents the Debye Hückel parameter, z_i is described as the charge of an ion I and thus a negative number for anions and positive for cations. I_m is the ionic strength.

The Debye Hückel equation it is only valid for very dilute solutions. The ions are considered as point charges and their interactions are based on purely electrostatic interactions. If this condition is no longer fulfilled, the extended Debye Hückel rule applies. This is valid for $I_m \leq 0.1$.[132]

$$\log \gamma_i\ (T) = -z_i^2 \cdot D(T) = -z_i^2 \cdot \frac{A(T)\sqrt{I_m}}{1 + B(T) r_i \sqrt{I_m}}$$

The second Debye Hückel term B(T) is now delivered by this equation. It is commonly defined with B(T). This equation extends the Debye Hückel equation by the size of the ions and their solvation shell. This is taken into account by the empirical ion parameter r_i.

The SIT model is an extension of the extended Debye Hückel equation. It is generally used for higher ionic strengths up to $I_m = 4$ m and additionally takes into account non-electrostatic interactions between ions with opposite charge. The activity coefficient is formulated using the SIT equation as follows:[132]

$$\log \gamma_i = -z_i^2 D(T) + \sum_k \varepsilon(j,k) m_k = -z_i^2 \cdot \frac{A(T)\sqrt{I_m}}{1 + B(T) r_i \sqrt{I_m}} + \sum_k \varepsilon(j,k) m_k$$

The ion interaction coefficient ε(j,k) describes the interaction of the ion j with the oppositely charged ion k. m_k is the concentration of ions k. A(T) is the first Debye-Hückel constant, while B(T) represents the second Debye-Hückel constant. A(T) and B(T) are commonly attributed to the values 0.509 and 1.50 $kg^{1/2}\,mol^{-1/2}$. The term z is the charge of the ions with $\Delta z_i^2 = z_{j,k}^2 - m \cdot z_j^2 - n \cdot z_k^2$ and $\Delta\varepsilon = \sum \varepsilon_{products} - \sum \varepsilon_{educts}$. Thus, the stability constant can be formulated as follows:

$$log\ \beta'\ (T) - \Delta z_i^2 D(T) = log\ \beta^0\ (T) - \Delta\varepsilon \cdot I_m$$

With the help of the equation, the thermodynamic stability constant β^0 can be obtained from a set of conditional stability constants $\beta'(T)$. These can then be plotted against each other using a linear SIT regression, where the intercept is log β^0 and the slope is $-\Delta\varepsilon$, which allows the calculation of the ε(j,k) value.[132]

The Pitzer approach allows a realistic description of concentrated salt systems. Within this equations, binary and ternary ion-ion interactions between neutral and solvated species are taken into account. However, this leads to a large number of parameters that make the equations very complex, so detailed information can be found in the literature.[133, 134]

3.4.1 Geochemical Modelling

For geochemical modelling, the software PHREEQ-C v3.7.3 with adapted Notepad++ and the ThermoChimie database were used.[135, 136] SIT is included in the ThermoChimie database.[43] Further, the geochemical modelling software Medusa/Spana was applied for the speciation diagrams with Oxalate.[137]

For the determination of Ca and Si concentrations in solution, the concentrations determined in chapter 4.2.2 were used.

For the speciation of the bentonite MX80 samples, the composition of montmorillonite (SWy-2) was used according to Steudel *et al.*.[138] (see Table 8). As already explained in chapter 1.6, montmorillonite is the main component of bentonite and therefore the relevant solid phase for the batch sorption experiments.

Table 8: The composition of montmorillonite (SWy-2) used for the modelling of bentonite with PHREEQ-C according to Steudel *et al*..[138]

SiO_2/ %	Al_2O_3 / %	MgO / %	Fe_2O_3 / %	CaO / %	Na_2O / %	K_2O / %
61.26	17.98	2.41	3.79	1.54	1.34	0.59

In all speciation diagrams, [Oxalate] was set to 10^{-3} M, while [EDTA] was set to 10^{-2} M. Instead of Eu(III) or Cm(III), Am(III) was used in the speciation diagrams, since it can be used analogously for this purpose (see Chapter 1.2). For all speciation diagrams, $[Am]_{tot} = 2 \cdot 10^{-8}$ M was used.

4. Results and Discussion

4.1 Sorption of Eu(III) on bentonite MX80 in presence of oxalate and EDTA

In this study, batch adsorption experiments were conducted to investigate the retention of Eu(III) on bentonite MX80 in the presence of oxalate and EDTA. These experiments were performed similarly to the ones conducted with C-S-H phases at high salt contents, as described in section 4.3 and 4.4. However, since the main focus of the study was put on C-S-H phases, the results of the batch sorption experiments and the characterization of the bentonite solid phase are presented in the Appendix, in the sections 7.5 - 7.7.

4.2 Characterization of the C-S-H phases

The C-S-H phases were prepared as described in section 3.1.2. The characterization for C-S-H phases prepared in ultrapure water at S/V = 20 g/L is thus shown in section 4.2.1. After 6 weeks of contacting in ultrapure water, the C-S-H phases are equilibrated in NaCl or $CaCl_2$ solutions for 7 days before the experiments. In the literature, C-S-H phases are described that were aged with different electrolyte solutions (*e.g.*, NaCl, MgO, $MgCl_2$) over a period of 24 hours to 3 months. Therefore, a period of 7 days was chosen. The characterization for C-S-H phases ageing in NaCl and $CaCl_2$ solutions is described in section 4.2.2.[71, 72, 91]

4.2.1 C-S-H phases prepared in ultrapure-water

Fourier-transform infrared spectroscopy (FTIR)

The C-S-H phases are characterized by FTIR. The focus is on the investigation of a possible carbonation. During the preparation of the C-S-H phases, $CaCO_3$ was burned to CaO. This was performed under ambient conditions. Due to the exposure of the CaO to atmospheric CO_2, there is a small possibility of carbonization of the C-S-H phase. This is controlled by FTIR. No significant effect of carbonation is observed and this is illustrated in Figure 26 using the C-S-H phase with C/S ~ 0.6 prepared in ultrapure water.

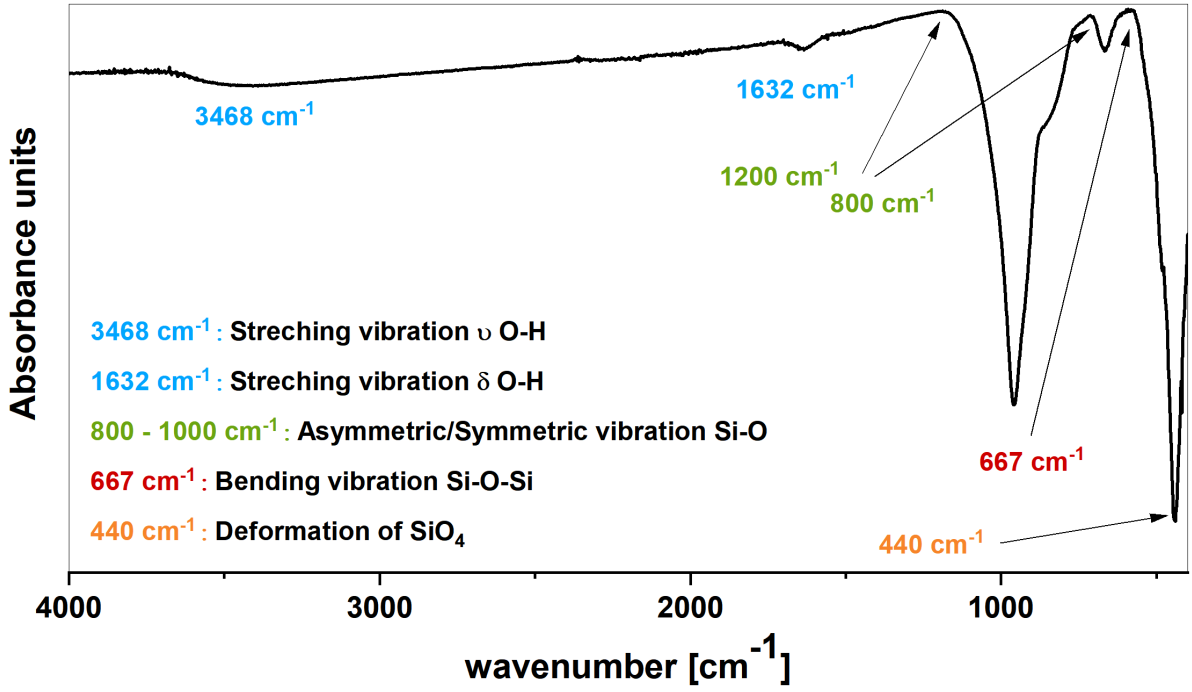

Figure 26: FTIR-Spectrum of the C-S-H phase with C/S ~ 0.6 prepared in ultrapure water. The spectrum shows the characteristic signals, while no carbonation is detected.

The typical signals for C-S-H phases are shown in the spectrum: A signal at 440 cm^{-1} is related to the deformation of the SiO_4 tetrahedra. The bending vibrations of Si-O-Si are represented by the signal at 667 cm^{-1}. The broad peak between 800 - 1200 cm^{-1} corresponds to the asymmetric and symmetric stretching vibrations of Si-O bonds. A peak between 1400 – 1500 cm^{-1} would indicate a possible carbonation of the sample, which is not the case for the C-S-H phase characterized here. The band at 1632 cm^{-1}

refers to the H-O-H bending vibrations and the peak at 3468 cm^{-1} shows the stretching vibrations of O-H groups. This is in good agreement to literature data.[139, 140] There is no evidence of carbonation for this C-S-H phase, due to the missing band between 1400 – 1500 cm^{-1}.

Thermogravimetry (TG)/Differential Scanning calorimetry (DSC)

To further characterize the C-S-H phases, TG and DSC are used as analytical techniques. TG is commonly used to gain insight on the dehydration behavior of the C-S-H phases as well as the possible presence of calcite, which may be present due to impurities in the original CaO material. The brief exposure of the burned CaO to atmospheric CO_2 can lead to a carbonatization of the C-S-H phase. Possible phase transformations can be detected with DSC. The results of both analytic methods are shown for C-S-H phases with C/S ~ 0.6, 1.0 and 1.3 aged in ultrapure water in Figure 27.

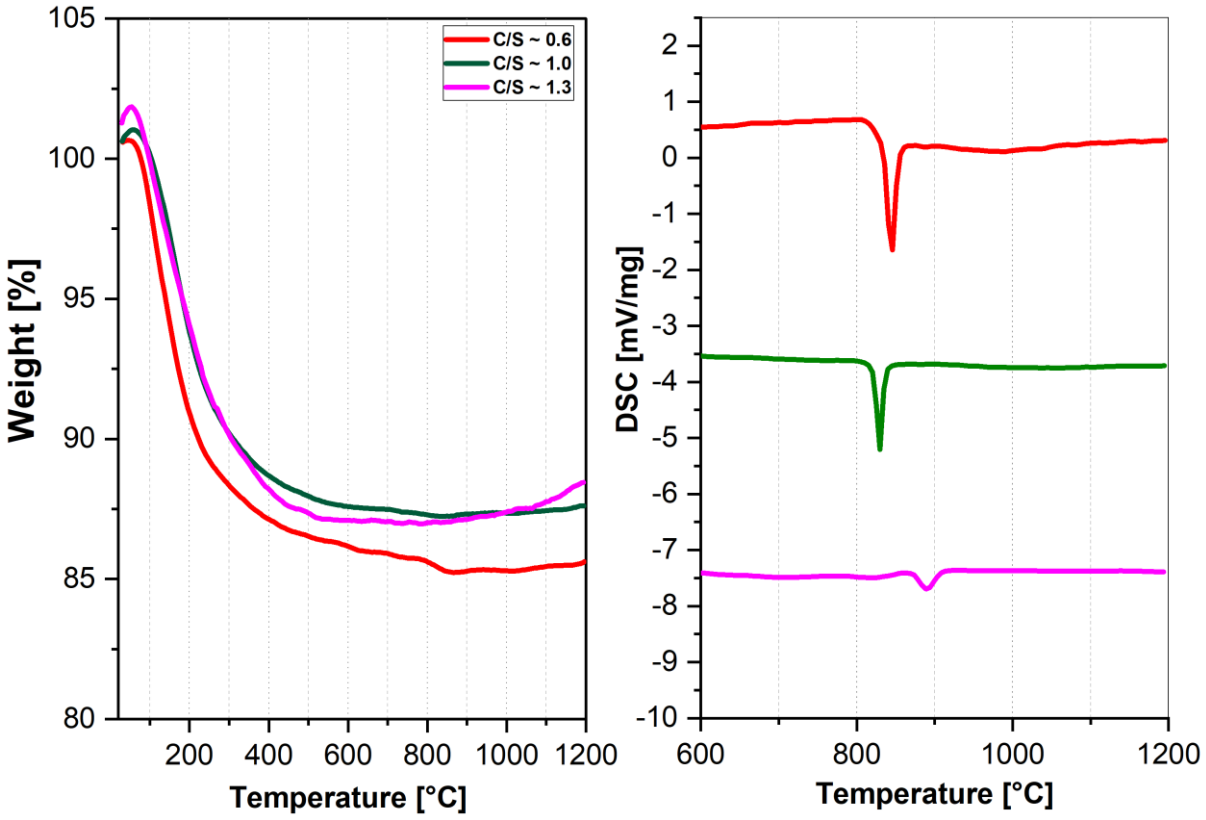

Figure 27: TG (left) and DSC (right) analysis for C-S-H phases with C/S ~ 0.6, 1.0 and 1.3 equilibrated in ultrapure water.

The typical dehydration process of the C-S-H phases is shown in the TG analysis, where a high mass loss is observed for the temperature range between 25 - 200 °C. For higher temperatures, a gradual mass loss is observed. A mass loss of 11 - 15% has been determined for the present samples. This is in good agreement with the literature.[141] A higher mass loss ~ 25 % could not be determined. The presence of portlandite can therefore be excluded. The presence of calcite is not determined here, due to the absence of a signal at T = 600 °C.[128] The DSC results clearly show a signal at temperatures between 800 - 900 °C. It shifts to lower temperatures for lower C/S ratios and to higher temperatures for higher C/S ratios This peak corresponds to the characteristic transformation from the C-S-H phase to β-wollastonite. The formation is of exothermic origin. The results are in good agreement with the literature.[142]

4.2.2 C-S-H phases equilibrated in NaCl and $CaCl_2$ solutions

After characterization and verification of the C-S-H phases contacting in ultrapure water, they are aged in NaCl and $CaCl_2$ solutions. The C-S-H phase is always pre-equilibrated with one of the two electrolytes at least 7 days before the start of the experiment. In addition, they were studied in the presence of EDTA, to obtain more information about the effect of EDTA on the C-S-H phases, as the C/S ratio may change after contact in NaCl and $CaCl_2$ solutions as well as in presence of the ligands. This is described in detail in the next section.

Aqueous phase characterization of [Ca] and [Si] in C-S-H systems

The characterization of [Ca] in solution is important to identify the possible dissolution of the C-S-H phase, since EDTA forms strong complexes with Ca (see Table 1). For [Si], however, no strong complexes with EDTA are known, so that the determination of the Si concentration in solution only serves to obtain the final C/S ratio. The corresponding [Ca] are therefore shown in Figure 28 (absence of EDTA) and Figure 29 (presence of EDTA), while those for [Si] are shown in the Appendix 7.1. Values for [Si] and [Ca] are utilized to determine the C/S ratio of the solid C-S-H phase in presence and absence of EDTA (see Table 9 and 10). A recalculation of the C/S ratio based on the experimentally measured [Ca] and [Si] was not possible due to the high relative [Ca] in the aqueous phase of the sorption experiments in $CaCl_2$. Instead, semi-quantitative estimates were calculated for $CaCl_2$ solutions at I_m = 0.1 m (see chapter 3.3.4).

In the following, the data in absence of EDTA are presented first. Values for aqueous [Ca] in the absence of the organic ligand are given in Figure 28 for C-S-H phases various C/S ~ 0.6 to ~ 1.3. They are shown in NaCl solutions for different ionic strength and sorption times.

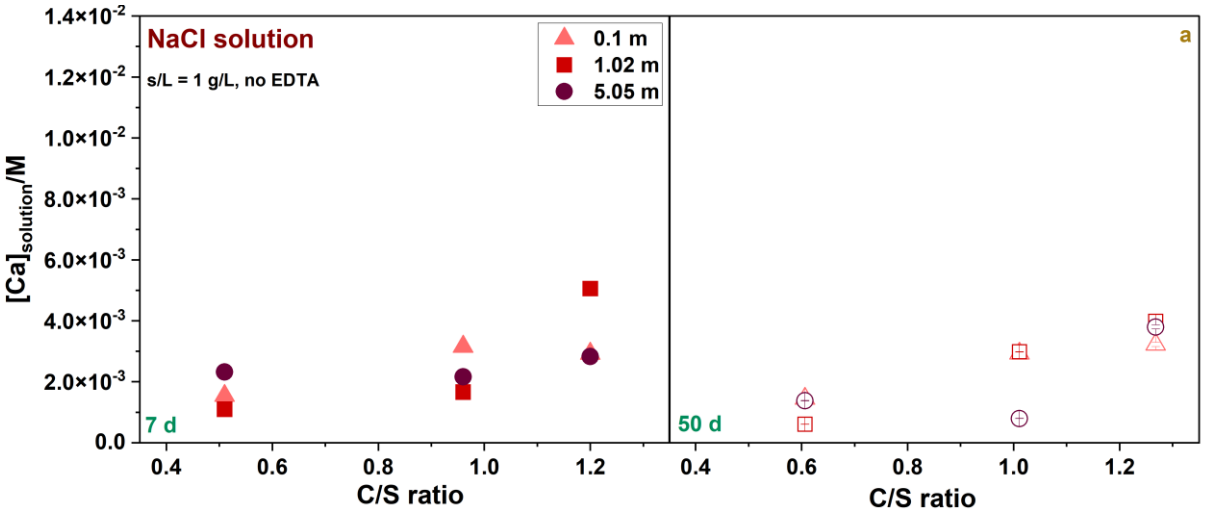

Figure 28: The $[Ca]_{aq}$ for C-S-H phases with different C/S ~ 0.6, 1.0 and 1.3. The data are shown at 7 d (left) and 50 d (right) in absence of EDTA in NaCl solution (I_m = 0.1 m in pink, 1.02 m in light red and 5.05 m in dark red) at S/V = 1 g/L.

In the absence of EDTA, [Ca] increases slightly with the increasing C/S ratio. This is observed for both contact times and for all ionic strength. It is in line with literature data, that $[Ca]_{aq}$ increases with increasing C/S ratio for C-S-H phases prepared in ultrapure water.[23, 107, 109, 143, 144]. It is also concluded that there is no significant impact of the different ionic strength.

The C/S ratios in absence of EDTA after contacting in NaCl solutions are shown in Table 9 below. In addition, the C/S ratios calculated for $CaCl_2$ solutions at I_m = 0.1 m are displayed.

Table 9: The final C/S ratios determined after contacting in ultrapure water and NaCl solutions of different ionic strength (I_m = 0.1 m, 1.02 m, 5.05 m). The C/S ratios in $CaCl_2$ solution were determined semi-quantitative for I_m = 0.1 m. Hereby the $[OH^-]$ dissolved is considered after the dilution of the original C-S-H suspension in $CaCl_2$, and assuming that 1 mol of Ca is dissolved per each two mols of OH^-. All data are shown in absence of EDTA. Contact times after 7 d and 50 d at S/V = 1 g/L are selected.

	target C/S	***C/S t = 7 d***	***C/S t = 7 d***	***C/S t = 50 d***	***C/S t = 7 d***
pure water	0.6	0.61±0.03	0.61±0.03	0.61±0.04	0.61±0.04
	1.1	0.99±0.09	0.99±0.09	1.01±0.03	1.01±0.03
	1.4	1.24±0.08	1.24±0.08	1.26±0.05	1.26±0.05
Electrolyte	-	***NaCl***	***$CaCl_2$***	***NaCl***	***$CaCl_2$***
I_m = 0.1 m	0.6	0.61±0.03	0.64±0.01	0.61±0.04	0.64±0.08
	1.1	1.00±0.06	1.09±0.03	1.01±0.06	1.09±0.07
	1.4	1.28±0.06	1.37±0.02	1.27±0.08	1.38±0.03
I_m = 1.02 m	0.6	0.61±0.02	-	0.63±0.02	-
	1.1	1.06±0.03	-	1.02±0.06	-
	1.4	1.22±0.09	-	1.25±0.09	-
I_m = 5.05 m	0.6	0.56±0.04	-	0.58±0.02	-
	1.1	1.05±0.03	-	1.09±0.03	-
	1.4	1.31±0.05	-	1.28±0.05	-

For C/S ≤ 1.0, there are no significant changes observed compared to the target C/S ratio after 7 and 50 d. For the higher C/S ratio, slightly lower values (C/S ~ 1.3) are monitored for the C-S-H phases equilibrated in NaCl solution compared to the target C/S ~ 1.4. This is in good agreement with Häusler *et al.,* who reported more significant changes for C/S > 1.25 in NaCl solutions.[71] No significant trend concerning the different sorption times or ionic trends is visible.

In $CaCl_2$ solution, slightly higher C/S ratios are observed for C/S ≤ 1.0 compared to the results in NaCl solution. For the highest C/S ~ 1.4 is reached. This observations are in good agreement to Plusquellec *et al.*.[70] The results in NaCl solution showed no significant effect of the different ionic strength on the C/S ratio. Thus, this is also assumed for $CaCl_2$ solutions. Consequently, the C/S ratios in $CaCl_2$ solutions are given as C/S = 0.6, 1.0 and 1.4 for further experiments.

Figure 29 shows the results for $[Ca]_{aq}$ in NaCl solutions of different ionic strengths in the presence of [EDTA] = 10^{-2} M contacted with C-S-H phases with different C/S ratios between ~ 0.6 – 1.3 for 7 and 50 d. The data quality for the systems at I_m = 1.02 m (t = 50 d) and I_m = 5.05 m (t = 7, 50 d) are insufficient to make an accurate statement.

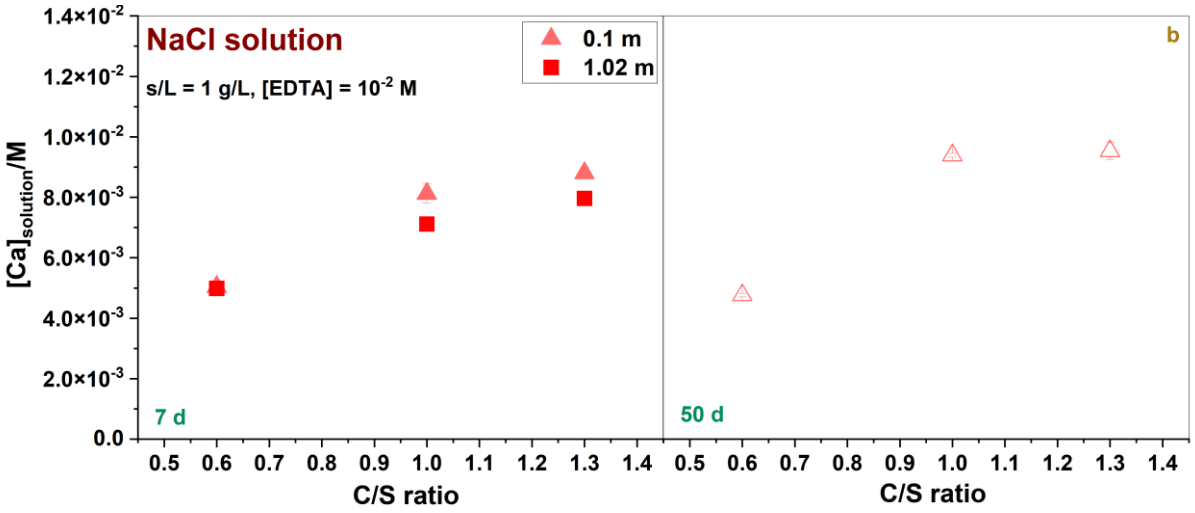

Figure 29: The $[Ca]_{aq}$ for C-S-H phases with different C/S ~ 0.6, 1.0 and 1.3. The data is shown at 7 d (left) and 50 d (right) in presence of [EDTA] = 10^{-2} M in NaCl solution (I_m = 0.1 m in pink, 1.02 m in light red) at S/V = 1 g/L. The data quality for the systems at I_m=1.02 m (t = 50d) and I_m = 5.05m (t = 7, 50d) is insufficient for accurate interpretation.

The trend that [Ca] increases with the C/S ratio is also clearly visible in the NaCl systems in the presence of EDTA after both contact times. This is in good agreement to the results in absence of EDTA. The measured [Ca] in the presence of EDTA are significantly higher compared to the EDTA-free systems. This is in line with expectations and can be explained by the formation of stable $Ca(EDTA)^{2-}$ complexes. Generally, there is no significant impact of the different ionic strength or the sorption times. The C/S ratios are given in Table 10.

Table 10: The final C/S ratio determined after the equilibration in ultrapure water and NaCl solutions of different ionic strength (I_m = 0.1 m, 1.02 m). The C/S ratios in $CaCl_2$ solution were determined semi-quantitative for I_m = 0.1 m. Hereby the $[OH^-]$ dissolved is considered after the dilution of the original C-S-H suspension in $CaCl_2$, and assuming that 1 mol of Ca is dissolved per each two mols of OH^-. All data are shown in absence of EDTA. Contact times after 7 d and 50 d at S/V = 1 g/L are selected. The data quality for the system at I_m = 1.02m (t = 50d) and I_m = 5.05m (t = 7, 50d) is insufficient for accurate interpretation.

	target C/S	***C/S t = 7 d***	***C/S t = 7 d***	***C/S t = 50 d***	***C/S t = 50 d***
Electrolyte	-	***NaCl***	***$CaCl_2$***	***NaCl***	***$CaCl_2$***
I_m = 0.1 m	0.6	0.52±0.01	0.65 ±0.05	0.53±0.08	0.65±0.05
	1.1	0.98±0.03	1.09±0.03	0.95±0.01	1.09±0.02
	1.4	1.26±0.02	1.38±0.01	1.25±0.03	1.37±0.04
I_m = 1.02 m	0.6	0.55±0.03	-	-	-
	1.1	1.01±0.02	-	-	-
	1.4	1.29±0.01	-	-	-

C/S ratios in Table 10 exhibit similarity to the C/S ratios obtained in presence and absence of EDTA in both electrolyte solutions (Table 9). In addition, no significant trends were observed with respect to the different ionic strengths or sorption times.

pH measurements

To determine the effects of different electrolyte solutions with different ionic strengths or organic ligands on C-S-H phases, the pH value of the liquid phase contacted with the C-S-H phase is measured. The pH is a key variable, since it affects the behavior (*e.g.*, deprotonation of organic compounds) of the majority of components in solution. Table 11 shows the pH_m recorded in absence of oxalate and EDTA. The corresponding formula for the calculation of pH_m is shown in chapter 3.3.1. The target C/S ratios of the corresponding C-S-H phases are illustrated here for a better representation, while the actual C/S ratios are shown in Table 9 and 10.

Table 11: The pH_m values for C-S-H phases with different target C/S ratios (C/S = 0.6, 1.1; 1.4), contacted in ultrapure water, NaCl (top) and $CaCl_2$ (bottom) solutions. All data are recorded for 7 and 50 d in the absence of the organic ligands.

„target“ C/S ratio	pH_m (ultrapure water)	pH_m I_m 0.1 m (7 d)	pH_m I_m 0.1 m (50 d)	pH_m I_m 1.02 m (7 d)	pH_m I_m 5.05 m (7 d)
S/V *[g/L]*	**20**	**1**	**1**	**1**	**1**
			NaCl solution		
0.6	9.9±0.3	10.1±0.1	9.8±0.1	9.9±0.2	9.4±0.4
1.1	12.1±0.2	11.6±0.1	11.4±0.1	11.4±0.1	11.3±0.2
1.4	12.5±0.1	11.7±0.1	11.7±0.1	11.5±0.1	11.4±0.1
			$CaCl_2$ solution		
0.6	9.9±0.3	10.1±0.5	9.2±0.3	10.0±0.1	9.4±0.1
1.1	12.1±0.2	11.9±0.1	11.2±0.2	11.5±0.3	11.1±0.1
1.4	12.5±0.1	11.9±0.1	11.3±0.2	11.7±0.2	11.3±0.1

Table 11 shows that the pH_m values increase with the C/S ratio. Those pH values as well as this behavior is in good agreement with literature data.[23, 143-145] It is well known, that as the C/S ratio increases, the Ca content of the C-S-H phase extends while the Si content decreases. Consequently, the pH increases with the C/S ratio.

The apparent decrease of the pH with higher ionic strength is directly related to the lower S/V in the C-S-H systems prepared in NaCl and $CaCl_2$ solutions. The latter systems were prepared at S/V = 1 g/L, whereas the C-S-H solutions in pure water were

prepared at S/V = 20 g/L. For this reason, the dissolution of Ca and Si has a significantly greater impact in the C/S ratio in the systems in and $CaCl_2$ solutions.

All pH_m values in the presence of [oxalate] = 10^{-3} M and [EDTA] = 10^{-2} M, 10^{-4} M are shown in Table 12. Since there are no significant trends observed with varying the ionic strength, the following pH_m values in the presence of the organic ligands are only shown for experiments with NaCl and $CaCl_2$ solutions at I_m = 1.02 m.

Table 12: The pH_m values for C-S-H phases with different C/S ratios, contacted in NaCl and $CaCl_2$ solutions (I_m = 1.02 m) are presented in presence of oxalate (c = 10^{-3} M, top) and EDTA (c = 10^{-2} and 10^{-4} M, bottom). Hereby contact times at 7 and 50 d are shown.

Target C/S ratio	pH_m (ultrapure water)	pH_m I_m 1.02 m (7 d)	pH_m I_m 1.02 m (50 d)	pH_m I_m 1.02 m (7 d)	pH_m I_m 1.02 m (50 d)
S/V *[g/L]*	**20**	**1**	**1**	**1**	**1**
		NaCl solution		**$CaCl_2$ solution**	
		Oxalate = 10^{-3} M			
0.6	9.9±0.3	9.9±0.2	10.1±0.1	9.3±0.5	9.4±0.2
1.1	12.1±0.2	11.5±0.1	11.6±0.2	11.2±0.1	11.2±0.1
1.4	12.5±0.1	11.6±0.2	11.8±0.1	11.3±0.1	11.6±0.1

Target C/S ratio	pH_m (ultrapure water)	pH_m I_m 1.02 m (7 d)	pH_m I_m 1.02 m (50 d)	pH_m I_m 1.02 m (7 d)	pH_m I_m 1.02 m (50 d)
S/V *[g/L]*	**20**	**1**	**1**		**1**
		NaCl solution			
		EDTA=10^{-2} M	***EDTA=10^{-2} M***	***EDTA=10^{-4} M***	***EDTA = 10^{-4} M***
0.6	9.9±0.3	10.0±0.2	9.5±0.3	10.0±0.2	9.8±0.3
1.1	12.1±0.2	11.6±0.2	11.4±0.1	11.6±0.3	11.6±0.3
1.4	12.5±0.1	11.7±0.1	11.7±0.2	11.8±0.1	11.7±0.3
		$CaCl_2$ solution			
		EDTA=10^{-2} M	***EDTA=10^{-2} M***	***EDTA=10^{-4} M***	***EDTA = 10^{-4} M***
0.6	9.9±0.3	9.4±0.2	9.0±0.1	9.1±0.1	9.1±0.1
1.1	12.1±0.2	11.3±0.1	11.2±0.2	11.1±0.1	11.0±0.1
1.4	12.5±0.1	11.4±0.3	11.8±0.1	11.4±0.1	11.2±0.1

Similar to the outcome of experiments in the absence of both ligands, increasing pH values are obtained with increasing C/S ratio. In general, no significant effect of the organic ligands can be observed for the pH measurements. Similarly, no significant effect is observed for different ionic strengths and contact times.

X-Ray Diffraction (XRD)

C-S-H phases (C/S ~ 1.0) contacted in NaCl and $CaCl_2$ solutions are studied by XRD to investigate the effect of different ionic strengths (see Figure 30). The figure includes also the diffractogram of the C-S-H equilibrated in ultrapure water. Reference spectra from the literature are shown at the bottom of the spectra for Tobermorite 14 Å, Portlandite, and NaCl and $CaCl_2$.[146]

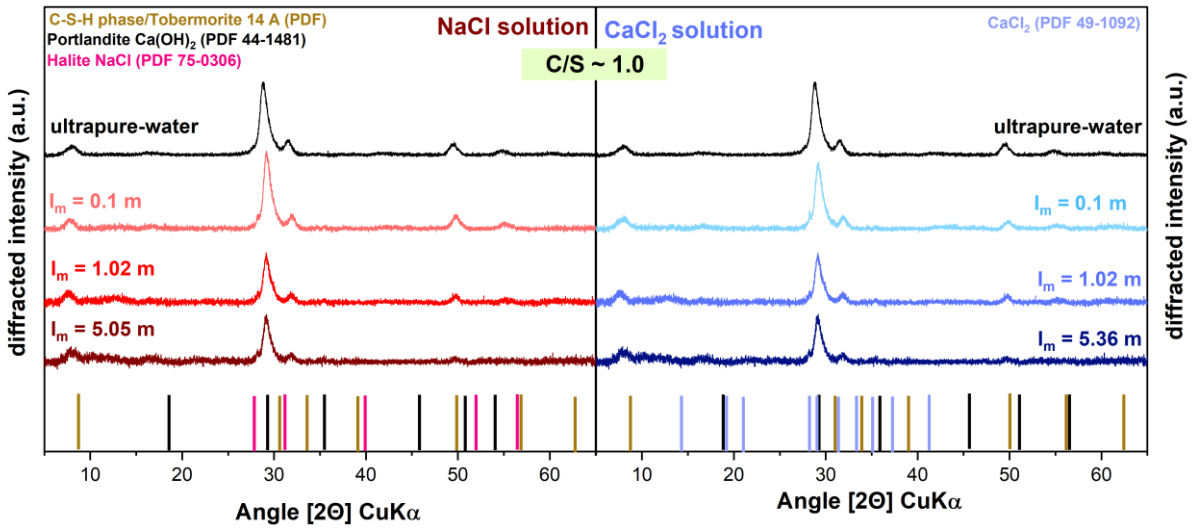

Figure 30: XRD spectra of C-S-H phases with C/S ~ 1.0 contacted in NaCl (left, red) and $CaCl_2$ (right, blue) at S/V = 1 g/L. Also shown is the C-S-H phase prepared in ultrapure water (top). All data are obtained in the absence of EDTA. The experiments are performed at different ionic strengths of I_m(NaCl) = 0.1, 1.02, 5.05 m and I_m($CaCl_2$) = 0.1, 1.02, 5.36 m after 7 d. Literature data are shown as dashes for Tobermorite 14 Å (brown), Portlandite (black), NaCl (pink) and $CaCl_2$ (blue).[146]

For all XRD spectra in both electrolytes and ultrapure water, peaks are visible at 2θ = 8°, 29.1°, 32°, 50°, and 55°. They are asymmetric and broad. The spectra are in excellent agreement with literature data.[23, 38, 91, 141, 147, 148] According to Taylor *et al.*, the C-S-H phases show a Tobermorite-related structure of 14 Å (see Figure 30).[149] Generally, no signals related to portlandite are detected. . In addition, no residues from

NaCl and $CaCl_2$ stock solutions are observed. This confirms the proper solid phase cleaning prior to the measurements.

Signal intensities for NaCl and $CaCl_2$ solutions at I_m = 0.1 m are comparable to C-S-H phases contacted in ultrapure water. The intensity of the signals decreases significantly for higher ionic strength. Häusler *et al*. concluded that the C-S-H phases in the presence of NaCl change to a less ordered structure. Within this, the interlayers are unevenly distributed and the interlayer spacings are independent of the electrolyte cation.[71]

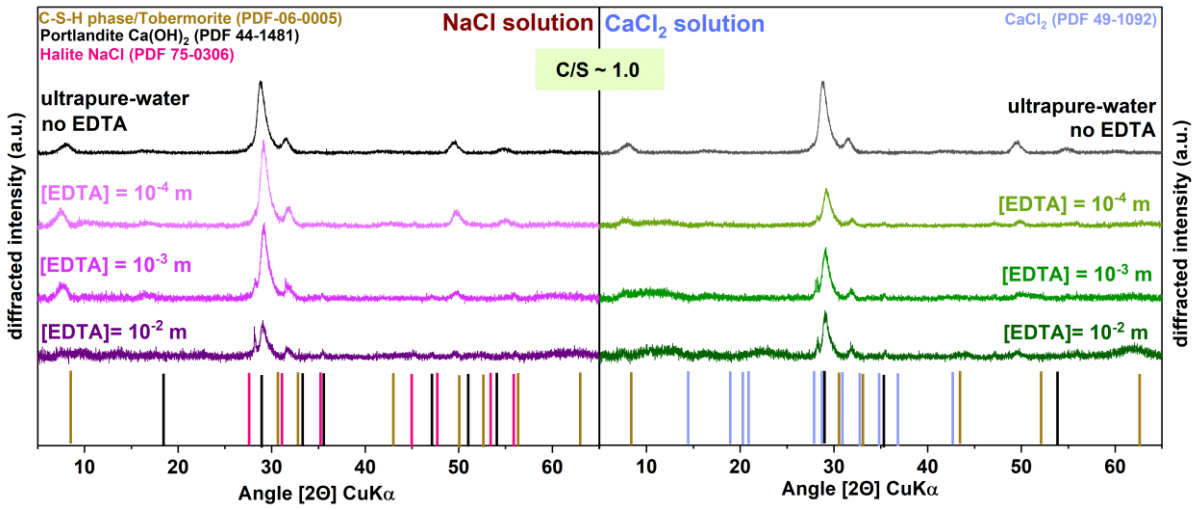

Figure 31: XRD spectra of C-S-H phases with C/S ~ 1.0 contacted in NaCl (left, red) and $CaCl_2$ (right, blue) at S/V = 1 g/L. Also shown is the C-S-H phase prepared in ultrapure water (top) in absence of EDTA. The data in NaCl and $CaCl_2$ are obtained in the presence of [EDTA] = 10^{-2} M. The experiments are performed at different ionic strengths of I_m(NaCl) = 0.1, 1.02, 5.05 m and I_m($CaCl_2$) = 0.1, 1.02, 5.36 m after 7 d. Literature data are shown as dashes for Tobermorite 14 Å (brown), Portlandite (black), NaCl (pink) and $CaCl_2$ (blue).[146]

At [EDTA] ≤ 10^{-3} M, again the characteristic signals for C-S-H phases are visible in both electrolyte solutions demonstrating no significant effect of EDTA.

At [EDTA] = 10^{-2} M in NaCl solution, the characteristic C-S-H signals decrease significantly, which might be due to a slight dissolution of the C-S-H phase.[91] Nevertheless, the crystallinity of the C-S-H phases is not affected, as they all show similar particle sizes between 9 – 11 nm, which were calculated with the Scherrer equation (see chapter 3.3.6). In addition, Figure 31 shows that the basal plane

reflection at 2θ = 8° decreases significantly in NaCl and $CaCl_2$ solutions. Instead, a broad signal appears. This signal represents the interlayer distances. The change in this signal may indicate a decreasing number of stacked layers.[147] Further, a sharp signal can be seen at 2θ = 28.16° in both electrolytes. This signal is slightly visible at low [EDTA] = 10^{-3} M and becomes more pronounced at higher [EDTA] = 10^{-2} M.

Moreover, the solubility of the $Ca_2(EDTA)\cdot 7H_2O(cr)$ species is between 0.035 – 0.06 M in NaCl solutions of different ionic strength and terms of EDTA.[150] Therefore, it is speculated, that this solid was formed during the drying process of the C-S-H phase.

SEM-EDX

In order to observe the effects of the ionic strength on the C-S-H phases, SEM images were taken. The SEM images of C-S-H phases with C/S ~ 1.0 and ~ 1.3 in NaCl solution (I_m = 1.02 m) and absence of EDTA are illustrated in Figure 32.

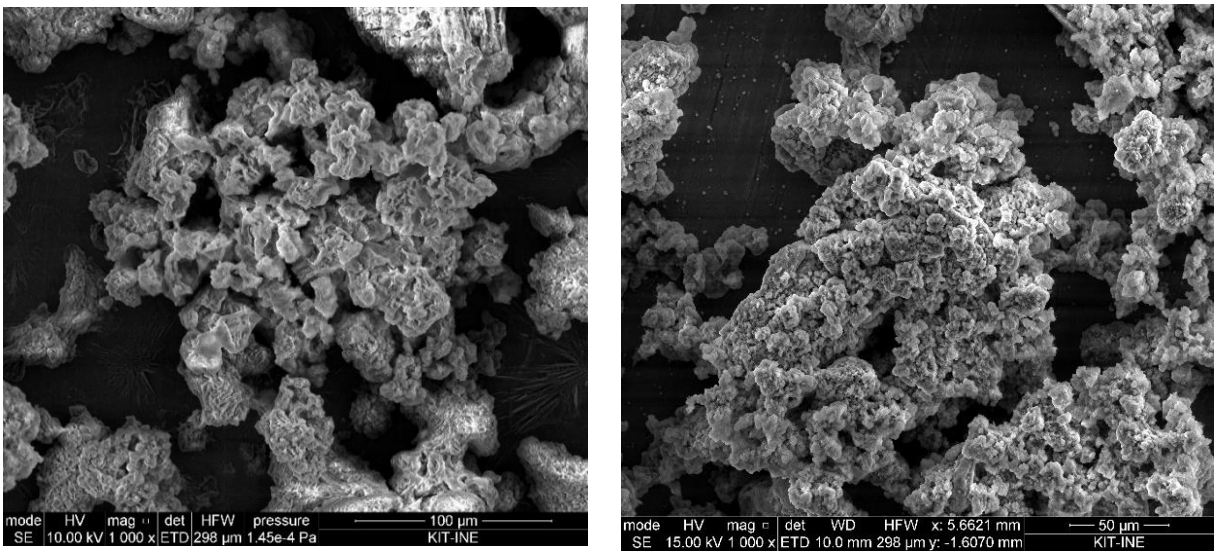

Figure 32: SEM images of C-S-H phases with C/S ~ 1.0 (left) and C/S ~ 1.3 (right) in absence of EDTA in NaCl solution (I_m = 1.02 m). A resolution of 50 - 100 µm was chosen.

Both SEM images show a similar structure: The “cauliflower”-like, twisted C-S-H surface without sub-particles. This is in good agreement to Pointeau *et al.*.[81] No significant effect due to the NaCl electrolyte solution was observed.

4.3 Sorption of Eu(III) on C-S-H phases in presence of oxalate

The retention of Eu(III) on C-S-H phases in the presence of oxalate is investigated in the frame of batch sorption experiments in this chapter. To quantify this retention, the logarithmic distribution coefficient (log R_d) was used. By varying different experimental parameters, such as ionic strength (I_m) and sorption time, the effect of these factors on the log R_d values was investigated.

4.3.1 Varying ionic strength (I_m) and sorption time

The log R_d values of Eu(III) on C-S-H phases at various C/S ratios in presence of [oxalate] = 10^{-3} M are displayed in Figure 33 for NaCl and $CaCl_2$ solutions of different ionic strength. Sorption times of 7 and 50 d are studied. Additionally, log R_d values in absence of the organic ligand are given in both electrolyte solutions.

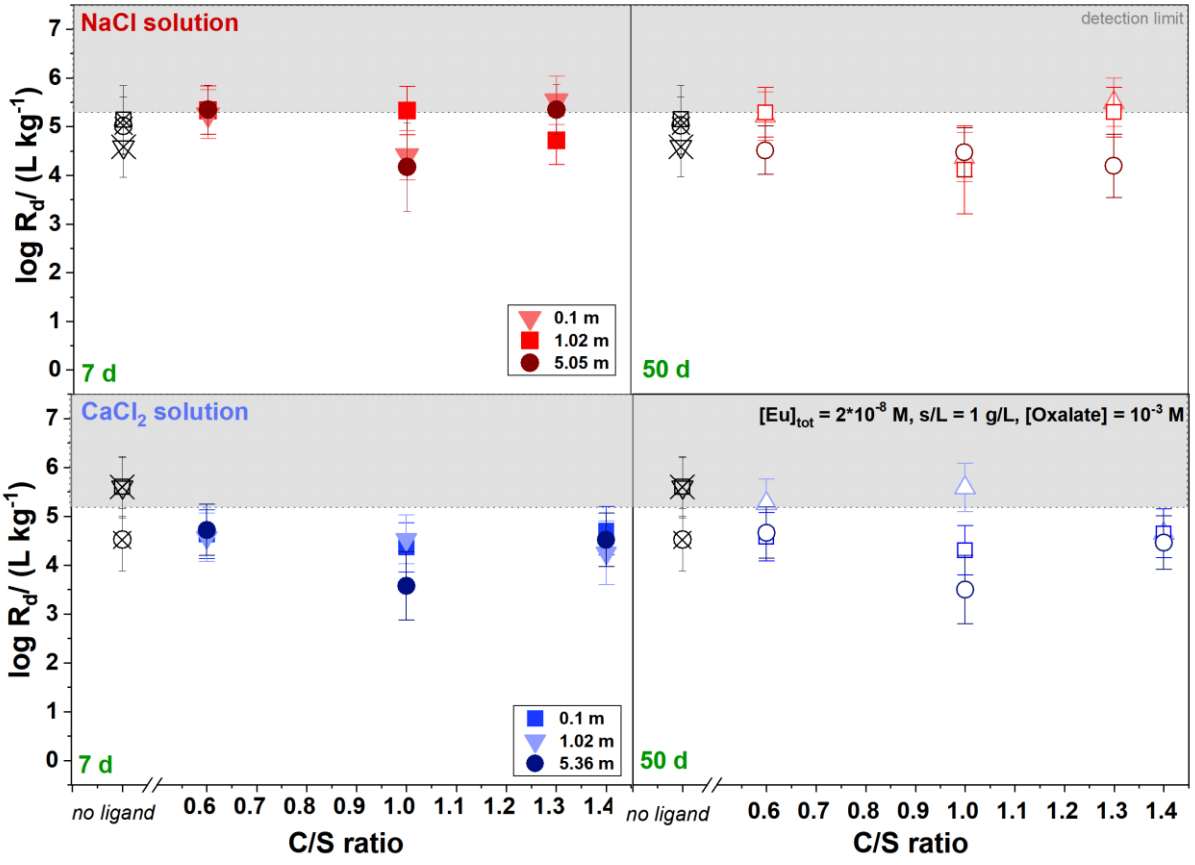

Figure 33: Logarithmic distribution coefficients (Log R_d/L kg^{-1}) for the adsorption of Eu(III) on C-S-H phases with various ratios from ~ 0.6 – 1.4 in presence of [Oxalate] = 10^{-3} m in NaCl (top) and $CaCl_2$ (bottom) solutions at different ionic strength after sorption time of 7 d (left) and 50 d (right) at S/V = 1 g/L.

Distribution coefficients of log R_d = 4 – 5 are shown for Eu(III) for both electrolytes and sorption times. This indicates a strong, almost quantitative retention. No significant effects are observed for different C/S ratios, sorption times or ionic strength. Similar distribution coefficients are obtained in the absence of oxalate. Already in chapter 1.3 the possible precipitation of Ca-oxalate was mentioned. Detailed speciation calculations are performed using the PHREEQ-C modeling software and the Thermochimie database. In addition, the modeling software Medusa/Spana was used. The results are shown in Figure 34.

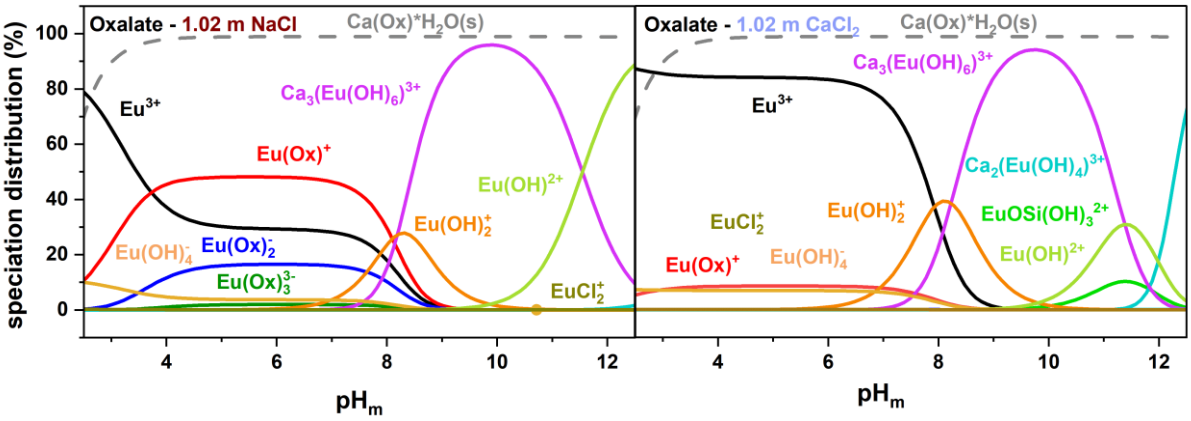

Figure 34: Speciation distribution of Eu(III) in presence of [oxalate] = 10^{-3} M. Most of the [oxalate] ~ $1.04 \cdot 10^{-5}$ M precipitates as $Ca(Ox) \cdot H_2O(s)$, while only a small amount of [Oxalate] ~ $1.04 \cdot 10^{-5}$ m remains in solution. [Ca] in NaCl solution corresponds to the pore water composition in C-S-H phases with C/S ~ 1.0. [Ca] for $CaCl_2$ solutions originates mostly from the stock solution. $Eu(III)_{tot}$ was fixed to $2 \cdot 10^{-8}$ M. Aqueous speciation of oxalate was performed with PHREEQ-C, while the solid $Ca(Ox) \cdot H_2O(s)$ species was calculated with Medusa/Spana.

The fact that oxalate has no significant effect on the sorption of Eu(III), is explained by the precipitation of solid Ca(Ox)(s) (solubility product: $K_L = 2.7 \cdot 10^{-9}$ M) with Ca either from the electrolyte ($CaCl_2$ solution) or dissolved from the C-S-H phase (NaCl solution).[24] Only a negligible amount of $1.04 \cdot 10^{-5}$ M remains in solution, where the Eu(III) hydroxide species predominate the aqueous speciation between pH 8 and 12. In addition, $Ca_3(Eu(OH)_6)^{3+}$, $Ca_2(Eu(OH)_4)^{3+}$ and $EuOSi(OH)_3^{2+}$ contribute to the speciation distribution in the alkaline pH range. No relevance of oxalate complexes can thus be stated and surface adsorbed Eu(III) species predominate resulting in high Eu(III) retention (see Figure 33). Dario *et al.* described similar observations for TiO_2 as a solid phase: Hereby oxalate has no effect on the sorption of Eu(III) on TiO_2 due

to the precipitation.[151] Thus, it can be concluded that oxalate has no effect on the retention of trivalent *Ln* and *An* under the present conditions. Therefore, the C-S-H phase-oxalate-Eu(III) system was not further investigated.

4.4 Sorption of Eu(III) on C-S-H phases in presence of EDTA

The results of the sorption of Eu(III) on C-S-H phases in presence of EDTA in NaCl and $CaCl_2$ solutions is presented in this section. Hereby batch sorption experiments with the variation of different experimental parameters, *e.g.,* ionic strength (I_m), [EDTA], sorption time, order of addition and varying solid-to-liquid ratio (S/V) are described. This chapter begins with the sorption of EDTA on C-S-H phases in the binary system. Then the ternary Eu(III)-EDTA-C-S-H system is described.

Binary system (EDTA/C-S-H phase)

4.4.1 EDTA uptake on C-S-H phases

To obtain insight into the sorption processes of EDTA on C-S-H phases at different C/S ratios, experiments were performed in the absence of Eu(III). The results are presented in Figure 35, in NaCl and $CaCl_2$ solutions at different ionic strength after 7 and 50 d

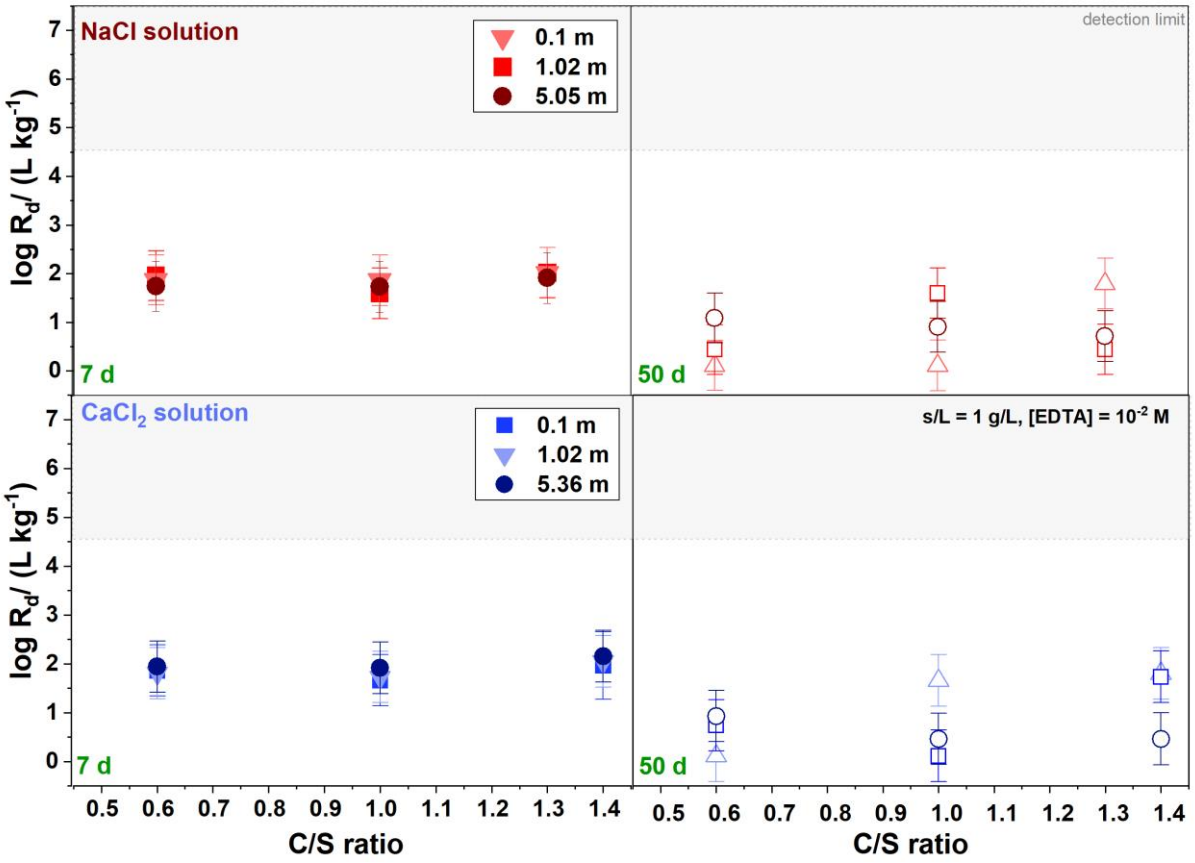

Figure 35: Logarithmic distribution coefficients (Log R_d/L kg^{-1}) for the sorption of [EDTA] = 10^{-2} M on C-S-H phases for various C/S ranging between ~ 0.6 – 1.4 in NaCl- (top) at I_m = 0.1, 1.02, 5.05 m and $CaCl_2$ solutions (bottom) at I_m = 0.1, 1.02, 5.36 m after sorption times of 7 d (left) and 50 d (right) at S/V = 1 g/L. The log R_d values are shown as tentatively.

Based on the observed results, the tentatively determined log R_d values range between 1 - 2 after both contact times. This suggests that there is an association of EDTA with the surface of the C-S-H phases. Pointeau *et al.* conducted batch sorption studies and described the sorption of [EDTA] = $1.1 \cdot 10^{-3}$ M on HCP at pH = 12.4.[92] They

demonstrated that EDTA exhibits log R_d ~ 1 between one and 50 d, with the speciation calculation being mainly dominated by the $Ca(EDTA)^{2-}$ species.

Figure 36 displays the remaining concentration of EDTA in the solution, which was calculated using the equation for the distribution coefficient from chapter 3.2.1.

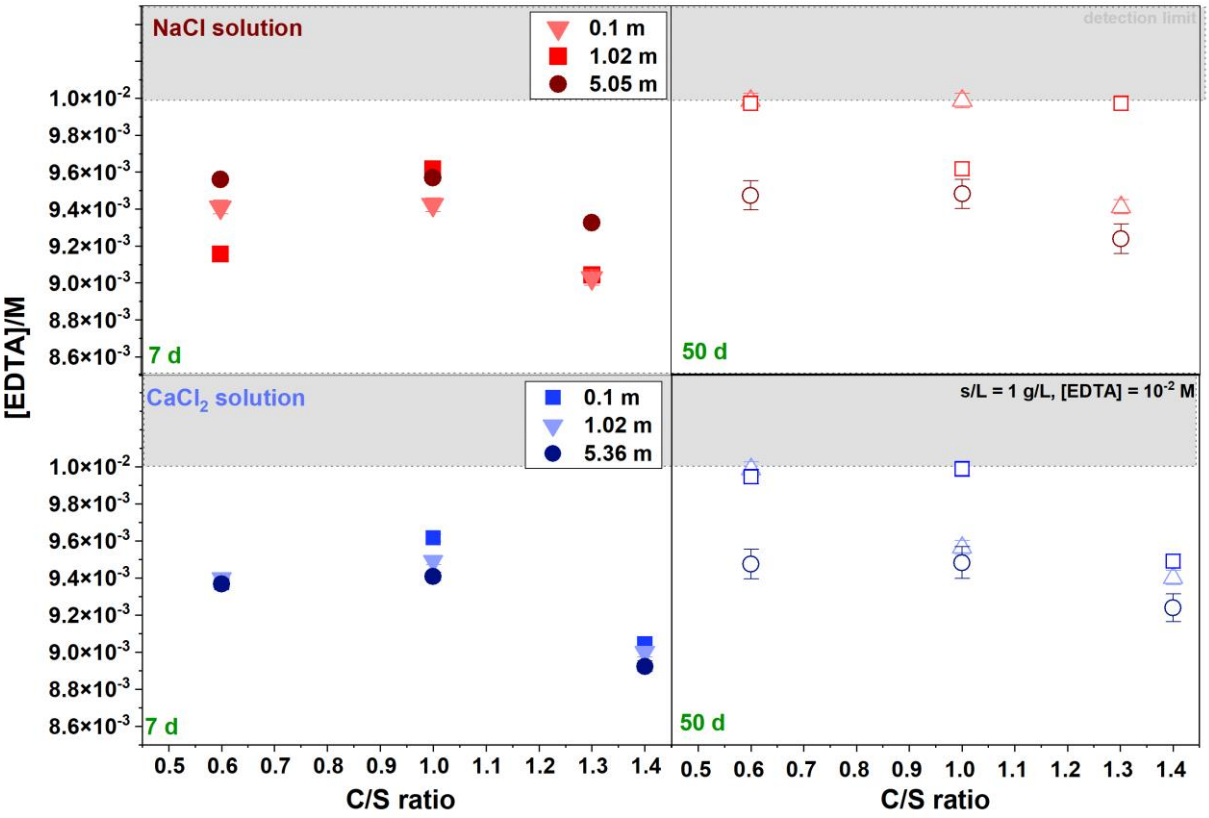

Figure 36: EDTA concentration in solution after the sorption experiment for C-S-H phases with various C/S ranging between ~ 0.6 – 1.4. The [EDTA] are monitored in NaCl- (top) at I_m = 0.1, 1.02, 5.05 m and $CaCl_2$ solutions (bottom) at I_m = 0.1, 1.02, 5.36 m solutions after sorption times of 7 (left) and 50 d (right) at S/V = 1 g/L.

After both sorption times, only a small quantity of EDTA ([EDTA] ~ $8.0 \cdot 10^{-4}$ – $2.0 \cdot 10^{-4}$ M) is associated with the solid C-S-H phase. Most of the used EDTA remains in solution, most likely in the form of $Ca(EDTA)^{2-}$ complexes with Ca from the C-S-H phase (NaCl) as well as from the electrolyte solution ($CaCl_2$).

Ternary system (Eu(III)/EDTA/C-S-H phase)

4.4.2 Varying [EDTA] at S/V = 1 g/L

Figure 37 shows the effect of varying EDTA concentrations ([EDTA] = 10^{-5} - 10^{-2} M) on the retention of Eu(III) on C-S-H phases using different C/S ratios after 7 and 50 d. These experiments were conducted in both NaCl and $CaCl_2$ solutions at a fixed ionic strength of 1.02 m. Additionally, the logarithmic distribution coefficient (log R_d) values in the absence of EDTA are shown for comparison.

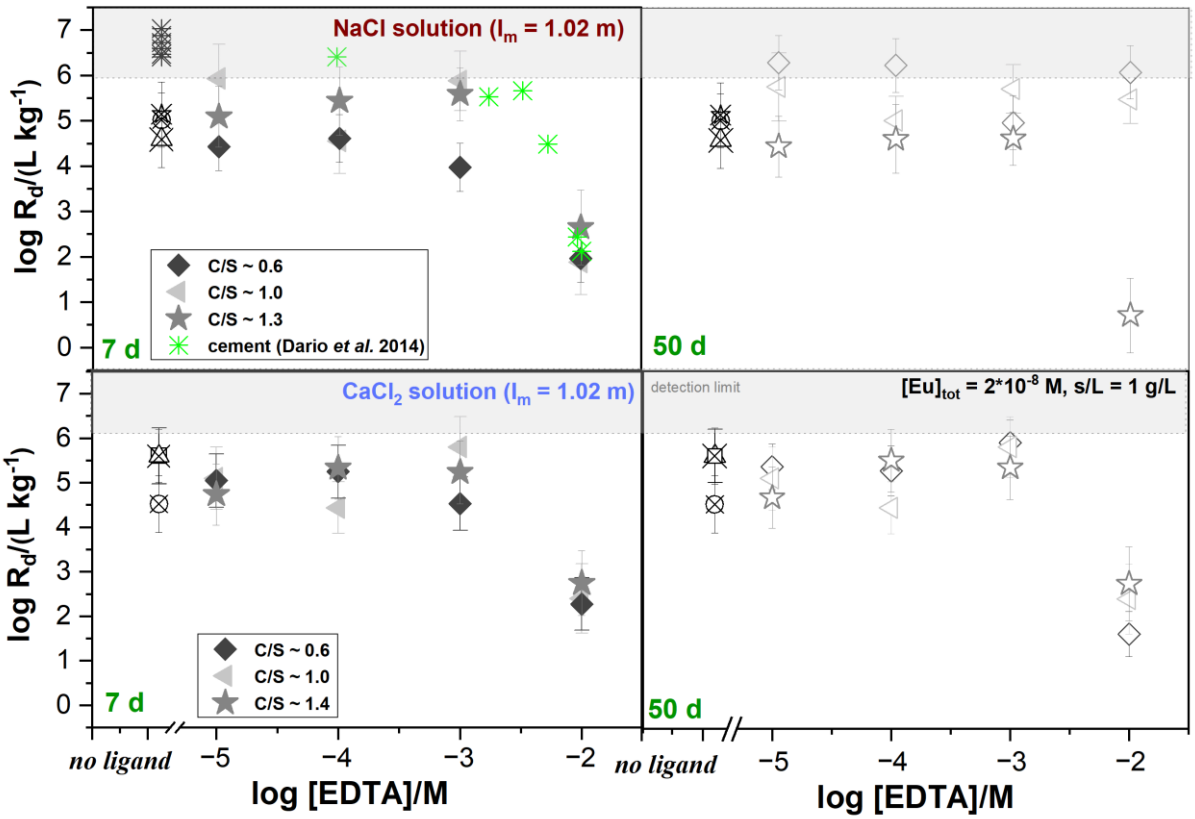

Figure 37: Logarithmic distribution coefficients (Log R_d/L kg^{-1}) for the adsorption of Eu(III) ($[Eu]_{tot}$ = $2 \cdot 10^{-8}$ M) on C-S-H phases of different ratios in presence of varying [EDTA] = 10^{-5} – 10^{-2} M in NaCl (top) and $CaCl_2$ (bottom) solutions at I_m = 1.02 m after sorption times of 7 (left) and 50 d (right) at S/V = 1 g/L. Data without EDTA are also shown. C/S ~ 0.6, 1.0, 1.3 are given for 7 d 50 d in NaCl solution, while C/S ~ 0.6, 1.0 and 1.4 are shown in $CaCl_2$ solutions. The figure in NaCl solution at 7 d includes data published by Dario *et al.*. They investigated the Eu(III) uptake on Portland cement (pH = 12.5) at S/V = 1 g/L with different concentrations of EDTA.[149]

At low [EDTA] ≤ 10^{-3} M, high retention of Eu(III) with log R_d ~ 5 - 6 is shown in both electrolyte solutions, independently of different C/S ratios and sorption times. This is

also illustrated for systems in the absence of EDTA. Therefore, it can be concluded that [EDTA] ≤ 10^{-3} M does not significantly affect the uptake of Eu(III) on C-S-H phases under the studied experimental conditions.

However, at higher EDTA concentrations ([EDTA] = 10^{-2} M), the retention of Eu(III) on C-S-H phases is significantly reduced to log R_d = 2 - 3 after 7 d. This is visible in both electrolyte solutions. After 50 d, the log R_d values increase again to 5 - 6 in NaCl solutions for C/S ≤ 1.0. In contrast, the log R_d values remain low for longer sorption times in NaCl solutions for C/S ~ 1.3 and in $CaCl_2$ solutions for all C/S ratios. The initially low retention at higher EDTA concentrations is attributed to the stabilization of Eu(III) with EDTA in solution. It is suggested that ternary species such as Eu(III)-OH-EDTA (in NaCl solutions) or Eu(III)-Ca-EDTA (in $CaCl_2$ solutions) may form.[39] In NaCl solutions for C/S ratios ≤ 1.0, the origin of this slow sorption kinetics It is not clear. In principle it is conceivable that a slow Eu(III) dissociation from the Eu(III)-Ca-EDTA complex is responsible for the reaction time dependence. Another reason could also be the slow Eu(III) incorporation into the solid phase leading to strong retention. See also the discussion in chapter 4.5. Dario *et al.* investigated the uptake of Eu(III) on Portland cement (pH = 12.5) at different [EDTA] ≥ 10^{-4} M at S/V = 1 g/L. Despite the slightly higher pH value in their work, these results agree well with the data of the present work.[151]

The ICP-OES results also show slightly higher $[Ca]_{aq}$ for C/S ~ 1.3 in NaCl solution compared to lower C/S ratios. This could be related to the formation of the ternary complexes described above. Guidone *et al.* recently investigated the effect of [GLU] > 10^{-2} M on the retention of Eu(III) and C-S-H phases (C/S = 0.8 and 1.4).[88] They also observed a decreasing retention at high ligand concentrations mostly in systems with high C/S ratio. In addition, at C/S = 1.4, the Ca content was observed to be one order of magnitude higher than at the lower C/S ratio. This was attributed to the formation of apparently very stable ternary / quaternary Ca-Eu(III)-OH-EDTA complexes.

4.4.3 Varying [EDTA] at S/V = 20 g/L

Sorption experiments with the ternary systems C-S-H-Eu(III)-EDTA were also conducted at S/V = 20 g/L. The retention of Eu(III) was investigated from low to high [EDTA] = 10^{-5} – 10^{-2} M on C-S-H phases with different target C/S ratios with C/S = 0.6, 1.1, 1.4. No C/S ratios were determined experimentally in this series. The corresponding results are illustrated in Figure 38 for NaCl and $CaCl_2$ solutions after 7 d. The [EDTA] in solution after the experiment are illustrated for [EDTA] = 10^{-2} M in Figure 39.

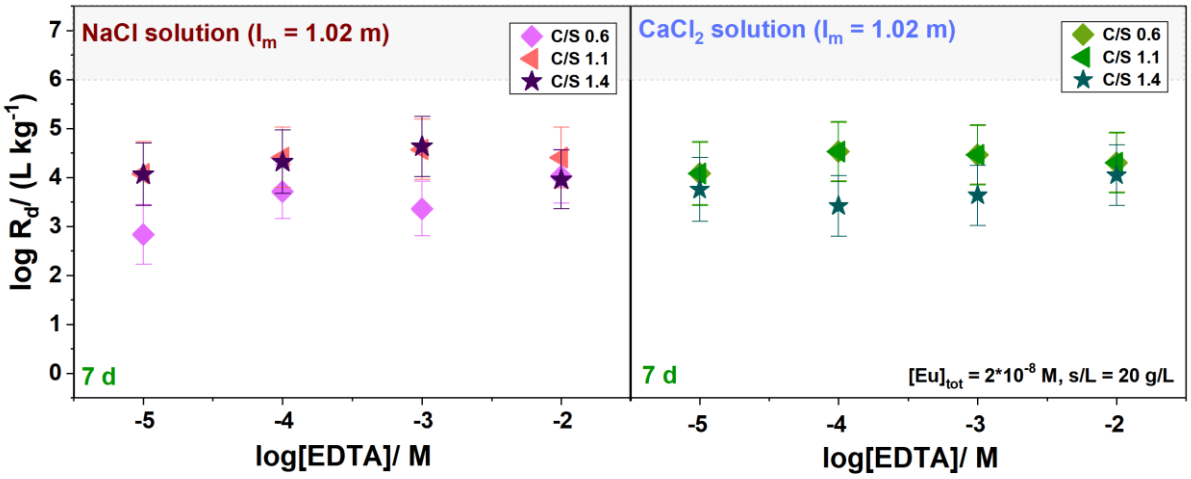

Figure 38: Logarithmic distribution coefficients (Log R_d/L kg^{-1}) for the uptake of [EDTA] = 10^{-5} - 10^{-2} M on C-S-H phases (C/S = 0.6, 1.1, 1.4) in NaCl (left) and $CaCl_2$ solutions (right) at I_m = 1.02 after sorption times of 7 d at S/V = 20 g/L. No C/S ratios were determined experimentally, so the target C/S ratios are used to describe the experiments.

High Eu(III) retention with log R_d = 4 – 5 is observed at the entire investigated [EDTA] concentration range. This observation is different to the results observed at [EDTA] = 10^{-2} M for S/V = 1 g/L (see chapter 4.4.2).

This discrepancy may be partly attributed to the increased sorption of EDTA on the surface at higher S/V, which decreases the aqueous concentration of the ligand available for complexation to ~ 60 % of the initial concentration (see Figure 39).

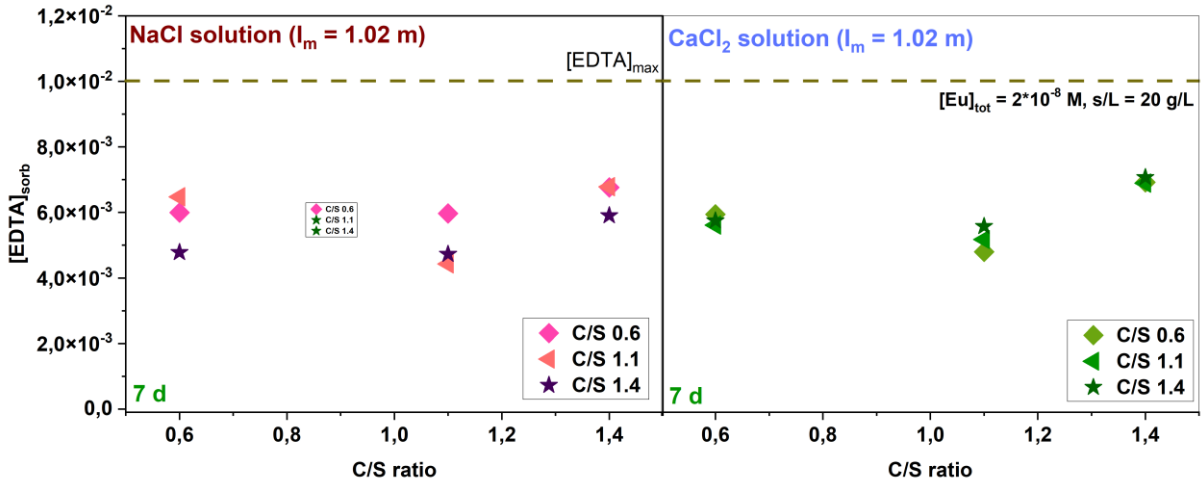

Figure 39: The remaining EDTA in solution after the experiments with Eu(III) in presence of [EDTA] = 10^{-2} M on C-S-H phases (C/S = 0.6, 1.1, 1.4) at S/V = 20 g/L in NaCl (left) and $CaCl_2$ solutions (right) at I_m = 1.02 m after sorption times of 7 d.

In contrast, more than 90% of the initial [EDTA] concentration remains in solution at S/V = 1 g/L. At the lower S/V, EDTA is primarily present in the solution and plays a role in stabilizing Ca and Eu(III) through the formation of ternary species such as Eu(III)-OH-EDTA or Eu(III)-Ca-EDTA. The explanation for the different behavior of EDTA = 10^{-2} M at S/V = 20 g/L compared to 1 g/L is not yet fully understood. It can be speculated, that EDTA associated with the C-S-H surface reacts with Eu(III). Consequently, the Eu(III) sorption is enhanced by sorption to or into the C-S-H phase and, in addition, by complexation to the surface adsorbed EDTA.

4.4.4 Varying ionic strength (I_m)

Eu(III) uptake on C-S-H phases

Since significant effects on the retention of Eu(III) on C-S-H phases are only observed in both electrolyte solutions at [EDTA] = 10^{-2} M, this concentration is used for further experiments. Figure 40 illustrates the sorption of Eu(III) on C-S-H phases in the presence of [EDTA] = 10^{-2} M in NaCl and $CaCl_2$ solutions with varying ionic strength. Hereby two contact times at 7 and 50 d are examined and also log R_d values in absence of the ligand are recorded.

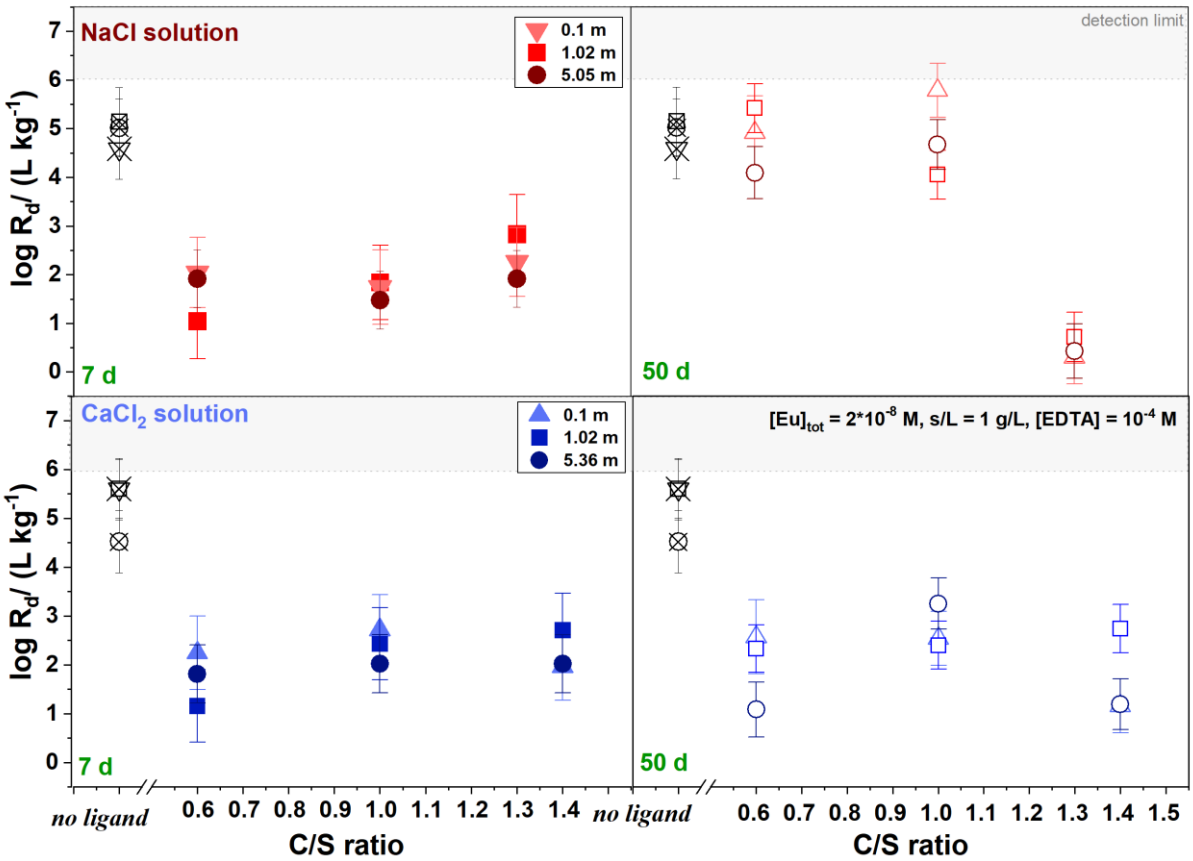

Figure 40: Logarithmic distribution coefficients (Log R_d/L kg^{-1}) for the adsorption of Eu(III) ($[Eu]_{tot} = 2 \cdot 10^{-8}$ M) on C-S-H phases for various C/S ranging between ~ 0.6 – 1.4 in presence of [EDTA] = 10^{-2} M in NaCl- (top) at I_m = 0.1, 1.02, 5.05 m and $CaCl_2$ solutions (bottom) at I_m = 0.1, 1.02, 5.36 m after sorption times of 7 (left) and 50 d (right) at S/V = 1 g/L. Data in absence of the ligand are also shown.

Eu(III) sorption is observed as already described and discussed in chapter 4.4.2: In NaCl solutions, the retention of Eu(III) is time dependent at C/S ≤ 1.0 and increases to

the level found in absence of EDTA. The retention low for C/S ~ 1.3. In $CaCl_2$ solutions, log R_d values are consistently low for both equilibration times and all C/S ratios. This can be explained by the stabilization of Eu(III) and Ca with EDTA in solution, leading to the formation of ternary Ca-Eu(III)-EDTA complexes (see section 4.4.2). The results visualized in Figure 40 further show that there is no significant impact of the different ionic strength.

For reaffirmation of the results, the Eu(III) retention on C-S-H phases is further investigated at [EDTA] = 10^{-4} M for both electrolytes at different ionic strength. The corresponding results are illustrated in Appendix 7.2. As expected and in good agreement with the results reported in section 4.4.2 a high Eu(III) retention with log R_d = 5 - 6 is observed in both electrolyte solutions.

4.4.5 Varying order of addition

The order in which the ligand and Eu(III) are added during sorption experiments has been reported to have a significant effect on the log R_d.[106] Such findings indicate the existence of kinetic effects. In order to examine, whether experimental data represent an equilibrium state, sorption studies are performed where the order of addition is varied (results are shown in Figure 41). Three different orders of addition to the solid phase were considered: 1) EDTA followed by Eu(III), 2) Eu(III) followed by EDTA, and 3) EDTA and Eu(III) added simultaneously. The first sampling was taken after a 7-day equilibration period. A detailed explanation of the order of addition of, how the experiments are conducted is given in chapter 3.2.1. These experiments were performed at [EDTA] = 10^{-2} M for different C/S ratios.

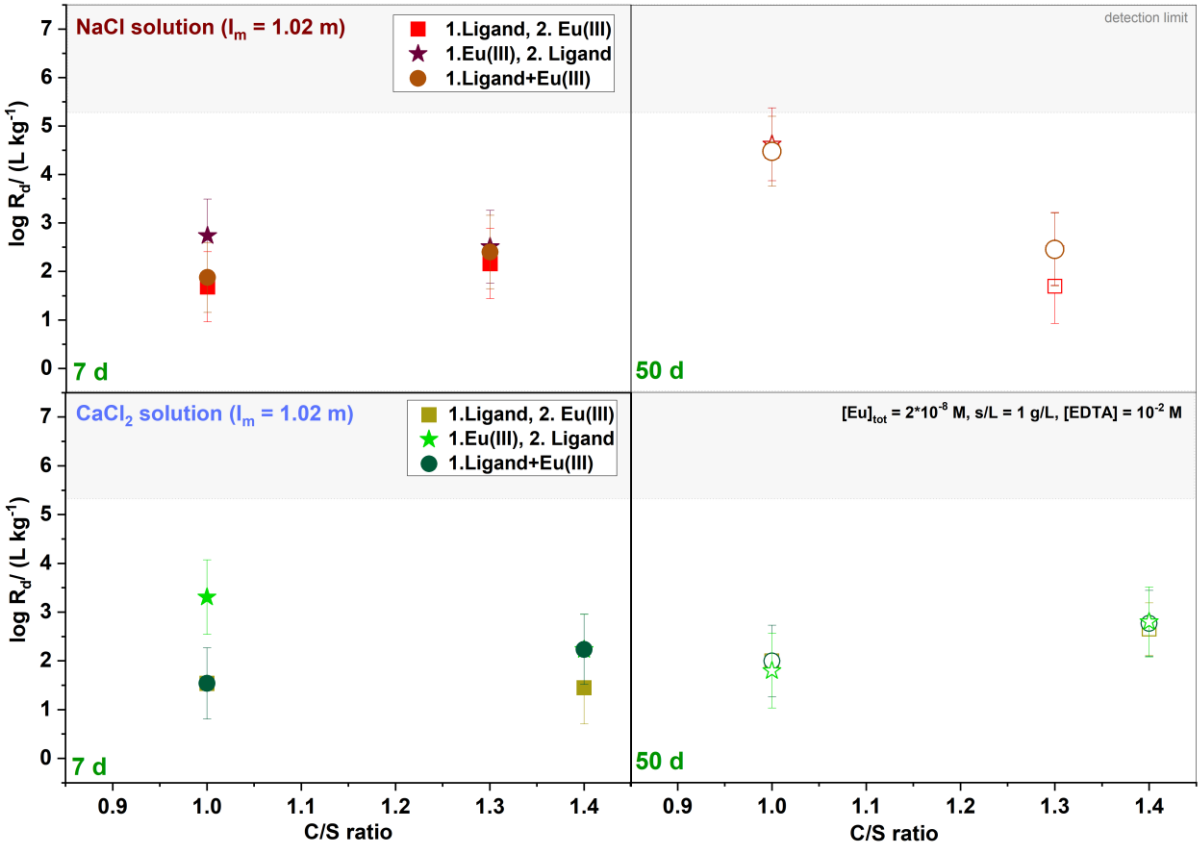

Figure 41: Logarithmic distribution coefficients (Log R_d/L kg^{-1}) for the adsorption of Eu(III) ($[Eu]_{tot}$ = $2 \cdot 10^{-8}$ M) on C-S-H phases at different C/S ~ 1.0 (both electrolytes), C/S ~ 1.3 (NaCl solution) and C/S ~ 1.4 ($CaCl_2$ solution) in presence of [EDTA] = 10^{-2} M in NaCl (top)- and $CaCl_2$ (top) solutions at I_m = 1.02 after sorption times of 7 (left) and 50 d (right) at different order of addition: 1) Ligand, Eu(III); 2) Eu(III), Ligand; 3) Ligand + Eu(III) at S/V = 1 g/L.

As mentioned earlier, previous work has shown significant effects of different order of

addition. Tasi *et al.* investigated the Pu-Cement interaction in presence of isosaccharinic acid (ISA).[106] ISA is also known as a strong complexing agent. They investigated two different addition sequences: (1) Pu and cement were pre-equilibrated, before the addition of ISA. (2) Pu was first contacted with ISA and then added to the cement. In particular, at high [ISA] = 10^{-2} M the authors observed the very slow dissociation of Pu from the aquatic complex followed by sorption to cement.

For EDTA no significant effect of the order of addition was observed. It is hypothesized that the dissociation kinetics of the aqueous Eu-EDTA complexes do not play a relevant role, which is due to the strong complexing properties of EDTA.

4.5 Cm(III) sorption onto C-S-H phases in presence of EDTA studied by TRLFS

TRLFS measurements were performed to characterize Cm(III) species in the Cm(III)/C-S-H/EDTA system in presence and absence of Ca. This is analogous to the corresponding Eu(III) systems. The studies were applied using Cm(III) ([Cm] = $1 \cdot 10^{-7}$ M) at C-S-H phases with various C/S ratios and different EDTA concentrations ([EDTA] = 10^{-2} – 10^{-4} M).

All TRLFS experiments were conducted in NaCl and $CaCl_2$ solutions of fixed I_m = 1.02 m at various sorption times between 7 – 365 d. Conditions of experiments using TRLFS were congruent with batch sorption experiments (see chapter 4.4.2).

No quantitative phase separation was performed for any of the samples. The samples were left sediment over the selected time period. For each measurement, the supernatant of the solution was measured first. Subsequently, the complete sample was measured as a suspension. To ensure accurate measurements of the suspension, the sample was continuously stirred with a stirring bar during the experiment. After each measurement, the sample was returned to PP-vials (*Sarstedt*) and stored under argon atmosphere.

From the batch sorption experiments, it was observed that Eu(III) showed reduced retention after a short sorption time of 7 d at [EDTA] = 10^{-2} M in NaCl and $CaCl_2$ solutions. However, after 50 d, the log R_d values increase significantly for C/S ~ 1.3 in NaCl solution. The slow incorporation of Eu(III) into the C-S-H phase is proposed as being responsible for this finding (but see discussion in chapter 4.4.2). For C/S ~ 1.3 in NaCl solutions and all C/S ratios in $CaCl_2$ solutions, the log R_d remain constantly low after both sorption times. This can be attributed to the stabilization of Eu(III) by EDTA in solution and may be related to the formation of ternary complexes such as Eu(III)-OH-EDTA or Eu(III)-Ca-EDTA. In addition, quaternary complexes such as Ca-Cm(III)-OH-EDTA are also suspected. TRLFS was used to identify the Cm(III) speciation in the system.

As part of this work, Cm(III) fluorescence emission spectra were also recorded in solution and in suspension without EDTA. These experiments were performed to compare the samples in presence and absence of the ligand. These data are presented in the Appendix 7.3.

4.5.1 TRLFS studies of the Cm(III)- C-S-H – EDTA – NaCl system

Fluorescence emission spectra of Cm(III)-containing solution and suspension contacted with C-S-H phases (C/S ~ 1.0) are recorded in the presence of [EDTA] = 10^{-2} M in NaCl solution (I_m = 1.02 m (NaCl) and shown in Figure 42. The corresponding fluorescence lifetimes are given in Table 13.

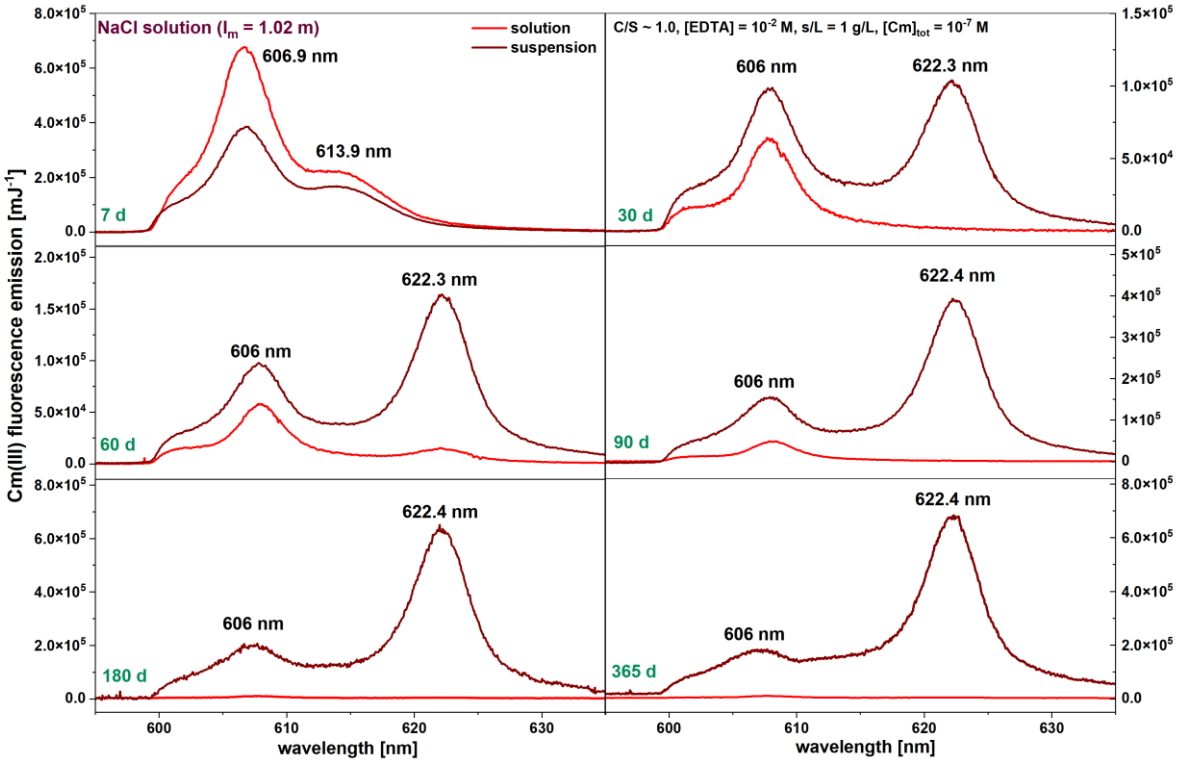

Figure 42: Fluorescence emission spectra of the Cm(III) containing solution (light red) and suspension (dark red) associated with C-S-H phases (C/S ~ 1.0) in the presence of [EDTA] = 10^{-2} M. The spectra are recorded in NaCl solution at I_m = 1.02 m between sorption times of 7 – 365 d at S/V = 1 g/L.

Two emission bands at 606.9- and 613.9 nm are detected after 7 d in both solution and suspension, indicating the presence of at least two different Cm(III) species. For the first species, the fluorescence lifetime of the sample measured in the supernatant is

determined with 280±11 µs. In the suspension, however, a longer lifetime of 315±20 µs was calculated. According to the Kimura equation (see section 1.4.1), the signal at 606.9 nm is attributed to a Cm(III) species with 1.4±1.0 water molecules in the first coordination sphere in solution and 1.1±1.0 water molecules in suspension. However, the Kimura equation can only be used as a rough estimate in the context of this work. This is explained in chapter 3.2.2. The former signal is interpreted as the ternary $Cm(OH)(EDTA)^{2-}$ complex, as previously proposed by DiBlasi and co-workers.[39] The signal at 613.9 nm shows a fluorescence lifetime of 164±14 µs (suspension), representing 3.1±1.0 water molecules in the first coordination sphere. This complex is possibly related to another ternary hydrolysis species $Cm(OH)_x(EDTA)^{-(x+1)}$, with $x > 1$.[39, 152] The fluorescence lifetime of $Cm(OH)(EDTA)^{2-}$ is higher compared to $Cm(OH)_x(EDTA)^{-(x+1)}$. Therefore, a higher amount of water molecules is attributed to the latter species. This is physically not reasonable, since additional quenchers are not considered in the Kimura equation (see chapter 3.2.2). Another reason for the reduced lifetime of $Cm(OH)_x(EDTA)^{-(x+1)}$ is given by Rabung *et al*., who determined the lifetime of Ca-Cm(III)-OH complexes. The "quenching effect" may be caused by the relatively large number of OH ions in the Cm(III) coordination sphere.[153] After 30 d, the signals described above disappear and two new bands at 606.0 – and ~ 622.3 – 622.4 nm appear. The peak at 622.3 – 622.4 nm appears only in suspension, indicating a species exclusively associated with the solid phase. For this signal, an averaged fluorescence lifetime of 1317±21 µs was calculated for the different contact times (Table 13). The long fluorescence lifetime and the significant shift in the emission band suggest a species without inner-sphere water molecules and a strong ligand field splitting. It is therefore classified as a Cm(III) species incorporated in the C-S-H phase. The signal at 606 nm is not an independent species, but a hot band of the incorporated species.[83]

The TRLFS measurements are in good agreement with the Batch sorption results. The low retention after 7 d is explained by the stabilization of Eu(III) by EDTA in the aqueous phase. For longer sorption times of more than 30 d, a high, almost quantitative retention was determined. This might be due to the incorporation of Cm(III) into the C-S-H phase. However, TRLFS experiments do not provide evidence for a reaction which is responsible for the slow sorption kinetics under those conditions. The kinetically controlled Cm(III) incorporation into C-S-H is known and also observed by

TRLFS measurements of Tits *et al*.[83] .However, this reaction will take place in all experiments reported here with mostly no significant observation of a delayed Cm/Eu(III) sorption over a period of tens of days.

Table 13: Fluorescence lifetimes (τ) and the corresponding amount of water molecules (N_{H2O}) of the different Cm(III) species detected in solution and suspension. All TRLFS measurements are performed in presence of [EDTA] = 10^{-2} M for the C-S-H phase (C/S ~ 1.0). The assignment of the ternary species Cm-OH-EDTA is considered as preliminary.

Species	**Peak**	**t**	**pH_m**	τ	**N_{H2O}**	τ	**N_{H2O}**
	nm	***d***		***µs***		***µs***	
				solution		*suspension*	
$Cm(OH)(EDTA)^{2-}$	606.9	7	11.2	280±11	1.4±1.0	315±20	1.1±1.0
$Cm(OH)_x(EDTA)^{-(x+1)}$	613.9	7	11.2	164±14	3.1±1.0	-	-
Incorporation	622.3	30	11.2	-	-	1633±18	0
	622.3	60	11.1	-	-	1141±15	0
	622.4	90	11.1	-	-	1231±35	0
	622.4	180	11.0	-	-	-	
	622.4	365	11.1	-	-	1263±14	0
Ø	**622.4**	**-**	**11.1**	**-**	**-**	**1317±21**	**0**

In order to explain the effect of EDTA at low concentrations of 10^{-3} M and 10^{-4} M, fluorescence emission spectra of Cm(III) on C-S-H phases (C/S ~ 1.3) are recorded in NaCl solution at I_m = 1.02 m (see Figure 43). For all samples, solution and suspension measurements between 7 – 365 d are performed. The corresponding lifetimes are listed in Table 14.

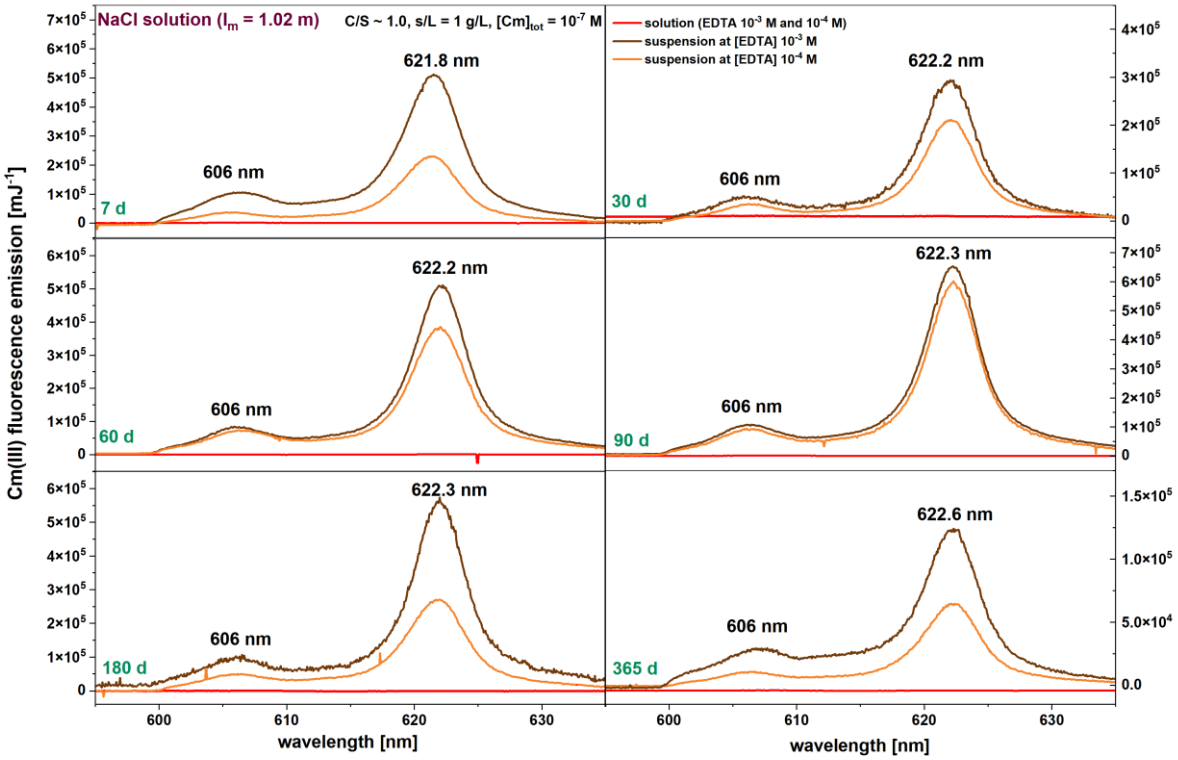

Figure 43: Fluorescence emission spectra of the Cm(III) containing solution and suspension with C-S-H phases (C/S ~ 1.0) in the presence of [EDTA] = 10^{-3} and 10^{-4} M. The former spectra are shown in orange, while the latter are illustrated in brown. The spectra are recorded in NaCl solution at I_m = 1.02 m between 7 – 365 d at S/V = 1 g/L.

Figure 43 clearly shows, that no significant Cm(III) signal is detected in solution after all sorption times. Thus, the emission bands observed in the suspension at 621.8 – 622.6 nm are almost exclusively associated with the solid phase for both [EDTA]. The signal intensities are lower for [EDTA] = 10^{-4} M. This cannot be explained at the moment. For the signal ~ 621.8 – 622.6 nm, average fluorescence lifetimes of 1280±20 µs ([EDTA] = 10^{-3} M) and 1030±31 µs ([EDTA] = 10^{-4} M) are determined, attributed to the hydration number of zero. This verifies that the Cm(III) species is fully incorporated into the C-S-H phase.[83]

The results are in excellent agreement with the batch sorption experiments: The high retention at [EDTA] ≤ 10^{-3} M is due to the incorporation of Cm(III) or Eu(III) into the C-S-H phase.

Table 14: Fluorescence lifetimes (τ) and the corresponding amount of water molecules (N_{H2O}) of the different Cm(III) species detected in solution and suspension. All TRLFS measurements are performed in presence of [EDTA] = 10^{-3} and 10^{-4} M for the C-S-H phase with C/S ~ 1.3.

Species	Peak	t	pH_m	τ	N_{H2O}
	nm	*d*		*µs*	
				suspension	
Incorporation species	621.8	7	11.1	1225±38	0
			11.5	1150±10	0
	622.2	30	11.1	1569±15	0
			11.8	885±37	0
	622.2	60	11.1	1026±14	0
			11.8	1038±21	0
	622.3	90	11.1	-	
			11.8	-	
	622.3	180	11.1	1146±20	0
			11.4	943±45	0
	622.6	365	11.1	1433±15	0
			11.4	1137±41	0
Ø	**622.2**	**-**	**11.1**	**1280±20**	**0**
	622.2		**11.6**	**1030±31**	**0**

Since the results for the batch sorption studies with C-S-H phases for C/S ~ 1.3 are different from those of C/S ~ 1.0, the fluorescence emission spectra of Cm(III) in solution and suspension are examined for the C-S-H phase with C/S ~ 1.3 in presence of [EDTA] = 10^{-2} M. All spectra are recorded in NaCl solution between 7 – 300 d (see Figure 44). Corresponding fluorescence lifetimes are shown in Table 15.

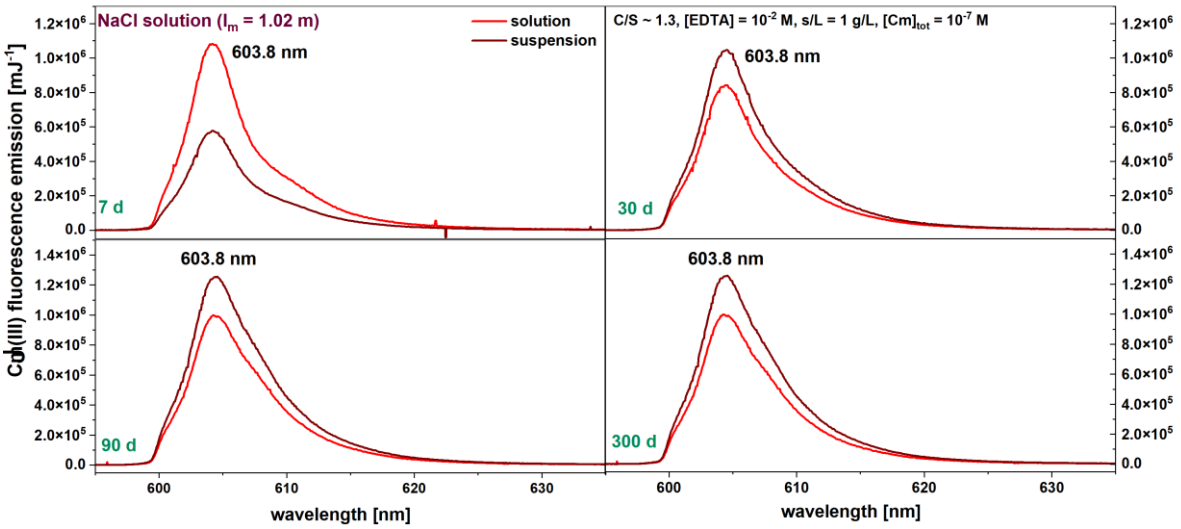

Figure 44: Fluorescence emission spectra of the Cm(III) containing solution (light red) and suspension (dark red) with C-S-H phases (C/S ~ 1.3) in the presence of [EDTA] = 10^{-2} M. The former spectra are shown in orange, while the latter are illustrated in brown. The spectra are recorded in NaCl solution at I_m = 1.02 m between 7 – 300 d at S/V = 1 g/L.

In contrast to the Cm(III) spectra at C/S ~ 1.0, only one signal at 603.8 nm is detected for all contact times. This is observed in both solution and suspension, indicating that almost all Cm(III) is present in the aqueous phase. Average fluorescence lifetimes are determined to be 163±12 µs (solution) and 158±15 µs (suspension), where 3.2±1.0 (solution) and 3.3±1.0 (suspension) water molecules are assigned. Trumm *et al.* and DiBlasi *et al*. also reported the binary Cm(EDTA)$^{2-}$ complex with an almost similar peak position of ~ 603.9 nm.[39, 152] This complex has a lifetime of 231±40 µs. Compared to the results obtained here, the peak position is almost identical, but the lifetime is significantly shorter. Following this interpretation, the presence of the ternary Ca-Cm(III)-EDTA species is inferred instead of the Cm(EDTA)$^{2-}$ complex. An exact explanation for this finding is currently not possible. Nevertheless, a speculative approach can be given, which is based on the structural investigations in chapter 4.7: In the Ca-Cm(III)-EDTA complex it is possible that the vibration frequency of the coordinated COOH functional groups changes due to the association with Ca. This could lead to a quenching effect for the ternary complex, resulting in a shorter lifetime compared to the binary Cm(EDTA)$^{2-}$ complex.[39] This aligns well with the batch sorption experiments, where a low retention (log R_d = 2 - 3) of Eu(III) on the C-S-H phase with C/S ~ 1.0 is observed for the studied period of 7 to 50 d. This is in contrast to the

investigated C-S-H phase with C/S ~ 1.0: Here a low retention is detected after 7 d, whereas an increasing retention (log R_d = 5 - 6) of Eu(III) is detected after 50 d (see chapter 4.4.2).

In previous ICP-OES studies it was shown that contacting C-S-H phases with 10^{-2} M EDTA solutions resulted in Ca concentrations increasing with the C/S ratio (chapter 4.2.2). The higher [Ca] obtained for C/S ~ 1.3 could favor the formation of ternary complexes.

Table 15: Fluorescence lifetimes (τ) and the corresponding amount of water molecules (N_{H2O}) of the different Cm(III) species detected in solution and suspension. All TRLFS measurements are performed in presence of [EDTA] = 10^{-2} M for the C-S-H phase with C/S ~ 1.3.

Species	**Peak**	**t**	**pH_m**	τ	**N_{H2O}**	τ	**N_{H2O}**
	nm	***d***		***µs***		***µs***	
				solution		*suspension*	
Ca-Cm(III)-EDTA	603.8	7	11.4	159±13	3.2±1.0	154±18	3.3±1.0
	603.8	30	11.3	175±10	2.8±1.0	157±16	3.3±1.0
	603.8	90	11.1	172±8	3.1±1.0	156±12	3.3±1.0
	603.8	300	10.8	145±17	3.6±1.0	163±15	3.1±1.0
Ø	**603.8**	**-**	**11.1**	**163±12**	**3.2±1.0**	**158±15**	**3.3±1.0**

4.5.2 TRLFS studies of the Cm(III)- C-S-H – EDTA – $CaCl_2$ system

The results of the batch sorption study in $CaCl_2$ yielded different results compared to that in the NaCl solution. Accordingly, Ca plays a decisive role. Figure 45 shows fluorescence emission spectra of Cm(III) in contact with [EDTA] = 10^{-2} M, C-S-H phases (C/S ~ 1.0) and $CaCl_2$ solutions (I_m = 1.02 m) between 7 – 365 d. All measurements, except the one taken at 7 d, are made in both solution and suspension. The corresponding fluorescence lifetimes are given in Table 16.

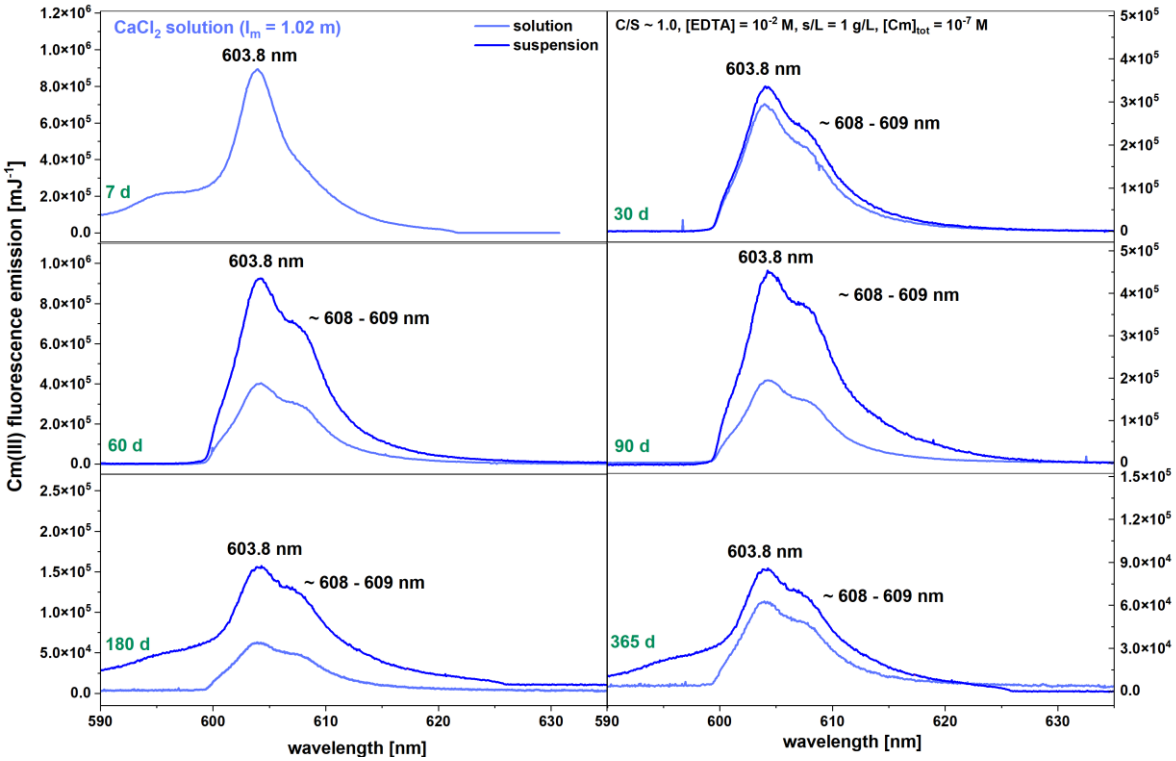

Figure 45: Fluorescence emission spectra of the Cm(III) containing solution (light blue) and suspension (dark blue) with C-S-H phases (C/S ~ 1.0) in the presence of [EDTA] = 10^{-2} M. The spectra are recorded in $CaCl_2$ solution at I_m = 1.02 m between 7 – 365 d at S/V = 1 g/L.

As discussed in the previous section the emission band at 603.8 nm can be assigned to the ternary Ca-Cm(III)-EDTA complex (see also DiBlasi *et al)*.[39] The presence of an additional species is indicated by the slightly bathochromic shifted shoulder. DiBlasi *et al.* postulated a quaternary species at higher wavelength of 610.1 nm, with a fluorescence lifetime of τ = 813±218 µS. The quaternary species is described with the formula Ca-Cm(III)-OH-EDTA. This species shows a much higher fluorescence lifetime, not observed in the present study Furthermore, the species reported by DiBlasi

et al. occurs at pH ≥ 12, whereas the pH value of the present sample is at pH = 11.3. Therefore, it is not possible at the current state of knowledge to make an accurate statement about the presence of quaternary species.[39] In addition it is noteworthy, that no incorporation of Cm(III) into the C-S-H phase is observed as a consequence of the strong stabilization of Cm(III) by Ca-Cm(III)-EDTA complexes in the aqueous phase.

The TRLFS results are consistent with the results of batch sorption experiments discussed in section 4.4.2.

Table 16: Fluorescence lifetimes (τ) and the corresponding amount of water molecules (N_{H2O}) of the different Cm(III) species detected in solution and suspension. All TRLFS measurements are performed in presence of [EDTA] = 10^{-2} M for the C-S-H phase with C/S ~ 1.4.

Species	**Peak**	**t**	**pH_m**	τ	**N_{H2O}**	τ	**N_{H2O}**
	nm	***d***		***µs***		***µs***	
				solution		*suspension*	
Ca-Cm(III)-EDTA	603.8	7	10.9	144±4	3.6±1.0	-	-
	603.8	30	10.8	176±12	2.8±1.0	175±20	2.8±1.0
	603.8	60	-	184±10	2.7±1.0	196±34	2.4±1.0
	603.8	90	10.7	179±22	2.8±1.0	141±11	3.7±1.0
	603.8	180	10.7	173±15	2.9±1.0	158±14	3.2±1.0
	603.8	365		139±9	3.8±1.0	141±10	3.7±1.0
Ø	**603.8**	**-**	**10.8**	**166±12**	**3.1**±1.0	**162±18**	**3.2**±1.0

Analogous to the batch sorption experiments, Cm(III) fluorescence spectra are also recorded at C/S ~ 1.4 in $CaCl_2$ solutions (I_m = 1.02 m) in presence of [EDTA] = 10^{-2} M. The corresponding spectra are shown in Figure 46. Fluorescence lifetimes related to the spectra are presented in Table 17.

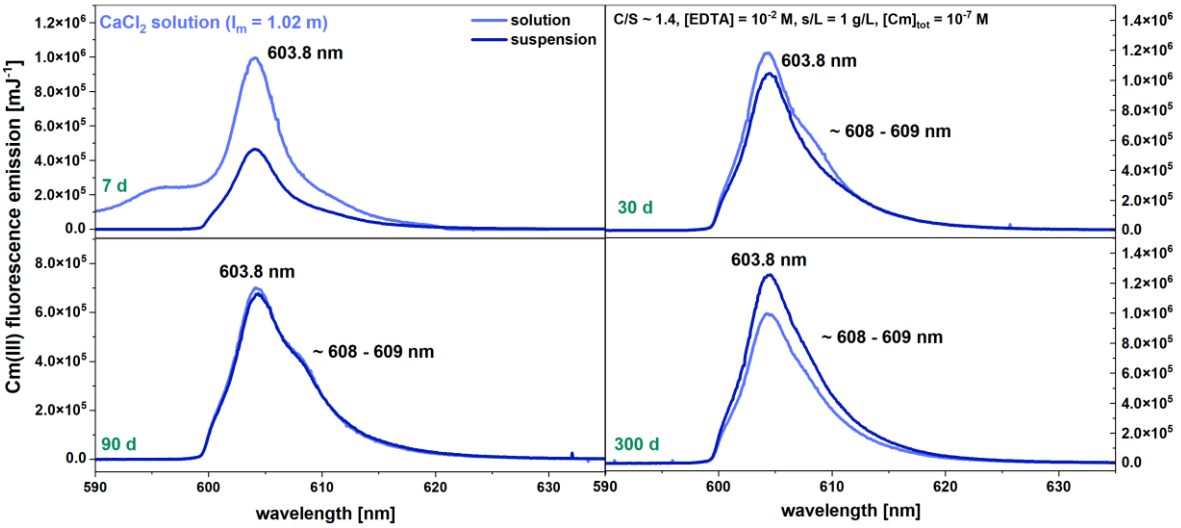

Figure 46: Fluorescence emission spectra of the Cm(III) containing solution (light blue) and suspension (dark blue) with C-S-H phases (C/S ~ 1.4) in the presence of [EDTA] = 10^{-2} M. The spectra are recorded in $CaCl_2$ solution at I_m = 1.02 m between 7 – 300 d at S/V = 1 g/L.

Spectra resemble closely those observed for experiments with C-S-H and C/S ~ 1.0. Correspondingly, the peak at 603.8 nm again is attributed to the Ca-Cm(III)-EDTA species.[39] In comparison to experiments with C-S-H phases with C/S ~ 1.0, the bathochromic shoulder between 607 – 609 nm is less pronounced for C/S ~ 1.4. An explanation for the increased prominence of the shoulder in C/S ~ 1.0 compared to C/S ~ 1.4 systems is presently not available. The TRLFS data shown in Figure 46 again are consistent with the outcome of batch sorption studies.

Table 17: Fluorescence lifetimes (τ) and the corresponding amount of water molecules (N_{H2O}) of the different Cm(III) species detected in solution and suspension. All TRLFS measurements are performed in presence of [EDTA] = 10^{-2} M for the C-S-H phase with C/S ~ 1.4.

Species	Peak	t	pH_m	τ	N_{H2O}	τ	N_{H2O}
	nm	*d*		*µs*		*µs*	
				solution		*suspension*	
Ca-Cm(III)-EDTA	603.8	7	11.3	159±11	3.2±1.0	155±14	3.3±1.0
	603.8	30	10.8	184±17	2.7±1.0	185±8	2.6±1.0
	603.8	90	10.8	167±21	3.0±1.0	165±10	3.1±1.0
	603.8	300	10.8	157±11	3.3±1.0	181±16	2.7±1.0
Ø	**603.8**	**-**	**10.9**	**167±14**	**3.1**±1.0	**172±15**	**2.9**±1.0

For completeness, fluorescence emission spectra of Cm(III) containing solutions and suspensions associated with the C-S-H phase at C/S ~ 1.0 are recorded to explain the effect at lower [EDTA] = 10^{-3} and 10^{-4} M are given in Figure 47 for $CaCl_2$ solutions (I_m = 1.02 m). The associated fluorescence lifetimes are shown in Table 18.

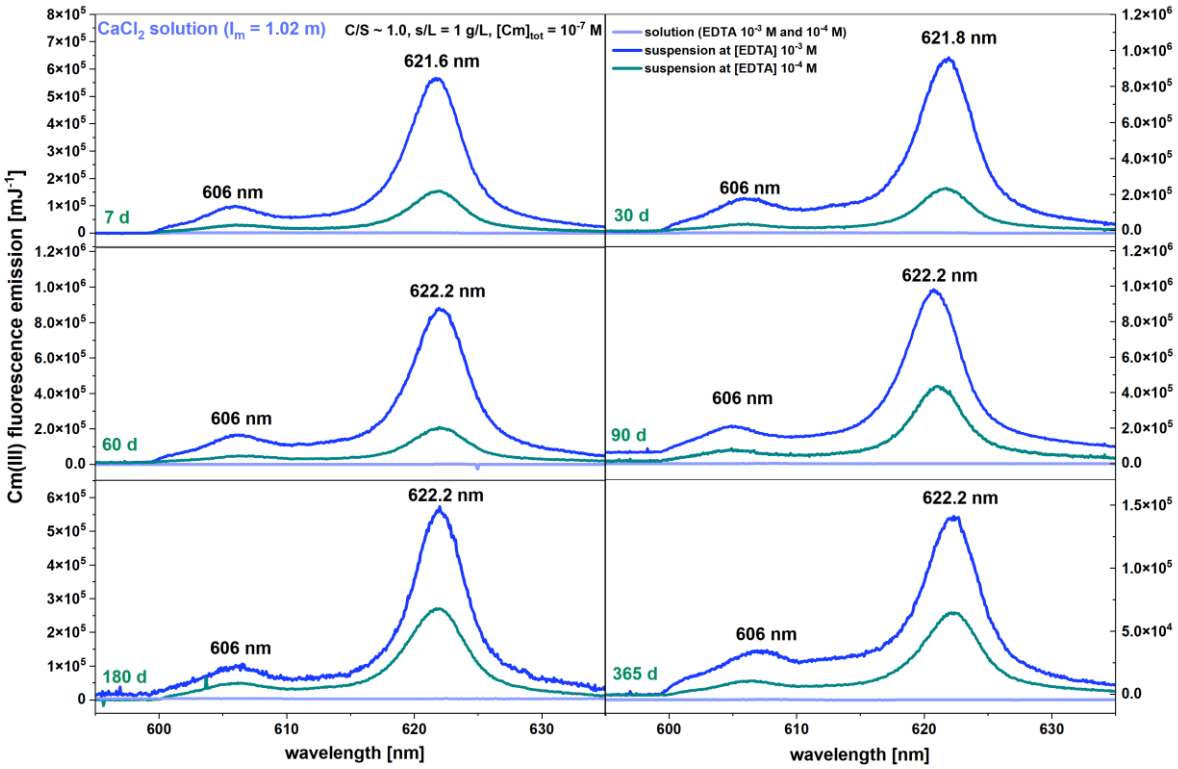

Figure 47: Fluorescence emission spectra of the Cm(III) solution (light blue) and suspension (dark blue) with C-S-H phases (C/S ~ 1.0) in the presence of [EDTA] = 10^{-3} and 10^{-4} M. The spectra are recorded in $CaCl_2$ solution at I_m = 1.02 m between 7 – 365 d at S/V = 1 g/L.

As expected no solution Cm(III) species can be detected. Strong sorption results in the formation of incorporated species with their characteristic spectroscopic features.

Table 18: Fluorescence lifetimes (τ) and the corresponding amount of water molecules (N_{H2O}) of the different Cm(III) species detected in solution and suspension. All TRLFS measurements are performed in presence of [EDTA] = 10^{-3} and 10^{-4} M for the C-S-H phase with C/S ~ 1.0.

Species	Peak	t	pH_m	τ	N_{H2O}
	nm	*d*		*µs*	
			suspension		
Incorporation species	621.6	7	10.8	1351±22	0
			11.0	1075±32	0
	621.8	30	11.0	706±53	0
			11.2	800±55	0
	622.2	60	11.1	2084±387	0
			11.0	1151±10	0
	622.2	90	11.1	-	-
			11.0	-	
	622.2	180	11.1	1156±12	0
			11.0	1766±141	0
	622.2	365	11.1	708±99	0
			11.0	1175±12	0
Ø	**622.2**	**-**	**11.0**	**1201±114**	**0**
	622.2		**11.0**	**1193±50**	**0**

4.6 Examination of the Eu/Cm(III) speciation

The batch sorption and Time-Resolved Laser Fluorescence Spectroscopy (TRLFS) experiments support the presence of the ternary species Ca-Cm(III)-EDTA. Depending on the pH and Ca content of the sample, the quaternary complex Ca-Cm(III)-OH-EDTA may also prevail according to the literature.[39] The formation of both complexes may significantly affect the Eu(III)/Cm(III) retention on C-S-H phases. A precise and detailed characterization of these species and the quantification of complex stabilities is required for their comprehensive consideration in geochemical modeling of cement systems.

For the examination of the Eu/Cm(III) speciation, fluorescence emission spectra of Cm(III) in the presence of EDTA are recorded (Figure 48,Table 19 and 20). This is a purely aquatic system and no C-S-H phase is added. In addition, experimental parameters such as [Ca] and pH_m are varied. Two distinct series of samples are prepared with different total ionic strengths (I_m = 0.51, 2.09 m). The ionic strength is primarily adjusted using NaCl, while the Ca concentration is systematically varied between 0.25% and 15% to each sample. The pH_m is ranging between 8.5 and 12.5, whereas an emission spectrum and a fluorescence lifetime are measured in 0.5 pH steps. More information about the sample preparation is given in chapter 3.2.2. From these data, the tentative stability constants are determined in several steps: First, a manual peak deconvolution of the fluorescence emission spectra, is performed (Figure 49 and 50). This step enables the derivation of the species distribution, as depicted in Figure 51. In the end, a linear slope analysis was conducted (see Figure 52).

Fluorescence emission spectra of Cm(III)

The Cm(III) fluorescence spectra are recorded in the presence of [EDTA] = 10^{-2} M at I_m = 0.51 and 2.09 m. The total ionic strength is mainly determined by NaCl, with a Ca contribution to the total ionic strength of 0.25%, 2.5% and 15%, respectively. This refers to [Ca] = 1.67 mM, 16.7 mM and 100 mM (I_m = 2.09 m) and [Ca] = 0.417 mM, 4.17 mM and 25 mM (I_m = 0.51 m) (see Figure 48). For a better overview, the spectra with a Ca content of 1.25 % and 6.25 %, which refers to [Ca] = 8.33 mM, 41.7 mM (I_m = 2.09 m) and [Ca] = 2.08 mM, 10.4 mM (I_m = 0.51 m) are illustrated in the Appendix

7.4. The fluorescence lifetimes are shown in Table 19, while the corresponding hydration sphere is illustrated in Table 20 for all samples.

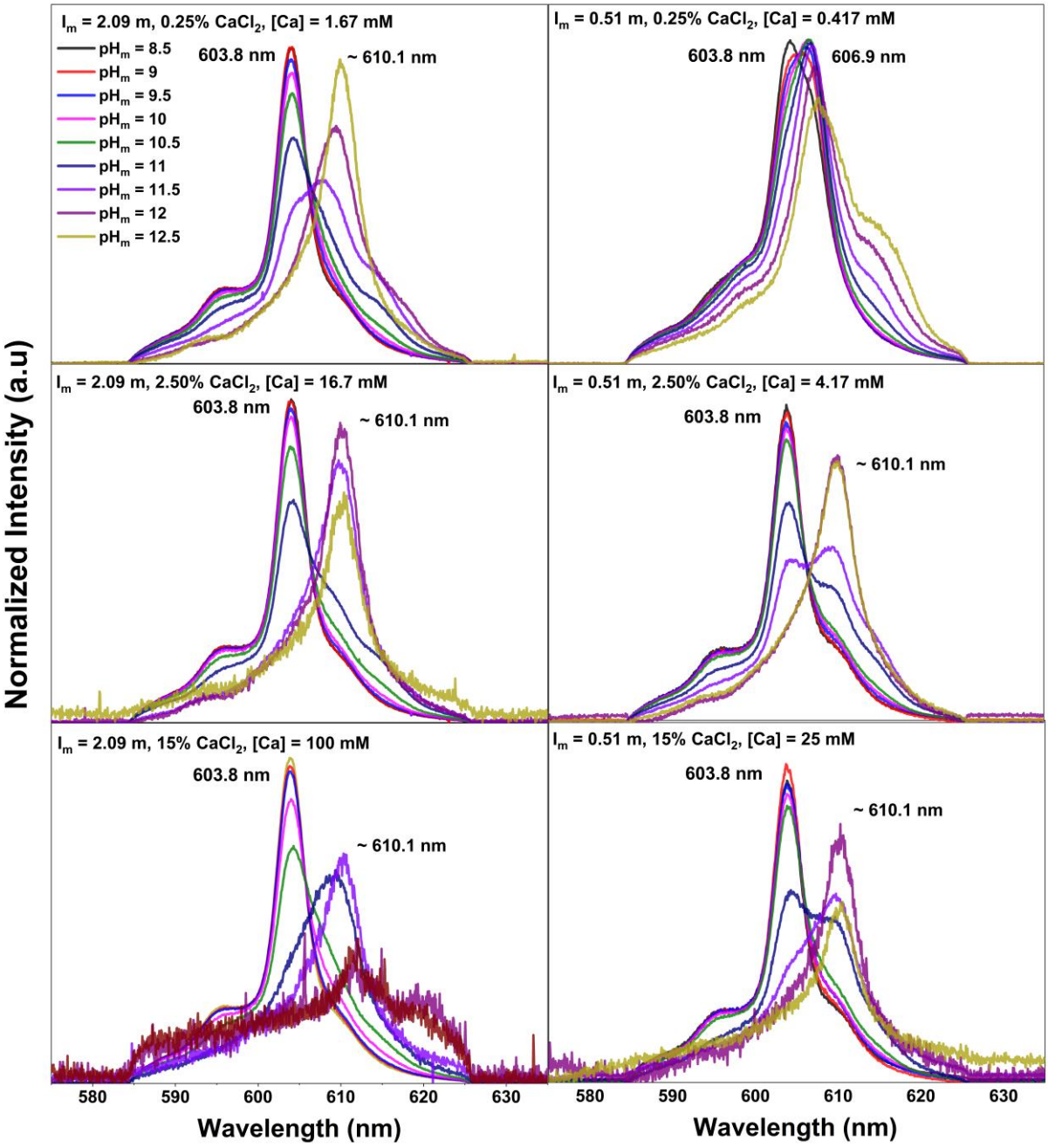

Figure 48: Cm(III) fluorescence emission spectra in presence of [EDTA] = 10^{-2} M at different [Ca] = 1.67 mM, 16.7 mM and 100 mM (I_m = 2.09 m, left) and [Ca] = 0.417 mM, 4.17 mM and 25 mM (I_m = 0.51 m, right) between pH_m = 8.5 – 12.5.

Between pH_m = 8.5 - 10.5, a signal at 603.8 nm is observed for all samples, except for the sample with the lowest Ca content (I_m = 0.51 m, [Ca] = 0.417 mM). This sample is

discussed in more detail at the end of this section. For the other samples, the signal at 603.8 nm corresponds to the ternary Ca-Cm(III)-EDTA species postulated by DiBlasi *et al*. on the basis of its peak position, fluorescence lifetime and number of water molecules (see Tables 19 and 20).[39] A possible overlap with the band of the binary $Cm(EDTA)^-$ complex is not assumed (see chapter 4.5.1). A bathochromic shoulder (λ = 608 - 610 nm) is observed between pH_m = 11 - 11.5. With increasing pH, this shoulder becomes more pronounced and dominates the spectra at the highest pH studied. In addition, the signal increases in intensity as the Ca content of the samples increases. Slightly longer fluorescence lifetimes are also observed at higher Ca concentrations (see Table 19). Hence, this signal is attributed to the quaternary Ca-Cm(III)-OH-EDTA species according to the literature.[39]

The sample with the lowest Ca content (I_m = 0.51 m, [Ca] = 0.417 mM) shows a different behavior: At pH_m = 8.5, an emission band is visible at 603.8 nm, showing a higher fluorescence lifetime of ~ 290 µs. This indicates the formation of the binary $Cm(EDTA)^-$ species (λ = 603.9 nm, τ = 231±40 µs).[39] Between pH_m = 9 – 12, a signal at 606.9 nm with τ ~ 350 µs is detected, which is therefore assigned to the ternary $Cm(OH)(EDTA)^{2-}$ species. At higher pH_m > 12, one sees a further red shift in the area of 607 - 608 nm, indicating the formation of another hydrolyzed species $Cm(OH)_x(EDTA)^{-(x+1)}$. It is assumed, that the Ca content of this sample is not sufficient to form the ternary or quaternary Ca-containing complexes. This is in good agreement with the literature.[39]

Table 19: Fluorescence emission lifetimes of aqueous Cm(III) species at I_m = 2.09 m (top) and 0.51 m (bottom) at [EDTA] = 10^{-2} M for pH_m = 8.5 – 12.5 with varying [Ca]. Hereby [Ca] = 1.67, 8.33, 16.7, 41.7, 100 mM (I_m = 2.09 m) and [Ca] = 0.417, 2.08, 4.17, 10.4 and 25 mM (I_m = 0.51 m) are considered.

Fluorescence lifetime (µs)					
I_m = 2.09 m					
	[Ca]/mM				
pH_m	*1.67*	*8.33*	*16.7*	*41.7*	*100*
8.5	141±30	137±15	136±12	142±16	138±14
9	133±40	138±14	139±16	143±14	136±13
9.5	150±15	143±16	141±22	143±24	132±16
10	151±18	140±17	140±19	142±18	115±12
10.5	156±18	133±28	130±15	137±13	118±15
11	153±16	128±16	124±16	190±17	235±9
11.5	166±6	218±16	350±10	336±9	210±14
12.0	282±9	383±5	415±10	-	-
12.5	455±13	-	834±29	-	-
I_m = 0.51 m					
pH_m	*0.417*	*2.08*	*4.17*	*10.4*	*25*
8.5	288±16	140±18	138±16	126±15	145±6
9	333±15	134±17	124±18	123±16	126±14
9.5	371±39	141±16	137±15	139±24	133±19
10	365±37	149±12	140±10	136±9	140±8
10.5	272±15	148±16	131±13	127±15	123±16
11	370±42	154±11	141±11	149±14	141±11
11.5	404±14	175±15	159±6	166±7	271±13
12.0	315±34	270±12	298±8	276±9	-
12.5	200±12	371±26	341±12	427±12	-

***"- "**These spectra could not be analyzed

Table 20: Number of inner sphere H_2O ligands calculated from the corresponding fluorescence lifetimes. Those are calculated at I_m = 2.09 m and 0.51 m in presence of [EDTA] = 10^{-2} M between pH_m 8.5 – 12.5 with varying [Ca] = 1.67, 8.33, 16.7, 41.7, 100 mM (I_m = 2.09 m) and [Ca] = 0.417, 2.08, 4.17, 10.4 and 25 mM (I_m = 0.51 m).

Number of inner sphere H_2O ligands					
I_m = 2.09 m					
	[Ca]/mM				
pH_m	*1.67*	*8.33*	*16.7*	*41.7*	*100*
8.5	3.7±1.0	3.8±1.0	3.8±1.0	3.6±1.0	3.8±1.0
9	3.9±1.0	3.8±1.0	3.7±1.0	3.6±1.0	3.8±1.0
9.5	3.4±1.0	3.6±1.0	3.7±1.0	3.6±1.0	4.0±1.0
10	3.4±1.0	3.7±1.0	3.7±1.0	3.6±1.0	4.7±1.0
10.5	3.2±1.0	3.9±1.0	4.0±1.0	3.8±1.0	4.5±1.0
11	3.3±1.0	4.1±1.0	4.3±1.0	2.5±1.0	1.8±1.0
11.5	3.0±1.0	2.1±1.0	0.9±1.0	1.0±1.0	2.2±1.0
12.0	1.4±1.0	0.8±1.0	0.7±1.0	-	-
12.5	0.5±1.0	-	-	-	-
I_m = 0.51 m					
pH_m	*0.417*	*2.08*	*4.17*	*10.4*	*25*
8.5	1.3±1.0	3.7±1.0	3.8±1.0	4.2±1.0	3.5±1.0
9	1.0±1.0	3.9±1.0	4.3±1.0	4.3±1.0	4.2±1.0
9.5	0.8±1.0	3.7±1.0	3.8±1.0	3.7±1.0	3.9±1.0
10	0.9±1.0	3.4±1.0	3.7±1.0	3.8±1.0	3.7±1.0
10.5	1.5±1.0	3.4±1.0	4.0±1.0	4.2±1.0	4.3±1.0
11	0.8±1.0	3.3±1.0	3.7±1.0	3.4±1.0	0.2±1.0
11.5	0.7±1.0	2.8±1.0	3.1±1.0	3.0±1.0	3.0±1.0
12.0	1.2±1.0	1.5±1.0	1.3±1.0	1.4±1.0	1.4±1.0
12.5	2.3±1.0	0.8±1.0	1.0±1.0	0.6±1.0	-

***"- "**These spectra could not be analyzed

Peak deconvolution

A Peak deconvolution is performed to determine the species distribution at different Ca concentrations and pH values. The measured fluorescence emission spectra can be described as linear combinations of the individual fluorescence spectra. For this, the spectra are normalized to equal areas. At this point the fluorescence intensity factor (FI) must be considered. The total intensities of the spectra fluctuate by ± 20%, which is also considered low. However, there are no systematic trends recognizable. Under the given experimental conditions, there is a monoexponentially decay determined for all spectra. This pattern is characteristic for systems where the ligand exchange rate is higher than the lifetime of the first excited state. Therefore, the determination of the relative intensity ratios is based on the thermodynamic equilibrium. The total emission intensity is only affected by differences in the FI factors. This is described in detail in the literature.[52] Since it is not possible to determine the precise FI for the individual species on the basis of the available data, it is assumed for the following data analysis that the FI for all species = 1. In order to conduct the deconvolution of the peaks, pure spectra must first be identified. The species considered in this work are Ca-Cm(III)-EDTA, Ca-Cm(III)-OH-EDTA and $Cm(OH)(EDTA)^{2-}$ with peak positions at λ = 603.9, 606.9 and 610.1 nm. Their pure spectra are shown in Figure 49. Hereby, the pure Ca-Cm(III)-EDTA species was first established with the spectrum at pH_m = 8.5 of the sample with [Ca] = 16.7 mM (I_m = 2.09 m). The other two pure species were derived from this sample. Additionally, for Ca-Cm(III)-OH-EDTA, the spectrum of this sample at pH = 12.5 was used. For the determination of the last pure species $Cm(OH)(EDTA)^2$, the spectrum at pH_m = 10 of the sample with [Ca] = 0.417 mM was applied. After the pure species were defined, they were correlated with each sample. This allowed the proportions of each species to be determined

The binary $Cm(EDTA)^-$ species is not included in the model, since TRLFS is unable to distinguish this complex from the ternary Ca-Cm(III)-EDTA species. However, the $Cm(EDTA)^-$ complex appears to be a significant fraction only in the sample with the lowest Ca content ([Ca] = 0.417 mM, I_m = 0.51 m). This sample is excluded from the preliminary model, due to the low Ca content.

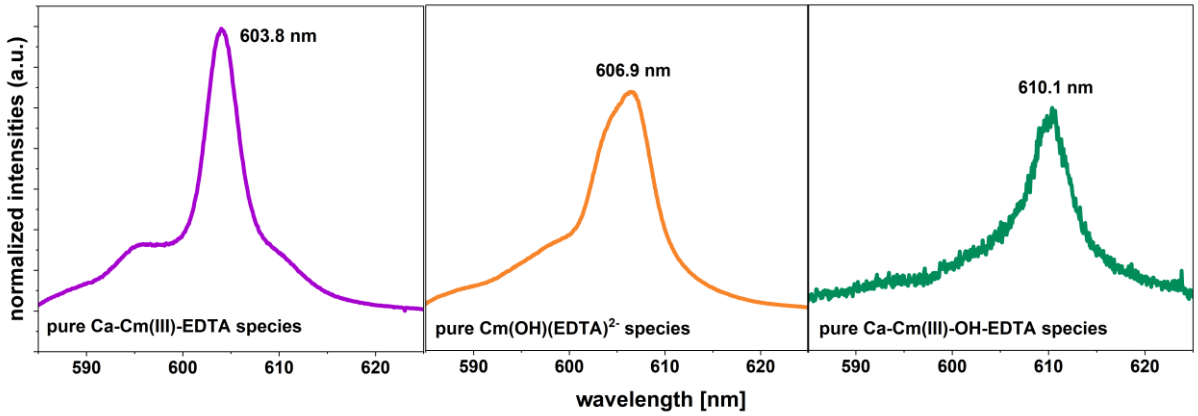

Figure 49: Pure spectra of the three different species: Ca-Cm(III)-EDTA (left), $Cm(OH)(EDTA)^{2-}$ (center) and Ca-Cm(III)-OH-EDTA (left). They are extracted from the experimental Cm(III) fluorescence spectra and used for the peak deconvolution.

The peak position of 603.8 nm is assigned to the ternary Ca-Cm(III)-EDTA species. The band at 606.9 nm corresponds to the ternary $Cm(OH)(EDTA)^{2-}$ species. According to the literature, this occurs mainly at low Ca contents ([Ca] < 1 mM).[39] Furthermore, the band at 610.1 nm is described as a quaternary Ca-Cm(III)-OH-EDTA species.

An example of a peak deconvolution is given by the probe with a Ca content of 1.25%. This corresponds to [Ca] = 8.33 mM at I_m = 2.09 m and [Ca] = 2.08 mM at I_m = 0.51 m. For the remaining samples, peak deconvolution was performed analogously to the selected examples.

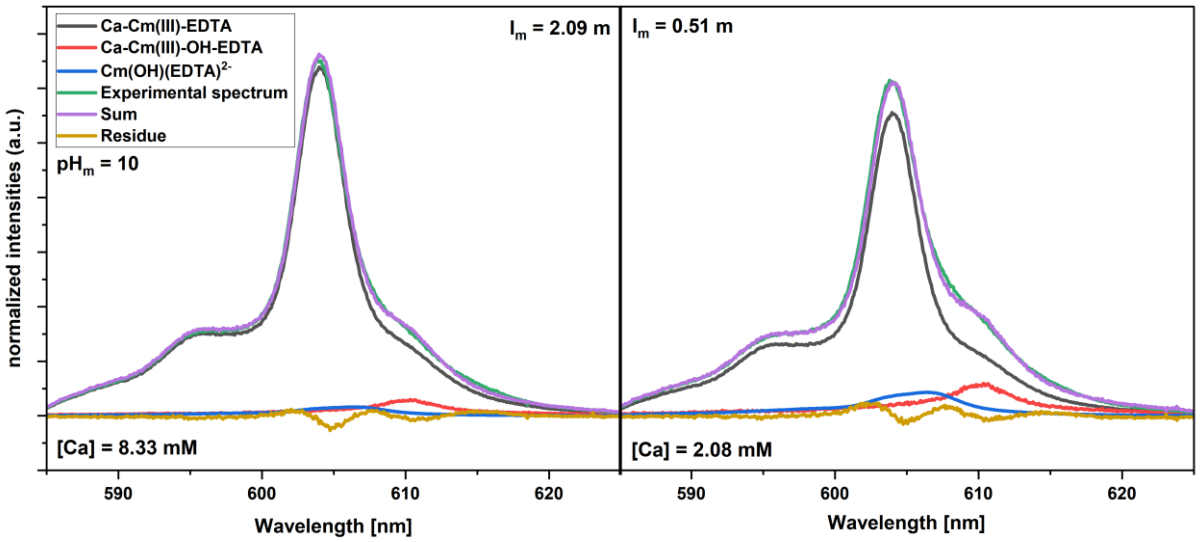

Figure 50: Peak deconvolution, exemplary shown for both ionic strength series I_m = 2.09 and 0.51 m and the Ca content of 1.25 % at pH_m = 10. This refers to [Ca] = 8.33 mM at I_m = 2.09 m and [Ca] = 2.08 mM at I_m = 0.51 m. The pure species such as Ca-Cm(III)-EDTA (purple), $Cm(OH)(EDTA)^{2-}$ (blue) and Ca-Cm(III)-OH-EDTA (red) are shown in addition. Further the residue is shown in brown.

Both spectra are dominated by the pure Ca-Cm(III)-EDTA species. Only minor abundance of the other two species contribute to the total spectrum and residues are small. The peak deconvolution is now used as the basis for constructing speciation diagrams.

Species distribution

The molar fractions of the species Ca-Cm(III)-EDTA, Ca-Cm(III)-OH-EDTA and $Cm(OH)(EDTA)^{2-}$ are determined from the peak deconvolution and presented as function of pH in the speciation diagrams given in Figure 51 for [Ca] = 1.67 mM, 16.7 mM and 100 mM (I_m = 2.09 m) and [Ca] = 0.417 mM, 4.17 mM and 25 mM (I_m = 0.51 m). The speciation diagrams for [Ca] = 8.33 mM, 41.7 mM (I_m = 2.09 m) and [Ca] = 2.08 mM, 10.4 mM (I_m = 0.51 m) are illustrated in the Appendix 7.4 as well as all molar fractions given in %.

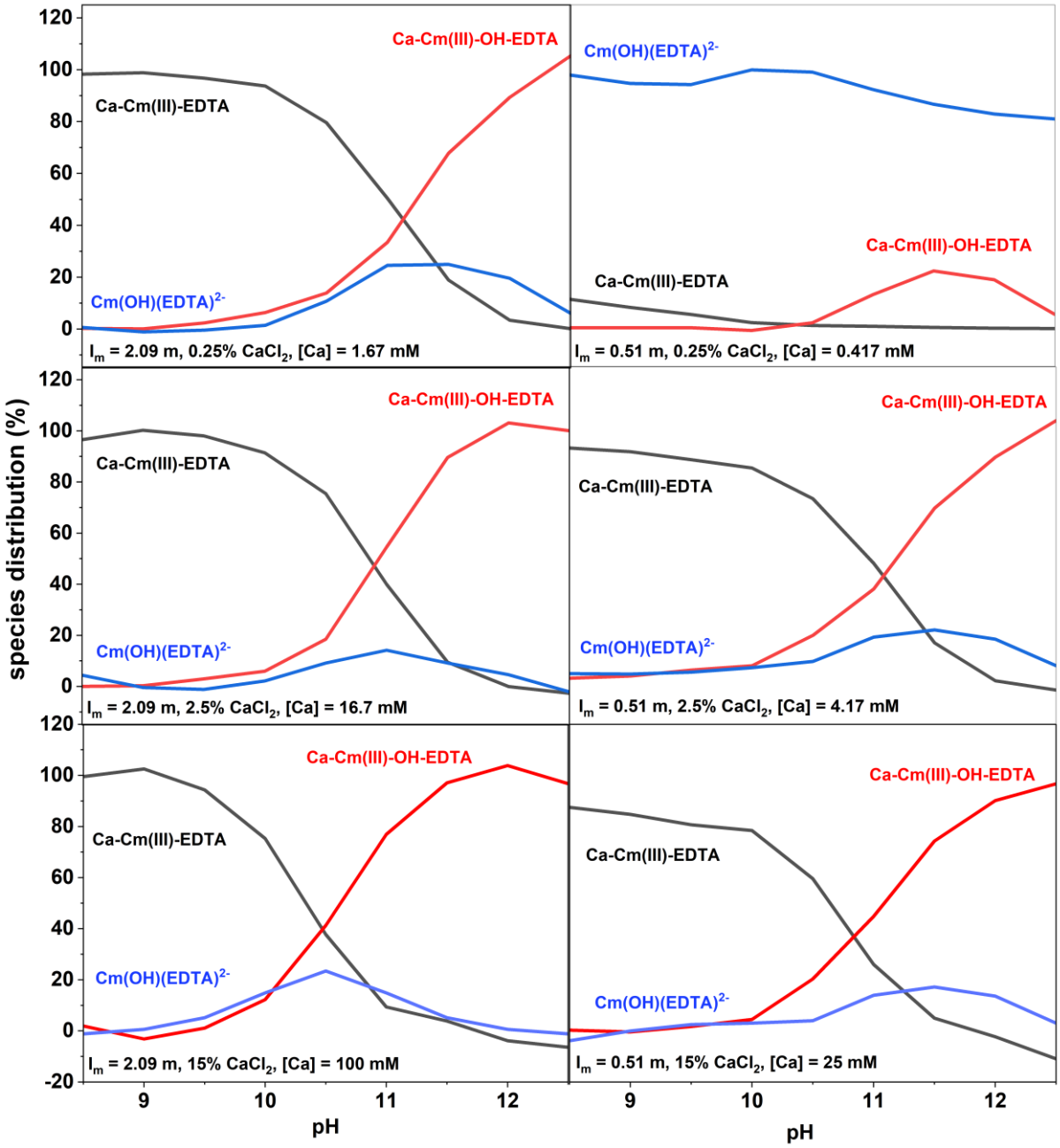

Figure 51: Molar fractions of the Ca-Cm(III)-EDTA (black), Ca-Cm(III)-OH-EDTA (red) and Cm(OH)(EDTA)$^{2-}$ (blue) complexes as function of the pH$_m$ of solutions for [Ca] = 1.67 mM, 16.7 mM and 100 mM (I$_m$ = 2.09 m, left) and [Ca] = 0.417 mM, 4.17 mM and 25 mM (I$_m$ = 0.51 m, right).

It is evident, that in the solution with the lowest Ca concentration (I$_m$ = 0.51 m, [Ca] = 0.417 mM), Ca-stabilized Cm(III) complexes play a subordinate role. The ternary Cm(OH)(EDTA)$^{2-}$ complex dominates over the whole pH range studied. However, especially at pH ≤ 8.5, that Cm(EDTA)$^{-}$ species is expected to be present in significant amounts. This species is not included in the preliminary model (see discussion above).

In all other solutions, the pH-dependent speciation is very similar and is dominated by the Ca-stabilized ternary and quaternary Cm(III)-EDTA complexes. This is in good agreement with the data obtained by DiBlasi *et al.*: They postulated the presence of the Ca-Cm(III)-EDTA complex between pH_m = 7 - 11, whereas the presence of the quaternary species Ca-Cm(III)-OH-EDTA was mainly detected at pH ≥ 12.[39]

Determination of stability constants (log β)

The sample with the lowest [Ca] = 0.417 mM from the series with I_m = 0.51 m was excluded from these calculations as it does not contain the Ca-stabilized ternary and quaternary Cm(III) EDTA complexes with significant contribution. The formation of the previously identified quaternary species can be described by the following equilibrium:

$$Ca\text{-}Cm(III)\text{-}EDTA + n(OH) \leftrightarrow Ca\text{-}Cm(III)\text{-}(OH)_n\text{-}EDTA$$

The equilibrium constant of this reaction is described by the law of mass action:

$$\beta^0{}_n = \frac{a(Ca-Cm(III)-(OH)_n-EDTA)}{a(Ca-Cm(III)-EDTA)\cdot a(OH)^n}$$

With a(X) being the activity of the respective species X. For a given ionic strength the conditional stability constant β‘ is valid, which is defined as follows:

$$\beta'_n = \frac{[Ca-Cm(III)-(OH)_n-EDTA]}{[Ca-Cm(III)-EDTA]\cdot[OH]^n} = \beta^0 \cdot \frac{\gamma(Ca-Cm(III)-(OH)_n-EDTA)}{\gamma(Ca-Cm(III)-EDTA)\cdot\gamma(OH)^n}$$

This equation can be rewritten as follows:

$$log\ \beta_n = \log\left(\frac{[Ca-Cm(III)-(OH)_n-EDTA]}{[Ca-Cm(III)-EDTA]}\right) + n\cdot log(OH^-)$$

$$\log\left(\frac{[Ca-Cm(III)-(OH)n-EDTA]}{[Ca-Cm(III)-EDTA]}\right) = log\ \beta_n - n\cdot log(OH^-)$$

A linear slope analysis can be used to determine the amount *n* of coordinating OH groups. This involves the graphical plot of $\log\left(\frac{[Ca-Cm(III)-(OH)n-EDTA]}{[Ca-Cm(III)-EDTA]}\right)$ versus $log\ (OH^-)$. A slope analysis is exemplarily shown in Figure 52 for samples with a Ca content of 2.50 %. This refers to [Ca] = 16.7 mM (I_m = 2.09 m) and [Ca] = 4.17 mM (I_m = 0.51 m). For all the other samples, similar slope analyses are performed and illustrated in Appendix 7.4.

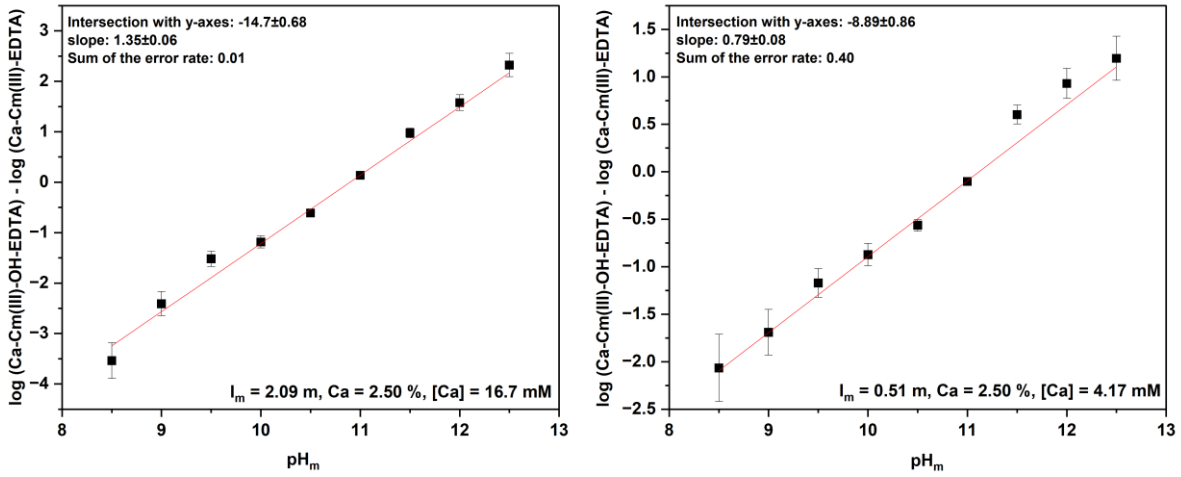

Figure 52: Slope analysis for the determination of the amount *n* of OH-groups in the quaternary Ca-Cm(III)-OH-EDTA species at I_m= 2.09 m (left) and 0.51 m (right) with Ca = 2.50 % ([Ca] = 16.7 mM, 4.17 mM) between pH_m = 8.5 – 12.5.

Using this procedure, an averaged *n* of 1.3±0.1 (I_m = 2.09 m) and 1.0±0.1 (I_m = 0.51 m) was obtained for each ionic strength series. The slope analysis shows, that the preliminary chemical model, based on the addition of one OH group to the ternary Ca-Cm(III)-EDTA complex, can be confirmed. However, there are certain points to be considered: Some of the slope analyses show a slight deviation from the linear fit (see Appendix 7.4, Figure 7.7). This is due to the fact that it is a preliminary model, where certain assumptions have been made: The FI factors were only estimated, and set to 1 for each species (see discussion above). Also, the peak deconvolution was performed assuming only the three species such as Ca-Cm(III)-EDTA, Ca-Cm(III)-OH-EDTA, and $Cm(OH)(EDTA)^{2-}$. Possible additional species, like the $Cm(EDTA)^-$ complex were not considered. Furthermore, the slope analysis was only performed between pH_m = 9 – 12. This is due to the fact that at pH_m = 8.5, the

ternary Ca containing complex predominated, while at pH_m = 12.5 it is most likely the Ca-Cm(III)-OH-EDTA complex. This leads to a large deviation in the slope analysis.

After determining the number of OH groups in the complexes, the conditional stability constants can be calculated using $\boldsymbol{log\ \beta_n = \log\left(\frac{[Ca-Cm(III)-(OH)_n-EDTA]}{[Ca-Cm(III)-EDTA]}\right) + n \cdot log(OH^-)}$. The first term of this formula is determined by the percentage of species at a certain pH. The OH^- concentration in the second term is determined by calculating the pOH from the measured pH_m. For this, the pK'_w of water was calculated for each ionic strength, using the SIT (see chapter 3.4). The concentration of hydroxide is then calculated by $pOH_m = pK'_w - pH_m$, with $pOH_m = -\log [OH^-]$. Using this approach, two tentatively stability constants log β' (I_m = 2.09 m) = 4.54±0.32 and log β' (I_m = 0.51 m) = 3.15±0.18) are observed for the following reaction.

$$Ca[Cm(EDTA)]^+ + OH^- \leftrightarrow Ca[Cm(OH)(EDTA)](aq)$$

The reaction above assumes that the stoichiometric number of Ca in the original ternary complex is 1. This assumption is based on the unlikely interaction of more than one Ca^{2+} ion with the positively charged species $Ca[Cm(EDTA)]^+$. The existence of these ternary and quaternary complexes is discussed in the literature.[39, 42, 44-48, 90]

4.7 Structural characterization Ca-stabilized ternary and quaternary complexes

The structural investigations of the ternary Ca-Am(III)-EDTA as well as the possible quaternary Ca-Am(III)-OH-EDTA species are performed by EXAFS spectroscopy. This is studied at two different pH_m values (pH_m = 8.7 and 11.2) as a function of the ionic strength of $CaCl_2$ ($I_m(CaCl_2)$ = 0.1 m, 1.02 m and 5.36 m). Figure 53 and 54 show the k^2-weighted EXAFS $\chi(k)$ functions and the corresponding Fourier-transformed spectra. In addition, one sample per series is measured and displayed without Ca and absence of $CaCl_2$ as background electrolyte.

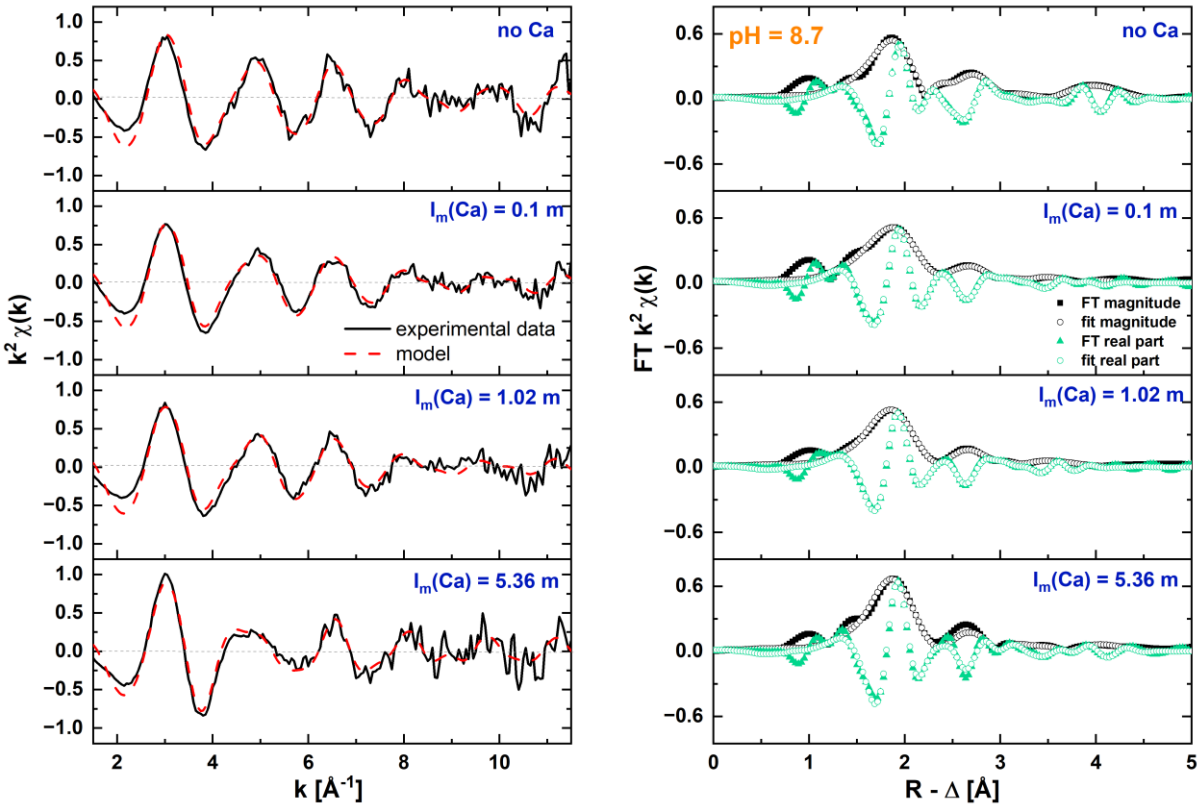

Figure 53: EXAFS measurements of the Am L_{III}-edge for aqueous samples in presence of [EDTA] = 10^{-2} M at pH_m = 8.7. The ionic strength is varied from 0.1 m, 1.02 m to 5.36 m using $CaCl_2$. Additionally, one sample without Ca (top) is displayed. Left: k^2-weighted EXAFS $\chi(k)$ functions (Black line) and the model (red dots). Right: Fourier-transformed spectra, FT magnitude (filled black dots), fit magnitude (open black dots), FT real part (green filled triangle) and fit real part (open green dots).

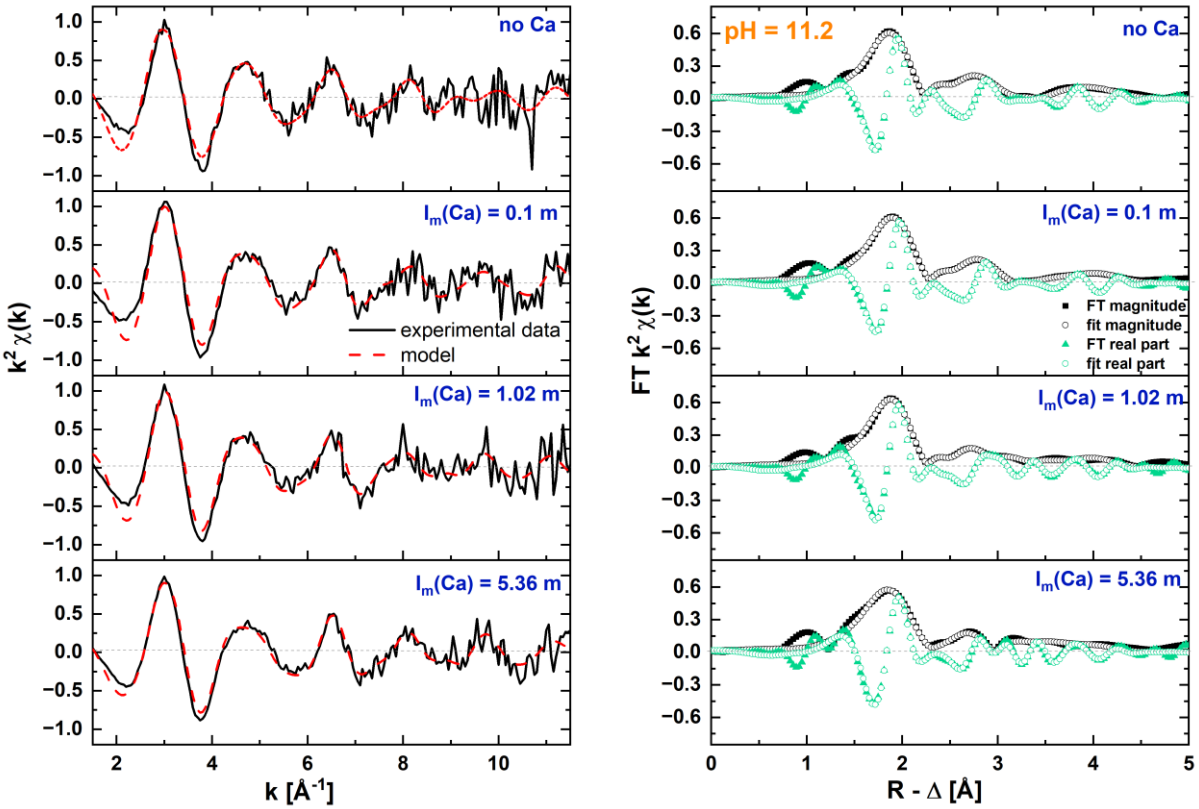

Figure 54: EXAFS measurements of the Am L_{III}-edge for aqueous samples in presence of [EDTA] = 10^{-2} M at pH_m = 11.2. The ionic strength is varied from 0.1 m, 1.02 m to 5.36 m using $CaCl_2$. Additionally, one sample without Ca (top) is displayed. Left: k^2-weighted EXAFS χ(k) functions (Black line) and the model (red dots). Right: Fourier-transformed spectra, FT magnitude (filled black dots), fit magnitude (open black dots), FT real part (green filled triangle) and fit real part (open green dots).

In general, there is no significant effect of increasing ionic strength for either series. The spectra are similar in phase and amplitude, indicating comparable bond distances. Five coordination shells are visible for all samples, which are shown in Figure 55: (i) The interatomic distance R between Am(III) and the four oxygen atoms from the COOH functional group of EDTA and two H_2O or OH ligands (Am-O); (ii) the distance between Am(III) and the nitrogen atoms of the EDTA molecule (Am-N_{EDTA}); (iii) interatomic distances between Am(III) and the carbon atoms of the COOH functional group of EDTA (Am-C_{COOH}); (iv) the distance between Am(III) and the inner carbon atoms of EDTA (Am-C_{EDTA}); (v) the interatomic distance between Am(III) and Ca (Am-Ca).

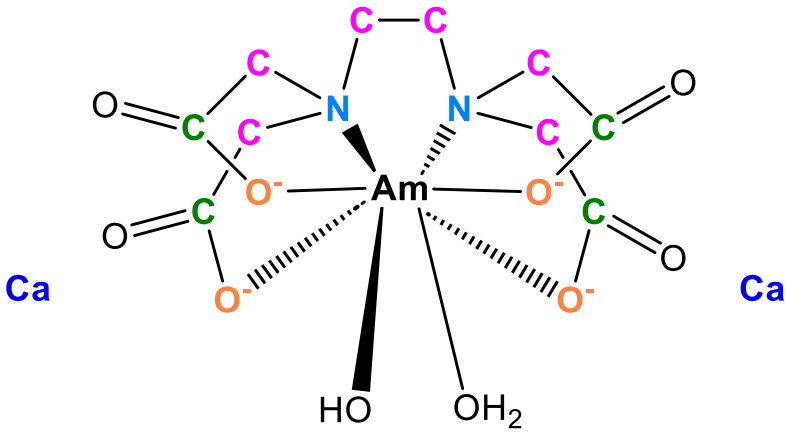

Figure 55: The EDTA molecule coordinated to the metal Am(III) center. In the EXAFS measurements, five different coordination shells are observed: (i) Am-O (orange); (ii) Am-C_{COOH} (green); (iii) Am-C_{EDTA} (pink); (iv) Am-N_{EDTA} (light blue) and (v) Am-Ca (dark blue). The complex illustrated here is adapted from DiBlasi *et al.*.[39]

The individual distances between the atoms and other important parameters, *e.g.,* the Debye-Waller factor (σ^2). The coordination numbers for the different shells *i* are given by N_i. ΔE_0 shows the change of photoelectron energy. Further the different [Ca] are shown for both series. All parameters are calculated based on the feffit code (v2.98) and listed in Table 21.

Table 21: Structural parameters after treatment of the EXAFS spectra: R represent the distance between two atoms, σ^2 is the Debye-Waller factor and N_i are the coordination numbers for the different shells. They are observed by fitting with the feffit code (v2.98). The data refer to the systems measured at pH_m = 8.7 (*blue*) and pH_m = 11.2 (*brown*). The data valid for both pH_m values is marked in black.

I_m(Ca)	shell	N_i	R	R	σ^2	σ^2	ΔE_0	ΔE_0
m	**-**	**-**	***Å***	***Å***	***Å***	***Å²***	***eV***	***eV***
No Ca	Am-O	6	**2.44±0.02**	**2.46±0.01**	**1**	**1**	**3.9**	**3.9**
	Am-C_{COOH}	4	**3.30±0.01**	**3.37±0.02**				
	Am-C_{EDTA}	6	**3.45±0.01**	**3.49±0.01**				
	Am-N_{EDTA}	2	**2.69±0.01**	**2.69±0.02**				
0.1	Am-O	6	**2.44±0.02**	**2.46±0.02**	**0.94**	**1**	**4.7**	**2.7**
	Am-C_{COOH}	4	**3.32±0.01**	**3.37±0.03**				
	Am-C_{EDTA}	6	**3.50±0.01**	**3.49±0.02**				
	Am-N_{EDTA}	2	**2.45±0.09**	**2.69±0.04**				
	Am-Ca	**1-2/2**	**4.19±0.01**	**4.05±0.03**				
1.02	Am-O	6	**2.41±0.02**	**2.46±0.02**	**0.83**	**1**	**3.5**	**2.5**
	Am-C_{COOH}	4	**3.32±0.01**	**3.34±0.03**				
	Am-C_{EDTA}	6	**3.49±0.01**	**3.52±0.02**				
	Am-N_{EDTA}	2	**2.60±0.09**	**2.68±0.04**				
	Am-Ca	**1-2/2**	**4.17±0.01**	**4.01±0.03**				
5.05	Am-O	6	**2.41±0.02**	**2.43±0.02**	**0.83**	**1**	**3.3**	**5.3**
	Am-C_{COOH}	4	**3.33±0.01**	**3.31±0.03**				
	Am-C_{EDTA}	6	**3.51±0.01**	**3.53±0.02**				
	Am-N_{EDTA}	2	**2.61±0.09**	**2.62±0.04**				
	Am-Ca	**1-2/2**	**4.19±0.01**	**4.00±0.03**				

In addition, the present structure patterns are in good agreement to the quantum chemical calculated, optimized structures by DiBlasi *et al.* such as $[(Pu(EDTA)(H2O)_2)Ca(H_2O)_4]^+$, $[(Pu(OH)_2(EDTA))Ca_3(H_2O)_{12}]^{3+}$ and

$[(Pu(OH)(EDTA)H_2O)Ca_2(H_2O)_8]^{2+}$, which are illustrated in Figure 56.[39] This comparison can be made because Pu(III) and Am(III) are considered chemically analogous (see section 1.2).

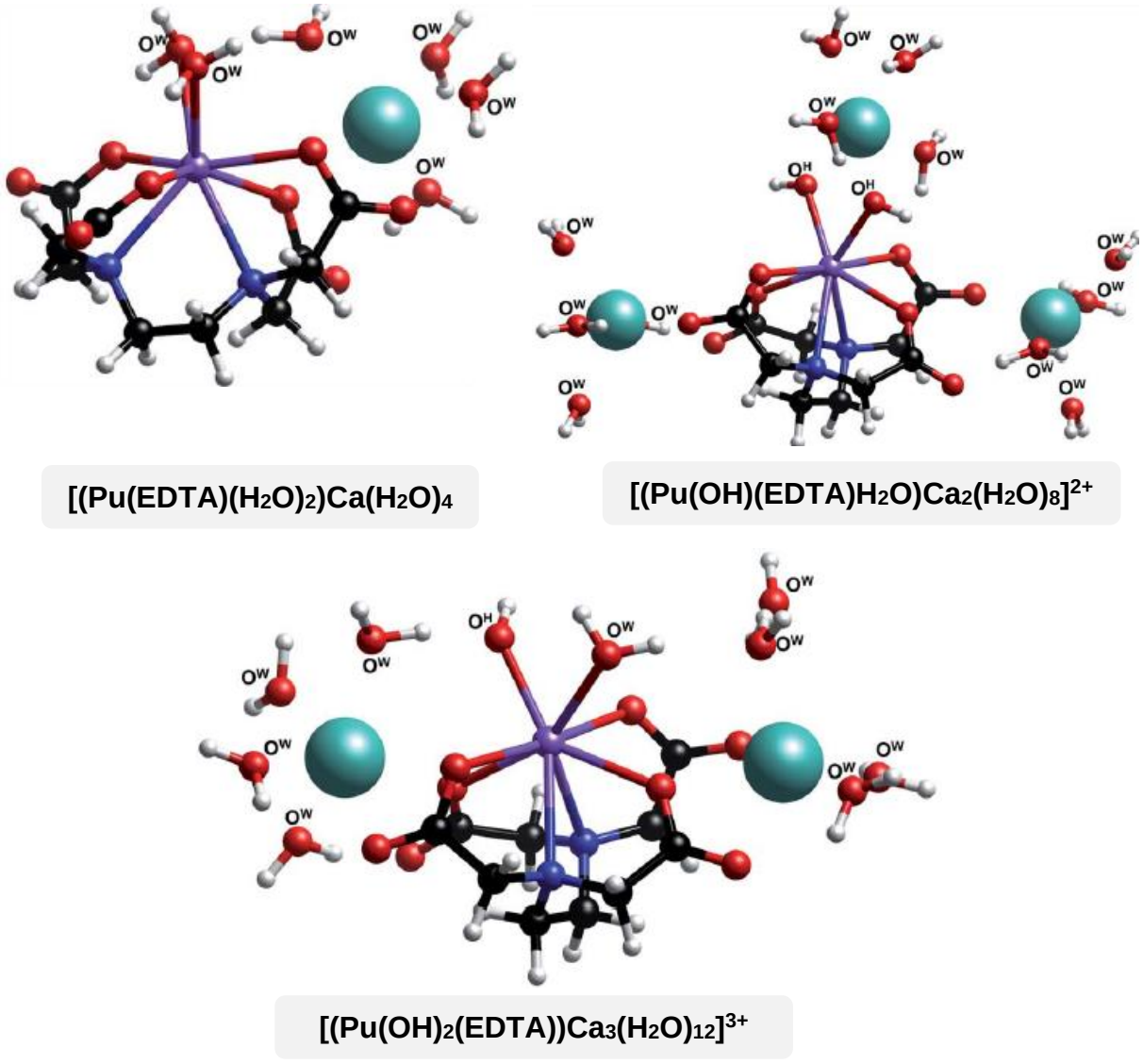

Figure 56: The quantum chemical calculated, optimized structures for quaternary $[(Pu(EDTA)(H2O)_2)Ca(H_2O)_4]^+$, $[(Pu(OH)_2(EDTA))Ca_3(H_2O)_{12}]^{3+}$ and $[(Pu(OH)(EDTA)H_2O)Ca_2(H_2O)_8]^{2+}$ species postulated by DiBlasi *et al.*.[39]

The interatomic distance between Am(III) and the oxygen atoms is determined to be 2.41±0.02 to 2.46±0.02. It is assumed that four oxygen atoms are supplied by EDTA. The other two oxygen atoms probably originate from the coordination of Am(III) with

H_2O (pH = 8.7) and H_2O/OH^- (pH = 11.2) ligands. These values are in good agreement with the Pu-O_{EDTA} distances ranging from 2.47 - 2.52 obtained by DiBlasi *et al.*.[39] They are also comparable to the Eu-O distance, reported by Thakur *et al.*.[37]

The coordination between Am(III) and the four carbon atoms of the EDTA carboxyl groups (Am-C_{COOH}) reveals distances of 3.30±0.01 to 3.37±0.03. This observation is consistent with the data reported by Thakur *et al*..[37] The distances between Am(III) and the inner carbon atoms of the EDTA molecule (Am-C_{EDTA}) are slightly larger, measuring 3.45±0.01 to 3.52±0.02.

The Am-N distance (Am-N_{EDTA}) is described as 2.60±0.09 - 2.69±0.04. However, an exception is noted in the sample with I_m = 0.1 m in the series with pH_m = 8.7, where the distance between Am and N is significantly reduced to 2.45±0.09 Å. The reason for this deviation cannot be explained at the moment. DiBlasi *et al.* observed an increase of the Am-N distance up to ~ 2.90 Å for the quaternary complex $[(Pu(OH)_{2(}EDTA))Ca_3(H_2O)_{12}]^{3+}$. For $[(Pu(EDTA)(H_2O)_2)Ca(H_2O)_4]^+$ the distance between Am-N ~ 2.72 Å is obtained, while for $[(Pu(OH)(EDTA)H_2O)Ca_2(H_2O)_8]^{2+}$, Am-N ~ 2.87 Å is found.[39] In the context of this work, the complexes $[(Pu(EDTA)(H_2O)_2)Ca(H_2O)_4]^+$ and $[(Pu(OH)(EDTA)H_2O)Ca_2(H_2O)_8]^{2+}$ agree best with the experimental data.

The largest deviation between the two series is observed for the Am-Ca distance (Am-Ca): A distance of 4.19±0.01 Å is obtained at pH_m = 8.7, while ~ 4.00±0.03 Å are observed at pH_m = 11.2. With increasing pH, more Ca^{2+} ions are associated with the complex. In addition, the distance to the central ion decreases. Both are most likely a consequence of the deprotonation of an H_2O molecule in the coordination sphere of the Am(III) central ion and the resulting increase in the negative charge of the complex. This difference is significant and could possibly indicate two different species.

In summary, the obtained spectra confirm the composition of the complex as interpreted from the TRLFS experiments and the pH dependence of the spectra (see section 4.6): The present species comprise one EDTA molecule. The complex at

pH_m = 8.7 shows the presence of one or two Ca atoms, while the species at pH_m = 11.2 clearly shows the presence of two Ca atoms.

As previously mentioned, a particularly good agreement of the present results is obtained with the three quaternary complexes: $[(Pu(EDTA)(H2O)_2)Ca(H_2O)_4]^+$, $[(Pu(OH)(EDTA)H_2O)Ca_2(H_2O)_8]^{2+}$ and $[Pu(OH)_2(EDTA))Ca_3(H_2O)_{12}]^{3+}$.[39] All three species show a rather similar structure: The Pu metal center is 8-fold coordinated. EDTA occupies 6 of the coordination sites through four Pu-O and two Pu-N bonds. For the remaining two coordination sites, the binding of OH or H_2O is postulated. The number of OH groups is related to the number of Ca atoms: The more OH groups there are, the more Ca atoms are needed to stabilize the complex. It is suggested that the Ca ions are associated with the O atom of the carboxyl groups in the outer coordination sphere of the Am(III) ion.

From the TRLFS results (see section 4.6) it was shown, that at pH_m = 8.7, the ternary Ca-Cm(III)-EDTA species is exclusively present. At pH_m = 11.2, there is a mixture of both Ca-Cm(III)-EDTA and Ca-Cm(III)-OH-EDTA species expected, along with a minor contribution of $Cm(OH)(EDTA)^{2-}$. This observation could explain the detected differences in Am-Ca distances. Compared to the complexes postulated by DiBlasi *et al.*, the structure at pH_m = 11.2 would be most similar to the $[(Pu(OH)(EDTA)H_2O)Ca_2(H_2O)_8]^{2+}$ complex, including one EDTA molecule and two Ca atoms.[39] The structure for the species at pH_m = 8.7, can be either referred to $[(Pu(EDTA)(H_2O)_2)Ca(H_2O)_4]^+$ or $[(Pu(OH)(EDTA)H_2O)Ca_2(H_2O)_8]^{2+}$ as it shows one or two Ca atoms. Unfortunately, the complexity of this system does not allow a clear determination of structures based on the current data set.

.

5 Conclusion and Outlook

This thesis was divided into two parts: In the first part, the impact of oxalate and EDTA on the retention of trivalent *An*(III)/*Ln*(III) on C-S-H phases at different ionic strength conditions was investigated. These studies were performed by batch sorption and TRLFS experiments. The high salt contents investigated in this work aim at reflecting saline pore waters to occur in northern German clay formations.

In the second part of this work, the examination of the Eu(III) and Cm(III) speciation and the structural characterization of ternary Ca-*An*(III)-EDTA and possibly quaternary Ca-*An*(III)-OH-EDTA complexes were emphasized. Experimental analyses were carried out utilizing TRLFS and EXAFS.

Part 1: *The investigation of the effect of oxalate and EDTA on the retention of Ln(III)/An(III) on C-S-H phases and bentonite MX80 at high ionic strength under variation of different experimental parameters.*

Generally the Eu(III) uptake on C-S-H phases in presence of oxalate was very strong and almost quantitatively, comparable to oxalate-free systems. In addition, it was independent from ionic strength, sorption time and C/S ratio. The presence of Ca led to the near-complete precipitation of Ca(Ox)(s), effectively extracting oxalate from the aqueous phase. The source of Ca was provided by either the C-S-H phase or from the $CaCl_2$ electrolyte solution.

Hence, the primary focus was directed towards the impact of EDTA on Eu(III) sorption. Near quantitative retention was also observed at [EDTA] ≤ 10^{-3} M, being independent of the ionic strength, C/S ratio and sorption time. This is similar to the sorption of Eu(III)/Cm(III) on C-S-H phases in the absence of EDTA under the conditions investigated. It can be concluded that EDTA at low concentrations of ≤ 10^{-3} M has no impact on the retention of Eu(III)/Cm(III) on C-S-H phases over the investigated time period of 365 d. The strong retention is due to an incorporation of Eu(III) into the C-S-H phase.

At [EDTA] = 10^{-2} M, a noteworthy decrease of sorption could be observed. In both NaCl and $CaCl_2$ solutions, log R_d = 1 - 2 were observed after 7 d. In cases of low Ca contents

(C/S ≤ 1.0), there was a subsequent increase in retention detected after 30 d. The observed reduced retention after 7 d is attributed to the formation of two ternary hydrolysis species, $Eu(OH)(EDTA)^{2-}$ and $Eu(OH)_x(EDTA)^{-(x+1)}$, which stabilize Eu(III) in the solution. In general, the increasing retention after longer contact times could be explained by a slow dissociation of Eu(III) from the Eu(III)-Ca-EDTA complex depending on the reaction time or a slow incorporation of Eu(III) into the solid phase. The complete elucidation of the slow kinetics has not yet been achieved.

If sufficient Ca is available [Ca] > $8.0 \cdot 10^{-3}$ M (NaCl solution, C/S ~ 1.3 or in $CaCl_2$ solution), the retention remains low even after longer contact times of 50 d. This is due to the formation of very stable ternary Ca-Eu/Cm(III)-EDTA complexes, where EDTA effectively stabilizes Eu(III) and Cm(III) in solution and suppresses their incorporation into the C-S-H phase. Additionally, the formation of a quaternary Ca-Cm(III)-OH-EDTA species at high pH_m is indicated. In general, no significant effect of the ionic strength could be observed either in NaCl or in $CaCl_2$ solution.

In addition, experiments on the order of addition of the organic ligand and Eu(III) were carried out, since previous experiments with other systems (*e.g*. ISA) had shown significant differences of this on the log R_d value. In the C-S-H-EDTA-Eu(III) system, the order of addition has no significant impact on the Eu(III) retention on C-S-H phases. It follows, that the dissociation kinetics of the Eu(III)-EDTA complexes are relatively fast, in contrast to analogous experiments with ISA.

Moreover, sorption studies were conducted at a higher solid-to-liquid ratio (S/V = 20 g/L). At this elevated S/V, an almost quantitative retention of Eu(III) is observed at all investigated [EDTA]. This is in contrast to the results obtained with S/V = 1 g/L at [EDTA] = 10^{-2} M. A definite explanation for the high retention of Eu(III) at high EDTA concentrations and S/V = 20 g/L cannot be given at the current state of knowledge. However, it can be speculated that the high retention is due to the adsorption of Eu(III) on- or in the C-S-H phase, which is further enhanced by the complexation of Eu with EDTA adsorbed on the surface.

Part 2: *The examination of the Eu(III) and Cm(III) speciation and structural characterization of ternary and quaternary Ca-stabilized Cm(III)-EDTA complexes in aqueous media.*

At the present state of the art, the lack of thermodynamic data poses a challenge for assessing the impact of ternary Ca-Cm(III)-EDTA or quaternary Ca-Cm(III)-(OH)-EDTA species under given conditions in a repository. Due to the high stability of the binary complex $Ca(EDTA)^{2-}$ (see chapter 1.3, Table 1, Figure 8), thermodynamic calculations using currently available thermodynamic data predict a negligible effect of EDTA on the strong retention of RN in cement systems due to the overwhelming competition of Ca for the complexation with EDTA. Sorption experiments conducted in Part 1 of this PhD thesis, evidence that the outcome of these calculations cannot explain experimental observations. The TRLFS data suggest the formation of ternary Ca-Cm(III)-EDTA complexes in solution in the pH range between 8.5 – 11. Between pH_m = 11 – 11.5, the contribution of the quaternary Ca-Cm(III)-OH-EDTA species increases with increasing Ca content. At pH ≥ 12, the quaternary species is predominant. The ternary $Cm(OH)(EDTA)^{2-}$ shows only a small contribution over the whole pH range. In a preliminary exercise conditional constants were estimated for the formation of quaternary species from the ternary species: Log β' (I_m = 2.09 m) = 4.54±0.32 and log β' (I_m = 0.51 m) = 3.15±0.18.

EXAFS supports the nature of Am(III) complexes interpreted from the Cm(III)-TRLFS study. At pH_m = 11.2, the quaternary Ca(II)-Am(III)-OH-EDTA species prevails with a structure similar to those of the previously studied $[(Pu(OH)(EDTA)H_2O)Ca_2(H_2O)_8]^{2+}$ complex. For the Am(III) species detected at pH_m = 8.7, the structure again is similar to that of the earlier investigated $[(Pu(EDTA)(H_2O)_2)Ca(H_2O)_4]^{+}$. Both, the Am(III) and Pu(III) centers are 8-fold coordinated. EDTA occupies 6 of the possible coordination sites through M-N and M-O bonds (M = Am(III)). The remaining coordination sites are probably occupied by OH or H_2O ligands. The Ca atoms are located in the outer coordination sphere of Am(III), and are associated with the non-chelating O atoms of the carboxyl groups.

The observations of this study provide detailed insight into the sorption of Cm(III) and Eu(III) on C-S-H phases in the presence of the organic ligands oxalate and EDTA. The

nature of the ternary and quaternary complexes has been characterized consistently by spectroscopic methods. The presence of Ca plays a critical role for the formation of EDTA complexes and thus for the retention of the trivalent actinides.

Apparently increased ionic strength conditions, as *e.g.,* such as those found in some northern German clay formations, do not significantly affect the retention of trivalent *Ln/An*.

6 References

1. IAEA, Classification of radioactive waste: Genaral Safety Guide GSG-1, Vienna, **2009**.
2. Hoth, P.; Wirth, H.; Reinhold, K.; Bräuer, V.; Krull, P.; Feldrappe, H., Endlagerung radioaktiver Abfälle in tiefen geologischen Formationen Deutschlands–Untersuchung und Bewertung von Tongesteinsformationen. *BGR Bundesanstalt für Geowissenschaften und Rohstoffe, Hannover/Germany,* **2007**.
3. Johansson, C. *Management of low and intermediate level waste in Sweden. Experiences and future plans*; **2002**.
4. Profile, B. *Radioactive Waste Management Programs in OECD/NEA Member Countries*; Tech. rep., Nuclear Energy Agency, **2013**.
5. Bundestag, D., „Standortauswahlgesetz vom 5. Mai 2017 (BGBl. I S. 1074), das zuletzt durch Artikel 2 Absatz 16 des Gesetzes vom 20. Juli 2017 (BGBl I S. 2808) geändert worden ist,“. *Bundesgesetzblatt Jahrgang 2017 Teil I Nr* **2017,** *26*, 1074-1102.
6. Gompper, K.; Geist, A.; Geckeis, H., Actinoidenabtrennung aus hochradioaktiven Abfällen. *Nachrichten aus der Chemie* **2010,** *58* (10), 1015-1019.
7. BGE *Zwischenbericht Teilgebiete gemäß § 13 StandAG*; 28.09.**2020**.
8. Pescatore, C. *Safety, safety case and society-Lessons from the experience of the Forum on Stakeholder Confidence and other NEA initiatives*; **2014**.
9. Brasser, T.; Droste, J.; Müller-Lyda, I.; Neles, J.; Sailer, M.; Schmidt, G.; Steinhoff, M., Endlagerung wärmeentwickelnder radioaktiver Abfälle in Deutschland. *GRS report, GRS-247, Gesellschaft für Anlagen-und Reaktorsicherheit* **2008**.
10. Tits, J.; Wieland, E., Actinide Sorption by Cementitious Materials. PSI Bericht Nr. 18-02. **2018**. *Paul Scherer Institute, CH-5232 Villingen, PSI, Switzerland.*
11. Wieland, E. *Sorption data base for the cementitious near-field of L/ILW and ILW repositories for provisional safety analyses for SGT-E2*; PSI Bericht Nr. 14-08. **2014**. *Paul Scherer Institute, CH-5232 Villingen, PSI, Switzerland.*
12. Emmerich, K.; Wolters, F.; Kahr, G.; Lagaly, G., Clay profiling: the classification of montmorillonites. *Clays and clay minerals* **2009,** *57* (1), 104-114.
13. BGE Endlager Konrad, https://www.bge.de/de/konrad/. (accessed 07.03.2024)

14. Brewitz, W., *Ablauf und Ergebnisse der Eignungsuntersuchung der Schachtanlage Konrad für die Endlagerung radioaktiver Abfälle: Zusammenfassung*. Gesellschaft für Strahlen-und Umweltforschung: **1982**.

15. Hummel, W.; Anderegg, G.; Puigdomènech, I.; Rao, L.; Tochiyama, O., The OECD/NEA TDB review of selected organic ligands. *Radiochimica acta* **2005,** *93* (11), 719-725.

16. Lersow, M.; Waggitt, P., *Disposal of all forms of radioactive waste and residues*. Book. Springer: **2020**.

17. Kursten, B.; Druyts, F.; Macdonald, D.; Smart, N.; Gens, R.; Wang, L.; Weetjens, E.; Govaerts, J., Review of corrosion studies of metallic barrier in geological disposal conditions with respect to Belgian Supercontainer concept. *Corrosion Engineering, Science and Technology* **2011,** *46* (2), 91-97.

18. Rübel, A. P.; Müller-Lyda, I.; Storck, R., *Die Klassifizierung radioaktiver Abfälle hinsichtlich der Endlagerung*. GRS: **2004**.

19. Osterhage, W.; Frey, H., Organisation der nuklearen Entsorgung. In *Transformation radioaktiver Abfälle: Von der Zwischenlagerung über die Endlagerung bis zur Transmutation*, Springer: **2022**; pp 141-147.

20. Crowder, M.; Pierce, R.; Scogin, J.; Daniel, W.; King, W., Small-scale testing of plutonium (IV) oxalate precipitation and calcination to plutonium oxide to support the MOX feed mission. *Savannah River National Laboratory: Aiken, SC* **2012**.

21. Choppin, G. R., Solution chemistry of the actinides. *Radiochimica acta* **1983,** *32* (1-3), 43-54.

22. Geckeis, H.; Röhlig, K. J.; Mengel, K., Endlagerung radioaktiver Abfälle. *Chemie in unserer Zeit* **2012,** *5* (46), 282-293.

23. Häußler, V.; Amayri, S.; Beck, A.; Platte, T.; Stern, T. A.; Vitova, T.; Reich, T., Uptake of actinides by calcium silicate hydrate (CSH) phases. *Applied Geochemistry* **2018,** *98*, 426-434.

24. Holleman, A. F., *Lehrbuch der anorganischen Chemie (102)*. Walter de Gruyter GmbH & Co KG: **2019**.

25. Huheey, J. E., *Anorganische Chemie, Prinzipien von Struktur und Reaktivität (3)*. Walter de Gruyter GmbH & Co KG: **2020.**

26. Keller, C., Radiochemie (1), Diesterweg **1981**.

27. Crosswhite, H.; Crosswhite, H.; Carnall, W.; Paszek, A., Spectrum analysis of U3+: LaCl3. *The Journal of Chemical Physics* **1980,** *72* (9), 5103-5117.

28. Altmaier, M.; Gaona, X.; Fanghänel, T., Recent advances in aqueous actinide chemistry and thermodynamics. *Chemical reviews* **2013,** *113* (2), 901-943.

29. Silva, R.; Nitsche, H., Actinide environmental chemistry. *Radiochimca Acta* **1995,** *70* (Supplement), 377-396.

30. Choppin, G. R., Comparative solution chemistry of the 4f and 5f elements. *Journal of alloys and compounds* **1995,** *223* (2), 174-179.

31. Shamov, G. A.; Schreckenbach, G., Density functional studies of actinyl aquo complexes studied using small-core effective core potentials and a scalar four-component relativistic method. *The Journal of Physical Chemistry A* **2005,** *109* (48), 10961-10974.

32. Choppin, G. R.; Rizkalla, E. N., Solution chemistry of actinides and lanthanides. *Handbook on the physics and chemistry of rare earths* **1994,** *18*, 559-590.

33. Hixon, A. E.; Powell, B. A., Plutonium environmental chemistry: mechanisms for the surface-mediated reduction of Pu (v/vi). *Environmental Science: Processes & Impacts* **2018,** *20* (10), 1306-1322.

34. Pearson, R. G., Hard and soft acids and bases. *Journal of the American Chemical society* **1963,** *85* (22), 3533-3539.

35. Zhang, F.; Ma, J.; Cao, Y., Phosphorus deficiency enhances root exudation of low-molecular weight organic acids and utilization of sparingly soluble inorganic phosphates by radish (Raghanus satiuvs L.) and rape (Brassica napus L.) plants. *Plant and soil* **1997,** *196*, 261-264.

36. Colàs, E.; Grivé, M.; Rojo, I.; Duro, L., The effect of gluconate and EDTA on thorium solubility under simulated cement porewater conditions. *Journal of Solution Chemistry* **2013,** *42* (8), 1680-1690.

37. Thakur, P.; Conca, J.; Choppin, G., Mixed Ligand Complexes of Am^{3+}, Cm^{3+} and Eu^{3+} with HEDTA and $HEDTA^{+}$ NTA-Complexation Thermodynamics and Structural Aspects. *Journal of solution chemistry* **2012,** *41*, 599-615.

38. Lothenbach, B.; Nonat, A., Calcium silicate hydrates: Solid and liquid phase composition. *Cement and Concrete Research* **2015,** *78*, 57-70.

39. DiBlasi, N. A.; Tasi, A. G.; Trumm, M.; Schnurr, A.; Gaona, X.; Fellhauer, D.; Dardenne, K.; Rothe, J.; Reed, D. T.; Hixon, A. E., Pu (iii) and Cm (iii) in the presence of EDTA: aqueous speciation, redox behavior, and the impact of Ca (ii). *RSC advances* **2022,** *12* (15), 9478-9493.

40. Mathur, J.; Thakur, P.; Dodge, C.; Francis, A.; Choppin, G., Coordination modes in the formation of the ternary Am (III), Cm (III), and Eu (III) complexes with EDTA and NTA: TRLFS, 13C NMR, EXAFS, and thermodynamics of the complexation. *Inorganic chemistry* **2006,** *45* (20), 8026-8035.

41. Thakur, P.; Pathak, P.; Gedris, T.; Choppin, G., Complexation of Eu (III), Am (III) and Cm (III) with dicarboxylates: thermodynamics and structural aspects of the binary and ternary complexes. *Journal of solution chemistry* **2009,** *38*, 265-287.

42. Griffiths, T. L.; Martin, L. R.; Zalupski, P. R.; Rawcliffe, J.; Sarsfield, M. J.; Evans, N. D.; Sharrad, C. A., Understanding the Solution Behavior of Minor Actinides in the Presence of $EDTA^{4-}$, Carbonate, and Hydroxide Ligands. *Inorganic Chemistry* **2013,** *52* (7), 3728-3737.

43. Giffaut, E.; Grivé, M.; Blanc, P.; Vieillard, P.; Colàs, E.; Gailhanou, H.; Gaboreau, S.; Marty, N.; Made, B.; Duro, L., Andra thermodynamic database for performance assessment: ThermoChimie. *Applied Geochemistry* **2014,** *49*, 225-236.

44. Chopping, G.; Liu, Q.; Sullivan, J., Calorimetric studies of curium complexation. *Inorganic Chemistry* **1985,** *24* (23), 3968-3969.

45. Thakur, P.; Conca, J.; Van De Burgt, L.; Choppin, G., Complexation and the laser luminescence studies of Eu (III), Am (III), and Cm (III) with EDTA, CDTA, and PDTA and their ternary complexation with dicarboxylates. *Journal of Coordination Chemistry* **2009,** *62* (23), 3719-3737.

46. Felmy, A. R.; Wang, Z.; Dixon, D. A.; Joly, A. G.; Rustad, J. R.; Mason, M. J., The aqueous complexation of Eu (III) with organic chelates at high-base concentration: Molecular and thermodynamic modeling results. ACS Publications: 2001.

47. Roughley, G., *Lanthanide ternary complexes relevant to the nuclear fuel cycle*. Diss., The University of Manchester (United Kingdom): **2012**.

48. Shalinets, A., Investigation of the complex formation of trivalent actinide and lanthanide elements by the method of electromigration. XV.

Ethylenediaminetetramethylphosphonic acid. *Sov. Radiochem.(Engl. Transl.) 14: No. 2, 279-284 (1972).* **1972**.

49. Haken, H.; Wolf, H. C., *Molekülphysik und Quantenchemie (3): Einführung in die experimentellen und theoretischen Grundlagen*. Springer-Verlag: **2003**.

50. Atkins, P. W.; De Paula, J., *Physikalische chemie (5)*. John Wiley & Sons: 2013.

51. Collins, R. N.; Saito, T.; Aoyagi, N.; Payne, T. E.; Kimura, T.; Waite, T. D., Applications of time-resolved laser fluorescence spectroscopy to the environmental biogeochemistry of actinides. *Journal of environmental quality* **2011,** *40* (3), 731-741.

52. Edelstein, N. M.; Klenze, R.; Fanghänel, T.; Hubert, S., Optical properties of Cm (III) in crystals and solutions and their application to Cm (III) speciation. *Coordination Chemistry Reviews* **2006,** *250* (7-8), 948-973.

53. Carnall, W.; Rajnak, K., Electronic energy level and intensity correlations in the spectra of the trivalent actinide aquo ions. II. Cm^{3+}. *The Journal of Chemical Physics* **1975,** *63* (8), 3510-3514.

54. Carnall, W. T., A systematic analysis of the spectra of trivalent actinide chlorides in D 3 h site symmetry. *The Journal of chemical physics* **1992,** *96* (12), 8713-8726.

55. Heller, A., Formation of Hot OH Bonds in the radiationless relaxations of excited rare earth ions in aqueous solutions. *Journal of the American Chemical Society* **1966,** *88* (9), 2058-2059.

56. Kimura, T.; Choppin, G. R., Luminescence study on determination of the hydration number of Cm (III). *Journal of Alloys and Compounds* **1994,** *213*, 313-317.

57. Lothenbach, B.; Wieland, E., A thermodynamic approach to the hydration of sulphate-resisting Portland cement. *Waste Management* **2006,** *26* (7), 706-719.

58. Ochs, M.; Mallants, D.; Wang, L., *Radionuclide and metal sorption on cement and concrete*. Springer: **2016**; Vol. 2.

59. Taylor, H. F., Cement Chemistry Academic Press. *London, England* **1990**, 5-22.

60. Li, K.; Pang, X., Sorption of radionuclides by cement-based barrier materials. *Cement and concrete research* **2014,** *65*, 52-57.

61. Jacques, D.; Wang, L.; Martens, E.; Mallants, D., Modelling chemical degradation of concrete during leaching with rain and soil water types. *Cement and Concrete Research* **2010,** *40* (8), 1306-1313.

62. Tits, J.; Gaona, X.; Laube, A.; Wieland, E., Influence of the redox state on the neptunium sorption under alkaline conditions: Batch sorption studies on titanium dioxide and calcium silicate hydrates. *Radiochimica Acta* **2014,** *102* (5), 385-400.

63. Richardson, I. G., The calcium silicate hydrates. *Cement and concrete research* **2008,** *38* (2), 137-158.

64. Nonat, A., The structure and stoichiometry of CSH. *Cement and concrete research* **2004,** *34* (9), 1521-1528.

65. Yan, Y.; Yang, S.-Y.; Miron, G. D.; Collings, I. E.; L'Hôpital, E.; Skibsted, J.; Winnefeld, F.; Scrivener, K.; Lothenbach, B., Effect of alkali hydroxide on calcium silicate hydrate (CSH). *Cement and Concrete Research* **2022,** *151*, 106636.

66. Iwaida, T.; Nagasaki, S.; Tanaka, S., Sorption study of strontium onto hydrated cement phases using a sequential desorption method. *Radiochimica Acta* **2000,** *88* (8), 483-487.

67. Iler, R. K., The chemistry of silica, Solubility, Polymerization. *Colloid and Surface Properties, and Biochemistry* **1979,** *866*.

68. Bach, T.; Chabas, E.; Pochard, I.; Coumes, C. C. D.; Haas, J.; Frizon, F.; Nonat, A., Retention of alkali ions by hydrated low-pH cements: Mechanism and Na^+/K^+ selectivity. *Cement and Concrete Research* **2013,** *51*, 14-21.

69. Hong, S.-Y.; Glasser, F., Alkali binding in cement pastes: Part I. The CSH phase. *Cement and Concrete Research* **1999,** *29* (12), 1893-1903.

70. Plusquellec, G.; Nonat, A., Interactions between calcium silicate hydrate (CSH) and calcium chloride, bromide and nitrate. *Cement and Concrete Research* **2016,** *90*, 89-96.

71. Häusler, F., CSH-Phasenbildung und Löslichkeitsverhalten vor dem Hintergrund der Anwendung von Zement in Endlagerkonzepten für radioaktive Abfälle, Diss. Technische Universität Bergakademie Freiberg. 2013.

72. Bernard, E.; Lothenbach, B.; Le Goff, F.; Pochard, I.; Dauzères, A., Effect of magnesium on calcium silicate hydrate (CSH). *Cement and Concrete Research* **2017,** *97*, 61-72.

73. Steefel, C.; Rutqvist, J.; Tsang, C.-F.; Liu, H.-H.; Sonnenthal, E.; Houseworth, J.; Birkholzer, J. *Reactive transport and coupled THM processes in engineering barrier systems (EBS)*; Ernest Orlando Lawrence Berkeley National Laboratory: **2010**.

74. Delavernhe, L.; Steudel, A.; Darbha, G.; Schäfer, T.; Schuhmann, R.; Wöll, C.; Geckeis, H.; Emmerich, K., Influence of mineralogical and morphological properties on the cation exchange behavior of dioctahedral smectites. *Colloids and Surfaces A: Physicochemical and Engineering Aspects* **2015,** *481*, 591-599.

75. Wang, X.; Chen, C.; Zhou, X.; Tan, X.; Hu, W., Diffusion and sorption of U (VI) in compacted bentonite studied by a capillary method. *Radiochimica Acta* **2005,** *93* (5), 273-278.

76. Wang, X.; Sun, Y.; Alsaedi, A.; Hayat, T.; Wang, X., Interaction mechanism of Eu (III) with MX-80 bentonite studied by batch, TRLFS and kinetic desorption techniques. *Chemical Engineering Journal* **2015,** *264*, 570-576.

77. Ghadiri, M.; Chrzanowski, W.; Rohanizadeh, R., Biomedical applications of cationic clay minerals. *RSC advances* **2015,** *5* (37), 29467-29481.

78. Grim, R. E., Applied clay mineralogy (84). McGraw-Hill Inc. **1962**.

79. Herbert, H.; Moog, H. C., Untersuchungen zur Quellung von Bentoniten in hochsalinaren Lösungen. *Abschlussbericht GRS-179, Förderkennzeichen* **2002,** *2*.

80. Blume, H.-P.; Brümmer, G. W.; Horn, R.; Kandeler, E.; Kögel-Knabner, I.; Kretzschmar, R.; Stahr, K.; Wilke, B.-M., *Scheffer/schachtschabel: Lehrbuch der bodenkunde*. Springer-Verlag: 2016.

81. Pointeau, I.; Piriou, B.; Fedoroff, M.; Barthes, M.-G.; Marmier, N.; Fromage, F., Sorption mechanisms of Eu3+ on CSH phases of hydrated cements. *Journal of Colloid and Interface Science* **2001,** *236* (2), 252-259.

82. Tits, J.; Wieland, E., Actinide Sorption by Cementitious Materials. **2018,** *PSI-Bericht 18-02. Paul Scherer Institute, CH-5232 Villingen, PSI, Switzerland.*

83. Tits, J.; Stumpf, T.; Rabung, T.; Wieland, E.; Fanghänel, T., Uptake of Cm (III) and Eu (III) by calcium silicate hydrates: a solution chemistry and time-resolved laser fluorescence spectroscopy study. *Environmental science & technology* **2003,** *37* (16), 3568-3573.

84. Schlegel, M. L.; Pointeau, I.; Coreau, N.; Reiller, P., Mechanism of europium retention by calcium silicate hydrates: an EXAFS study. *Environmental science & technology* **2004,** *38* (16), 4423-4431.

85. Macé, N.; Wieland, E.; Dähn, R.; Tits, J.; Scheinost, A. C., EXAFS investigation on U (VI) immobilization in hardened cement paste: Influence of experimental conditions on speciation. *Radiochimica Acta* **2013,** *101* (6), 379-389.

86. Stumpf, T.; Tits, J.; Walther, C.; Wieland, E.; Fanghänel, T., Uptake of trivalent actinides (curium (III)) by hardened cement paste: a time-resolved laser fluorescence spectroscopy study. *Journal of colloid and interface science* **2004,** *276* (1), 118-124.

87. Mandaliev, P.; Stumpf, T.; Tits, J.; Dähn, R.; Walther, C.; Wieland, E., Uptake of Eu (III) by 11 Å tobermorite and xonotlite: a TRLFS and EXAFS study. *Geochimica et Cosmochimica Acta* **2011,** *75* (8), 2017-2029.

88. Guidone, R. E. Impact of formate, citrate and gluconate on the retention behavior of Pu(III/IV), Cm(III) and Eu(III) by cement phases, Diss., Karlsruhe Institute of Technology (KIT), **2023.**

89. Tasi, A.; Gaona, X.; Fellhauer, D.; Böttle, M.; Rothe, J.; Dardenne, K.; Schild, D.; Grivé, M.; Colàs, E.; Bruno, J., Redox behavior and solubility of plutonium under alkaline, reducing conditions. *Radiochimica Acta* **2018,** *106* (4), 259-279.

90. Tasi, A.; Gaona, X.; Fellhauer, D.; Böttle, M.; Rothe, J.; Dardenne, K.; Polly, R.; Grivé, M.; Colas, E.; Bruno, J., Thermodynamic description of the plutonium–α–d–isosaccharinic acid system ii: Formation of quaternary Ca (II)–Pu (IV)–OH–ISA complexes. *Applied Geochemistry* **2018,** *98*, 351-366.

91. Maragkou, E.; Pashalidis, I., Investigations on the interaction of EDTA with calcium silicate hydrate and its impact on the U (VI) sorption. *Coatings* **2021,** *11* (9), 1037.

92. Pointeau, I.; Coreau, N.; Reiller, P. E., Uptake of anionic radionuclides onto degraded cement pastes and competing effect of organic ligands. *Radiochimica Acta* **2008,** *96* (6), 367-374.

93. Szabo, P.; Tasi, A.; Gaona, X.; Maier, A.; Hedström, S.; Altmaier, M.; Geckeis, H., Uptake of selected organic ligands by hardened cement paste: Studies on proxy ligands for the degradation of polyacrylonitrile and general considerations on the role of different functionalities in the uptake process. *Frontiers in Nuclear Engineering* **2022,** *1*, 997398.

94. Marta, B.; Jana Kittnerová, K.; Barbora, D., Comparative study of Eu and U sorption on cementitious materials in the presence of organic substances. Springer: **2023**.

95. Ochs, M.; Dolder, F.; Tachi, Y., Decrease of radionuclide sorption in hydrated cement systems by organic ligands: Comparative evaluation using experimental data and thermodynamic calculations for ISA/EDTA-actinide-cement systems. *Applied Geochemistry* **2022,** *136*, 105161.

96. Khoeini, M.; Bazgir, S.; Tamizifar, M.; Nemati, A.; Arzani, K., Investigation of the modification process and morphology of organosilane modified nanoclay. *Ceramics-Silikáty* **2009,** *53* (4), 254-259.

97. Bradbury, M.; Baeyens, B., Sorption of Eu on Na-and Ca-montmorillonites: Experimental investigations and modelling with cation exchange and surface complexation. *Geochimica et Cosmochimica Acta* **2002,** *66* (13), 2325-2334.

98. Dzombak, D. A.; Morel, F. M., *Surface complexation modeling: hydrous ferric oxide*. John Wiley & Sons: **1991**.

99. Coppin, F.; Berger, G.; Bauer, A.; Castet, S.; Loubet, M., Sorption of lanthanides on smectite and kaolinite. *Chemical Geology* **2002,** *182* (1), 57-68.

100. Hartmann, E.; Brendebach, B.; Polly, R.; Geckeis, H.; Stumpf, T., Characterization and quantification of Sm (III)/and Cm (III)/clay mineral outer-sphere species by TRLFS in D_2O and EXAFS studies. *Journal of colloid and interface science* **2011,** *353* (2), 562-568.

101. Schnurr, A.; Marsac, R.; Rabung, T.; Lützenkirchen, J.; Geckeis, H., Sorption of Cm (III) and Eu (III) onto clay minerals under saline conditions: Batch adsorption, laser-fluorescence spectroscopy and modeling. *Geochimica et Cosmochimica Acta* **2015,** *151*, 192-202.

102. Schnurr, A. Untersuchungen zur Radionuklidsorption an Tonmineraloberflächen bei hohen Ionenstärken. Diss, Karlsruhe Institute of Technology (KIT), **2015**.

103. Sheng, G.; Shao, D. D.; Fan, Q. H.; Xu, D.; Chen, Y.; Wang, X., Effect of pH and ionic strength on sorption of Eu (III) to MX-80 bentonite: batch and XAFS study. *rca-Radiochimica Acta* **2009,** *97* (11), 621-630.

104. Bradbury, M. H.; Baeyens, B., Porewater chemistry in compacted re-saturated MX-80 bentonite. *Journal of Contaminant Hydrology* **2003,** *61* (1-4), 329-338.

105. Guo, N.; Yang, J.; Zhang, R.; Ye, Y.; Wu, W.; Guo, Z., Effects of organic acids on Eu (III) sorption on Na-bentonite. *Journal of Radioanalytical and Nuclear Chemistry* **2015,** *303* (3), 2185-2192.

106. Tasi, A.; Gaona, X.; Rabung, T.; Fellhauer, D.; Rothe, J.; Dardenne, K.; Lützenkirchen, J.; Grivé, M.; Colàs, E.; Bruno, J., Plutonium retention in the isosaccharinate–cement system. *Applied Geochemistry* **2021,** *126*, 104862.

107. Gaboreau, S.; Grangeon, S.; Claret, F.; Ihiawakrim, D.; Ersen, O.; Montouillout, V.; Maubec, N.; Roosz, C.; Henocq, P.; Carteret, C., Hydration Properties and Interlayer Organization in Synthetic CSH. *Langmuir* **2020,** *36* (32), 9449-9464.

108. Svensson, D.; Dueck, A.; Nilsson, U.; Olsson, S.; Sanden, T.; Lydmark, S.; Jaegerwall, S.; Pedersen, K.; Hansen, S., Alternative buffer material. Status of the ongoing laboratory investigation of reference materials and test package 1. **2011**.

109. L Hopital, É. Aluminium and alkali uptake in calcium silicate hydrates (CSH). Switzerland: EPFL, 2014: 15–23, **2014**.

110. Rothe, J.; Butorin, S.; Dardenne, K.; Denecke, M.; Kienzler, B.; Löble, M.; Metz, V.; Seibert, A.; Steppert, M.; Vitova, T., The INE-Beamline for actinide science at ANKA. *Review of scientific instruments* **2012,** *83* (4).

111. Cramer, S. P., X-ray spectroscopy with synchrotron radiation. *Biological and Medical Physics, Biomedical Engineering* **2020**.

112. Lindau, A. T. I.; Scofield, K. J.; Williams, J. K. G., Center for X-Ray optics.

113. De Broglie, L., The wave nature of the electron. *Nobel lecture* **1929,** *12*, 244-256.

114. Koningsberger, D.; Mojet, B.; Van Dorssen, G.; Ramaker, D., XAFS spectroscopy; fundamental principles and data analysis. *Topics in catalysis* **2000,** *10*, 143-155.

115. Mobilio, S.; Boscherini, F.; Meneghini, C., *Synchrotron Radiation*. Springer: **2016**.

116. Brendebach, B.; Banik, N.; Marquardt, C. M.; Rothe, J.; Denecke, M.; Geckeis, H., X-ray absorption spectroscopic study of trivalent and tetravalent actinides in solution at varying pH values. *Radiochimica Acta* **2009,** *97* (12), 701-708.

117. Neck, V.; Altmaier, M.; Müller, R.; Bauer, A.; Fanghänel, T.; Kim, J.-I., Solubility of crystalline thorium dioxide. *Radiochimica Acta* **2003,** *91* (5), 253-262.

118. Altmaier, M.; Neck, V.; Fanghänel, T., Solubility of Zr (IV), Th (IV) and Pu (IV) hydrous oxides in CaCl2 solutions and the formation of ternary Ca-M (IV)-OH complexes. *Radiochimica Acta* **2008,** *96* (9-11), 541-550.

119. Olesik, J. W., Elemental analysis using icp-oes and icp/ms. *Analytical Chemistry* **1991,** *63* (1), 12A-21A.

120. Scientific, T. F., Comparison of ICP-OES and ICP-MS for Trace Element Analysis. *ThermoFisher Scientific* **2020**.

121. Khan, S. R.; Sharma, B.; Chawla, P. A.; Bhatia, R., Inductively coupled plasma optical emission spectrometry (ICP-OES): a powerful analytical technique for elemental analysis. *Food Analytical Methods* **2022**, 1-23.

122. Ritgen, U., *Analytical Chemistry I*. Springer Nature: **2023.**

123. Gey, M., Instrumentelle Analytik und Bioanalytik, 2., überarb. u. erw. Aufl. Springer, Berlin: 2008.

124. Monshi, A.; Foroughi, M. R.; Monshi, M. R., Modified Scherrer equation to estimate more accurately nano-crystallite size using XRD. *World journal of nano science and engineering* **2012,** *2* (3), 154-160.

125. Taniguchi, N., Fundamentals and applications of nano technology. *Kogyo Chosakai* **1988**.

126. Girão, A. V.; Caputo, G.; Ferro, M. C., Application of scanning electron microscopy–energy dispersive X-ray spectroscopy (SEM-EDS). In *Comprehensive analytical chemistry*, Elsevier: **2017;** Vol. 75, pp 153-168.

127. Goldstein, J. I.; Newbury, D. E.; Michael, J. R.; Ritchie, N. W.; Scott, J. H. J.; Joy, D. C., *Scanning electron microscopy and X-ray microanalysis*. springer: 2017.

128. Scrivener, K.; Snellings, R.; Lothenbach, B., *A practical guide to microstructural analysis of cementitious materials*. Crc Press: **2018**.

129. Brunauer, S.; Emmett, P. H.; Teller, E., Adsorption of gases in multimolecular layers. *Journal of the American chemical society* **1938,** *60* (2), 309-319.

130. Thommes, M.; Kaneko, K.; Neimark, A. V.; Olivier, J. P.; Rodriguez-Reinoso, F.; Rouquerol, J.; Sing, K. S., Physisorption of gases, with special reference to the

evaluation of surface area and pore size distribution (IUPAC Technical Report). *Pure and applied chemistry* **2015,** *87* (9-10), 1051-1069.

131. Book, G., Compendium of chemical terminology. *International Union of Pure and Applied Chemistry* **2014,** *528*.

132. Guillamont, R.; Fanghänel, T.; Neck, V.; Fuger, J.; Palmer, D.; Grenthe, I.; Rand, M., Update on the chemical thermodynamics of U, Np, Pu, Am and Tc. OECD NEA, Elsevier: **2003**.

133. Pitzer, K. S., Ion interaction approach: theory and data correlation. In *Activity coefficients in electrolyte solutions*, CRC Press: **2018**; pp 75-153.

134. Felmy, A. R.; Rai, D., Application of Pitzer's equations for modeling the aqueous thermodynamics of actinide species in natural waters: a review. *Journal of Solution Chemistry* **1999,** *28*, 533-553.

135. DL, P., User's guide to PHREEQC (version 2)-a computer program for speciation, batch reaction, one-dimensional transport, and inverse geochemical calculations. Water-Resources Investigations Report 99-4259. US Geological Survey. **1999**.

136. Parkhurst, D. L.; Appelo, C., Description of input and examples for PHREEQC version 3—a computer program for speciation, batch-reaction, one-dimensional transport, and inverse geochemical calculations. *US geological survey techniques and methods* **2013,** *6* (A43), 497.

137. Puigdomènech, I.; Colàs, E.; Grivè, M.; Campos, I.; García, D., A tool to draw chemical equilibrium diagrams using SIT: Applications to geochemical systems and radionuclide solubility. *MRS Online Proceedings Library* **2014,** *1665*, 111-116.

138. Steudel, A.; Batenburg, L.; Fischer, H.; Weidler, P.; Emmerich, K., Alteration of swelling clay minerals by acid activation. *Applied Clay Science* **2009,** *44* (1-2), 105-115.

139. Yu, P.; Kirkpatrick, R. J.; Poe, B.; McMillan, P. F.; Cong, X., Structure of calcium silicate hydrate (C-S-H): Near-, Mid-, and Far-infrared spectroscopy. *Journal of the American Ceramic Society* **1999,** *82* (3), 742-748.

140. Wu, B.; Ye, G., Study of carbonation rate of synthetic CSH by XRD, NMR and FTIR. *Heron* **2019,** *64* (1-2), 21-38.

141. Garbev, K.; Bornefeld, M.; Beuchle, G.; Stemmermann, P., Cell dimensions and composition of nanocrystalline calcium silicate hydrate solid solutions. Part 2: X-ray and thermogravimetry study. *Journal of the American Ceramic Society* **2008,** *91* (9), 3015-3023.

142. Rodriguez, E. T.; Garbev, K.; Merz, D.; Black, L.; Richardson, I. G., Thermal stability of CSH phases and applicability of Richardson and Groves' and Richardson C-(A)-SH (I) models to synthetic CSH. *Cement and Concrete research* **2017,** *93*, 45-56.

143. Androniuk, I. Effects of cement organic additives on the adsorption of uranyl ions on calcium silicate hydrate phases: experimental determination and computational molecular modelling. Ecole nationale supérieure Mines-Télécom Atlantique Bretagne Pays de la Loire, **2017**.

144. Tits, J.; Wieland, E.; Müller, C.; Landesman, C.; Bradbury, M., Strontium binding by calcium silicate hydrates. *Journal of colloid and interface science* **2006,** *300* (1), 78-87.

145. Myers, R. J.; L'Hôpital, E.; Provis, J. L.; Lothenbach, B., Effect of temperature and aluminium on calcium (alumino) silicate hydrate chemistry under equilibrium conditions. *Cement and Concrete Research* **2015,** *68*, 83-93.

146. ICDD PDF-2 (2016) Crystallography Open Database Version 4.2. **2016**.

147. Grangeon, S.; Claret, F.; Linard, Y.; Chiaberge, C., X-ray diffraction: a powerful tool to probe and understand the structure of nanocrystalline calcium silicate hydrates. *Acta Crystallographica Section B: Structural Science, Crystal Engineering and Materials* **2013,** *69* (5), 465-473.

148. Barzgar, S.; Lothenbach, B.; Tarik, M.; Di Giacomo, A.; Ludwig, C., The effect of sodium hydroxide on Al uptake by calcium silicate hydrates (CSH). *Journal of colloid and interface science* **2020,** *572*, 246-256.

149. Taylor, H. F., Proposed structure for calcium silicate hydrate gel. *Journal of the American Ceramic Society* **1986,** *69* (6), 464-467.

150. Xiong, Y.; Kirkes, L.; Westfall, T., Experimental determination of solubilities of di-calcium ethylenediaminetetraacetic acid hydrate [$Ca_2C_{10}H_{12}N_2O_8 \cdot 7H_2O$ (s)] in NaCl and $MgCl_2$ solutions to high ionic strengths and its Pitzer model: Applications to

geological disposal of nuclear waste and other low temperature environments. *Chemical Geology* **2017,** *454*, 15-24.

151. Dario, M.; Molera, M.; Allard, B. *Effect of organic ligands on the sorption of europium on TiO_2 and cement at high pH*; Swedish Nuclear Fuel and Waste Management Co.: 2004.

152. Trumm, M.; Tasi, A.; Schnurr, A.; DiBlasi, N.; Gaona, X., Structural characterisation of hydrolysed Cm-(III)-EDTA solution species under alkaline conditions: a TRLFS, vibronic side-band and quantum chemical study. *Molecular Physics* **2022**, e2033864.

153. Rabung, T.; Altmaier, M.; Neck, V.; Fanghänel, T., A TRLFS study of Cm (III) hydroxide complexes in alkaline $CaCl_2$ solutions. *Radiochimica Acta* **2008,** *96* (9-11), 551-560.

154. Jia, W.; Lu, S., Effect of pH, foreign ions and temperature on radionickel sorption onto bentonite from Inner Mongolia, China. *Journal of Radioanalytical and Nuclear Chemistry* **2014,** *299* (3), 1417-1426.

155. Shao, D.; Xu, D.; Wang, S.; Fang, Q.; Wu, W.; Dong, Y.; Wang, X., Modeling of radionickel sorption on MX-80 bentonite as a function of pH and ionic strength. *Science in China Series B: Chemistry* **2009,** *52* (3), 362-371.

156. Hu, J.; Xu, D.; Chen, L.; Wang, X., Characterization of MX-80 bentonite and its sorption of radionickel in the presence of humic and fulvic acids. *Journal of radioanalytical and nuclear chemistry* **2009,** *279* (3), 701-708.

157. Hartmann, E. Sorption von *Ln* (III)-*An* (III) und U (VI) an Tonmineralen und natürlichen Tongesteinen. Karlsruher Inst. für Technologie, Diss., 2010, 2010.

158. Rabung, T.; Pierret, M.; Bauer, A.; Geckeis, H.; Bradbury, M.; Baeyens, B., Sorption of Eu (III)/Cm (III) on Ca-montmorillonite and Na-illite. Part 1: Batch sorption and time-resolved laser fluorescence spectroscopy experiments. *Geochimica et Cosmochimica Acta* **2005,** *69* (23), 5393-5402.

7. Appendix

7.1 Aqueous phase characterization of [Ca] and [Si] in C-S-H systems

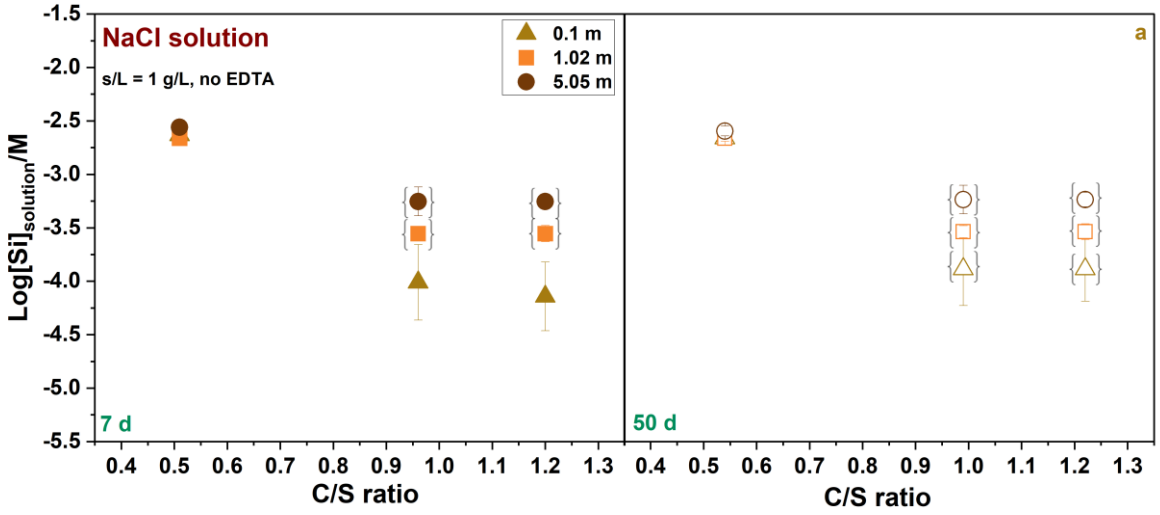

Figure 7.1: $[Si]_{aq}$ for C-S-H phases with different C/S ~ 0.6, 1.0 and 1.3. Data is shown at 7 d (left) and 50 d (right) in absence of EDTA in NaCl solution (I_m = 0.1 m in light brown, 1.02 m in orange and 5.05 m in dark brown) at S/V = 1 g/L. The symbols in brackets reflect to the measurements at the detection limit.

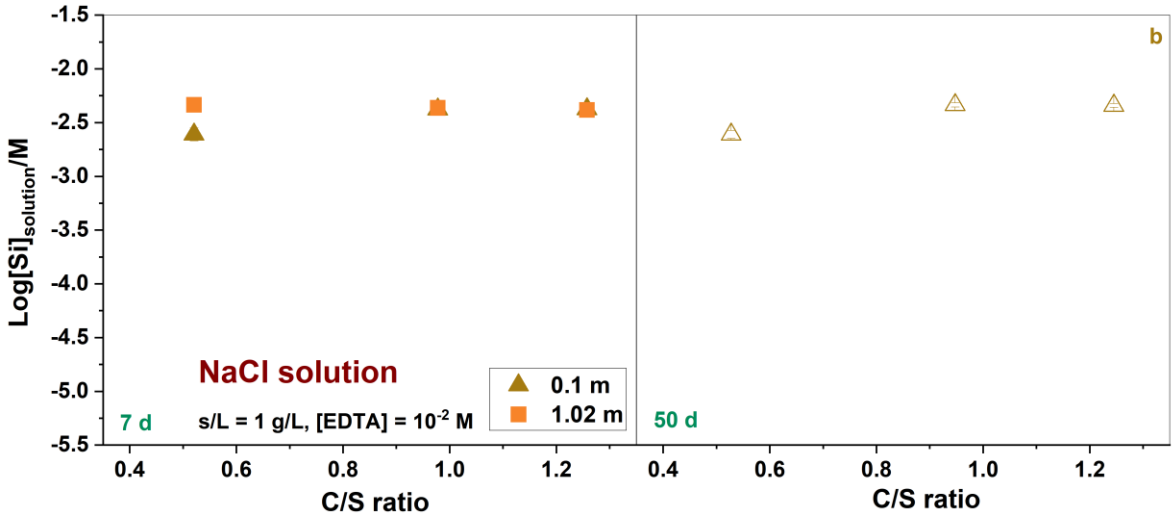

Figure 7.2: $[Si]_{aq}$ for C-S-H phases with different C/S ~ 0.6, 1.0 and 1.3. Data is shown at 7 d (left) and 50 d (right) in presence of [EDTA] = 10^{-2} M in NaCl solution (I_m = 0.1 m in light brown and 1.02 m in orange) at S/V = 1 g/L.

7.2 Sorption of Eu(III) on C-S-H phases in presence of EDTA

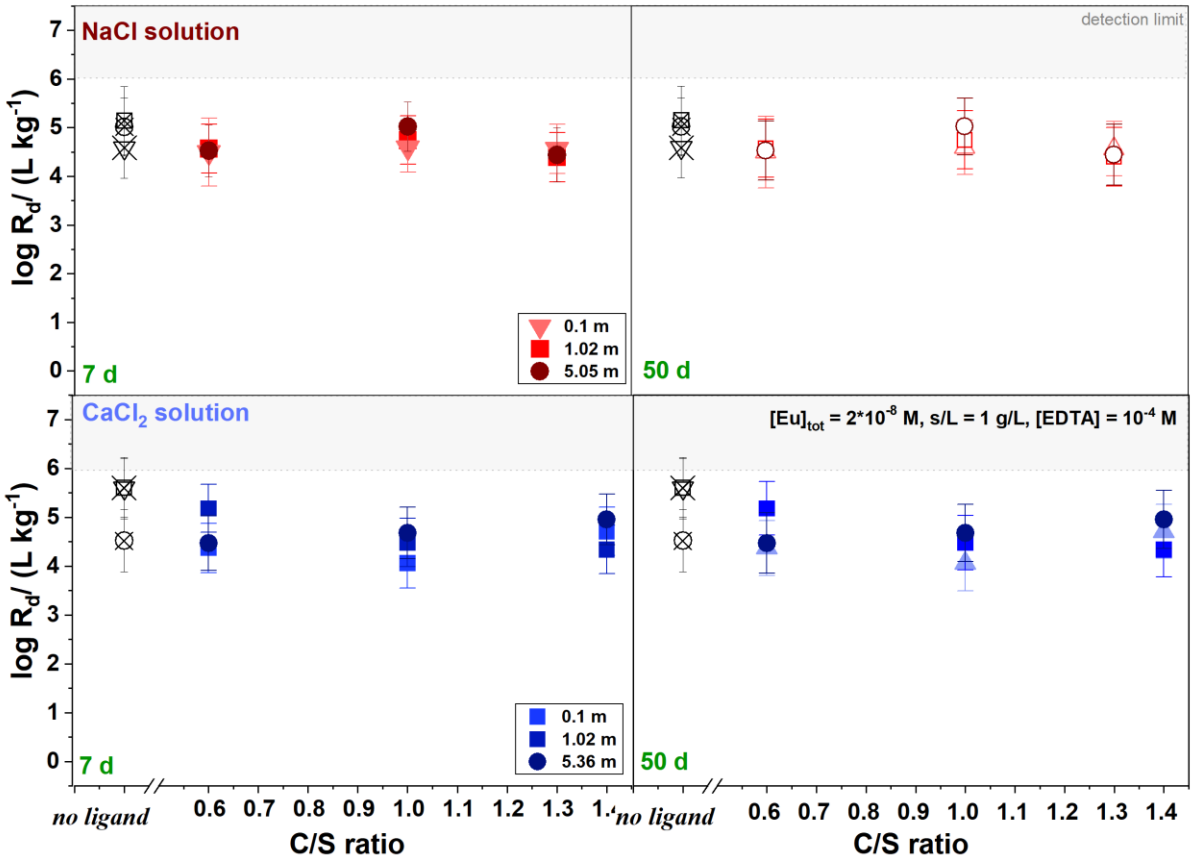

Figure 7.3: Logarithmic distribution coefficients (Log R_d/L kg^{-1}) for the adsorption of Eu(III) ([Eu]$_{tot}$ = 2·10^{-8} M) on C-S-H phases with various C/S ~ 0.6 – 1.4 in presence of [EDTA] = 10^{-4} M in NaCl- (top) at I_m = 0.1, 1.02, 5.05 m and $CaCl_2$ solutions (bottom) at I_m = 0.1, 1.02, 5.05 m after 7 (left) and 50 d (right) at 1 g/L. Data in absence of the ligand are also shown.

7.3 TRLFS studies in NaCl and $CaCl_2$ solutions in absence of EDTA

Cm(III) fluorescence emission spectra on C-S-H phases (C/S ~ 1.0, C/S ~ 1.3 (NaCl solution; C/S ~ 1.4 ($CaCl_2$ solutions) are shown in solution and suspension in the absence of EDTA over a time range between 7 - 90 d. The spectra shown in Figure 7.4 are illustrated in NaCl and $CaCl_2$ solutions (I_m = 1.02 m). The corresponding fluorescence lifetimes are seen in Table 7.1.

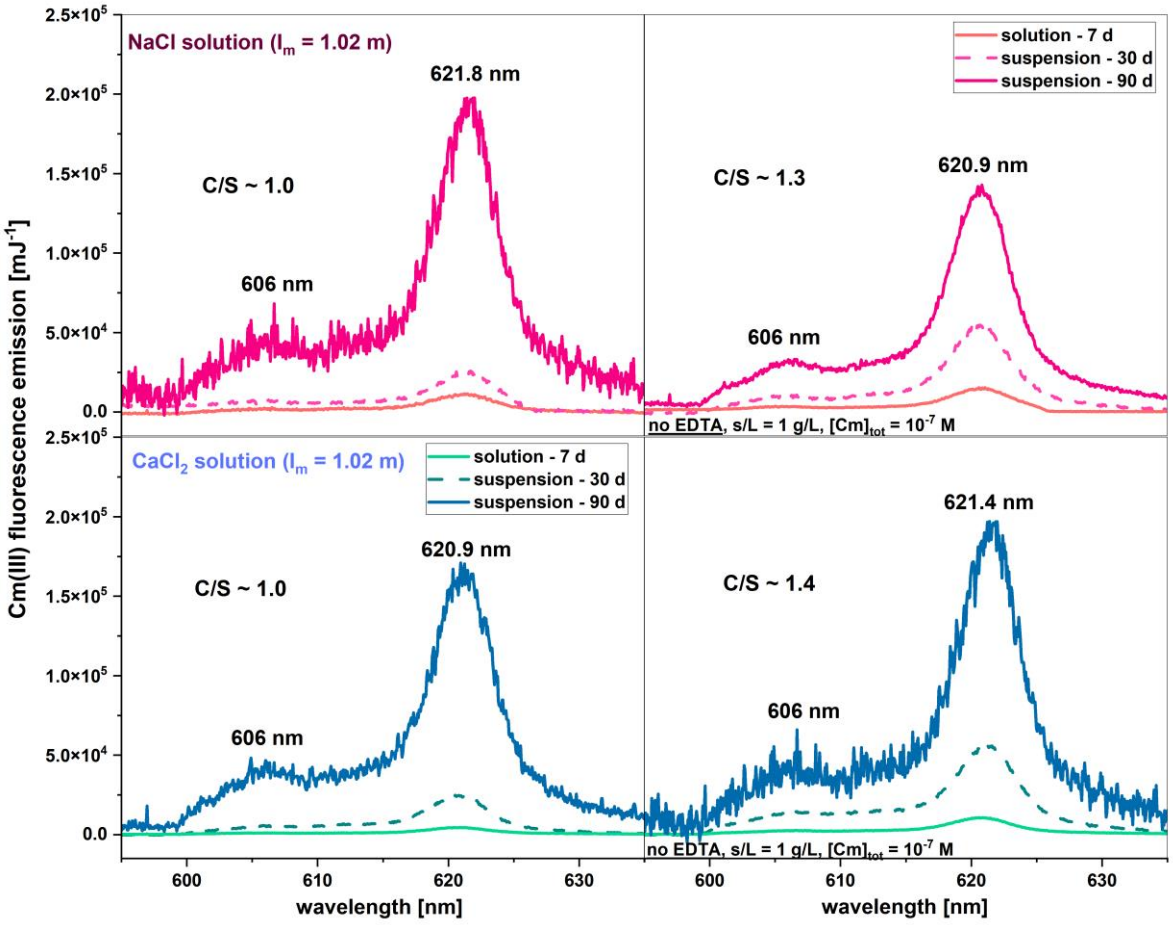

Figure 7.4: Fluorescence emission spectra of Cm(III) on C-S-H phase in absence of EDTA in NaCl and $CaCl_2$ solutions at I_m = 1.02 m for C/S ~ 1.0 (left) and C/S ~ 1.3 (NaCl) and C/S ~ 1.4 ($CaCl_2$) (right).). The samples are recorded for sorption times of t = 7, 30 and 90 d in suspension and solution.

In the solution, there is no Cm(III) fluorescence signal observed for either electrolyte. However, in suspension, two signals occur at 606 nm and 620.9 – 621.8 nm. For the signal ranging between ~ 620.9 – 621.8 nm, average fluorescence lifetimes of 1436±30 µs (C/S ~ 1.0) and 1062±25 µs (C/S ~ 1.3) are observed in NaCl solution,

while 1320±31 µs (C/S ~ 1.0) and 1411±19 µs (C/S ~ 1.4) are calculated in $CaCl_2$ solutions. Consequently, fluorescence lifetimes in NaCl and $CaCl_2$ solutions are similar. Zero water molecules are attributed to these bands, designating them as the incorporation species of Cm(III) detailed in section 4.5. The former signal at 606 nm, refers to a hot band as described in previous sections of chapter 4.5. Similar fluorescence emission spectra and lifetimes were also observed at low EDTA concentrations. This confirms the hypothesis that EDTA at low concentrations does not affect the sorption of Cm(III) to C-S-H phases at different C/S ratios.

Table 7.1*:* Fluorescence lifetimes and the corresponding amount of water molecules of the different Cm(III) species detected in solution and suspension. All TRLFS measurements are performed in absence of EDTA on C-S-H phases with different C/S (C/S ~ 1.0 and C/S ~ 1.3 (NaCl solutions), C/S ~ 1.4 ($CaCl_2$ solutions).

Species	Peak (nm)	Sorption time (d)	pH	Lifetime (µs)	N_{H2O}
C/S ~ 1.0 - NaCl					
Incorporation species	621.8	7	11.0	1448±37	0
		90	10.9	1423±23	0
Ø	**621.8**		**11.0**	**1436±30**	**0**
C/S ~ 1.0 – $CaCl_2$					
Incorporation species	620.9	7	10.8	1408±18	0
		90		1231±43	0
Ø	**620.9**		**10.8**	**1320±31**	**0**
C/S ~ 1.3 - NaCl					
Incorporation species	620.9	7	11.1	1062±25	0
		90		-	
C/S ~ 1.4 – $CaCl_2$					
Incorporation species	621.4	7	10.9	1411±19	0
		90		-	

7.4 Examination of the Eu(III) and Cm(III) speciation

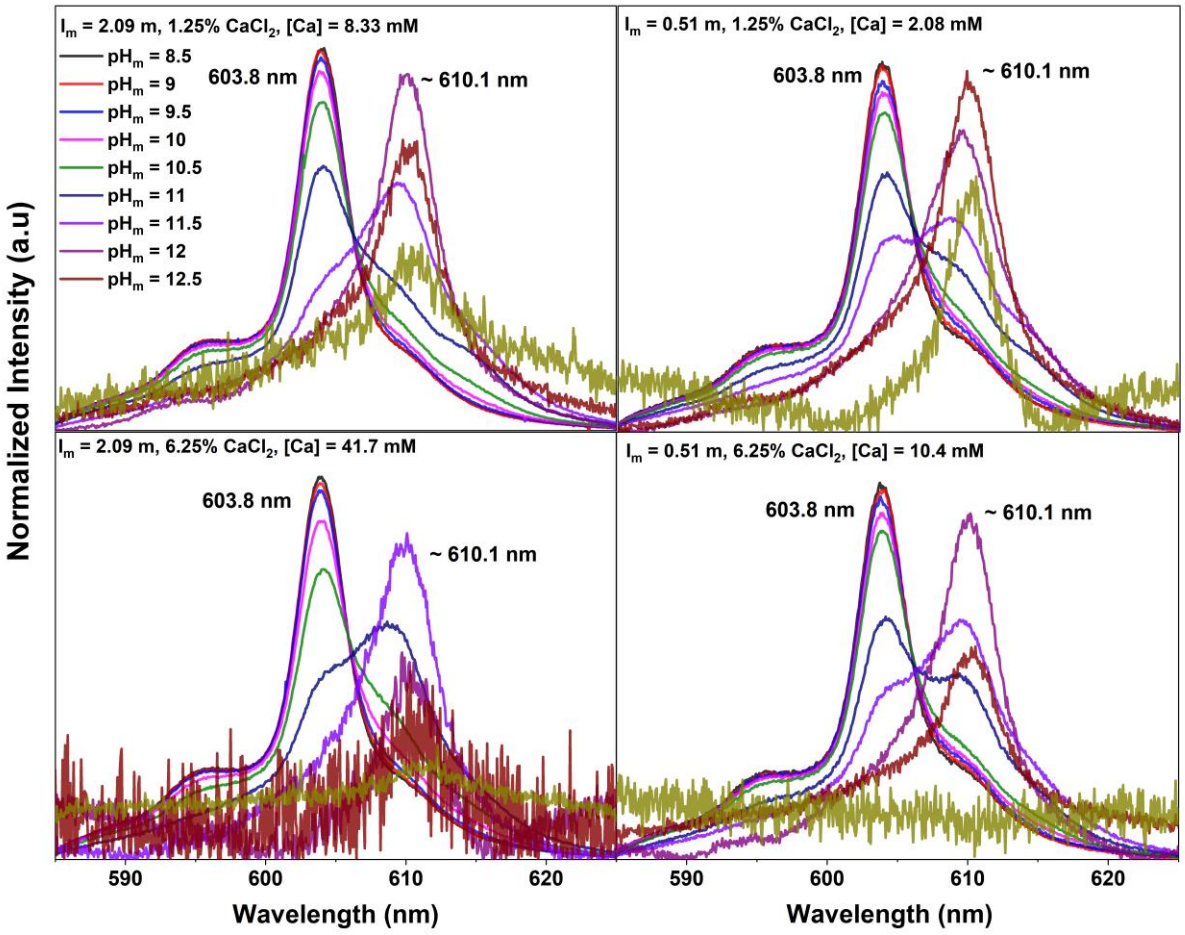

Figure 7.5: Cm(III) fluorescence emission spectra in presence of [EDTA] = 10^{-2} M) for the series with a total ionic strength I_m = 0.5 M (right) and 2 M (left). The Calcium amount of every sample was varied from 1.25 % (top) to 6.25 % (bottom). For every 0.5 pH step, a spectrum was recorded for pH_m = 8.5 – 12.5.

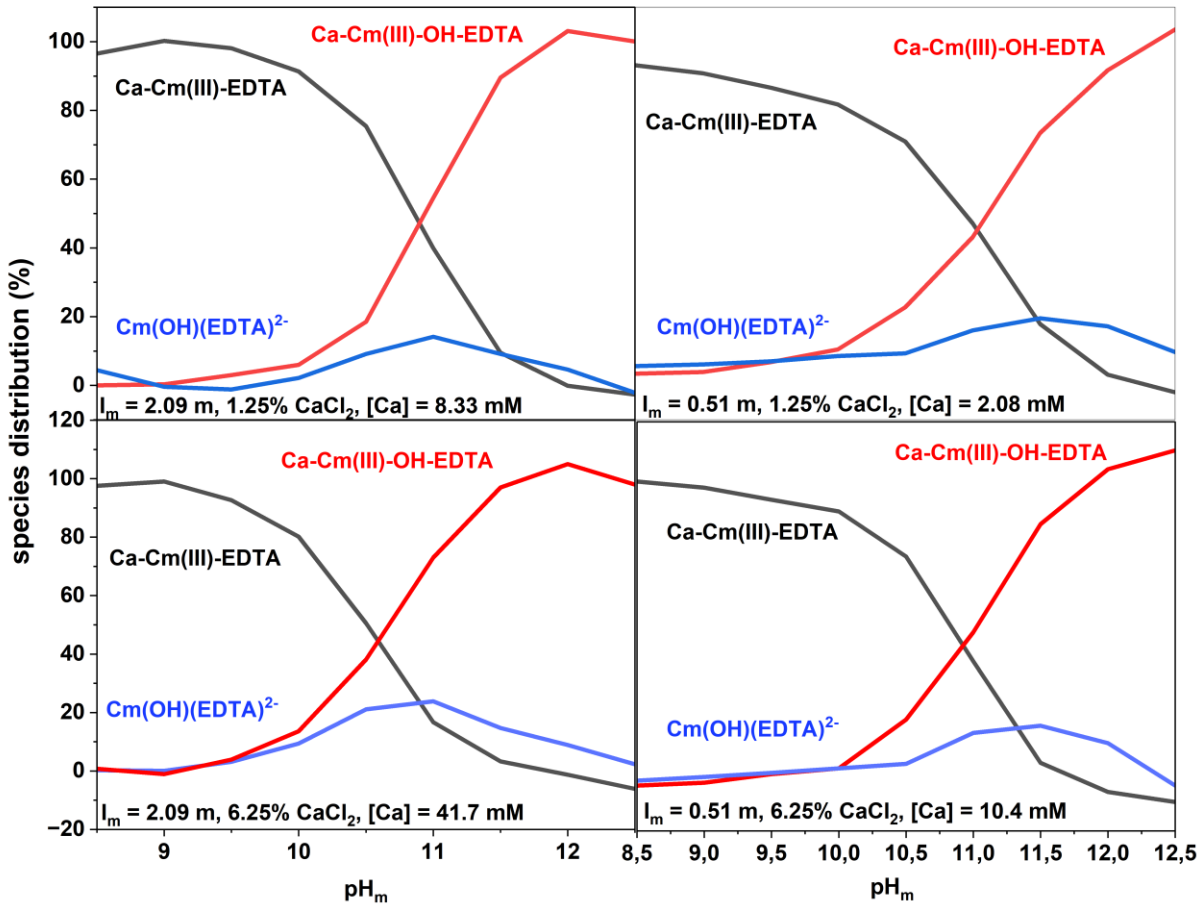

Figure 7.6: Speciation diagrams, including the species Ca-Cm(III)-EDTA, Ca-Cm(III)-OH-EDTA and Ca(OH)(EDTA)$^{2-}$ after the peak deconvolution. The samples show [Ca] = 8.33 mM, 41.7 mM (I_m = 2.09 m, left) and [Ca] = 2.08 mM, 10.4 mM (I_m = 0.51 m, right). Species distributions are given in percentage between pH_m = 8.5 – 12.5.

Table 7.2: Percentage proportion of the assumed species a = Ca-Cm-(III)-EDTA, b = Ca-Cm(III)-OH-EDTA and c = $Cm(OH)(EDTA)^{2-}$ for the formation of the speciation diagrams. The data for I = 2.09 m are listed for the samples Ca content of 0.25 %, 1.25 %, 2.5 %, 6.25 % and 15 %. This corresponds to the following [Ca] = 1.67 mM, 8.33 mM, 16.7 mM, 41.7 mM and 100 mM between pH_m = 8.5 – 12.5.

Species	pH_m								
	8.5	**9**	**9.5**	**10**	**10.5**	**11**	**11.5**	**12**	**12.5**
I_m = 2.09 m, Ca = 0.25 %, [Ca] = 1.67 mM									
a	98±9.8	98±9.8	98±9.8	90±9.0	85±8.5	50±5.0	15±1.5	5.0±0.5	1.0±0.1
b	1.0±0.1	1.0±0.1	2.0±0.2	5.0±0.5	8.0±0.8	30±3.0	68±6.8	100±10	100±10
c	1.0±0.1	1.0±0.1	1.0±0.1	5.0±0.5	5.0±0.5	25±2.5	30±3.0	10±1.0	10±1.0
I_m = 2.09 m, Ca = 1.25 %, [Ca] = 8.33 mM									
a	100±10	100±10	98±9.8	92±9.2	73±7.3	50±5.0	5.0±0.5	1.0±0.1	1.0±0.1
b	1.0±0.1	1.0±0.1	2.0±0.2	6.0±0.6	13±1.3	33±3.3	98±9.8	100±10	100±10
c	1.0±0.1	1.0±0.1	1.0±0.1	3.0±0.3	15±1.5	18±1.8	15	10±1.0	10±1.0
I_m = 2.09 m, Ca = 2.50 %, [Ca] = 16.7 mM									
a	100±10	100±10	96±9.6	93±9.3	75±7.5	45±4.5	1.0±0.1	1.0±0.1	1.0±0.1
b	1.0±0.1	1.0±0.1	4.0±0.4	7.0±0.7	16±1.6	50±5.0	99±9.9	100±10	100±10
c	1.0±0.1	1.0±0.1	1.0±0.1	1.0±0.1	1.0±0.1	1.0±0.1	1.0±0.1	1.0±0.1	1.0±0.1
I_m = 2.09 m, Ca = 6.25 %, [Ca] = 41.7 mM									
a	98±9.8	99±9.9	90±9.0	82±8.2	55±5.5	10±1.0	1.0±0.1	1.0±0.1	1.0±0.1
b	1.0±0.1	1.0±0.1	5.0±0.5	13±1.3	35±3.5	75±7.5	100±10	100±10	100±10
c	1.0±0.1	1.0±0.1	5.0±0.5	7.0±0.7	20±2.0	30±3.0	10±1.0	5.0±0.5	5.0±0.5
I_m = 2.09 m, Ca = 15 %, [Ca] = 100 mM									
a	100±10	100±10	99±9.9	71±7.1	45±4.5	1.0±0.1	1.0±0.1	01.0±0.1	1.0±0.1
b	1.0±0.1	1.0±0.1	3.0±0.3	9.0±0.9	30±3.0	75±7.5	98±9.8	99±9.9	99±9.9
c	1.0±0.1	1.0±0.1	1.0±0.1	20±2.0	30±3.0	40±4.0	1.0±0.1	1.0±0.1	1.0±0.1

Table 7.3: Percentage proportion of the assumed species a = Ca-Cm-(III)-EDTA, b = Ca-Cm(III)-OH-EDTA and c = $Cm(OH)(EDTA)^{2-}$ for the formation of the speciation diagrams. The data for I = 0.51 m are listed for the samples Ca content of 0.25 %, 1.25 %, 2.5 %, 6.25 % and 15 %. This corresponds to [Ca] = 0.417 mM, 2.08 mM, 4.17 mM, 10.4 mM and 25 mM between pH_m = 8.5 – 12.5.

Species	pH_m								
	8.5	**9**	**9.5**	**10**	**10.5**	**11**	**11.5**	**12**	**12.5**
I_m = 0.51 m, Ca = 0.25 %, [Ca] = 0.417 mM									
a	10±1.0	10±1.0	5.0±0.5	1.0±0.1	2.0±0.2	1.0±0.1	1.0±0.1	1.0±0.1	1.0±0.1
b	1.0±0.1	1.0±0.1	1.0±0.1	1.0±0.1	1.0±0.1	12±1.2	25±2.5	18±1.8	5.0±0.5
c	100±10	90±9.0	95±9.5	100	100±10	92±9.2	85±8.5	85±8.5	80±8.0
I_m = 0.51 m, Ca = 1.25 %, [Ca] = 2.08 mM									
a	93±9.3	91±9.1	87±8.7	80±8.0	73±7.3	49±4.9	15±1.5	1.0±0.1	1.0±0.1
b	3.0±0.3	5.0±0.5	6.0±0.6	12±1.2	20±2.0	45±4.5	70±7.0	100±10	100±10
c	6.0±0.6	5.0±0.5	8.0±0.8	8.0±0.8	10±1.0	13±1.3	24±2.4	15±1.5	10±1.0
I_m = 0.51 m, Ca = 2.50 %, [Ca] = 4.17 mM									
a	93±9.3	92±9.2	90±9.0	82±8.2	78±7.8	48±4.8	15±1.5	1.0±0.1	1.0±0.1
b	3.0±0.3	5.0±0.5	5.0±0.5	11±1.1	15±1.5	43±4.3	63±6.3	100±10	100±10
c	5.0±0.5	5.0±0.5	5.0±0.5	8.0±0.8	10±1.0	15±1.5	30±3.0	12±1.2	10±1.0
I_m = 0.51 m, Ca = 6.25 %, [Ca] = 10.4 mM									
a	92±9.2	92±9.2	86±8.6	82±8.2	75±7.5	40±4.0	5.0±0.5	1.0±0.1	1.0±0.1
b	3.0±0.3	5.0±0.5	6.0±0.6	11±1.1	17±1.7	52±5.2	78±7.8	100±10	100±10
c	5.0±0.5	5.0±0.5	8.0±0.8	8.0±0.8	10±1.0	15±1.5	28±2.8	10±1.0	10±1.0
I_m = 0.51 m, Ca = 15 %, [Ca] = 25 mM									
a	92±9.2	91±9.1	85±8.5	80±8.0	74±7.4	25±2.5	1.0±0.1	1.0±0.1	1.0±0.1
b	5.0±0.5	5.0±0.5	7.0±0.7	11±1.1	20±2.0	55±5.5	75±7.5	100±10	100±10
c	1.0±0.1	5.0±0.5	8.0±0.8	8.0±0.8	9.0±0.9	30±3.0	28±2.8	10±1.0	10±1.0

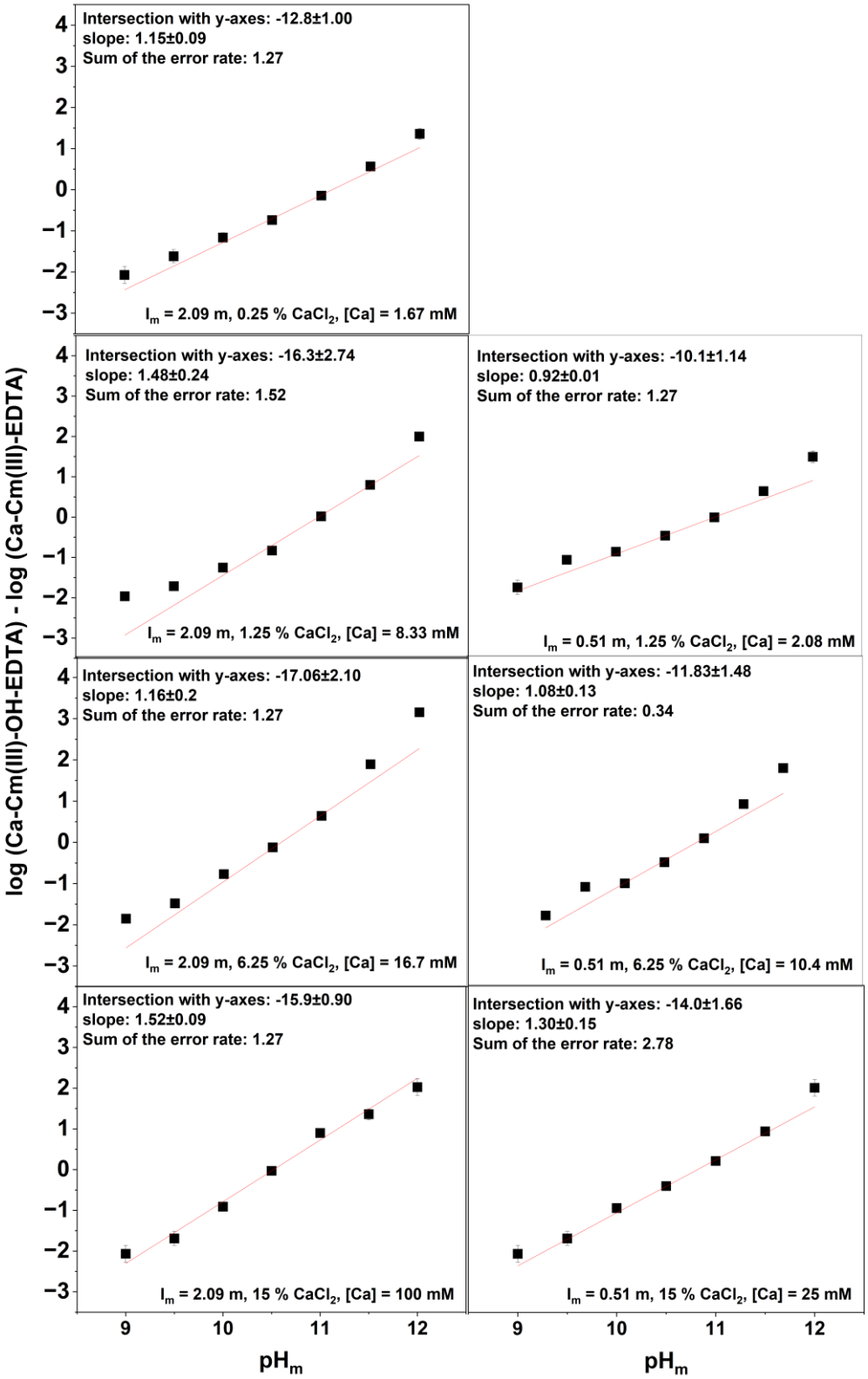

Figure 7.7: Slope analysis for the determination of the amount of OH-groups in the quaternary Ca-Cm(III)-OH-EDTA species at I_m(NaCl) = 2.09 (left) and 0.51 (right), with Ca = 0.25, 1.25, 6.25 and 15 %. This corresponds to [Ca] = 1.67 mM, 8.22 mM, 16.7 mM and 100 mM at I_m = 2.09 m (left) and [Ca] = 2.08 mM, 10.4 mM and 25 mM at I_m = 0.51 m. The sample with 0.25 % Ca content ([Ca] = 0.417 mM at 0.51 m is excluded hereby due to the low Ca content.

7.5 Characterization of bentonite MX 80

XRD/FTIR

The FTIR spectrum of bentonite MX80 is illustrated in Figure 7.8 a), while the XRD spectrum is visible in Figure 7.8 b).

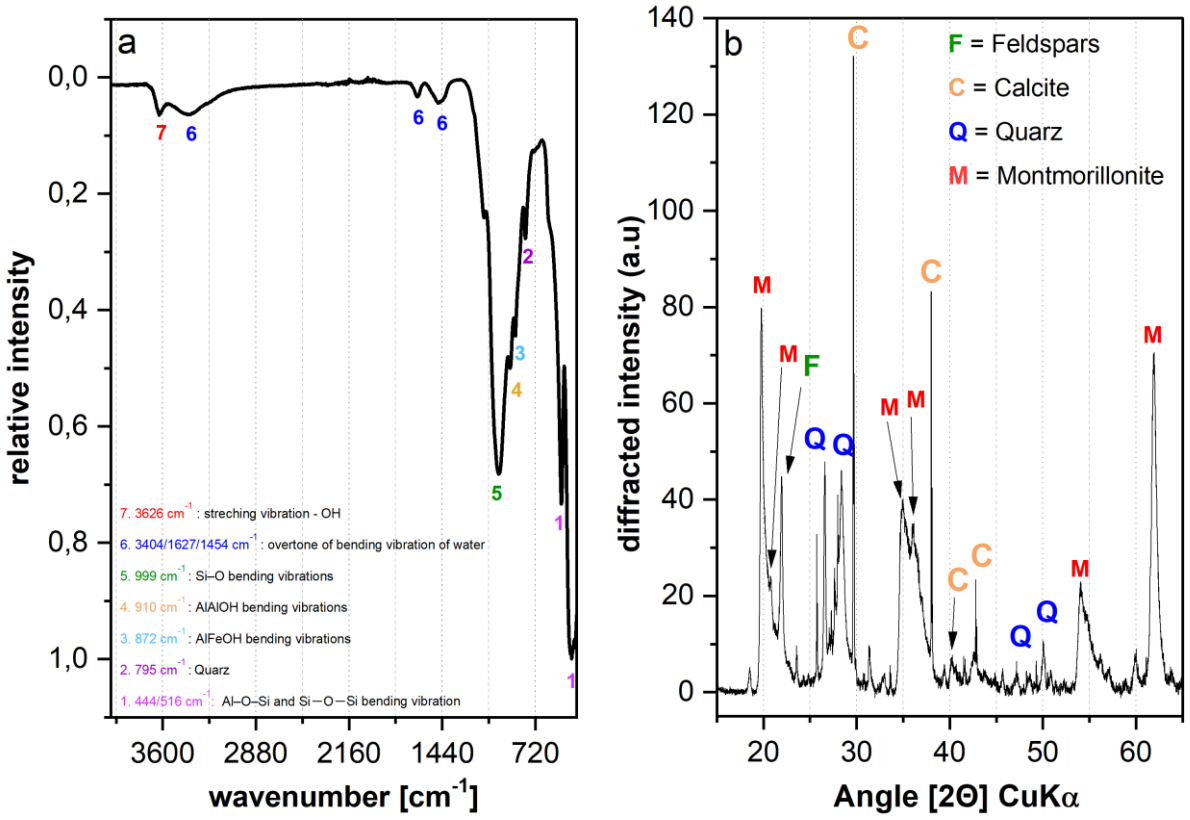

Figure 7.8: a) The FTIR spectrum (right) of bentonite MX80 shows the different bending and stretching vibrations of different species. **b)** The XRD spectrum (left) was measured with Cu K-a radiation source (λ = 0.15418 nm, I = 25 mA, U = 40 kV). Hereby a step width of 0.013 ° and a step counting of 2 s was used. 2Theta was set from 2 – 70 °.

In the FTIR spectrum, signals between 444 and 516 cm^{-1} are attributed to Al-O-Si and Si-O-Si bending vibrations. The weakly visible band at 795 cm^{-1} is indicative of quartz. Al-Al-OH bending and Al-Fe-OH vibrations are displayed at 910 cm^{-1} and 872 cm^{-1}, respectively. Another intense band at 999 cm^{-1} shows Si-O bending vibrations. The signals between 3404 – 1454 cm^{-1} can be described as overtones of the bending vibrations of water, while the weak band at 3626 cm^{-1} comes from the stretching vibration of -OH.[154, 155]

The XRD spectrum shows montmorillonite as the main fraction with the following peaks: 7.1 °, 19,9°, 21,1°, 35.1°, 36.2°, 39.6°, 54° and 62.2°. This is in good agreement to literature data. [103, 155] It is further known, that the composition of bentonite includes quartz, feldspars and calcite, which is additionally shown in Figure 7.8.

N_2 BET

In case of the bentonite MX80 samples, different particle size fractions are investigated: 200, 250 and >250 µm (see Table 7.4). The original bentonite MX80 is >250 µm, while the smaller particle size fractions are obtained by sieving.

Table 7.4: Specific surface area determination of bentonite MX80 samples before and after sieving.

Particle size fraction	Specific surface [m^2/g]
> 250 µm	**28.83 m^2/g**
250 µm	**29.27 m^2/g**
200 µm	**29.68 m^2/g**

The bentonite MX80 sample at >250 µm, *i.e*., without further treatment, shows a specific surface area of 28.83 m^2/g, while the sieved fractions show specific surface areas up to 29.68 m^2/g at 200 µm. The specific surface area reported in the literature is described with 21 – 28.9 m^2/g.[156, 157] From this it is visible, that the former value is slightly lower, but the latter value is in excellent agreement with the experimentally determined value in this work. The specific surface areas of the samples with different particle sizes are very similar for all samples. Therefore, bentonite without further treatment was used for all experiments.

7.6 Eu(III) sorption on bentonite MX 80 in presence of oxalate

The retention of Eu(III) on bentonite MX80 in the presence of [oxalate] = 10^{-3} M is investigated in the frame of Batch sorption experiments in this chapter. To quantify this retention, the logarithmic distribution coefficient (log R_d) was used. By varying different experimental parameters, such as the ionic strength (I_m) and the sorption time, the effect of these factors on the log R_d values was investigated. This analysis provides valuable insights into the sorption behavior of Eu(III) on bentonite MX80 in the presence of oxalate for a better comprehension of the overall sorption process.

Varying ionic strength and sorption time

The log R_d values of Eu(III) on bentonite MX 80 in presence of [oxalate] = 10^{-3} M are displayed diluted to concentrated NaCl and $CaCl_2$ solutions after 7 and 50 d of contact time within Figure 7.9 between pH_m = 3 – 12. It should be noted, that the bentonite used in this work is not purified (see chapter 7.5). Thus, it may contain soluble components such as NaCl and $CaSO_4$. This can result in [Ca] and [Na] in solution, which are higher than the actual ionic strength of the electrolyte solution. Therefore, it is particularly noticeable at the lowest ionic strength used here (I_m = 0.1 m). This is to be taken into account in further experiments.[104]

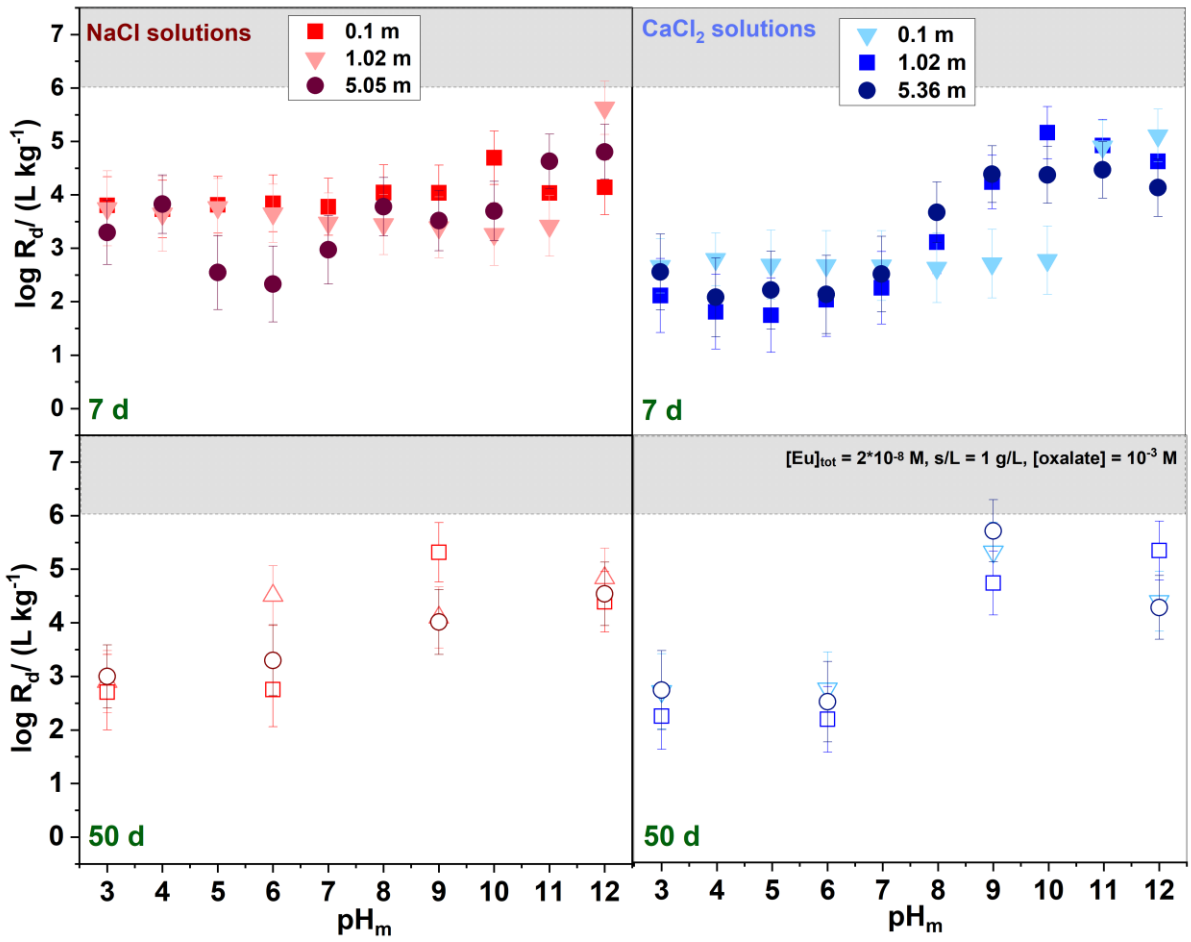

Figure 7.9: Logarithmic distribution coefficients (R_d / L/kg) for the adsorption of Eu(III) on bentonite MX 80 in presence of [oxalate] = 10^{-3} M as a function of pH_m. The data are displayed in NaCl (left) at I_m = 0.1, 1.02, 5.05 m and $CaCl_2$ solutions (right) at I_m = 0.1, 1.02, 5.36 m after sorption times of 7 (top) and 50 d (bottom). Hereby [Eu] = $2 \cdot 10^{-8}$ M and S/V = 1 g/L are used between pH_m = 3 – 12.

A slight pH dependency is visible in NaCl solution after 7 d of sorption time: Hereby log R_d ~ 3 – 4 are shown for pH_m = 3 – 12, while log R_d ~ 4 - 5 are reached for pH > 10. This behavior is more pronounced after 50 d. For $CaCl_2$ solutions, a strong pH dependence is observed after both contact times, resulting in low log R_d = 2 – 3 for pH_m < 8 and increasing log R_d = 3 – 5 for pH > 8. With respect to the different ionic strength of the electrolyte solutions, no significant effect is detected on the retention of Eu(III). Further no visible impact of oxalate is observed in this context. This is explained analogous to chapter 4.3.1 with the precipitation of solid Ca(Ox)(s) due to the low solubility product (K_L = 2.7 x 10^{-9} M).[24] This assumption is currently also applied to the NaCl system, since bentonite contains soluble components of *e.g.* $CaSO_4$. Bradbury and Baeyens describe the composition of the bentonite pore water at pH = 8 and an

ionic strength of I_m = 0.327, where among other elements, [Ca] = $1.02 \cdot 10^{-2}$ M was observed.[104] However, a direct comparison of their data with the data obtained in this thesis is not possible, since the general conditions such as pH, electrolyte solution and ionic strength differ.

7.7 Sorption of Eu(III) on bentonite MX 80 in presence of EDTA

The retention of Eu(III) on bentonite MX80 in the presence of [EDTA] = 10^{-4} M is studied in this chapter in the framework of Batch sorption experiments. The logarithmic distribution coefficient (log R_d) was used to quantify this retention. Analogous to section 7.6, different experimental parameters such as ionic strength (I_m) and sorption time are varied.This analysis provides valuable insights into the sorption behavior of Eu(III) on bentonite MX80 in the presence of oxalate for a better understanding of the overall sorption process.

Varying ionic strength (I_m) and sorption time

The logarithmic distribution coefficient for the Eu(III) retention on bentonite MX80 in the presence of EDTA as a function of pH is shown in Figure 7.10. NaCl and $CaCl_2$ solutions of different ionic strength are considered for two different sorption times at t = 7 and 50 d between pH_m = 3 – 12.

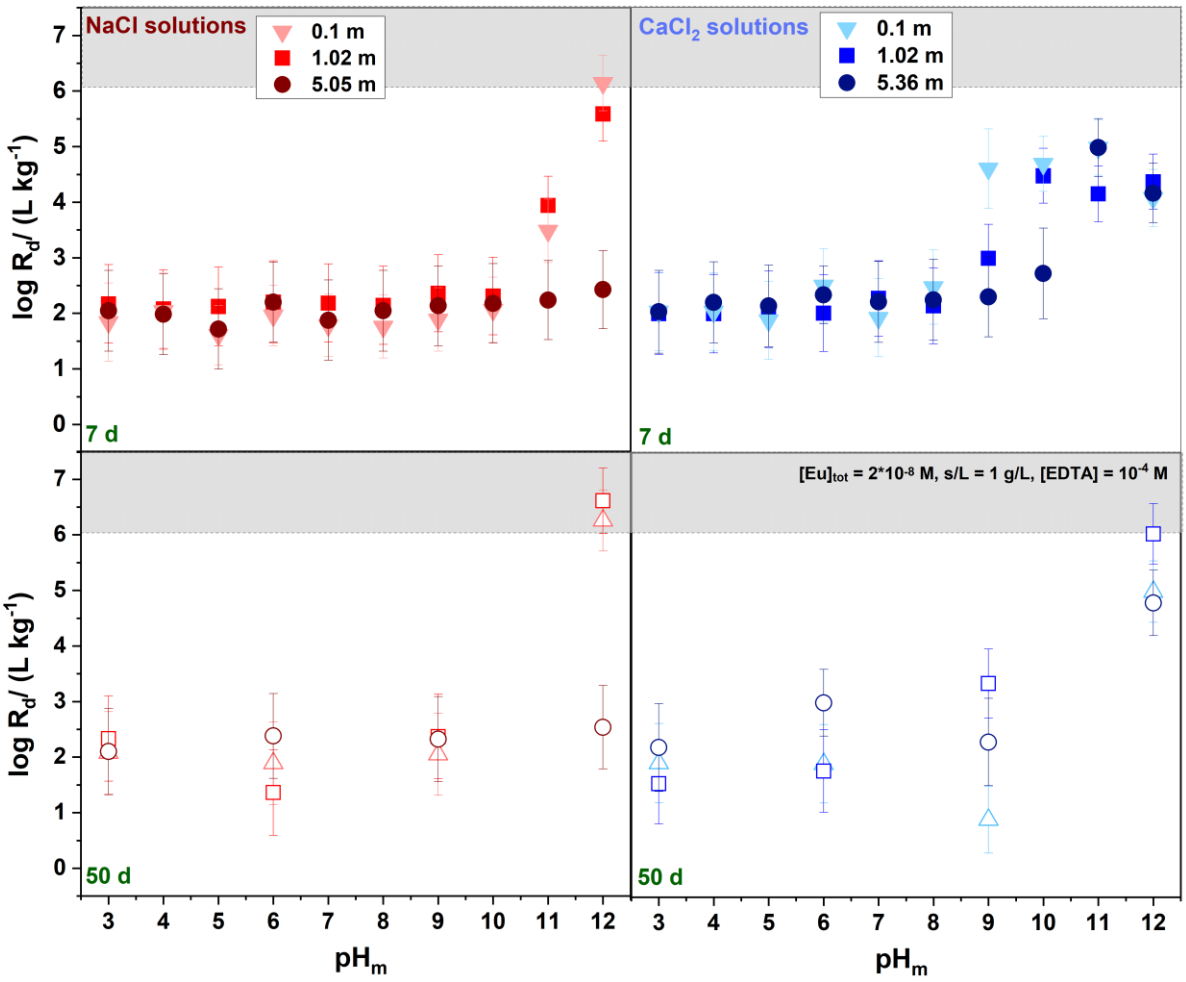

Figure 7.10: Logarithmic distribution coefficients (R_d / L/kg) for the adsorption of Eu(III) on bentonite MX 80 in presence of [EDTA] = 10^{-4} M as a function of pH_m. The data are displayed in NaCl (left) at I_m = 0.1, 1.02, 5.05 m and $CaCl_2$ solutions (right) at I_m = 0.1, 1.02, 5.36 m after sorption times of 7 (top) and 50 d (bottom). Hereby [Eu] = $2 \cdot 10^{-8}$ M and S/V = 1 g/L are used between pH_m = 3 – 12.

In NaCl solutions, a consistently low retention of Eu(III) (log R_d ~ 2 – 3) is observed at $pH_m \leq 10$ for both sorption times. At pH_m = 11, increasing log R_d ~ 4 – 5 are detected. At pH = 12, log R_d ~ 6 are shown. This is only valid after 7 and 50 d of contact time for

NaCl solutions with I_m = 0.1 m and 1.02 m. For the highest ionic strength, a different behavior is obtained for pH ≥ 11: The retention of Eu(III) remains low over the whole pH range. For $CaCl_2$ solutions, a very similar trend compared to NaCl solutions is observed for both sorption times. The retention remains low with log R_d ~ 2 – 3 at pH_m < 9. Subsequently, the retention increases for pH > 9 (log R_d ~ 5 - 6). No significant effect of the different ionic strengths is observed. In order to explain the observed sorption behavior, a species distribution of the aqueous phase is calculated with the geochemical modeling software PHREEQ-C including the ThermoChimie database (see chapter 3.4.1). The observed data are illustrated in Figure 7.11.

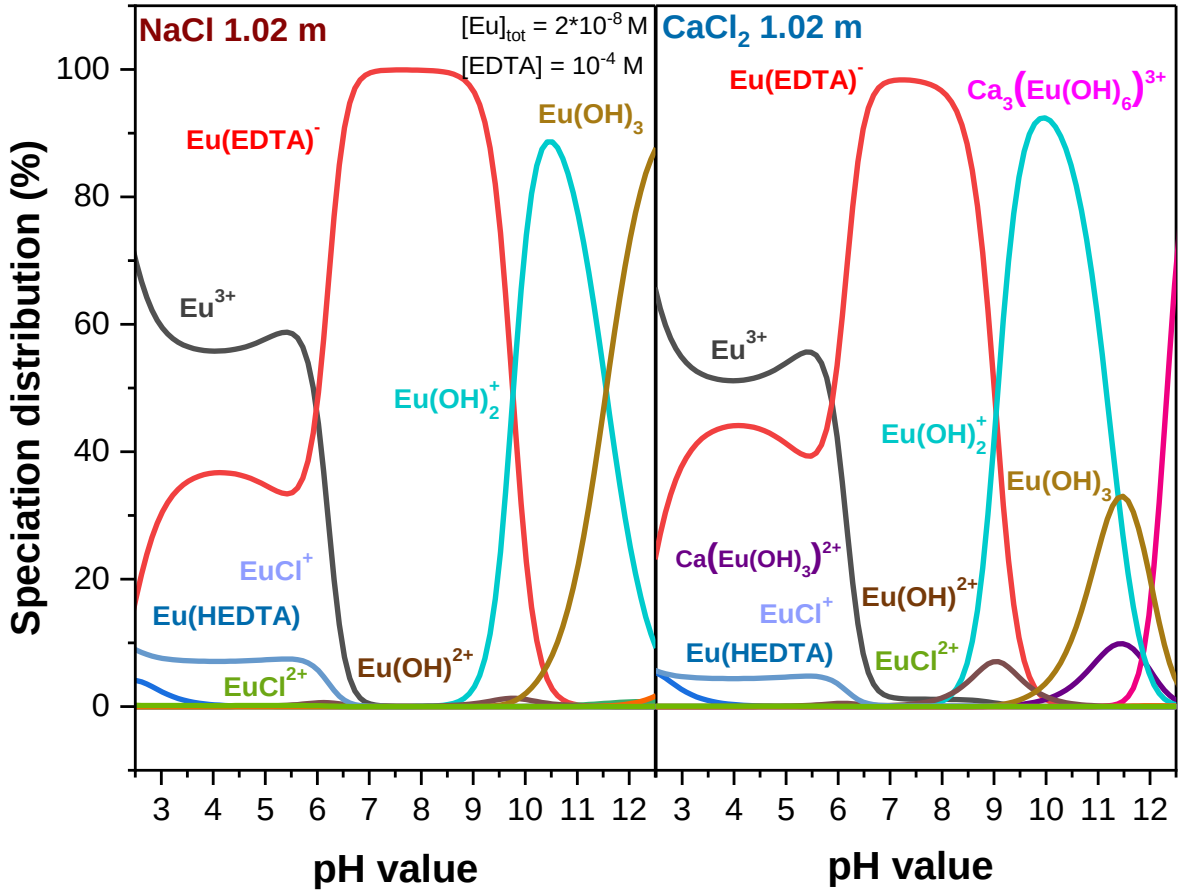

Figure 7.11: Aqueous speciation diagrams, obtained with the geochemical modelling software PHREEQ-C and the ThermoChimie database for the Eu(III) sorption on bentonite MX80 in presence of [EDTA] = 10^{-4} M in NaCl (left) and $CaCl_2$ (right) solution at I_m = 1.02 m.

According to Wang *et al.*, the mineral edge site of montmorillonite in bentonite MX 80 shows a positive surface charge at pH < 4.1, while a negatively charged surface is

observed at pH > 4.1.[76] However, it is important to consider that due to the isomorphic substitution in the octahedral layers, the basal areas are negatively charged regardless of the pH value. In all cases there is also a competition between EDTA and OH groups of the clay surface with regard to the sorption of Eu(III). Between pH = 3 - 10, the formation of aqueous $Eu(EDTA)^-$ complexes predominates over the association of Eu(III) with the OH groups of the clay surface. Consequently, the retention is reduced. At pH > 10, the Eu(III) hydroxo-complexes mainly contribute to the aqueous speciation of Eu(III). Consequently the retention of Eu(III) is increased and EDTA complexes play only a minor role. This leads to an increasing retention of Eu(III) with increasing pH value and is also observed in $CaCl_2$ solutions. The different behavior in NaCl solution with an ionic strength of 5.05 m at pH > 10 cannot be explained at the present state of the art and needs to be further investigated.

Varying the EDTA concentration

Figure 7.12 shows the Eu(III) sorption on bentonite MX 80 in presence of varying EDTA concentrations for NaCl and $CaCl_2$ solutions after 7 d of sorption time. Hereby log R_d values at pH_m = 5 and pH_m = 11 are shown.

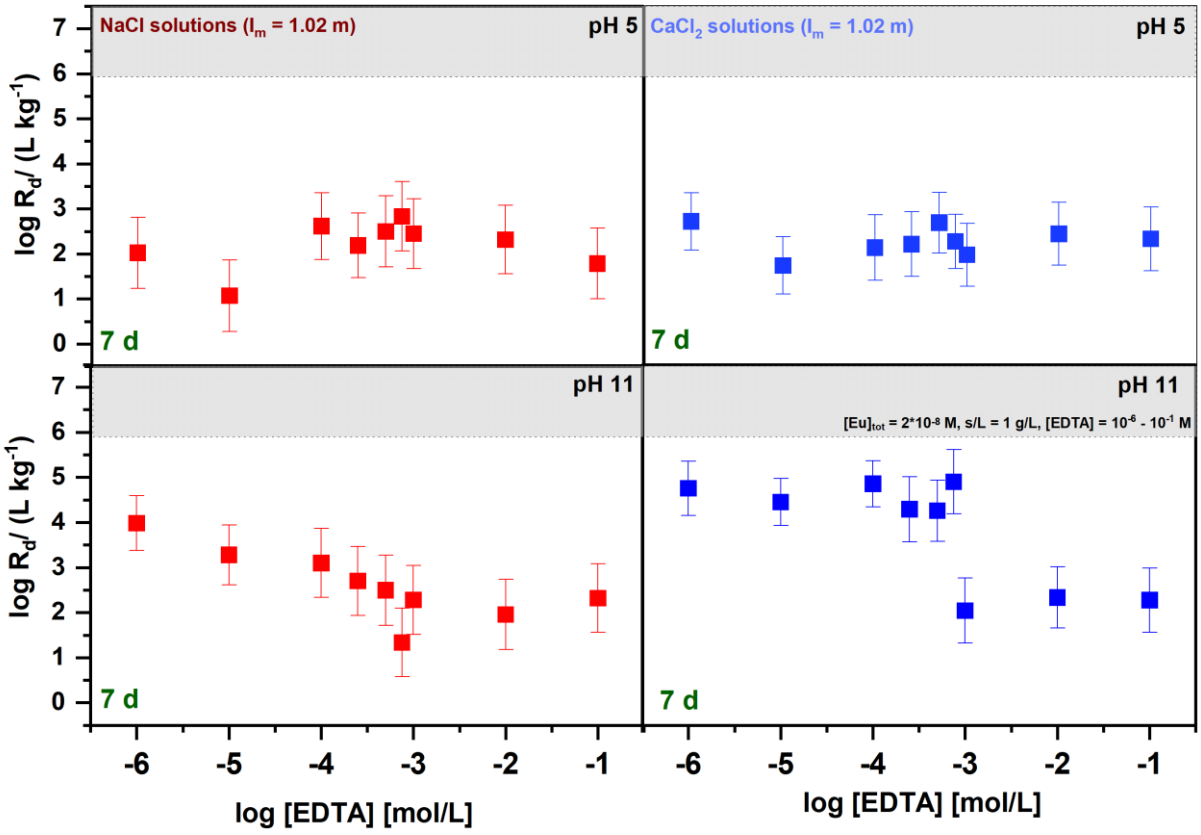

Figure 7.12: Logarithmic distribution coefficients for the adsorption of Eu(III) on bentonite in presence of [EDTA] = 10^{-6} – 0.1 m in NaCl (left) and $CaCl_2$ (right) at pH_m = 5 (top) and pH_m = 11 (bottom) at an ionic strength of 1.02 m for NaCl and $CaCl_2$ solutions at 7 d of sorption time. Hereby [Eu] = $2 \cdot 10^{-8}$ M and S/V = 1 g/L are used.

At pH_m = 5, log R_d ~ 2 - 3 are reached in NaCl and $CaCl_2$ solutions, independent from the varying EDTA concentrations. A precise explanation for this phenomenon can currently not be given. However, it can be speculated that at low EDTA concentrations ([EDTA] < 10^{-3} M) and pH_m = 5, only inner-sphere sorption of Eu^{3+} occurs at the edge sites. This is in good agreement with the surface species SO-Eu^{2+} postulated by Schnurr *et al.*.[101] At higher EDTA concentrations ([EDTA] ≤ 10^{-2} M), a part of the present EDTA can also be absorbed at the mineral surface, so that an Eu(III)

distribution between EDTA complexes in solution and EDTA at the clay surface occurs. This which could lead to the low log R_d values.

At pH_m = 11, in NaCl solution, there is a gradually shift from log R_d ~ 4 to log R_d ~ 2 with increasing EDTA concentration. In $CaCl_2$ solutions, retention is rapidly decreasing from log R_d ~ 5 to log R_d ~ 2, between [EDTA] = 10^{-3} M and [EDTA] = 10^{-2} M. Hereby it is concluded, that the inner-sphere sorption dominates again for [EDTA] ≤ 10^{-3} M, since EDTA complexes play a minor role in this pH region according to Figure 7.11. This is in line with the studies of Schnurr *et al*..[101] At [EDTA] > 10^{-3} M, in both electrolytes, Eu(III) and Ca may be stabilized in solution by EDTA to form ternary Eu(III)-OH-EDTA complexes. This cannot be verified by the speciation calculation, due to the lack of thermodynamic data.

Conclusion bentonite

The uptake of Eu(III) on bentonite MX 80 in the presence of oxalate and EDTA shows no significant effect of different ionic strengths and sorption times up to 50 d. The exception are the log R_d values at $pH_m > 10$ in 5.05 m NaCl solution, which are much lower compared to the log R_d values in 0.1 m and 1.02 m NaCl solutions. The reason for this effect needs to be further investigated.

In the presence of oxalate, medium retention of Eu(III) is observed for $pH_m < 10$ (log $R_d \sim 3 – 4$). For $pH_m > 10$, slightly increasing log $R_d \sim 4 – 5$ are found after both sorption times. In $CaCl_2$ solution, the Eu(III) sorption on bentonite is pH depended: Hereby low log $R_d \sim 2 – 3$ are observed at $pH_m < 8$, while increasing log $R_d \sim 4 – 5$ are obtained for higher $pH_m > 8$. For oxalate, Ca(Ox)(s) precipitates in $CaCl_2$ solutions. This is also expected in NaCl solution, since small amounts of [Ca] are sufficient for the precipitation of Ca(Ox). The exact amount of Ca in the pore water must still be determined. With EDTA as organic ligand and in respect to the sorption of Eu(III), there is in all cases a competition between EDTA and the OH groups of the clay surface. Between pH = 3 and 10, the formation of aqueous $Eu(EDTA)^-$ complexes outweighs the association of Eu(III) with the OH groups of the clay surface. As a result, the retention is reduced. At higher pH values, the association of Eu(III) with the OH groups of the clay surface predominate, while the EDTA complexes no longer play a significant role. This behavior is also observed in $CaCl_2$ solution. The variation of EDTA concentration showed that in NaCl and $CaCl_2$ solutions no significant effect can be detected at $pH_m = 5$. At $pH_m = 11$, decreasing log R_d values were observed in NaCl and $CaCl_2$ solutions with increasing EDTA concentration. In NaCl solutions, the successive decrease in log R_d values with increasing EDTA concentration is due to the stabilization of Eu(III) in solution, which may be related to the formation of ternary Eu(III)-OH-EDTA complexes. In $CaCl_2$, similar to the NaCl solutions, the strong decrease of the log R_d values at $[EDTA] = 10^{-3}$ M could be explained by the stabilization of Eu(III) in solution and the formation of ternary Eu(III)-OH-EDTA/Eu(III)-Ca-EDTA complexes.

8. List of Figures and Tables

Figures

Tables

Figures Appendix

Tables Appendix

9 List of Abbreviations

An	Actinide
BET	Brunauer-Emmett-Teller
C-S-H	Calcium-Silicate-Hydrate
C/S	Calcium-to-Silicon-ratio
DSC	Differential Scanning Caloriemetry
EDTA	Ethylenediaminetetraacetic acid
EDX	Energy Dispersive X-ray Spectroscopy
e.g.	*exempli gratia*
et al.	and others
EXAFS	Extended X-ray- Absorption Fine Structure
FTIR	Fourier-Transformed-Infrared Spectroscopy
GLU	Gluconate
HAW	Highly Active Radioactive Waste
HLW	High Level Radioactive Waste
HCP	Hydrated cement paste
IC	Internal conversion
ICP-OES	*Inductively coupled plasma-optical emission spectroscopy*
i.e.	*id est*
INE	Institute For Nuclear Waste Disposal
I_m	Ionic strength in molal units
ISC	Intersystem Crossing
KARA	Karlsruhe Research Accelerator
KIT	Karlsruhe Institute for Technology
L-/ILW	Low- and intermediate level radioactive waste
Ln	Lanthanide
NEA-TDB	Nuclear Energy Agency – Thermochemical Database
M	Metal
OPA	Opalinus Clay

RN	Radionuclide
RT	Room temperature
RS	Russel Saunders
S	Solid
SIT	Specific Ion Interaction Theory
SEM	Scanning Electron Microscopy
S/V	Solid-to-liquid-ratio
TRLFS	Time Resolved Laser fluorescence spectroscopy
TG	Thermogravimetry
VR	Vibronic relaxation
XRD	X-ray power diffraction

10. Acknowledgements

An dieser Stelle möchte ich mich bei Herrn Professor Dr. Horst Geckeis für die Möglichkeit bedanken, diese Doktorarbeit zu schreiben. Weiterhin möchte ich mich für die Bereitstellung der notwendigen Materialien und Ausrüstung bedanken. Außerdem möchte ich mich für die sehr hilfreichen Besprechungen sowie die Unterstützung bedanken.

Mein Dank gilt auch Dr. Andrej Skerencak-Frech, der mir immer mit Rat und Tat zur Seite stand. Vielen Dank für Deine Geduld, Zeit und für die hilfreichen Tipps und Anregungen zu meiner Arbeit! Weiterer großer Dank gilt Dr. Xavier Gaona und Dr. Marcus Altmaier. Danke für die Anregungen, die Zeit und die Geduld mit der ihr mich unterstützt habt. An dieser Stelle möchte ich auch Dr. Agost Tasi erwähnen, der mir meine ersten Schritte am INE sehr erleichtert hat. Zusätzlich möchte ich Dir für deine Unterstützung meiner Doktorarbeit danken.

Großer Dank geht an dieser Stelle auch an Stephanie Kraft, die mich in allen Belangen zu den ICP-OES Messungen eine große Hilfe war. Außerdem möchte ich mich bei Tobias Hippel bedanken, der mir bei vielen Fragen rund um den Laser geholfen hat. Weiterhin möchte ich mich bei Dieter Schild für die Unterstützung bei meinen SEM-Proben bedanken.

Außerdem möchte ich mich ganz herzlich bei unseren Strahlenschutzbeauftragten Gerhard Christill, Illonca Bachmann und Thorsten Hoffmann bedanken. Ihr habt mir bei allen Arbeitsschritten im Labor sehr geholfen. Ohne euch wäre diese Arbeit gar nicht möglich gewesen. Danke für eure Mühen sowie hilfreichen Anregungen im Laboralltag. Weiterhin möchte ich mich bei Jonas Rentmeister für die tolle Unterstützung und Hilfe bei allen Fragen zu meiner Agron-Box bedanken.

Vielen Dank auch an Kathy Dardenne und Jörg Rothe, die mir mit meinen EXAFS Proben geholfen haben. Vielen Dank für die Geduld und die Zeit, die ihr in mich investiert habt.

An dieser Stelle möchte ich mich auch bei Daniel Glückman, Phillipp Müller, Paul Fürst, Christian Vollmer, Hanna Kaufmann, Nadine Gill, Cedric Reitz, Lukas Zunftmeister und

Nils Huber bedanken. Vielen Dank für die leicht chaotischen Mittagspausen, die guten wissenschaftlichen Gespräche und das humorvolle Miteinander. An dieser Stelle möchte ich mich auch für die moralische Unterstützung bedanken!

Weiterhin möchte ich mich bei Iuliia Androniuk und Rosa Guidone bedanken. Danke, dass ihr mir alle möglichen Fragen zum Thema Zement beantwortet habt. Vielen Dank auch an euch beide für die tollen Zeiten bei verschiedenen Konferenzen!

An dieser Stelle möchte ich auch Hannah Wunderlich hervorheben. Liebe Hannah, vielen Dank für Deine tolle Freundschaft seit dem ersten Tag an der Uni. Danke für deine Unterstützung, Hilfe und dass du mich auf meinem Weg bis hierher begleitet hast! Auf viele weitere tolle Jahre mit Dir!

Großen Dank möchte ich an dieser Stelle auch an Jurij Galanzew richten. Danke, dass Du mich immer moralisch aber auch fachlich unterstützt. Danke, dass du mir jeden Tag den Rücken freihältst und immer für mich da bist!

Weiterhin geht großer Dank an meine Freunde Kim Riedle, Lisa Lauinger, Benjamin Pumphrey, Stefanie Baier, Ann-Marie Bäuerle, Simon Barth und Jessica Pelloth für die seelische und moralische Unterstützung während meines gesamten Studiums. Danke das ihr immer für mich da seid!

Auch möchte ich an dieser Stelle meiner Familie danken, ohne die ich meine Doktorarbeit nicht hätte durchführen können. Danke das ihr mich bereits mein ganzes Leben lang begleitet!